Power-System State Estimation based on PMUs: Static and Dynamic Approaches - from Theory to Real Implementation

THÈSE N^{O} 7665 (2017)

PRÉSENTÉE LE 9 JUIN 2017

À LA FACULTÉ DES SCIENCES ET TECHNIQUES DE L'INGÉNIEUR

GROUPE SCI STI RC

PROGRAMME DOCTORAL EN ENERGIE

ÉCOLE POLYTECHNIQUE FÉDÉRALE DE LAUSANNE

POUR L'OBTENTION DU GRADE DE DOCTEUR ÈS SCIENCES

PAR

Lorenzo ZANNI

acceptée sur proposition du jury:

Dr J. Van Herle, président du jury
Dr S.-R. Cherkaoui, Prof. M. Paolone, directeurs de thèse
Dr W. Sattinger, rapporteur
Prof. A. Abur, rapporteur
Prof. J.-Y. Le Boudec, rapporteur

ÉCOLE POLYTECHNIQUE
FÉDÉRALE DE LAUSANNE

Suisse
2017

Perfection is not attainable, but if
we relentlessly chase perfection,
we will catch excellence.

To my parents Paola and Andrea,
my grandparents Novella, Mirella, Franco and Nerio,
and my uncle Luca.

Acknowledgements

First of all, I would like to sincerely thank my two supervisors, Rachid and Mario, for the guidance and support during the four years of PhD. Additionally, I express my gratitude to Mario for his trust since we met for the first time. I truly thank Prof. Jean-Yves Le Boudec that substantially contributed to my scientific works. A special thank goes to Prof. Ali Abur for the opportunity to do an internship in his lab at Northeastern University, in Boston.
Then, I want to thank all the people I worked and collaborated with: the amazing colleagues, the secretaries as well as the system administrators, the technicians and, last but not least, our industrial partners (National Instruments, Romande Energie, Services industriels de Lausanne and Alliander).
A huge thank goes to my friends both in Lausanne and in Italy for the fun we had together during aperitifs, dinners, nights and holidays. In Lausanne, I particularly thank Paolo, Marco, Asja, Nadia, Chiara, Francesco and Alessio. In Bologna, special thanks go to my cousins (Fede, Je, Nik), Depe&Co, Tox, Mauri, Riki&Co, Franzo&Co. Football has been an important part of my life, so I thank all my football mates. A unique thank goes to Mélanie for the special moments we spent together during the last year.
Finally, I am extremely grateful to my family for all the love and support that were fundamental in this successful journey.

Lorenzo

Abstract

An increasing number of phasor measurement units (PMUs) are being deployed in power systems in order to enhance the situational awareness and, in the near future, we expect that many networks will be extensively equipped with PMUs. These devices provide accurate and synchronized voltage/current phasors (called *synchrophasors*) at a reporting rate up to 60 measurements-per-second, which is a significantly different type of information with respect to the commonly-used voltage/current magnitude and power measurements of remote terminal units (RTUs). The large availability of synchrophasor measurements might improve existing power-system functions or even disrupt the status quo of several automation processes.

Power-system state estimation (SE) is a functionality that might largely benefit from the use of synchrophasor measurements (the power-system state consists of the set of nodal phase-to-ground voltage phasors at all network buses). Best current practice consists in estimating the network state every few tens of seconds (or even minutes) by using asynchronous measurements of RTUs. A measurement infrastructure exclusively composed of PMUs allows SE to become a linear and not iterative process that uses a set of phase-aligned synchrophasor measurements and is characterized by a refresh rate of tens of estimates-per-second and sub-second time-latency. This is what we call *real-time SE*.

PMUs are commonly associated with transmission systems, but are gaining consideration also in the context of distribution networks in order to implement fast control schemes due to the presence of highly-volatile distributed generation and for fault location purposes. Therefore, SE may become a future functionality of distribution management systems (DMSs). The estimated state can be exploited by several DMS functions, such as voltage control, congestion management and even fault management.

Even if SE is a well-established power-system function, it still deserves research in view of the proliferation of PMUs. Indeed, a relevant change of the measurement infrastructure leads to modifications of the SE algorithms. Moreover, improvements in terms of accuracy, computational time and time-latency are required in order to make SE suitable for a wide range of applications, from control to fault management.

In this dissertation, we first describe in detail the advantages of using exclusively synchrophasor measurements for the most common SE algorithms, i.e., weighted least squares (WLS), least absolute value (LAV) and Kalman filter (KF). Then, we propose

new methodologies that improve the accuracy and/or computational performance of WLS and KF. The results of the three above-mentioned SE algorithms are compared via numerical simulations and also by using measurements provided by PMUs installed in two real power-systems. Finally, we illustrate a fault location method that is based on the SE theory.

We developed two methods for the on-line estimation of the process-model uncertainties used by the KF, because power-system operating conditions are continuously varying. Our goal is to improve the estimation accuracy by effectively filtering the measurement noise. We designed a heuristic method for quasi-static conditions and a rigorous method that is also able to deal with step changes of the system state. The former is fast and suitable for real-time implementation, whereas the latter has a significantly higher computational burden. A performance assessment involving KF and WLS is conducted for both transmission and distribution networks.

Zero-injections represent equality constraints in the SE problem. The information associated with zero-injection buses is precious and can be exploited in a particularly efficient manner for the specific case of linear WLS. We propose a method based on LQ-decomposition that strictly satisfies the equality constraints while reducing the state-vector dimension by the number of constraints. Therefore, the computational time is significantly reduced for networks that include a large number of zero-injection buses. Moreover, the proposed method preserves the structure of the linear WLS equations and makes the problem less ill-conditioned.

An important contribution of this dissertation consists in the validation of the theoretical findings via real-scale experiments. We deployed PMUs at every bus in a sub-transmission network and a distribution feeder, both located in Switzerland. First, we demonstrate the practical feasibility of running SE at high refresh-rate (50 estimates-per-second) and low time-latency (below 70 ms). Second, for the two case studies we compare and discuss the results of WLS, LAV and KF by using real synchrophasor measurements.

Applications related to fault management have stringent accuracy and timing requirements. We intend to prove that PMU-based real-time SE exhibits unique accuracy, refresh rate and time-latency, which satisfy the requirements of fault location and, potentially, protective relaying. We propose a fault detection and faulted-line identification method based on WLS-SE. Although it requires a massive deployment of PMUs, this method works for any network and fault type as well as in presence of large amount of distributed generation. Provided that the PMU cost will drop in the coming years, the proposed approach is particularly interesting for distribution networks where fault management can be largely improved.

Keywords: smart grid, power system state estimation, synchrophasor, phasor measurement unit (PMU), linear state estimation, dynamic estimation, weighted least squares, least absolute value, adaptive Kalman filter, measurement noise covariance matrix, process noise covariance matrix, covariance estimation, step processes, pos-

itive definite, zero injection, equality constraints, normal equation, ill-conditioned problem, phasor data concentrator, fault location, protective relaying.

Résumé

Un nombre croissant de “phasor measurement units (PMUs)” vont être déployés dans les réseaux électriques, afin d’améliorer le monitoring et, dans un futur proche, nous pensons que plusieurs réseaux seront en grand partie équipés avec des PMUs. Ces dispositifs fournissent des mesures de phaseurs de tension et de courant, appelés “synchrophaseurs”, qui sont précises, synchronisées, très fréquentes (jusqu’à 60 mesures par seconde). Ce type de mesure est considérablement différent des mesures fournies par “remote terminal units (RTUs)” consistant en des amplitudes de tension et de courant ainsi que des puissances. Une vaste pénétration de PMUs peut améliorer les fonctionnalités existantes ou même changer radicalement le principe de nombreux systèmes d’automation.

L’estimation d’état des réseaux électriques peut bénéficier de l’utilisation des synchrophaseurs (l’état d’un réseau électrique est composé par les phaseurs de tension entre phase et terre dans tous les nœuds). Actuellement, l’état du réseau est estimé chaque dizaine de secondes (ou même chaque minute) en utilisant les mesures asynchrones des RTUs. Au contraire, si nous utilisons une infrastructure de mesure composée exclusivement par des PMUs, l’estimation d’état devient un algorithme qui possède les caractéristiques suivantes : linéaire et non itératif ; taux de rafraîchissement de quelques dizaines d’estimations par seconde ; temps de latence inférieur à une seconde. Nous appelons celui-ci un estimateur d’état en temps réel.

Les PMUs sont souvent associées aux réseaux de transmission, mais il y a un intérêt croissant de les installer aussi dans les réseaux de distribution, afin de contrôler les instabilités causées par la génération distribuée et de localiser les défauts. C’est pourquoi l’estimation d’état pourrait devenir une future fonctionnalité des “distribution management systems (DMSs)” modernes. L’état estimé pourra être utilisé par différentes applications, comme le contrôle de la tension, le contrôle des congestions des lignes, et aussi pour la gestion des défauts.

Bien que l’estimation d’état soit une fonctionnalité consolidée dans le domaine des réseaux électriques, l’avènement des PMUs introduit des nouveaux sujets de recherche. Des modifications doivent être apportées aux algorithmes d’estimation d’état et une considérable amélioration de précision et prestations computationnelles est nécessaire, afin d’élargir la gamme des applications qui peuvent utiliser l’état estimé (du contrôle à la gestion des défauts).

Dans cette thèse, premièrement nous décrivons les avantages à utiliser les synchropha-

seurs par les algorithmes d'estimation d'état les plus communs, comme la méthode des moindres carrés pondérés (MMCP), la méthode des moindres valeurs absolues (MMVA) et le filtre de Kalman (FK). Ensuite, nous proposons des nouvelles méthodes, afin d'améliorer la précision et la prestation computationnelle du MMCP et du FK. Nous comparons les résultats des trois estimateurs mentionnés ci-dessus, soit avec des simulations numériques, soit en utilisant des mesures prises par des PMUs installées dans deux réseaux électriques réels. Enfin, nous présentons une méthode de localisation de défauts qui est basée sur la théorie de l'estimation d'état.

Nous avons développé deux méthodes pour l'estimation des incertitudes du modèle de processus utilisé par le FK ; ils permettent de mettre à jour fréquemment les paramètres du modèle de processus, afin de suivre les conditions opérationnelles du réseau qui changent en continu. L'objectif est d'atteindre une meilleure précision de l'état estimé, grâce à un filtrage efficace du bruit de mesure. Une méthode heuristique a été développée pour fonctionner en régime permanent ou légèrement variable et une méthode rigoureuse a été développée pour suivre l'état du réseau aussi pendant une variation soudaine. Le premier est plus rapide et prêt à une implémentation en temps réel, tandis que le temps computationnel exigé par la deuxième méthode est beaucoup plus élevé. Nous avons effectué une évaluation des performances du FK et du MMCP avec des réseaux de transmission et de distribution.

Les injections-nulles ajoutent des contraintes d'égalité dans le problème d'estimation d'état. Cette information est précieuse et peut être exploitée par le MMCP linéaire. Nous proposons une méthode basée sur la décomposition-LQ qui satisfait les contraintes d'égalité et, en même temps, réduit la dimension du vecteur d'état par le nombre des contraintes. C'est pourquoi, cette méthode baisse considérablement le temps computationnel dans le cas d'un réseau qui a beaucoup de nœuds à injection-nulles. De plus, la structure des équations du MMCP est préservée et le conditionnement du problème est amélioré.

Une contribution très importante de cette thèse consiste à valider les résultats théoriques avec des expériences réelles. Nous avons déployé des PMUs dans chaque nœud de deux réseaux en Suisse : un réseau de sub-transmission et un feeder de distribution. Premièrement, nous visons à démontrer la faisabilité d'implémenter un estimateur d'état qui donne une estimation chaque 20 millisecondes et qui a une latence en dessous de 70 millisecondes. Deuxièmement, nous comparons et discutons les résultats de MMCP, MMVA et FK qui utilisent les mesures réelles des PMUs.

Les besoins opérationnels des applications pour la gestion des défauts sont très stricts en termes de précision et de timing. Nous voulons démontrer que l'estimation d'état basée sur les PMUs possède les caractéristiques nécessaires pour être utilisée pour la localisation des défauts et, potentiellement, comme relais de protection. Nous avons développé une méthode capable de détecter un défaut et d'identifier la ligne correspondante. Cette méthode est basée sur la théorie de l'estimation d'état avec le MMCP. Malgré qu'elle nécessite un déploiement massif des PMUs, cette méthode fonctionne pour tous les types de réseau et de défaut, même en présence d'une grande

quantité de génération distribuée. A condition que le coût des PMUs baisse dans les prochaines années, cette approche est particulièrement intéressante pour les réseaux de distribution dans lesquels il y a encore une marge d'amélioration significative dans la gestion des défauts.

Mots clefs : réseau électrique intelligent, estimation d'état linéaire, synchrophaseur, phasor measurement unit (PMU), méthode des moindres carrés pondérés, méthode des moindres valeurs absolues, filtre de Kalman, matrice de covariance du bruit de mesure, matrice de covariance du bruit du processus, estimation des matrices de covariance, injections-nulles, contraintes d'égalité, localisation de défauts, relais de protection.

Contents

List of Figures

List of Tables

List of Symbols

$\mathbf{A}$	state-transition matrix
a, b, c	phase indexes in a three-phase power system
d	number of network branches
$\mathbf{e}$	measurement error vector
f	power-system frequency
$\mathbf{G}$	gain matrix of the LWLS
$\mathbf{H}$	measurement matrix
$\mathbf{I}$	identity matrix
J	objective function of the LWLS
k	time-step index
$\mathbf{K}$	*hat matrix* of the LWLS
$\mathbf{L}$	Kalman gain
m	number of measurements
n	number of state variables
N	number of previous time-steps used for the on-line estimation of the DKF process model uncertainties
p	number of equality constraints due to zero-injection buses
$\mathbf{P}_{k\|k-1}$	prediction-error covariance matrix of the DKF
$\mathbf{P}_{k\|k}$	estimation-error covariance matrix of the DKF
$\mathbf{Q}$	process noise covariance matrix
$\mathbf{R}$	measurement noise covariance matrix
$\mathbf{r}$	measurement residual vector
$\mathbf{r}^N$	normalized measurement residual vector
$\mathbf{r}^N_{\mathbf{x}}$	normalized state-estimate residual vector
s	number of network buses
$\mathbf{S}$	residual sensitivity matrix of the LWLS
T	number of simulation time-steps
$\mathbf{T}$	covariance matrix of the innovations
$\mathbf{v}$	measurement noise vector
V	voltage magnitude
$\mathbf{x}$	state vector
w	number of zero-injection buses
$\mathbf{w}$	process noise vector

$\mathbf{y}$	innovation vector
$\mathbf{z}$	measurement vector
δ	voltage phase-angle
$\mathbf{\Omega}$	covariance matrix of the LWLS measurement residuals

List of Acronyms

ACF	auto correlation function
AKF	adaptive Kalman filter
CT	current transformer
DESL	distributed electric system laboratory
DG	distributed generation
DKF	discrete Kalman filter
DMS	distribution management systems
EKF	extended Kalman filter
EMS	energy management system
EPFL	École Polytechnique Fédérale de Lausanne, which is the french name of the Swiss
FPGA	field-programmable gate array
GPS	global positioning satellite
GUM	Guide to the expression of uncertainty in measurement
KF	Kalman filter
LAV	least absolute value
LHS	left-hand side
LNR	largest normalized residual
LQD	LQ-decomposition
LWLS	linear weighted least-squares
MEP-ZIB	maximum estimated power at the zero-injection buses
NE	normal equation
PDC	phasor data concentrator
PECE	prediction-error covariance estimation
PMU	phasor measurement unit
PT	potential transformer
pu	per unit
PV	photovoltaic
QRD	QR-decomposition
RHS	right-hand side
RMSE	root mean square error
RTS	real-time simulator
RTSE	real-time state estimation
RTU	remote terminal unit

SCADA	supervisory control and data acquisition system
SE	state estimation
TVE	total vector error
WLS	weighted least-squares

Nomenclature

Static state: set of nodal voltage phasors at all network buses.

Dynamic state: dynamic state variables of the generator machines, such as phase-angle and speed.

Measurement model: mathematical model that expresses the relationship between the measurements and the state variables at a time-step k.

Process model: mathematical model of the time evolution of the system state at a time-step k as a function of the system state at time-step $k-1$ and of the controllable inputs at a time-step $k-1$.

Static estimator: state estimator that computes the system state by using only the incoming set of measurements at a time-step k.

Dynamic estimator: state estimator that, at each time-step k, computes the probability density function of the system state in two stages: first, it predicts the state from time-step $k-1$ to time-step k by exploiting a process model; then, it compute the estimated state by using the incoming measurements at time-step k. Thus, unlike static estimators, a dynamic estimator uses also the information contained in the previous state-estimate.

Tracking estimator: static estimator that uses the incoming measurements at a time-step k to update the previous estimate at time-step $k-1$, instead of fully executing the iterative estimation from a flat-start initialization at every time-step.

Robust estimator: state estimator with high *breakdown-point*. The breakdown-point is the smallest number of bad data that can lead state estimation to an incorrect solution. Note that the breakdown point is highly influenced by the measurement redundancy; indeed, a poor redundancy limits the number of bad data that the estimator can reject.

Real-time state estimator: state estimator characterized by high refresh-rate and low latency.

Hybrid state estimator: state estimator that uses both SCADA measurements provided by RTUs and synchrophasor measurements provided by PMUs.

Conventional or SCADA measurements: measurements provided by RTUs, which

typically consist of voltage/current magnitudes and power flows/injections.

Synchrophasor: accurate and time-synchronized phasor measured by PMUs.

Critical measurement: measurement whose loss makes the network unobservable.

Leverage measurement: a measurement characterized by a structure of the measurement equation that is different from that of the other measurements. Specifically, the row of the measurement matrix $\mathbf{H}$ corresponding to a leverage measurement has very different (smaller or larger) entries compared to the other rows. This creates a kind of insensitivity of the state estimator with respect to this measurement, i.e., the measurement residual (defined as the difference between the raw and the estimated measurement) corresponding to a leverage measurement remains small even in presence of a large error.

Pseudo-measurement: measurements with large uncertainties that represent predictions typically based on historical data or forecasts.

Virtual measurement: measurements with very small uncertainties that are used to approximate the exact information associated with zero-injections.

Introduction

Context and Motivation

In general, the state of a power system refers to the minimum set of independent variables from which all the power-system quantities (voltages, current/power flows/injections, etc.) can be computed. This is why the state fully defines the power-system operating conditions. In this dissertation, the *state* always refers to the so-called *static state* that is typically defined as the set of nodal phase-to-ground voltage phasors at all network buses. We do not treat the estimation of the *dynamic states* that consist in the state variables of the generator machines, such as rotor speed and angle.

The knowledge of the state is fundamental in the operation of the transmission system as it is required by several functions, such as security control and economic dispatch. Therefore, the procedure that infers the power-system state has to be accurate and reliable.

Until the 1970s, the power-system state was computed by means of a load-flow calculation that used the raw measurements of voltages and powers [1]. This procedure had several weaknesses: for instance, it was vulnerable to missing measurements and the presence of measurement errors affected dramatically the load-flow solution. To overcome these limitations, Schweppe proposed to combine load-flow and statistical estimation theory and introduced *state estimation* (SE) in power systems [2, 3, 4]. SE consists in solving an optimization problem that processes the raw measurements and a network model[1] with the aim of determining the most likely estimate of the power-system state, which is called *estimated state* [5, 6]. Intuitively, SE evaluates how well the measurements fit the constraints given by the network model. Provided that the network is observable[2] and there is sufficient *measurement redundancy*[3], the state

[1] The network model consists of the combination of network topology and electrical parameters of the network components.

[2] A network is *observable* if all the state variables can be uniquely computed for a given set of measurements and network topology [7].

[3] Measurement redundancy is defined as the ratio between the number of measurements and the number of state variables; a sufficiently high redundancy is fundamental to guarantee the benefits of SE, such as the ability to identify measurement and network-model errors.

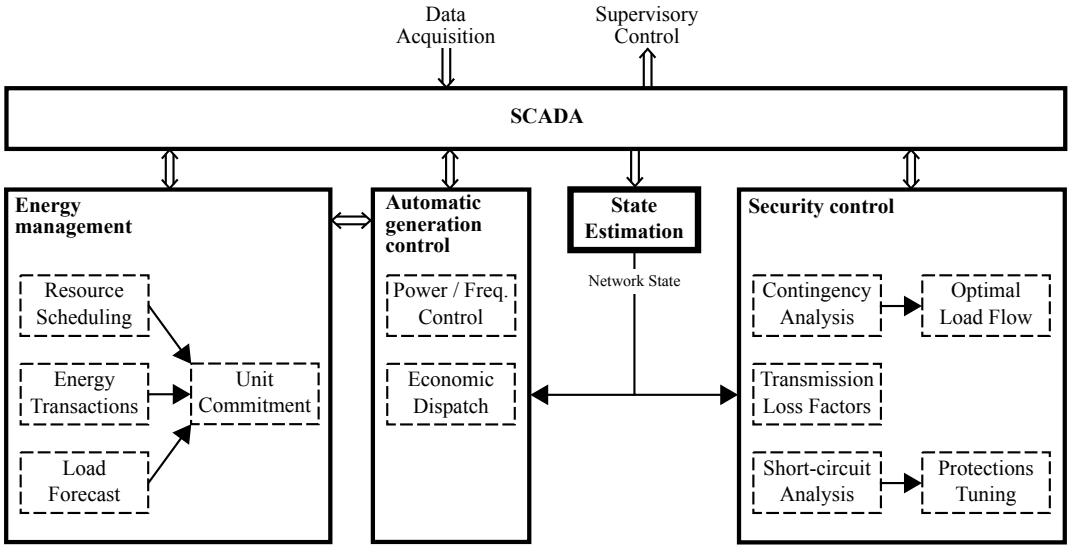

Figure 1 – Typical structure of an EMS.

estimator is able to filter the measurement noise, tolerate measurement losses, identify *bad data*[4] in the measurement set [8, 9, 10] and determine network-model errors [11, 12, 13]. The foregoing properties of SE allow the system operator to obtain an estimated state that is more reliable than the raw measurements as well as to compute quantities that are not directly measured by a meter.

In the last decades, SE has become a core situation-awareness component for power-system operators [14, 15, 16]. As depicted in Fig. 1, the SE solution constitutes the essential input of several functions of modern energy management system (EMS). An EMS is located at every power-system control center and helps the grid operator to optimally and securely manage the electrical assets. The EMS includes a supervisory control and data acquisition system (SCADA) that collects telemetered measurements from various devices, such as remote terminal units (RTUs), and provides the measurements to the state estimator.

Moreover, the increasing penetration of distributed energy resources at medium and low voltage levels is calling for monitoring and control also in distribution systems. Therefore, SE may become a standard functionality of distribution management systems (DMSs). The estimated state can be exploited by several DMS functions, such as voltage control, congestion management and even fault management as we will explain later in this dissertation.

Traditionally, SE is supplied with measurements provided by RTUs that consist of voltage/current magnitudes and power flows/injections, which are commonly called

[4] A bad datum or bad measurement is defined as a measurement that contains a gross error. This can be due to several causes, such as malfunctioning telecommunication, meter failure, erroneous wire-connection or software bug.

conventional measurements or *SCADA measurements*. The availability of this type of measurements has lead to the development of state estimators with the following characteristics:

1. The estimation algorithm is non-linear and iterative due to the non-linearity of the function that links power and current-magnitude measurements to the voltage state-variables;
2. The refresh-rate is in the order of tens of seconds or minutes due to the low acquisition-rate of RTUs and the high-computation time of the SE algorithm;
3. RTU measurements are usually not time-stamped or are time-stamped with poor accuracy (not sub-second); in the former case, they are time-stamped in the SCADA by inferring the delay added by both RTU processing and telecommunication network. Therefore, the time-skew between measurements can introduce significant and unknown errors in the estimated state;
4. One of the buses has to be chosen as the the reference bus for the voltage phase-angle that is fixed to an arbitrarily selected value (usually equal to zero) at this bus.

Concerning the SE methods, the most widely-used algorithm in power-system SE is the *weighted least-squares* (WLS).The success of the WLS has been driven by its statistical properties and low computational complexity that have eased the development of efficient techniques (e.g., the fast-decoupled version [17]) and have enabled the use of sparse matrix tools.

Nowadays, the increasing deployment of phasor measurement units (PMUs) enables the incorporation of phasor measurements in power-system SE. PMUs provide accurate and time-stamped phasors, called *synchrophasors*, at a typical reporting rate of 30, 50 or 60 measurements per second [18]. Note that PMUs measure magnitude and phase-angle of voltage/current phasors and, thus, they are capable of directly measure the power-system state. The synchronization is usually provided by the global positioning satellite (GPS) system, but can be also disseminated with dedicated communication protocols characterized by jitter below 100 ns. The PMU technology is experiencing a fast evolution triggered by the hardware-cost reduction and by the increasing requirements of several power-system applications [19].

The voltage and current synchrophasors provided by PMUs can be included in the measurement set to enhance the SE performance; a state estimator that uses both conventional and PMU measurements is typically called *hybrid state estimator* [20, 21, 22, 23, 24, 25]. However, the improvement is still limited if SCADA measurements are necessary to achieve the network observability or to ensure a sufficient measurement redundancy.

As PMUs start populating the network, in some portions of the grid the observability and redundancy requirements are matched only with PMUs [26, 27, 28]. The fact that the state of these portions of the grid can be estimated by using exclusively synchrophasor measurements leads to a remarkable improvement of the SE performance [29, 30]. The main benefits for SE relying only on this type of measurements are listed here below:

1. When only voltage and current phasors are used, the equations linking measurements and state variables, called *measurement model*, are linear. Therefore, we can employ linear SE that is characterized by lower computational time, increased numerical stability and no approximations in the measurement model. For instance, it is well known that the linear WLS (LWLS) is not iterative as the estimated state is given by the solution of an exact quadratic problem;
2. Each synchrophasor measurement is time-stamped and its phase-angle is aligned. Hence, the measurements can be phase-aligned at the data collection point, even if they are received at different time-instants. This ensures a superior accuracy of the SE solution as the set of measured phasors is coherent with respect to time;
3. The very high PMU reporting-rate leads to a SE process characterized by high refresh-rate and low latency, which is typically called *real-time SE* (RTSE);
4. As PMUs directly measure the phasor phase-angle, we do not need to choose a reference bus where the voltage phase-angle is fixed. All the phase-angle measurements are processed at the same time by the state estimator [31].

Besides, a PMU measures the phasors in each of the three phases, so that we can use three-phase SE. The advantage consists in the possibility to account for network-parameter asymmetries and for imbalances in the network operating-conditions.

Thanks to the linearity of the measurement model and the high refresh-rate, two alternative SE techniques can be reconsidered for power-system SE: the least absolute value (LAV) [32] and the Kalman filter (KF) [33]. WLS and LAV belong to the category of *static estimators*, i.e., estimators that exploit only the information contained in the incoming set of measurements. The KF is a *dynamic estimator* because, in addition to the incoming measurements, it also makes use of the so-called *process model* that is a mathematical representation of the time-evolution of the power-system state. To avoid confusion throughout the dissertation, we clarify that static and dynamic estimators will be used to estimate only the static state of the power-system (voltage phasors at all network buses) and not the dynamic states (state variables of the generators).

The LAV estimator applied to linear SE with PMUs has been thoroughly investigated in [34, 35, 36]. The results prove that the LAV is competitive with the LWLS in terms of accuracy and computational time.

Regarding the KF, most of the contributions have investigated various versions of non-linear KF, which are described in Section 1.4.2. The classic linear version of the KF is typically called *discrete KF* (DKF). However, from the best of our knowledge, the topic of DKF based on PMUs is tackled only in [37].

In this dissertation, we present and demonstrate the advantages of using a measurement infrastructure exclusively composed of PMUs for linear power-system SE. Indeed, in the near future we expect to have an increasing number of networks that are observable with synchrophasor measurements. Particular attention is dedicated to the DKF that has been proposed in many different versions in the literature. We focus on the validation of the persistent process-model and on the estimation of its uncertainty (i.e., the error covariances); we also provide an extensive performance assessment of the DKF with respect to the LWLS. Another important and original contribution of this dissertation consists in the presentation of the SE results obtained in two real power-systems equipped with PMUs, which allow us to validate the theoretical findings in real-scale experiments. Finally, we prove that the outstanding characteristics of PMU-based SE in terms of accuracy, refresh rate and latency can fulfill the stringent requirements dictated by fault-location and even protections schemes. This peculiarity might set the foundations for a new category of protection systems.

Dissertation outline

This dissertation is organized as follows.

In Chapter 1, we introduce the linear SE problem that uses only synchrophasor measurements provided by PMUs. First, we describe the typical features of the linear measurement model that links phasor measurements and state variables. In particular, we illustrate the procedure to derive the measurement matrix and the measurement-noise covariance matrix. Then, we illustrate the formulation and characteristics of three algorithms that are commonly used for linear power-system SE: LWLS, LAV and DKF.

Chapter 2 is entirely dedicated to the study of the DKF applied to power-system SE. We propose two methods for the estimation of the time-varying uncertainties of the process-model. The first is a heuristic method that continuously assesses the process-noise variances in order to maintain an effective filtering action in changing network operating-conditions, although it exhibits significant error during step changes. The second method, called prediction-error covariance estimation (PECE), consists in a convex optimization problem that is able to cope with step-processes. The adequacy of the persistent process-model is statistically validated. We also theoretically prove and numerically validate the better accuracy of the DKF with respect to the LWLS, provided that a correct process-model is employed.

In Chapter 3, we discuss the problem of LWLS-SE with linear equality constraints associated with zero-injection buses. In particular, we propose a method based on LQ-decomposition that strictly satisfies the equality constraints and reduces the dimension of the state vector. We demonstrate the performance improvement of the proposed method with respect to other well-known approaches to handle zero-injections via numerical simulations.

In Chapter 4, we describe the implementation of RTSE in two real power systems: a sub-transmission network and a distribution feeder equipped with PMUs. We briefly describe the adopted measurement infrastructure, then we thoroughly analyze and compare the SE results provided by the LWLS, LAV and DKF. These real-scale experiments allow us to validate the findings of Chapters 1, 2 and 3 as well as to assess the RTSE performance in real power networks.

In Chapter 5, we propose a new method based on LWLS-SE for fault detection and faulted-line identification. We conducted extensive tests by considering different network configurations and fault types as well as with a large amount of generation. We evaluated both accuracy and time-latency performance of the proposed approach.

Finally, in Chapter 6 we provide the main outcomes of this dissertation and possible directions for future research.

Original Contributions

The list of the original contributions of this dissertation is given in the following.

1. *Included in Chapter 2* – We consider a persistent process-model (already used for DKF-SE of power-systems) that is characterized by time-varying and unknown uncertainties. Then, we propose a heuristic method that estimates the process-noise variances used by the DKF from a set of previous state-estimates. This method is conceived to maintain an effective filtering action in different network operating-conditions that include quasi-static conditions but not step changes in the system state. It is straightforward to implement and the user needs to set a single parameter that is the number of previous state-estimates. Additionally, it is designed to be computationally fast so that it is suitable for deployment in real-time embedded hardware. It is worth pointing out that, although we test the proposed heuristic method only in power-system SE, it can be also used in other application fields as long as the assumptions hold.

2. *Included in Chapter 2* – We propose a method, called *prediction-error covariance estimation* (PECE), that, in addition to effectively filter the measurement noise in quasi-static conditions, is able to follow the state during step changes.

The measurement model is assumed to be linear, known and time-invariant. The PECE method consists in a convex optimization problem that infers the prediction-error covariances from a set of previous innovations and is proved to have a unique solution. Thanks to a set of constraints, the inferred prediction-error covariance matrix is always positive semi-definite, which ensures the DKF numerical stability. As for the heuristic method of point (1), the user needs to set a single parameter that is the number of previous innovations. With respect to the heuristic method, the PECE method is based on a rigorous theory and is able to cope with step-varying processes, but it has a significantly higher computational burden. To the best of our knowledge, no other method proposed in the literature relying on the same assumptions is able to achieve the accuracy performance of the PECE method in both quasi-static conditions and during step changes. The PECE method can be applied also in other domains as long as the assumptions hold.

3. *Included in Chapter 2* – We present an extensive performance assessment of the methods proposed in points (1) and (2) with respect to the classic LWLS via numerical simulations. We assume that the measurements are affected only by random noise and no systematic errors are present. We generated several scenarios considering a transmission networks and a distribution feeder in quasi-static conditions and when step changes in the state variables occur. We showed that the DKF outperforms the LWLS in terms of accuracy when the network is in quasi-static conditions. During a step change in the system state, the DKF employing the PECE method of point (2) is able to accurately track the state, whereas the DKF employing the heuristic method of point (1) experiences a delay. The computational time of the DKF employing the heuristic method is comparable with the LWLS one for the adopted case studies (medium size networks), whereas the PECE method is computationally more expensive.

4. *Included in Chapter 2* – Making reference to a DKF employing the heuristic method of point (1), we statistically validate the adequacy of the persistent process-model via numerical simulations. Moreover, we theoretically prove and numerically validate the better accuracy of the DKF with respect to the LWLS, provided that a correct process-model is employed.

5. *Included in Chapter 3* – In the context of LWLS-SE with linear equality constraints associated with zero-injection buses, we propose a method based on LQ-decomposition that strictly satisfies the equality constraints and reduces the number of state variables, thus reducing the computational time. Other advantages of this method consist in making the problem less ill-conditioned and in preserving both the structure of the LWLS normal equation and the positive semi-definiteness of the coefficient matrix.

6. *Included in Chapter 4* – We validate the theoretical findings via real-scale exper-

iments. We installed PMUs at every bus in two real power-systems consisting of a sub-transmission network and a distribution feeder. Network observability and a high redundancy level are achieved by using exclusively synchrophasor measurements. We describe the field implementation comprising sensor and PMU installations, telecommunication network, phasor data concentrator and RTSE. We demonstrate the feasibility of running RTSE at high refresh-rate (50 estimates-per-second) and low time-latency (below 70 ms). Then, the fundamental contribution consists in the presentation and detailed discussion of the results of different linear SE algorithms (LWLS, LAV and DKF) for the two case studies.

7. *Included in Chapter 5* – We propose a fault detection and faulted-line identification method based on LWLS-RTSE that uses synchrophasor measurements. It does not need any model of loads/generators and has no prior knowledge of the fault type and of the neutral connection, even though it requires that a PMU is installed at every bus. We assume that every PMU measure the voltage and current-injection phasors at the respective bus. We evaluated the faulted-line identification accuracy by conducting extensive tests including different network configurations and fault types as well as large amount of generation. We also computed the time-latency and we demonstrated that PMU-based RTSE can satisfy the requirements of fault location and, potentially, protective relaying. Therefore, it may theoretically combine the execution of protection and fault-location functions that are usually separated processes. The proposed approach is particularly interesting for distribution networks where fault management can be largely improved.

1 Theory on PMU-based power-system state estimation

In this chapter we introduce the formulation of the PMU-based state estimation problem. First, we describe the characteristics of the linear measurement model that links the phasor measurements to the state variables. Second, we illustrate the formulation and features of static and dynamic algorithms that we use in this dissertation: linear weighted least squares (LWLS), least absolute value (LAV) and discrete Kalman filter (DKF).

1.1 Linear Measurement Model

The main ingredient of a power-system state estimator is the measurement model that is the function linking the state variables with the measurements. In this dissertation, we assume to use only PMU synchrophasor measurements; therefore, the measurement model becomes linear and exact provided that the phasors of both state variables and measurements are expressed in rectangular coordinates. In most of the literature on power-system SE and also in this dissertation, the state variables are the bus-voltage phasors in the entire network. It is worth mentioning that current flows have been used as state variables in distribution system SE [38]; in general, also bus current-injections or branch voltages can be used, or even a mix of them, provided that they are independent state variables.

Let us consider a three-phase power-system composed of a set of buses $\mathcal{S}$ with cardinality $s = |\mathcal{S}|$ and a set of branches $\mathcal{D}$ with cardinality $d = |\mathcal{D}|$[1]. The triplet of the three phases is $\mathcal{P} = \{a, b, c\}$. The network state is denoted by $\mathbf{x} \in \mathbb{R}^n$, where $n = 3 \cdot 2s$ is the cardinality of the set of state variables $\mathcal{N}$. The state is composed of the real and imaginary parts of the bus phase-to-ground voltage phasors in every phase (a, b, c) at

[1] The operator $|\ \ |$ denotes the cardinality of a set.

every bus $i \in \mathcal{S}$:

$$\mathbf{x} = [\mathbf{V}_{1,re}^{a,b,c}, \ldots, \mathbf{V}_{i,re}^{a,b,c}, \ldots, \mathbf{V}_{s,re}^{a,b,c}, \mathbf{V}_{1,im}^{a,b,c}, \ldots, \mathbf{V}_{i,im}^{a,b,c}, \ldots, \mathbf{V}_{s,im}^{a,b,c}]^T \tag{1.1}$$

where

$$\begin{aligned} \mathbf{V}_{i,re}^{a,b,c} &= [V_{i,re}^{a}, V_{i,re}^{b}, V_{i,re}^{c}] \\ \mathbf{V}_{i,im}^{a,b,c} &= [V_{i,im}^{a}, V_{i,im}^{b}, V_{i,im}^{c}] \end{aligned} \tag{1.2}$$

are, respectively, the real and imaginary parts of the voltage phasor at bus $i \in \mathcal{S}$ in the three phases a, b and c. Note that we have not chosen any reference bus for the voltage phase-angle as it is directly measured by PMUs [31]. All the voltage phase-angle measurements are processed simultaneously by the state estimator together with the other measurements; therefore, the state estimator can identify errors also in phase-angle measurements, given a sufficient level of redundancy.

Let us define three sets of measurements: $\mathcal{M}_1$ is the set of buses where PMUs measure phase-to-ground voltage phasors, $\mathcal{M}_2$ is the set of buses where PMUs measure current-injection phasors, and $\mathcal{M}_3$ is the set of branches where PMUs measure current-flow phasors. Then, the complete set of phasor measurements $\mathcal{M}$ with cardinality $m = |\mathcal{M}|$ is assumed to be composed of:

- $3 \cdot m_1$ bus phase-to-ground voltage phasors, where $m_1 = |\mathcal{M}_1|$;
- $3 \cdot m_2$ bus current-injection phasors, where $m_2 = |\mathcal{M}_2|$;
- $3 \cdot m_3$ current-flow phasors, where $m_3 = |\mathcal{M}_3|$;

Therefore, the measurement vector $\mathbf{z} \in \mathbb{R}^m$ is equal to:

$$\mathbf{z} = [\, \mathbf{z}_V, \mathbf{z}_{I_{\text{inj}}}, \mathbf{z}_{I_{\text{flow}}} \,]^T \tag{1.3}$$

where

$$\begin{aligned} \mathbf{z}_V &= [\, \mathbf{V}_{1,re}^{a,b,c}, \ldots, \mathbf{V}_{i,re}^{a,b,c}, \ldots, \mathbf{V}_{m_1,re}^{a,b,c}, \mathbf{V}_{1,im}^{a,b,c}, \ldots, \mathbf{V}_{i,im}^{a,b,c}, \ldots, \mathbf{V}_{m_1,im}^{a,b,c} \,] \quad i \in \mathcal{M}_1 \\ \mathbf{z}_{I_{\text{inj}}} &= [\, \mathbf{I}_{1,re}^{a,b,c}, \ldots, \mathbf{I}_{i,re}^{a,b,c}, \ldots, \mathbf{I}_{m_2,re}^{a,b,c}, \mathbf{I}_{1,im}^{a,b,c}, \ldots, \mathbf{I}_{i,im}^{a,b,c}, \ldots, \mathbf{I}_{m_2,im}^{a,b,c} \,] \quad i \in \mathcal{M}_2 \\ \mathbf{z}_{I_{\text{flow}}} &= [\, \mathbf{I}_{1,re}^{a,b,c}, \ldots, \mathbf{I}_{i,re}^{a,b,c}, \ldots, \mathbf{I}_{m_3,re}^{a,b,c}, \mathbf{I}_{1,im}^{a,b,c}, \ldots, \mathbf{I}_{i,im}^{a,b,c}, \ldots, \mathbf{I}_{m_3,im}^{a,b,c} \,] \quad i \in \mathcal{M}_3. \end{aligned} \tag{1.4}$$

In the remainder of this dissertation, the bus phase-to-ground voltage is simply called voltage and the bus current-injection is simply called current-injection, where not

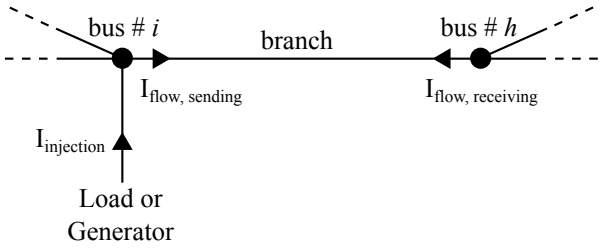

Figure 1.1 – Convention employed for current injections and flows with positive sign.

otherwise specified. Moreover, Fig. 1.1 shows the current directions that are assumed to have positive sign. The convention employed for the current injections is as follows: the positive sign denotes a current entering in a bus. Concerning the current flows, the positive sign denotes a current exiting from a bus. On each branch there are two current flows at both ends; if we consider a generic branch between buses # i and # h where $i < h$, we call *sending-end current flow* the current flow departing from the bus with the smallest index (bus # i) and *receiving-end current flow* the current flow departing from the bus with the largest index (bus # h).

The linear measurement model that relates the measurements to the state variables is

$$\mathbf{z} = \mathbf{H}\mathbf{x} + \mathbf{v} \tag{1.5}$$

where $\mathbf{H}$ is a $m \times n$ matrix called *measurement matrix* and $\mathbf{v}$ is the *measurement noise*. The measurement noise is assumed to be white and Gaussian:

$$p(\mathbf{v}) \sim \mathcal{N}(0, \mathbf{R}) \tag{1.6}$$

where $\mathbf{R}$ is the *measurement noise covariance matrix*.

1.1.1 The measurement matrix H

The linearity of the measurement model makes $\mathbf{H}$ an exact matrix linking the measurements with the state variables, whereas in conventional non-linear SE the matrix $\mathbf{H}$ is a Jacobian matrix. Besides, $\mathbf{H}$ does not depend anymore on the state variables, so that it remains constant in time with no need to update it at every time-step. It needs to be recalculated only in case of changes in the network topology or in the composition of the measurement set. Indeed, the elements of $\mathbf{H}$ are calculated from the network topology and the electrical parameters of the network components, such as transmission lines and transformers. In Appendix A.1, we provide the derivation of the blocks of $\mathbf{H}$ related to three type of measurements: voltage phasors, current-injection phasors and current-flow phasors.

In addition to the aforementioned real-time phasor measurements from PMUs, in this

dissertation we will also consider pseudo-measurements and zero-injection buses. Details are given in what follows.

Pseudo-measurements are, typically, nodal power-injection measurements consisting in predictions based on historical data or forecasts; therefore, the uncertainty associated with pseudo-measurements is large. To maintain the linearity of the measurement model, power-injection pseudo-measurements at a bus can be transformed in an equivalent current-phasors by assuming to know the voltage at that bus. Even if the voltage is not directly measured, we can assume that it is close to 1 per unit (pu) in normal operating conditions. This procedure has been already proposed in the literature, e.g., [38].

Zero-injection buses are network buses characterized by an injected power strictly equal to zero, which is, for instance, the case of interconnection substations. In linear SE, zero-injections are treated as current phasors with real and imaginary parts equal to zero. As this information contains no error, it constitutes a set of equality constraints that can be added to power-system SE. In the literature there are several methods to include equality constraints in SE. This subject is treated in Chapter 3 with focus on linear SE. A simple yet approximated way to include equality constraints in SE is to convert the constraining equations in additional measurements with very small uncertainties, so-called *virtual measurements* [39, 40].

It is important to point out that in this dissertation we make a clear distinction between virtual measurements and pseudo-measurements, whereas in the literature virtual measurements are often considered as a particular type of pseudo-measurements. Virtual measurements approximate the exact information linked to zero-injections and pseudo-measurements are predictions characterized by large uncertainties that are typically based on historical data or forecasts.

1.1.2 The measurement noise covariance matrix R

In this dissertation, we assume that the measurement noise covariance matrix $\mathbf{R}$ is diagonal, which implies that there is no correlation between measurements (i.e., the measurements are independent and identically distributed).

This is a common assumption in power-system SE, although there are cases where this correlation is not negligible and accounting for that in the matrix $\mathbf{R}$ can lead to an improvement of the SE accuracy. For example, this is the case of single-phase measurements that are derived from three-phase multifunction meters [41], or when we use pseudo-measurements that can be correlated between each other [42]. Whereas, we assume that:

- the measurements are provided by different sensors installed in every phase;

- the cross-talk interferences between nearby sensors are negligible;
- the measurements in every phase are treated separately and not merged in a single-phase measurement.

Besides, it has been demonstrated that the correlation between the multiple channels of the same PMU can be neglected without affecting the SE accuracy [42].

Each diagonal entry of $\mathbf{R}$ is the variance of a measurement, which includes the cumulative uncertainty of both sensor and PMU. In this dissertation, a *sensor* refers to an electrical device that transforms the input voltage or current signal taken from the electrical network into signals that can be acquired by instruments or meters. Examples of sensors are potential and current transformers (PTs and CTs), capacitor dividers or Rogowsky coils. In the context of PMU-based SE, the sensor interfaces the network voltage and current signals with a PMU.

The measurement uncertainty introduced by sensor and PMU is generally characterized by a component associated with a random effect (uncertainty of type A) and a component associated with a systematic effect (uncertainty of type B). The definitions of error and uncertainty are given in the *Guide to the expression of uncertainty in measurement* (GUM) [43], and briefly recalled here below.

A measurement result is always affected by an *error* that has two components called *systematic* and *random*. Note that the measurement error cannot be known exactly. The GUM defines the two error components as follows [43]:

> Random error presumably arises from unpredictable or stochastic temporal and spatial variations of influence quantities. The effects of such variations, hereafter termed *random effects*, give rise to variations in repeated observations of the measurand. Although it is not possible to compensate for the random error of a measurement result, it can usually be reduced by increasing the number of observations; its expectation or expected value is zero.
>
> Systematic error, like random error, cannot be eliminated but it too can often be reduced. If a systematic error arises from a recognized effect of an influence quantity on a measurement result, hereafter termed a *systematic effect*, the effect can be quantified and, if it is significant in size relative to the required accuracy of the measurement, a correction or correction factor can be applied to compensate for the effect. It is assumed that, after correction, the expectation or expected value of the error arising from a systematic effect is zero.

Then, the *uncertainty* of a measurement result represents the lack of exact knowledge of the measurand. The measurement result can be corrected from the recognized systematic effects, but it is still only an estimate of the value of the measurand, because of the uncertainty arising from random effects and from imperfect correction of the systematic effects.

In the GUM, the uncertainty components are grouped into two categories based on their method of evaluation, *type A* or *type B* evaluation, that is used to obtain the uncertainty characterizing a random or systematic effect, respectively. Both types of evaluation are based on probability distributions and the uncertainty components resulting from either type are quantified by variances or standard deviations.

Therefore, the estimated variance characterizing an uncertainty component obtained from a type A evaluation is calculated from series of repeated observations and is the statistically estimated variance, and the estimated standard deviation is called a *type A standard uncertainty*. The type A evaluation estimates the expected value and the variance of a random quantity as the arithmetic mean and the square root of the experimental standard deviation of the observations, respectively.

For an uncertainty component obtained from a type B evaluation, the estimated variance is evaluated using available knowledge (not from repeated observations), and the estimated standard deviation is called a *type B standard uncertainty*. The latter is evaluated by scientific judgment based on all of the available information, such as previous measurement data, experience, manufacturer's specifications (e.g., instrument accuracy-class[2]), calibration certificates, etc.

If no information is available on the uncertainty distribution, one may assume that a normal distribution was used to calculate the quoted uncertainty, and recover the standard uncertainty by dividing the quoted uncertainty by a *coverage factor* for the normal distribution, which is usually 3.

The type A uncertainty of a voltage or current measurement result accounts for the random noise introduced by grid phenomena (e.g., thermal effects, converters), sensor and A/D converter of the PMU. This noise, and thus the uncertainty, is highly dependent upon the grid, the type of employed sensor and the PMU hardware/software. Note also that, given multiple measurements of a certain quantity, it is also not trivial to separate the noise from the variations of this quantity. To remove the quantity's variations, one should make the difference between two or more measurements of the same quantity taken from distinct meters. From the analysis of actual PMU data, the distribution of the type A uncertainty can be considered Gaussian [44].

The type B uncertainty of a sensor is specified by its class by means of the Standard IEC 61869 that gives the maximum magnitude and phase-angle errors. For instance, for CTs and PTs one should make reference to [45] and [46], respectively. Sometimes the sensor's calibration certificates are available so that the systematic effect can be compensated. As stated in the GUM, in this specific case we can assume that the expected value of the error arising from the sensor's systematic effect is zero. The type

[2]The accuracy class is a designation assigned to a measurement instruments the errors of which remain within specified limits under prescribed conditions of use

B uncertainty of a PMU is commonly derived by its total vector error (TVE) that is defined in [47]. When separate values for the magnitude and phase-angle errors are given, then these values are considered; otherwise, we need to make assumptions on how the TVE is distributed between voltage magnitude and phase-angle (e.g., [40]). If we assume a normal distribution, the type B uncertainty can be calculated by dividing the uncertainty by a coverage factor, typically equal to 3.

The total uncertainty of a measurement is the sum of the type A and type B uncertainties of sensor and PMU. This uncertainty, expressed as a variance, composes the generic diagonal element of the measurement noise covariance matrix $\mathbf{R}$.

The uncertainty of the instrumentation measuring voltage or current is commonly given in terms of magnitude and phase-angle. In the linear measurement model presented in 1.1, the phasor measurements are expressed in rectangular coordinates; thus, we need to project the uncertainty from polar to rectangular coordinates. To this end, we use the procedure reported in [48, Chapter 6.4]. The final formulas used to perform the projection are recalled here below.

Let us assume to have a voltage-phasor measurement expressed in terms of magnitude V and phase-angle δ, and the corresponding uncertainties σ_V and σ_δ, respectively. The variances of the projected real and imaginary parts of the voltage phasor are

$$\begin{aligned}\sigma^2_{V_{re}} &= V^2 e^{-2\sigma^2_\delta}\Big[\cos^2\delta\Big(\cosh(2\sigma^2_\delta)-\cosh(\sigma^2_\delta)\Big)\\ &\quad+\sin^2\delta\Big(\sinh(2\sigma^2_\delta)-\sinh(\sigma^2_\delta)\Big)\Big]\\ &\quad+\sigma^2_V e^{-2\sigma^2_\delta}\Big[\cos^2\delta\Big(2\cosh(2\sigma^2_\delta)-\cosh(\sigma^2_\delta)\Big)\\ &\quad+\sin^2\delta\Big(2\sinh(2\sigma^2_\delta)-\sinh(\sigma^2_\delta)\Big)\Big] \qquad (1.7)\end{aligned}$$

$$\begin{aligned}\sigma^2_{V_{im}} &= V^2 e^{-2\sigma^2_\delta}\Big[\sin^2\delta\Big(\cosh(2\sigma^2_\delta)-\cosh(\sigma^2_\delta)\Big)\\ &\quad+\cos^2\delta\Big(\sinh(2\sigma^2_\delta)-\sinh(\sigma^2_\delta)\Big)\Big]\\ &\quad+\sigma^2_V e^{-2\sigma^2_\delta}\Big[\sin^2\delta\Big(2\cosh(2\sigma^2_\delta)-\cosh(\sigma^2_\delta)\Big)\\ &\quad+\cos^2\delta\Big(2\sinh(2\sigma^2_\delta)-\sinh(\sigma^2_\delta)\Big)\Big]\,. \qquad (1.8)\end{aligned}$$

In the literature, the measurement uncertainty is calculated in different ways: (1) as a constant value [6, Chapter 7.2], [24], (2) as a percentage of the measured quantity

[49, 50], or (3) as a combination of the two [51, 23].

In the works presented in this dissertation, we will always specify the assumptions on the measurement uncertainty. Based on these assumptions, $\mathbf{R}$ will be considered time-variant or -invariant.

1.2 Linear weighted least squares

The WLS estimator is a *static estimator* as it does not exploit any time-variant dependency of either the measurements or the state variables. It minimizes the sum of the squared residuals weighted by the measurement variances, a residual being the difference between the measurement and the fitted value obtained with the model. The WLS relies on the following assumptions:

1. The measurement noise is Gaussian-distributed with mean value equal to zero.
2. The measurements are uncorrelated, so that $\mathbf{R}$ is diagonal.
3. Matrix $\mathbf{H}$ is of full rank, which means that the network is observable. Specifically: (1) $m \geq n$, which is a necessary condition for the network observability, and (2) rank$(\mathbf{H}) = n$.

Given the linear measurement model in (1.5) and defining the estimated state as $\widehat{\mathbf{x}}$, the LWLS residual is defined as

$$\mathbf{r} = \mathbf{z} - \mathbf{H}\widehat{\mathbf{x}}\,. \tag{1.9}$$

We use the *hat* "$\widehat{\ }$" to denote estimated quantities throughout the dissertation. The LWLS consists in solving an unconstrained optimization problem that minimizes the following objective function:

$$\min_{\widehat{\mathbf{x}}} \quad J(\widehat{\mathbf{x}}) = \frac{1}{2}\mathbf{r}^T\mathbf{R}^{-1}\mathbf{r} \tag{1.10}$$

that, as $\mathbf{R}$ is assumed to be diagonal, can be also written as

$$\min_{\widehat{\mathbf{x}}} \quad J(\widehat{\mathbf{x}}) = \frac{1}{2}\sum_{i=1}^{m}\frac{r_i^2}{R_{ii}}\,. \tag{1.11}$$

The solution of this optimization problem reduces to the well-known *normal equation* (NE):

$$\mathbf{G}\widehat{\mathbf{x}} = \mathbf{H}^T\mathbf{R}^{-1}\mathbf{z} \tag{1.12}$$

where $\mathbf{G}$ is the so-called *gain matrix*:

$$\mathbf{G} = \mathbf{H}^T\mathbf{R}^{-1}\mathbf{H} \,. \tag{1.13}$$

Equation (1.12) is a system of linear equations of the well-known form $\mathbf{A}\widehat{\mathbf{x}} = \mathbf{b}$, where $\mathbf{A}$ is the *coefficient matrix* and corresponds to $\mathbf{G}$, and $\mathbf{b}$ corresponds to $\mathbf{H}^T\mathbf{R}^{-1}\mathbf{z}$. The NE is usually solved by Cholesky factorization as $\mathbf{G}$ is positive definite. Therefore, $\mathbf{G}$ does not need to be inverted. The covariance matrix of the estimated state is given by

$$\text{cov}(\widehat{\mathbf{x}}) = \mathbf{G}^{-1} \,. \tag{1.14}$$

It is also interesting to give the relation between measurements $\mathbf{z}$ and estimated-measurements $\widehat{\mathbf{z}}$, which is given by the following expression:

$$\widehat{\mathbf{z}} = \mathbf{H}\widehat{\mathbf{x}} = \mathbf{H}\mathbf{G}^{-1}\mathbf{H}^T\mathbf{R}^{-1}\mathbf{z} = \mathbf{K}\mathbf{z} \tag{1.15}$$

The row entries of $\mathbf{K}$ (so-called *hat matrix*) indicate the local redundancy of every measurement. For instance, a large diagonal element (relative to the off-diagonal elements) implies that the estimated value of a measurement is almost entirely determined by its measured value, i.e., the local redundancy is poor.

The residual vector is linked to the measurement-error vector $\mathbf{e} = \mathbf{z} - \mathbf{H}\mathbf{x}$ by the so-called *residual sensitivity matrix* $\mathbf{S}$, which represents the sensitivity of the residuals to the measurement errors:

$$\mathbf{r} = \mathbf{z} - \widehat{\mathbf{z}} = (\mathbf{I} - \mathbf{K})\mathbf{e} = \mathbf{S}\mathbf{e} \tag{1.16}$$

The matrices $\mathbf{K}$ and $\mathbf{S}$ can be checked to identify critical and leverage measurements, which are both defined in what follows.

A *critical measurement* is defined as a measurement whose loss makes the network unobservable, i.e., decreases the rank of $\mathbf{H}$. A critical measurement appears in parts of the network characterized by low local redundancy. Several topological or numerical methods for the observability analysis and the identification of critical measurements have been proposed in the literature, e.g., [52, 53].

A *leverage measurement* is defined as a measurement characterized by a structure of the measurement equation that is different from that of the other measurements [54]. Specifically, the row of $\mathbf{H}$ corresponding to a leverage measurement has very different (smaller or larger) entries compared to the other rows. This creates a kind of insensitivity of the state estimator with respect to this measurement, i.e., the residual of a leverage measurement remains small even in presence of a large measurement error. Leverage measurements can be identified with various methods proposed in the literature, e.g., [55].

Both critical and leverage measurements have very small (identically zero for critical measurements) residuals even when the measurements are affected by a large error, which means that the corresponding diagonal element of $\mathbf{S}$ is very small (identically zero for critical measurements). Therefore, the effects of critical and leverage measurements are similar, the main difference lying in the fact that the elimination of leverage measurement does not lead to a loss of network observability.

As it is known, the WLS is vulnerable to bad data as they lead to biased estimates. Therefore, the WLS solution needs to be given to a bad-data processor that detects, identifies and removes bad data. A widely-used method for bad-data processing is the largest normalized residual test (LNR) [8, 6]. First, the residual vector is computed using (1.9), then its covariance matrix is calculated as

$$\text{cov}(\mathbf{r}) = \mathbf{\Omega} = \mathbf{R} - \mathbf{H}\mathbf{G}^{-1}\mathbf{H}^T = \mathbf{R}\mathbf{S} \tag{1.17}$$

and the normalized residual of the i^{th} measurement is

$$r_i^N = \frac{|r_i|}{\sqrt{\Omega_{ii}}}\,. \tag{1.18}$$

The normalized residuals are Gaussian-distributed as $\sim \mathcal{N}(0,1)$. Therefore, the LNR test detects the presence of bad data when the LNR exceeds a statistical threshold, usually 3 or 4. In this case, the measurement with the LNR is flagged as bad data and the SE is re-computed without using this measurement. We repeat the procedure until no more bad data are detected. The LNR test can reliably identify only a single bad-data or multiple non-interacting bad-data (i.e., simultaneous bad-data whose residuals are not correlated). In presence of multiple interacting bad-data (i.e., simultaneous bad-data whose residuals are correlated), the hypothesis testing identification method is proven to have superior performance [9, 6].

1.3 Least absolute value

The LAV belongs to the category of *robust estimators*[3], because it possesses an intrinsic bad-data rejection capability and has no need to employ a separate bad-data processor [32]. The LAV is the most employed robust estimator in power-system SE, as it can be made computationally efficient by exploiting the power system's properties. Despite its desirable bad-data rejection property, the LAV has two main shortcomings: the computational time is not competitive with that of the WLS, and the algorithm remains vulnerable against *leverage measurements* (see Section 1.2 for the definition of leverage

[3] A robust estimator is an estimator with high *breakdown-point*, i.e., the smallest number of bad data that can lead to an incorrect SE solution. Note that the breakdown point is highly influenced by the measurement redundancy; indeed, a poor redundancy limits the number of bad data that the estimator can reject.

measurements). However, these weaknesses can be alleviated when the measurement model is linear thanks to the use of PMUs [34]. The remarkable improvements of the LAV performance are listed here below:

- the LAV computational time becomes comparable to that of the LWLS, especially when bad data are present;
- the LAV optimization problem reduces to a linear-programming problem;
- the vulnerability to leverage measurements can be eliminated by strategic scaling of the measurement matrix without affecting the SE solution.

The LAV is an optimization problem that minimizes the sum of the absolute values of the residuals:

$$\begin{aligned} \min \quad & \mathbf{c}^T|\mathbf{r}| \\ \text{subject to:} \quad & \mathbf{z} - \mathbf{H}\widehat{\mathbf{x}} = \mathbf{r} \end{aligned} \tag{1.19}$$

where $\mathbf{c}$ is a vector of ones. Note that the LAV does not require the measurement noise covariance matrix $\mathbf{R}$. The computation of the $\mathbf{R}$ entries is not trivial, as shown in Section 1.1.2.

In [34], the optimization problem (1.19) is re-arranged as an equivalent linear programming problem. The procedure is recalled in what follows. First, the problem is formulated as

$$\begin{aligned} \min \quad & \bar{\mathbf{c}}^T|\bar{\mathbf{r}}| \\ \text{subject to:} \quad & \bar{\mathbf{M}}\bar{\mathbf{r}} = \mathbf{z} \\ & \bar{r}_i \geq 0 \quad i = 1, ..., 2n + 2m \end{aligned} \tag{1.20}$$

where

$$\begin{aligned} \bar{\mathbf{c}}^T &= [\mathbf{0}_{2n} \quad \mathbf{1}_{2m}] \\ \bar{\mathbf{r}} &= [\mathbf{x}_a \quad \mathbf{x}_b \quad \mathbf{r}_a \quad \mathbf{r}_b]^T \\ \bar{\mathbf{M}} &= [\mathbf{H} \quad -\mathbf{H} \quad \mathbf{I}_m \quad -\mathbf{I}_m] \,. \end{aligned} \tag{1.21}$$

In (1.21), $\mathbf{0}_{2n}$ is a $1 \times 2n$ vector of zeros, $\mathbf{1}_{2m}$ is a $1 \times 2m$ vector of ones, $\mathbf{I}_m$ is a $m \times m$ identity matrix, $\mathbf{x}_a$ and $\mathbf{x}_b$ are $1 \times n$ vectors, and $\mathbf{r}_a$ and $\mathbf{r}_b$ are $1 \times m$ vectors. Finally, we can compute the estimated state and the residual as

$$\begin{aligned} \mathbf{x} &= \mathbf{x}_a^T - \mathbf{x}_b^T \\ \mathbf{r} &= \mathbf{r}_a^T - \mathbf{r}_b^T \,. \end{aligned} \tag{1.22}$$

1.4 Dynamic linear estimation via discrete Kalman filter

The SE accuracy can be further enhanced by filtering the measurement noise. This can be accomplished by using dynamic SE. We recall that dynamic SE models the time-evolution of the physical process by means of a process model. Dynamic SE consists in computing the probability density function of the system state in two steps: the *prediction step*, also called *time update*, exploits a process model to predict the state; the *estimation step*, also called *measurement update*, introduces the incoming measurements to compute the estimated state. Hence, a sort of memory is introduced in the state estimator, because it also employs prior information contained in the state estimates of the previous time-steps.

1.4.1 General process-model and discrete Kalman filter

Let us consider a general process model consisting in the following discrete-time time-variant linear equation [56]:

$$\mathbf{x}_k = \mathbf{A}_k \mathbf{x}_{k-1} + \mathbf{B}_k \mathbf{u}_k + \mathbf{w}_k \tag{1.23}$$

where

- k is the time-step index;
- $\mathbf{x} \in \mathbb{R}^n$ is the system state;
- $\mathbf{u} \in \mathbb{R}^{u_c}$ is a set $\mathcal{U}_c$ of known controllable variables and $u_c = |\mathcal{U}_c|$;
- $\mathbf{w} \in \mathbb{R}^n$ is the process noise;
- $\mathbf{A}$ is an $n \times n$ matrix, called *state-transition matrix*, that links the state at time-step $k-1$ with the state at time-step k;
- $\mathbf{B}$ is an $n \times u_c$ matrix that links the state with the controllable variables;

The process noise $\mathbf{w}_k$ is assumed to be a Gaussian-white sequence:

$$p(\mathbf{w}_k) \sim \mathcal{N}(0, \mathbf{Q}_k) \tag{1.24}$$

where $\mathbf{Q}_k$ is the *process noise covariance matrix*. Note that the matrices $\mathbf{A}_k$, $\mathbf{B}_k$ and $\mathbf{Q}_k$ are, in general, time-variant.

In standard theory of dynamic state estimators, it is also assumed that the process noise $\mathbf{w}_k$ in (1.23) and the measurement noise $\mathbf{v}_k$ in (1.5) are uncorrelated:

$$\mathbb{E}[\mathbf{w}_k \mathbf{v}_k^T] = \mathbf{0}\,. \tag{1.25}$$

One of the most common dynamic estimators is the KF. The DKF is the linear KF resulting from the linear process and measurement models defined in (1.23) and (1.5), respectively.. The DKF relies on the following assumptions:

1. The process and measurement models are linear;
2. The process and measurement noises are Gaussian-distributed with mean value equal to zero, as denoted by (1.6) and (1.24), respectively;
3. The process and measurement noises are uncorrelated, as denoted by (1.25);
4. Matrix $\mathbf{H}$ is of full rank, which means that the network is observable. Specifically: (1) $m \geq n$, which is a necessary condition for the network observability, and (2) rank$(\mathbf{H}) = n$.

The DKF recursive equations are given here below [56]:

Prediction step

$$\widehat{\mathbf{x}}_{k|k-1} = \mathbf{A}_k \widehat{\mathbf{x}}_{k-1|k-1} + \mathbf{B}_k \mathbf{u}_k \tag{1.26}$$

$$\mathbf{P}_{k|k-1} = \mathbf{A}_k \mathbf{P}_{k-1|k-1} \mathbf{A}_k^T + \mathbf{Q}_k \tag{1.27}$$

Estimation step

$$\mathbf{L}_k = \mathbf{P}_{k|k-1} \mathbf{H}^T (\mathbf{H} \mathbf{P}_{k|k-1} \mathbf{H}^T + \mathbf{R}_k)^{-1} \tag{1.28}$$

$$\widehat{\mathbf{x}}_{k|k} = \widehat{\mathbf{x}}_{k|k-1} + \mathbf{L}_k (\mathbf{z}_k - \mathbf{H} \widehat{\mathbf{x}}_{k|k-1}) \tag{1.29}$$

$$\mathbf{P}_{k|k} = (\mathbf{I} - \mathbf{L}_k \mathbf{H}) \mathbf{P}_{k|k-1} \tag{1.30}$$

where $\widehat{\mathbf{x}}_{k|k-1}$ is the predicted state given the knowledge of the process prior to time-step k, $\mathbf{L}_k$ is the Kalman gain, $\widehat{\mathbf{x}}_{k|k}$ is the estimated state given $\mathbf{z}_k$, and $\mathbf{I}$ is the identity matrix. Finally, $\mathbf{P}_{k|k-1}$ and $\mathbf{P}_{k|k}$ are the covariance matrices of the prediction and estimation errors, respectively. Note that $\mathbf{H}$ lacks of the subscript k, because it is time-invariant except for sporadic changes in the network topology.

From (1.26)–(1.30), it is clear that the KF optimality strongly depends on the selection of the correct values of $\mathbf{Q}_k$ and $\mathbf{R}_k$. We will thoroughly discuss the assessment of the

process-model uncertainty in Chapter 2.

After the prediction step, we can also define the innovation $\mathbf{y}_k$ and its covariance matrix $\mathbf{T}_k$ as

$$\mathbf{y}_k = \mathbf{z}_k - \mathbf{H}\widehat{\mathbf{x}}_{k|k-1} \tag{1.31}$$

$$\mathbf{T}_k = \mathbf{H}\mathbf{P}_{k|k-1}\mathbf{H}^T + \mathbf{R}_k \,. \tag{1.32}$$

The innovation plays an important role in Kalman filtering as it is used to check the optimality of the filter as well as for bad-data detection/identification.

1.4.2 Historical notes on Kalman filter in power-system state estimation

In this section, we present in a chronological order some relevant contributions that deal with power-system state estimation via KF. Other works that are inadvertently missed constitute equally important contributions.

Since 1960 when R. Kalman presented the KF in his famous work [33], the research on KF applied to power-system SE has been limited to few contributions. In principle, the KF can provide an estimation accuracy better than the WLS, but this goes at the expense of a higher algorithm complexity. Specifically, some of the problems related to the KF implementation are listed here below:

1. the need of a process model that matches the power-system state dynamics that we are interested to track, which is not trivial to be determined and may involve the definition of several parameters;
2. the development of complementary applications becomes more challenging. For instance, a bad-data processor has to take into account that a large residual can be due not only to a measurement error, but also to a sudden state-change that violates the process model;
3. the higher computational time does not facilitate real-time implementation.

In 1970, Schweppe mentioned the possibility to use a process model already in his first work [2] and shortly after Debs and Larsonn dedicated an entire paper to power-system SE via KF [57]. They propose a linear KF that employs a linear process model and a DC load-flow approximation[4] for the measurement model. The employed process model

[4]The DC load-flow approximation consists in assuming loss-less lines (resistance equal to zero) and voltages equal to nominal values of 1 pu at every bus. Therefore, losses and reactive-powers are

is the well-known random-walk process-model denoted by

$$\mathbf{x}_k = \mathbf{x}_{k-1} + \mathbf{w}_k \tag{1.33}$$

where the only parameter to be set is the process-noise covariance matrix $\mathbf{Q}_k$. This matrix is assessed by an a-priori direct search that is known to be a neither robust nor optimal approach as the simulated scenarios cannot take into account all the operating conditions. The KF and WLS results are compared as a function of the process-noise covariance matrix and of the time-resolution of the measurements. This contribution remained a sporadic attempt and KF was rapidly abandoned in favor of the WLS.

Nishiya et al. [49] propose a method that is able to discriminate between three anomalies, i.e. occurrence of bad data, changes in network configuration and sudden state-variations. It consists in examining the innovation of a non-linear version of the KF, so-called *extended KF* (EKF), that uses (1.33) as process model. In particular, the skewness of the distribution of the innovation sequence is an indicator of the presence of bad-data. Then, if the normalized innovations of the power-flow measurements exceed a certain threshold, a change in the network configuration is suspected and the network topology is re-estimated. Otherwise, the large values of the normalized innovations are attributed to a sudden state-variation.

Da Silva et al. [51] propose an EKF that tracks the state of power systems operating under quasi-static conditions. They use the general process-model of (1.23) where $\mathbf{A}$ and $\mathbf{B}$ are assessed on-line by means of the Holt's linear exponential smoothing method presented in [58], whereas $\mathbf{Q}$ is kept constant. Nevertheless, the authors suggest adaptive estimation of $\mathbf{Q}$ for improved performance. It is shown that the KF looses track of the state trajectory when a sudden change occurs. In this case, the advice of the authors is either to disregard the prediction or to use more frequent measurements. In addition, a bad-data processing algorithm based on both innovation and residual vectors is proposed.

In [59], the authors present an EKF that incorporates short-term load forecasting based on artificial neural network to obtain a realistic process model. The estimation step is iterative as they include second-order terms in the approximation of the non-linear measurement function. The scheme for anomaly identification proposed in [49] is used.

The EKF proposed in [60] incorporates a weight exponential-function in order to increase the robustness of the filter. It includes second-order terms in the EKF as in [59]. The performance is shown in presence of the three anomalies mentioned in [49].

The Authors of [61] explored a process model based on the load-flow equations. The

disregarded and the voltage phase-angles are linearly related to active powers. See [1, Chapters 9.7 and 14.5] for further details.

EKF performance are assessed by employing the DC load-flow approximation. In [62], this approximation is not employed in order to include also the voltage magnitude in the state vector by using active- and reactive-power measurements. They use an iterated version of the EKF called *iterated EKF*.

In what follows, we present the recent works on power-system SE via KF and it is worth pointing out that all of them assume to have PMU data in the measurement set.

In [63] and [64], Jain and Shivakumar evaluate the impact of using PMU phasor measurements in combination with SCADA measurements on the estimation accuracy of an EKF state estimator. They employ the process model proposed in [51]. Later in 2009, they also published a literature review on tracking and dynamic SE techniques [65]. A *tracking estimator* is a static estimator that uses new measurements to update the past estimate instead of fully executing the iterative estimation from a *flat-start*[5] initialization at every time-step [66, 58].

The Authors of [50] propose to use an unscented KF [67], which is a KF that is able to deal with highly non-linear models and does not need the computation of the Jacobian matrices. They use the scheme for anomaly identification proposed in [49] and they employ the process model proposed in [51]. Due to the fact that $\mathbf{Q}$ is kept constant, it is shown that the unscented KF estimation performance is degraded as soon as a sudden state-change occurs, because the consequent state variation is not taken into account in the process model. Once the anomaly is detected, the authors recommend to increase $\mathbf{Q}$ or $\mathbf{P}_{k|k-1}$, as was already suggested in [51]. Another alternative is to re-initialize the state vector with a static estimator.

The Authors of [37] propose a two-stage KF: a DKF uses only PMU phasor measurements to estimate the static state, i.e., voltage magnitudes and phase-angles; the estimated static-state is passed to an EKF that estimates the dynamic state, i.e., the generator speeds and rotor-angles. The DKF is a novel *adaptive KF* (AKF) with inflatable noise variances. The AKF with inflatable noise variances inflates $\mathbf{R}$ and/or $\mathbf{Q}$ in case of measurement errors and/or unexpected state-variations, respectively. It employs the persistent model already proposed in [57]. The method is tested in fault condition and in presence of bad-data.

In [68] a mixed-integer programming formulation of a distribution state estimator based on PMUs is presented. The process model is the one used in [51] where the parameters, including $\mathbf{Q}$, are determined by trial-and-error. Then, they propose a new formulation of the estimation step that is capable of simultaneously discarding predicted values whenever sudden state-changes are detected. The method is applicable

[5] A flat-start means that all voltage phase-angles are set to zero and all voltage magnitudes are set to 1 pu. This is a typical initial guess in iterative procedure (e.g., load flow or SE) as it is close to the power-system state in normal operating conditions where the voltage magnitudes are close to the rated values and the voltage phase-angle differences are small.

only if the state variables are the same as the measurement quantities. Therefore, indirect voltage phasor measurements at buses without PMUs are calculated via voltage and current measurements of adjacent buses by using the line parameters.

In [69], a real-time simulator (RTS) is used to test and compare three non-linear KFs: EKF, unscented KF and cubature KF. Indeed, they use both SCADA and PMU measurements. The cubature KF, invented by the authors of [70], is designed to handle high-dimensional non-linear problems under the Gaussian assumption of the noise distributions.

1.4.3 PMU-based state estimation via discrete Kalman filter

Many contributions cited in the previous Section 1.4.2 focused on how to improve the approximation of model non-linearities and on the definition of new process models aiming at accurately represent the power-system time-behavior. These issues are no longer a concern when we consider state estimators based exclusively on PMUs.

The measurement model is linear (see Section 1.1) and the state is estimated every 20 ms with reference to a 50 Hz system. The first observation is that it makes no sense to predict the state for such a short-time period. Thanks to the high-resolution PMU measurements, the power-system can be considered to be in quasi-static conditions during normal operation. We can assume that the state does not change significantly from one time-step to the other, so that a good approximation of matrix $\mathbf{A}$ in (1.23) is the identity matrix. In addition, the power-system inputs are usually not controllable from the SE perspective, thus, we can remove the controllable inputs $\mathbf{u}$ in (1.23). Therefore, the process model already proposed in [57, 37] is suitable for these conditions and is recalled here below:

$$\mathbf{x}_k = \mathbf{x}_{k-1} + \mathbf{w}_k \,. \tag{1.34}$$

This model is the autoregressive integrated moving average – ARIMA (0,1,0), also called *persistent model* or *random-walk*. A remarkable advantage of using this process model is that it requires the setting of a single parameter, i.e., $\mathbf{Q}$.

The linearity of both the process and measurement models enables the use of the DKF. In the following, the DKF equations that were given in Section 1.4.1 for a general process model are presented for the persistent process-model:

Prediction step

$$\widehat{\mathbf{x}}_{k|k-1} = \widehat{\mathbf{x}}_{k-1|k-1} \tag{1.35}$$

$$\mathbf{P}_{k|k-1} = \mathbf{P}_{k-1|k-1} + \mathbf{Q}_k \tag{1.36}$$

Estimation step

$$\mathbf{L}_k = \mathbf{P}_{k|k-1}\mathbf{H}^T(\mathbf{H}\mathbf{P}_{k|k-1}\mathbf{H}^T + \mathbf{R}_k)^{-1} \tag{1.37}$$

$$\widehat{\mathbf{x}}_{k|k} = \widehat{\mathbf{x}}_{k|k-1} + \mathbf{L}_k(\mathbf{z}_k - \mathbf{H}\widehat{\mathbf{x}}_{k|k-1}) \tag{1.38}$$

$$\mathbf{P}_{k|k} = (\mathbf{I} - \mathbf{L}_k\mathbf{H})\mathbf{P}_{k|k-1} \tag{1.39}$$

2 Adaptive Kalman filtering for the on-line estimation of the process-model uncertainties

In this chapter, we deal with the on-line estimation of time-varying uncertainties associated with the process-model used by a discrete Kalman filter (DKF). We present a heuristic method that assesses the process-noise variances from the previous estimates and we statistically validate the adequacy of the persistent process-model in quasi-static conditions. Then, we define a convex optimization problem that is able to cope with step-processes by inferring the prediction-error covariances from a set of previous innovations; indeed, this method is called prediction-error covariance estimation (PECE). The two above-mentioned methods are tested in the context of power-system state estimation, but they can be applied also in other domains as long as the assumptions hold.

2.1 Introduction

In Chapter 1 we explained how the assumption of a measurement infrastructure fully based on PMUs leads to the definition of two linear models:

- *Persistent process-model* (1.34)

$$\mathbf{x}_k = \mathbf{x}_{k-1} + \mathbf{w}_k \tag{2.1}$$

  where $p(\mathbf{w}) \sim \mathcal{N}(0, \mathbf{Q}_k)$ in which $\mathbf{Q}_k$ is, in general, time-variant.

- *Measurement model* (1.5)

$$\mathbf{z}_k = \mathbf{H}\mathbf{x}_k + \mathbf{v}_k \tag{2.2}$$

  where $\mathbf{H}$ is time-invariant and $p(\mathbf{v}) \sim \mathcal{N}(0, \mathbf{R}_k)$, whereas $\mathbf{R}_k$ is, in general, time-variant.

Then, we gave the corresponding DKF equations in (1.35)–(1.39), which involve the definition of the covariance matrices of the measurement noise $\mathbf{R}$ and of the process noise $\mathbf{Q}$. The KF optimality depends upon the proper assessment of both covariance matrices. Indeed, a well-known challenge in the application of the KF to real systems is the identification of the parameters of the stochastic-error distributions.

$\mathbf{R}$ represents the uncertainties associated with the measurements. As presented in Section 1.1.2, these uncertainties consist of systematic and random errors. The random errors may come from different sources, such as thermal noise and converters, whereas the systematic errors are mainly introduced by the sensors, such as PTs and CTs. It is known that, typically, the systematic errors of voltage and current measurements in power systems are predominant. However, in this section we assume to have the calibration certificates of the sensors so that we can neglect the systematic errors, as explained in Section 1.1.2. Therefore, the diagonal elements of $\mathbf{R}$ represent the variances of the random errors that are assumed to have a Gaussian-white distribution. Besides, $\mathbf{R}$ is diagonal as we neglect the correlations between measurements for the reasons mentioned in Section 1.1.2.

$\mathbf{Q}$ represents the process-model uncertainties associated with each state variable. The assessment of $\mathbf{Q}$ is complicated as the power-system state is continuously moving. In the literature dealing with KF-based power-systems SE (see Section 1.4.2), $\mathbf{Q}$ is usually fixed to a certain value assessed from historical data, which is typically the largest value that allows the process model to remain valid even in worst case scenarios. This can be a very sub-optimal procedure, because it cannot adapt to the continuously-changing operating conditions of the network. For instance, if we set a very large value of $\mathbf{Q}$, the process model is never violated and the KF never looses track of the system, but the KF becomes essentially a LWLS; therefore, we do not exploit the filtering capability of the KF as we use it in a very sub-optimal way. Especially in our case where we use the persistent process-model, every variation of the power-system state is attributed to the process noise and, thus, is reflected in the process-noise covariance matrix. Therefore, we need to use an AKF that performs an on-line assessment of the process-model uncertainties. This is a quite challenging task and, indeed, it is still a research subject in many different domains, especially in the area of automatic control.

Another hidden hypothesis is that the process noise has to be smaller than the measurement noise in order to allow the KF to effectively filter the measurement noise. If it is not the case, it is logical to think that the measurements are already very close to the optimal estimate achievable and, again, the KF cannot do much better than a WLS. Indeed, when the process noise is larger than the measurement noise, the entries of $\mathbf{Q}$ are larger than those of $\mathbf{R}$ and it is known that the KF solution approaches the WLS one as $\mathbf{Q} \to \infty$ [57]. The aforementioned hypothesis is satisfied thanks to the high time-resolution measurements of PMUs, which allows us to consider the power system to be in quasi-static conditions, except for sporadic events, such as changes of

network configuration, load inrushes, faults or load/generator disconnections.

In this chapter, we present two methods that continuously-estimate the process-model uncertainty in order to adapt it to different power-system operating conditions. Our goal is to enhance the SE accuracy by filtering the measurement noise. The resiliency against bad data and network-model errors is not treated in this chapter.

In Section 2.2, we provide the literature review on the assessment of the KF covariance matrices.

In Section 2.3, we formally prove the better accuracy of the KF over the WLS if the process model is correct.

In Section 2.4, we present a heuristic method for the assessment of $\mathbf{Q}$ that was firstly proposed in [71] and further investigated in [72]. This method is effective in terms of estimation accuracy when the network is in quasi-static conditions and is suitable for real-time applications as the computation of $\mathbf{Q}$ takes less than a millisecond.

In Section 2.5, we present a more sophisticated method that is able to track sudden changes of the system state. It consists in a constrained convex optimization problem that has the computational time as main drawback.

2.2 Literature review on the estimation of the Kalman filter covariances

In the early 1970's, Mehra [73] classified into four categories the methods for the estimation of the KF covariances: Bayesian [74, 75], maximum likelihood [76, 77, 78], correlation [79, 80, 81, 82, 83, 84, 85, 86, 87, 88], and covariance matching [89].

The Bayesian and maximum-likelihood estimation methods are characterized by a high level of complexity and are usually employed for the case of time-invariant systems. As observed in [78], a relevant advantage of these approaches is that they can be applied also when measurements are available at irregular intervals, which is quite common in real applications.

Correlation techniques estimate the measurement and process-noise covariance matrices by exploiting the sample autocorrelation functions of the innovations at different lags. In [79, 80, 82, 83, 84, 85, 86, 87], the authors consider only time-invariant systems, whereas [81] extends the problem formulation to time-variant systems. However, as remarked in [73] and shown in [81], the correlation methods provide sound results mainly for time-invariant systems. In [83], the authors propose a least-squares optimization problem based on the correlations between the innovations; this method is able to ensure the positive semi-definiteness of both $\mathbf{R}$ and $\mathbf{Q}$, which is essential

to guarantee the KF numerical stability and, thus, the accuracy of the solution (see Section 2.5.2). Then, a follow-up of this paper is presented in [86], where the authors present new conditions for the uniqueness of the covariance estimates as well as an optimal weighting to be used in the least-squares objective to ensure minimum variance in the estimates. The work presented in [88] deals with adaptive estimation of both $\mathbf{R}$ and $\mathbf{Q}$ for time-variant models. The method is based on the correlation-innovations approach and includes an approach to ensure the positive definiteness of the covariance matrices.

Covariance-matching methods consist in adaptive algorithms that, at every sampling step, assess the KF parameters directly from the past state estimates. They are particularly effective in case either $\mathbf{R}$ or $\mathbf{Q}$ is known, as stated in [73]. Myers and Tapley [89] use a direct estimation of both $\mathbf{R}$ and $\mathbf{Q}$ from their sample covariances at every sampling step.

Correlation and covariance-matching techniques need ad-hoc procedures in order to ensure the positive semi-definiteness of the estimated covariance matrices, which is not guaranteed by the method itself. The authors of [89] use an approximated countermeasure to ensure positive diagonal elements of the covariance matrices, which consists in replacing the estimated diagonal elements with their absolute values. Similarly, in [88] the positive definiteness of the estimated $\mathbf{R}$ and $\mathbf{Q}$ is ensured with further processing of the two matrices after their estimation; therefore, also this method is approximated. An effective way to ensure the positive semi-definiteness of the estimated covariance matrices is to solve a constrained optimization problem, as in [83].

In the context of power systems, very few papers deal with the evaluation of the KF process-model uncertainty. The value of $\mathbf{Q}$ is usually assumed to be constant, which leads to a non-adaptive filter that could have very poor estimation accuracy with respect to a filter whose stochastic parameters are frequently updated. In [37], the authors formulate an optimization problem that is only able to inflate the process-noise variances when a step-variation in the power-system state occurs. The authors mention that the inflated $\mathbf{Q}$ could be decreased by employing an exponential decay with time constant to be defined by the user.

2.3 Estimation accuracy: Kalman filter vs. weighted least squares

The content of this section is based on [72]. The accuracies of KF vs. WLS are theoretically compared as explained in what follows. To formally quantify this difference, it is useful to recall that the KF process makes use of all the available measurements, past and present, whereas the WLS algorithm uses only measurements of the current time-step. The former should intuitively perform better, provided that the process model hypotheses that underlie the KF are correct. The following theorem formalizes

this aspect. It states that the estimation error with the KF algorithm is always less than the estimation error with the WLS algorithm, the difference being given equal to the mean square difference between the two methods:

Theorem 1. *Assume that the true (unknown) state* $\mathbf{x}_k$ *satisfies the process model in* (2.1)*. Assume that the system parameters are known. Let* $\widehat{\mathbf{x}}_{k,WLS}$ *and* $\widehat{\mathbf{x}}_{k,KF}$ *be the state estimates obtained at time-step* k *with the WLS and KF algorithms, respectively. Then, denoting* $\mathbb{E}$ *as the expected value operator,*

$$\mathbb{E}\Big[\|\mathbf{x}_k - \widehat{\mathbf{x}}_{k,WLS}\|^2\Big] = \mathbb{E}\Big[\|\mathbf{x}_k - \widehat{\mathbf{x}}_{k,KF}\|^2\Big] + \mathbb{E}\Big[\|\widehat{\mathbf{x}}_{k,WLS} - \widehat{\mathbf{x}}_{k,KF}\|^2\Big] \tag{2.3}$$

Proof. First of all, by standard KF theory, e.g., [90], the estimation of the non-observable state is equal to its conditional expectation, given the sequence of measurements, i.e.,

$$\widehat{\mathbf{x}}_{k,KF} = \mathbb{E}[\mathbf{x}_k|\mathcal{F}_k] \tag{2.4}$$

where $\mathcal{F}_k$ the σ-field generated by all measurements up to and including time-step k.

Second, consider the Hilbert space of random vectors (with values in $\mathbb{R}^n$) equipped with the inner product $\langle \mathbf{V}, \mathbf{W}\rangle_H \triangleq \mathbb{E}[\sum_{i=1}^n V_i W_i]$. It is requested to show that the random vector $\mathbf{x}_k - \widehat{\mathbf{x}}_{k,KF}$ is orthogonal,[1] in the sense of this Hilbert space, to all random vectors $\mathbf{W}$ that are $\mathcal{F}_k$-measurable (i.e., that are a function of the measurements up to time k; in this context, the initial conditions of the estimation algorithms are assumed to be known and non-random). Note that what needs to be shown is that:

$$\mathbb{E}\Big[\langle \mathbf{W}, \mathbf{x}_k\rangle\Big] = \mathbb{E}\Big[\langle \mathbf{W}, \widehat{\mathbf{x}}_{k,KF}\rangle\Big] \tag{2.5}$$

with $\langle \mathbf{W}, \mathbf{x}_k\rangle = \sum_{i=1}^n W_i x_{k,i}$.

To prove (2.5), observe that, for any (real-valued) random variable U that is measurable with respect to $\mathcal{F}_k$, it can be written that $\mathbb{E}[U|\mathcal{F}_k] = U$ and further [90]:

$$\mathbb{E}[U x_{k,i}|\mathcal{F}_k] = U\mathbb{E}[x_{k,i}|\mathcal{F}_k] = U\,\widehat{x}_{k,KF,i}$$

Note that such a U can be any non-linear real-valued function of $(\mathbf{z}_1, \ldots, \mathbf{z}_k)$. Take expectations on both sides and use the fact that the expectation of the conditional expectation is the same as the original expectation (*law of total expectation* [90]) and obtain

$$\mathbb{E}[U x_{k,i}] = \mathbb{E}[U\,\widehat{x}_{k,KF,i}] \tag{2.6}$$

Consider now any $\mathcal{F}_k$-measurable random vector $\mathbf{W}$, apply (2.6) to $U = W_i$ for all

[1] We remind here that when two vectors are orthogonal, their inner product is equal to zero.

coordinates i and sum over i; then it becomes

$$\mathbb{E}\left[\sum_{i=1}^{n} W_i x_{k,i}\right] = \mathbb{E}\left[\sum_{i=1}^{n} W_i \widehat{x}_{k,KF,i}\right] \tag{2.7}$$

which shows (2.5) as required and it means that

$$\mathbb{E}\left[\sum_{i=1}^{n} W_i (\widehat{x}_{k,i} - \widehat{x}_{k,KF,i})\right] = \mathbb{E}[\langle \mathbf{W}, \mathbf{x}_k - \widehat{\mathbf{x}}_{k,KF} \rangle] = 0 \tag{2.8}$$

namely $\mathbf{W}$ and $\mathbf{x}_k - \widehat{\mathbf{x}}_{k,KF}$ are orthogonal.

Now observe that both $\widehat{\mathbf{x}}_{k,WLS}$ and $\widehat{\mathbf{x}}_{k,KF}$ are $\mathcal{F}_k$-measurable because they are derived from the measurements. Therefore, the previous result can be applied to (2.3) then follows from Pythagoras's equality. (QED)

Final remark: The theorem applies as long as the process model in (2.1) holds. This explains why it is important to verify the adequacy of the process model.

2.4 New heuristic method for the on-line assessment of Q

The content of this section is based on [71] and [72]. The original contributions are the following:

1. The formulation of a new heuristic method for the on-line assessment of $\mathbf{Q}$ [71], which is conceived to be deployable in real-time embedded hardware;
2. A comparative assessment of the performance (accuracy and computational time) of the DKF and the LWLS estimators [72] via numerical simulations on a transmission network (New England 39-bus system) and a distribution feeder (IEEE 123-bus test feeder);
3. The numerical proof of Theorem 1 [72];
4. The numerical validation of the correctness of the persistent process-model when the process-noise covariance matrix is assessed via the heuristic method of point 1 [72].

2.4.1 Analytical formulation

The method described here below assesses the diagonal elements of $\mathbf{Q}$ by using a moving window composed of the previous N estimated states. The estimated value of $\mathbf{Q}$ is denoted by $\widehat{\mathbf{Q}}$.

The idea behind the formulation of this method is the following. In quasi-static conditions the sample variance of the last N state estimates aims at representing the process-model uncertainty, although the latter tends to be overestimated as we will show in Section 2.5.2. Instead, when the state changes monotonically (increasing or decreasing), the diagonal values of $\mathbf{Q}$ increase and the method is able to rapidly (but not instantaneously) increase $\widehat{\mathbf{Q}}$. Hence, the method is able to react to quick variations of the system state.

Note that the proposed method is based on the fact that $\mathbf{Q}$ is not supposed to change dramatically from one time-step to the other; therefore, $\mathbf{Q}$ should be updated more frequently than the system-state dynamics that we want to track. Indeed, we make reference to PMU-based state estimators characterized by a refresh rate of 50 estimates-per-second in order to accurately track most of the grid-state changes (except for large steps, as illustrated in Section 2.5).

The analytical formulation of the proposed method is given here below. At time-step k and denoting the state estimate with $\widehat{\mathbf{x}}$, the procedure to estimate $\mathbf{Q}_k$ consists in the following steps:

- The i^{th} element of a vector $\mathbf{g} \in \mathbb{R}^n$ is computed as the sample variance of the i^{th} elements of the last N estimated states:

$$g_i = \text{var}[\widehat{x}_{k-1|k-1,i}, \ldots, \widehat{x}_{k-N|k-N,i}] \tag{2.9}$$

- Then, the elements of $\mathbf{g}$ constitute the diagonal of the estimated $\mathbf{Q}_k$:

$$\widehat{\mathbf{Q}}_k = \text{diag}(\mathbf{g}). \tag{2.10}$$

Matrix $\widehat{\mathbf{Q}}$ is diagonal and, in general, the diagonal elements are different from each other. The larger N, the larger the entries of $\widehat{\mathbf{Q}}$. Parameter N can be determined by pre-tuning as we do in Section 2.4.2.

This method is simple and straightforward to implement. In Section 2.4.2 we show that it also provides a good estimation accuracy although, being heuristic, it remains sub-optimal. Additionally, it is not specific for power-system SE and can be applied also to other fields.

2.4.2 Simulations and results

In this section, we evaluate the SE accuracy via the procedure described here below:

1. The network true state and the true values of the measurements are computed each 20 ms via a load-flow calculation;

2. The measurements used in SE are generated by adding Gaussian-white random noise to the true quantities computed in *step* #1 (we assume to have no systematic errors as stated at the beginning of this chapter);
3. The estimated state is computed by using the network model, the measurements and, in case of dynamic estimators, also a process model;
4. The SE accuracy is obtained by comparing the estimated state with the true state computed in *step* #1.

Further details on the simulation procedure are given in the following sections that present the testing results for a transmission network and a distribution feeder. It is important to mention that the results shown in this section are obtained by removing the first 500 time-steps from the original simulation. The reason is that the KF initial state is usually set to an arbitrary value (e.g., a flat-start) that might be far away from the true state. Therefore, the KF is characterized by an initial phase in which the state estimate approaches the true state. In this initial stage, we set a constant and high value of Q in order to accelerate the approach. After N time-steps, the value of Q used by the DKF is assessed by the heuristic method described in Section 2.4.1. After 500 time-steps, the effects of this initial phase are negligible as we use values of N that are much lower than 500.

Transmission network

We consider the New England 39-bus system; as the network is balanced, the direct sequence is estimated. A schematic of the network and the measurement configuration are shown in Fig. 2.1. The network data can be found in [91, Appendix A]. We assume that bus #31 is the connection point of the system to an external network so that the voltage at bus #31 is not fixed. The equivalent circuit of the external network is modeled with a fixed voltage source in series with a short-circuit impedance, which are called SB and Z_{sc} in Fig. 2.1, respectively. The voltage source SB represents the slack-bus in the load-flow calculation.The value of Z_{sc} is computed by assuming a rated voltage of 380 kV, a short-circuit power of 50 GVA. The base power is 100 MVA. The network is assumed to be in quasi-static conditions, which means that the network state is moving slowly and no sudden changes are present.The active powers and the voltage magnitudes at the generator buses are fixed to the values specified in [91, Appendix A]. In order to reproduce realistic time-series, the load active/reactive powers come from real power measurements provided at 50 measurements-per-second by PMUs installed in the 125-kV sub-transmission network of Lausanne, Switzerland. The values of these real power measurements are adapted to the values specified in [91, Appendix A]. As an example, Fig. 2.2 shows the time-evolution of the active and reactive powers absorbed by the load at bus #4. Note that the simulation time is 30 s that corresponds to $T = 1500$ time-steps, because the PMU reporting-rate is 50 measurements-per-second.

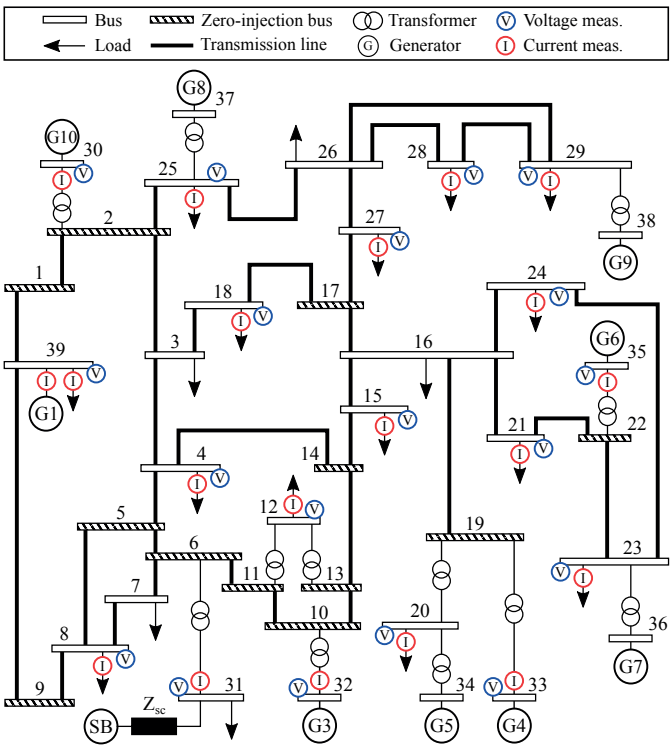

Figure 2.1 – Network topology of the New England 39-bus system together with the adopted measurement configuration.

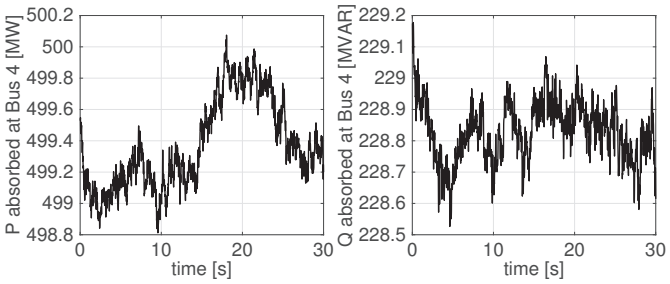

Figure 2.2 – Time evolution of the active and reactive powers absorbed by the load at bus #4.

The PMU placement shown in Fig. 2.1 ensures the full-network observability, i.e., matrix $\mathbf{H}$ has full rank. There are 19 buses equipped with PMUs that measure the nodal-voltage phasor and the current-injection phasor at the respective bus. We also exploit the 12 zero-injection buses as virtual measurements that consist in null values with small uncertainty. The total number of measurements is $m = 100$ and the state dimension is $n = 78$ so that the redundancy level is about 1.3. This small redundancy is chosen in order to have a quite large estimation uncertainty on the nodal voltages that are not directly measured. As a consequence, the SE accuracy improvement due to the DKF noise filtering is more pronounced and the DKF results are significantly better than the LWLS ones. As the redundancy level increases, the difference between the DKF and LWLS results becomes smaller. A comparison between the DKF and LWLS accuracies for different measurement types and redundancy levels is provided in Tab. 2.1.

The measurement noise is assumed to be a Gaussian-white sequence where the covariance matrix $\mathbf{R}$ is diagonal, time-invariant and known. These hypotheses are justified by the following considerations:

- the noise mean-value is considered to be zero as we assume to compensate the systematic errors of the sensors by using their calibration certificates, as explained in Section 1.1.2;
- $\mathbf{R}$ is considered to be diagonal, because the measurements are assumed to be uncorrelated for the reasons presented in Section 1.1.2;
- $\mathbf{R}$ is approximated as a time-invariant matrix, because the random-noise characteristics do not change significantly when the power system is in normal operating conditions[2].

The standard deviations of the real and imaginary parts of voltage and current measurements are assumed to be 0.001 pu. We also performed tests where $\mathbf{R}$ was time-varying as the noise standard-deviations were calculated as a percentage of the measured values; however, the SE results were similar to those presented in what follows.

The SE numerical results for the transmission network case are presented and discussed in the following. First of all, we perform a tuning of parameter N that is used to assess $\mathbf{Q}$ (see Section 2.4.1). We run the same simulation composed of $T = 1500$ time-steps with different values of N and we compute the root mean square error

[2]This assumption may not be valid when some particular event occurs, such as a fault, where the voltage and current magnitudes can vary dramatically. Further research is needed to examine these cases.

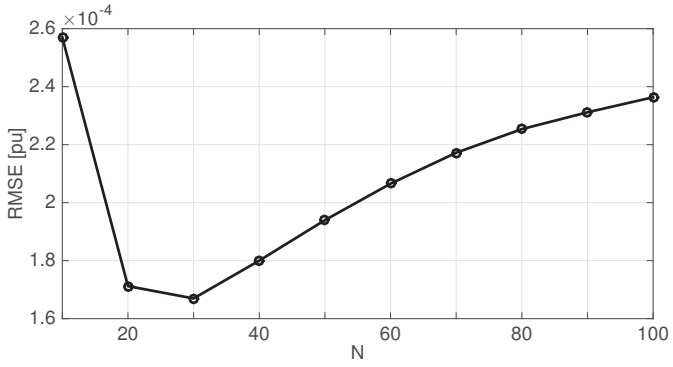

Figure 2.3 – RMSE of the DKF as a function of the parameter N.

(RMSE) of the DKF estimates as follows:

$$\text{RMSE} = \sqrt{\frac{1}{T+n}\sum_{k=1}^{T}\sum_{i=1}^{n}(x_{k,i}^{est} - x_{k,i}^{true})^2}\,. \tag{2.11}$$

Fig. 2.3 shows that $N = 30$ provides the best accuracy for this specific case; this value is used for the simulations in this section.

Assuming to have the perfect knowledge of the measurement model (i.e., of $\mathbf{H}$ and $\mathbf{R}$), the KF optimality depends on how accurate the process model is. More precisely, we need to verify that the covariance properties of the model do hold. To this end, we define the i^{th} element of the vector of the normalized state-estimate residuals at time-step k as

$$r_{\mathbf{x},i}^{N} = \frac{\widehat{x}_{k|k,i} - \widehat{x}_{k-1|k-1,i}}{\sqrt{Q_{k-1,ii}}} \tag{2.12}$$

and we check whether these residuals are uncorrelated. Fig. 2.4 shows the time evolution of the residuals and the sample auto correlation functions (ACFs). For brevity, we show only the plots related to the real part of the voltage at bus #37 where the largest estimation error is observed, but similar results are obtained for the other state variables. We observe the time evolution of the residuals to check whether the stationarity assumption is satisfied, which is the case. A more formal verification is to analyze the sample ACFs. The latter are computed by considering the first $\sim\sqrt{T}$ lags, where we recall that $T = 1\,500$ is the number of simulation time-steps. If the residuals are uncorrelated, the ACFs should be within the noise margins $\pm 1,96/\sqrt{T}$ with 95% of probability [92]. The noise margins are the two straight lines in the ACF plot of Fig. 2.4. It can be seen that the above-mentioned condition is fulfilled; therefore, the normalized residuals of the state estimates are uncorrelated and the DKF process model can be considered to be accurate. Note that the sample ACF is a statistically distributed quantity. The fact that, in few cases, the ACFs are slightly beyond the

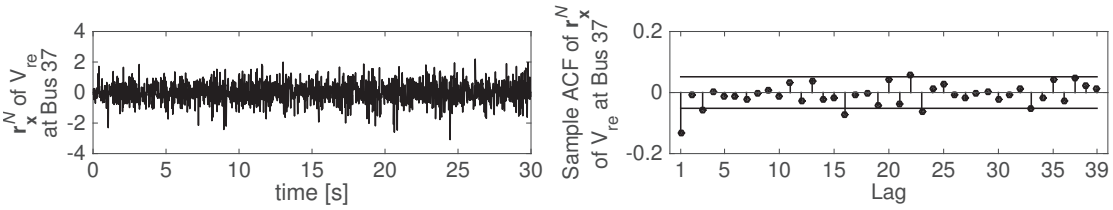

Figure 2.4 – Normalized residuals of the estimates of the real part of the voltage at bus #37. Left plot: time evolution of the residuals. Right plot: sample ACFs of the residuals.

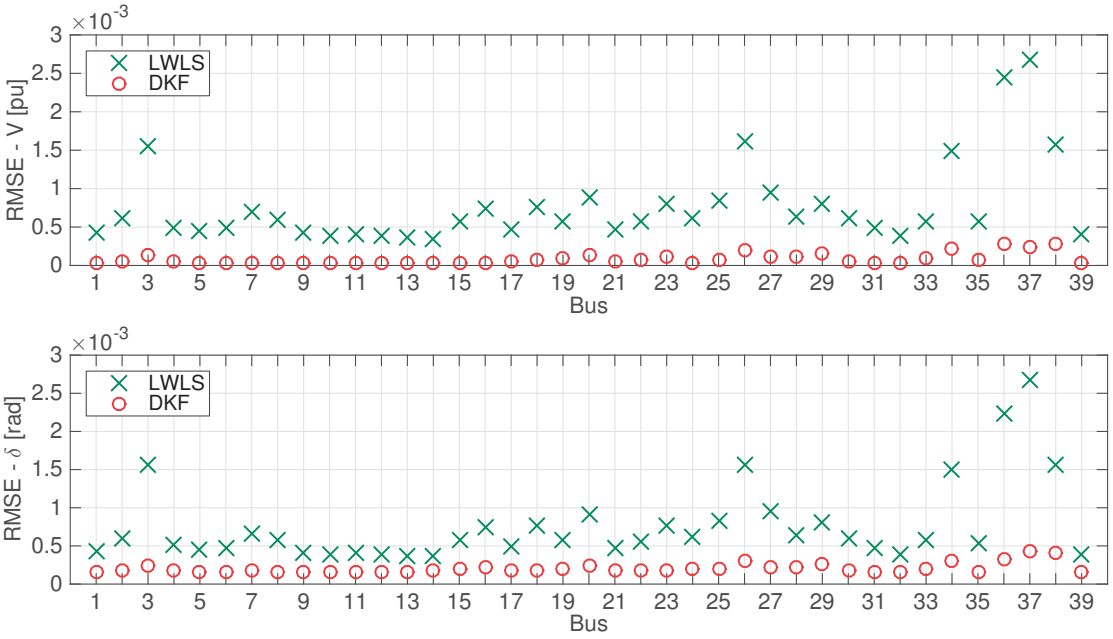

Figure 2.5 – RMSEs of the DKF and LWLS at each bus.

noise margins does not violate the validity of the result and the numerical proof of the statistical correctness of the process model.

Fig. 2.5 shows the RMSE of the voltage magnitude V and phase-angle δ at each bus; it can be seen that the DKF errors are, on average, significantly smaller than those of the LWLS. Fig. 2.6 shows the RMSE of the voltage magnitude and phase-angle at each time-step. The DKF accuracy is better during the entire simulation. Fig. 2.7 shows the time evolution of the voltage magnitude and phase-angle at bus #37. This figure reflects the results presented in Figs. 2.5 and 2.6: the DKF is able to effectively filter the measurement noise and to closely track the true state, whereas the LWLS state estimates are characterized by a much larger variance.

We also make a comparison with a DKF that uses a matrix $\mathbf{Q}$ that is constant in time and is diagonal with all the entries equal to a value Q_d (called $DKF_{Q\ sampling}$). In Fig. 2.8, we plot the RMSE of $\text{DKF}_{\text{Q sampling}}$ as a function of $Q_d = 1 \div 10^{-16}$. We also display the

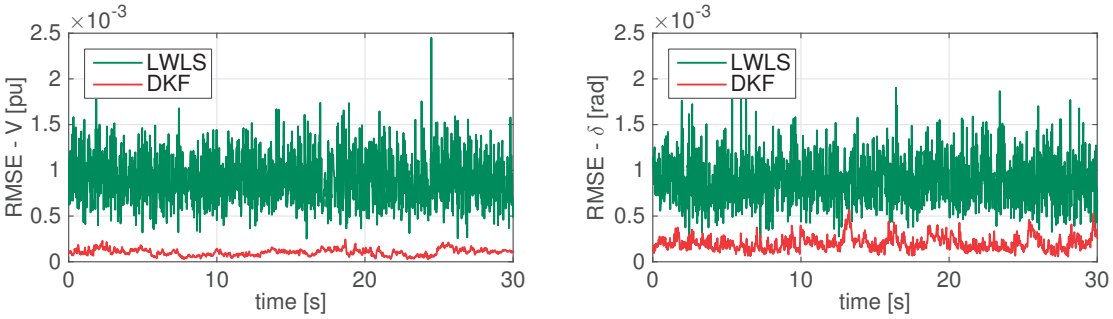

Figure 2.6 – Time evolution of the RMSEs of the DKF and LWLS.

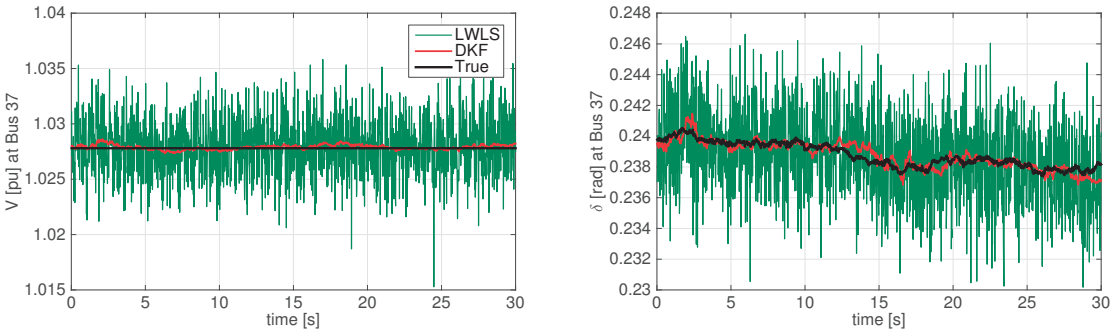

Figure 2.7 – Time evolution of the voltage magnitude V and phase-angle δ at bus #37. The true value and the values estimated by DKF and LWLS are displayed.

RMSEs of the LWLS and of the DKF that uses a value of $\mathbf{Q}$ assessed continuously with the heuristic method of Section 2.4.1 (called $DKF_{Q\ assessed}$), which are straight lines as they are independent of Q_d. The curve of the $\text{DKF}_{\text{Q sampling}}$ approaches the LWLS for large values of Q_d and has a minimum in $Q_d = 10^{-9}$. The RMSE of the $\text{DKF}_{\text{Q assessed}}$ is close to this minimum. Therefore, in this specific case, the $\text{DKF}_{\text{Q assessed}}$ is, on average, as accurate as a DKF that uses the best constant value of $\mathbf{Q}$ obtained from an extensive search. The advantage of the $\text{DKF}_{\text{Q assessed}}$ consists in being able to adapt its process model uncertainty to changing operating conditions as it can dynamically change the value of $\mathbf{Q}$.

Finally, we verify whether the quantitative conclusion of Theorem 1 in Section 2.3 numerically holds. Intuitively, this has to be the case in view of the results of Fig. 2.8. Fig. 2.9 shows the left- and right-hand sides (LHS and RHS, respectively) of (2.3). The LHS and RHS are close to each other, which means that the equality is in expectation. The expectations are estimated by empirical averages; therefore, a small discrepancy is expected. In Fig. 2.9, the contributions of the two terms of the RHS of (2.3) are also shown; the contribution of the second one is predominant, which proves that the DKF is applied correctly.

It is worth clarifying that the above-presented results refer to the measurement con-

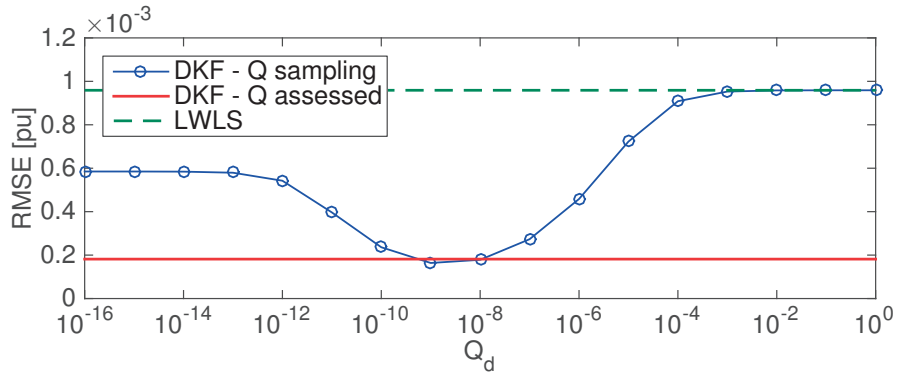

Figure 2.8 – RMSE of the $\text{DKF}_{\text{Q sampling}}$, $\text{DKF}_{\text{Q assessed}}$ and LWLS as a function of Q_d.

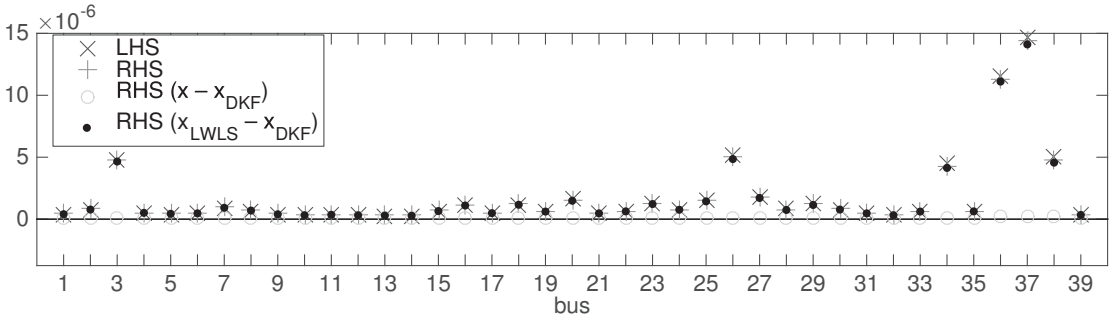

Figure 2.9 – Numerical validation of Theorem 1. We show the LHS vs. RHS of (2.3). The separate contribution of the two terms of the RHS is also shown.

Table 2.1 – RMSEs of the DKF and LWLS for different measurement configurations.

Network	RMSE_{LWLS}	RMSE_{DKF}	RMSE_{LWLS}/ RMSE_{DKF}
Conf. 1	$9.4 \cdot 10^{-4}$	$1.8 \cdot 10^{-4}$	5.2
Conf. 2	$1.9 \cdot 10^{-4}$	$8.0 \cdot 10^{-5}$	2.4
Conf. 3	$1.6 \cdot 10^{-4}$	$7.6 \cdot 10^{-5}$	2.1
Conf. 4	$1.5 \cdot 10^{-4}$	$7.2 \cdot 10^{-5}$	2.1

figuration depicted in Fig. 2.1. It is interesting to how the SE accuracy of the DKF and LWLS estimators changes as a function of the chosen measurements. To this end, Tab. 2.1 presents the RMSEs of the two state estimators for different measurement configurations that are listed here below:

- Configuration 1: the one depicted in Fig. 2.1;
- Configuration 2: voltage and the current-injection measurements at all the buses but zero-injection buses;
- Configuration 3: voltage measurements at all the buses and current-flow measurements at the sending side of every line;
- Configuration 4: voltage measurements at all the buses and current-flow measurements at the sending and receiving sides of every line.

As the redundancy level augments, the DKF keeps being more accurate than the LWLS, but the ratio between the LWLS and DKF errors decreases. The advantage of using a DKF for reducing the measurement noise is stronger for low redundancy levels.

Distribution feeder

In this section, most of the simulation conditions and results are the same as for the transmission network presented in the previous section. Therefore, the reader can make reference to the section on the transmission network for the definitions and explanations of repeated items.

We employ the IEEE 123-bus test feeder [93]. The power absorptions/injections are assumed to be different in the three phases and mutual coupling between phases is present; therefore, SE is performed in the three-phase domain. A schematic of the network and the measurement configuration are shown in 2.10. We assume that the network has a rated voltage equal to 15 kV and the line parameters correspond to the unbalanced configuration #602 specified in [93]. The value of the short-circuit impedance Z_{sc} is computed by assuming a short-circuit power of 300 MVA and a resistance-to-reactance ratio $R_{sc}/X_{sc} = 1/10$. The base power is 10 MVA. A photovoltaic (PV) plant and a mini-hydro plant are placed at buses #92 and #112, respectively, and inject only active power into the grid. The active/reactive powers absorbed by loads as well as the active power injected by generators come from real power measurements provided at 50 measurements-per-second by PMUs installed in the 20-kV distribution network of the Swiss Federal Institute of Technology of Lausanne (the french name is École Polytechnique Fédérale de Lausanne – EPFL), Switzerland. Fig. 2.11 shows the time evolution of the aggregated active and reactive powers absorbed by all the loads and the active power injected by a PV and a mini-hydro plants. Note that the PV injection

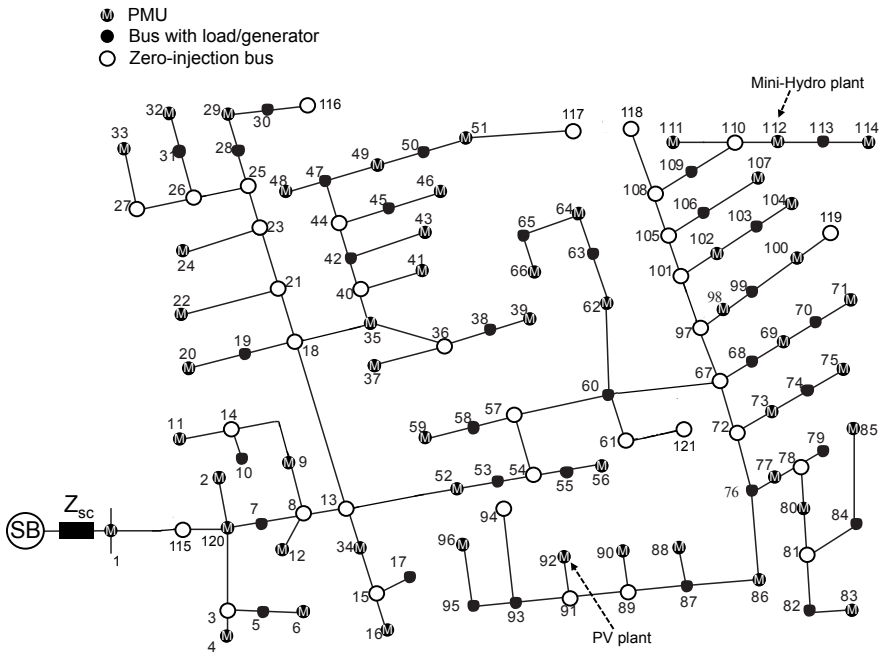

Figure 2.10 – Network topology of the IEEE 123-bus test feeder together with the adopted measurement configuration. This topology is obtained by setting the switch positions specified by the benchmark and is composed of 121 buses.

is characterized by quick variations that generate fast changes in the state variables as we will observe later in this section.

SE exploits the information related to the 35 zero-injection buses as virtual measurements and uses the real-time phasor measurements provided by 51 PMUs. The locations of zero-injection buses and PMUs are given in Fig. 2.10 and ensure the full-network observability (i.e., $\mathbf{H}$ has full rank). The total number of measurements is $m = 822$ and the state dimension is $n = 726$, which results in a redundancy level of about 1.2. The noise characteristics are the same given in the transmission network section, but we decrease the standard deviation of the current measurements from 0.001 pu to 0.0001 pu, because the base value of the current is quite large for this network.

For the above-described 123-bus test feeder, the result of a pre-tuning of parameter N shown in Fig. 2.12 is that $N = 30$ provides the best DKF accuracy; this value will be used in the simulations presented in the following.

Fig. 2.13 shows the time evolution of the residuals defined in (2.12) and the sample ACFs in each phase of bus #61 where the largest estimation error is observed (similar results are obtained for the other state variables). We observe that the residuals are uncorrelated and the correctness of the DKF process model is verified.

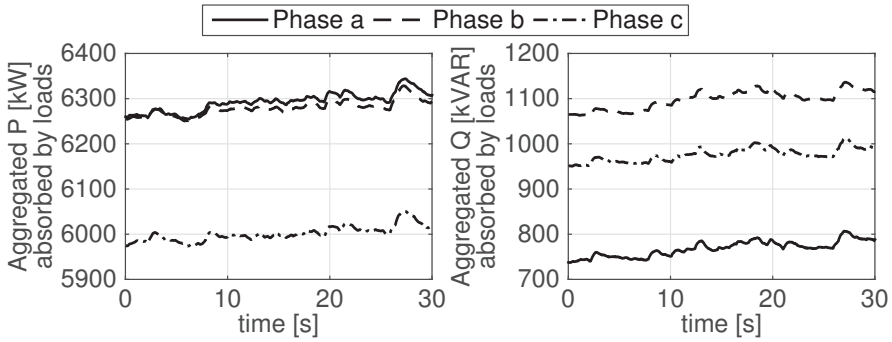

(a) Aggreagated active and reactive powers absorbed by all the loads.

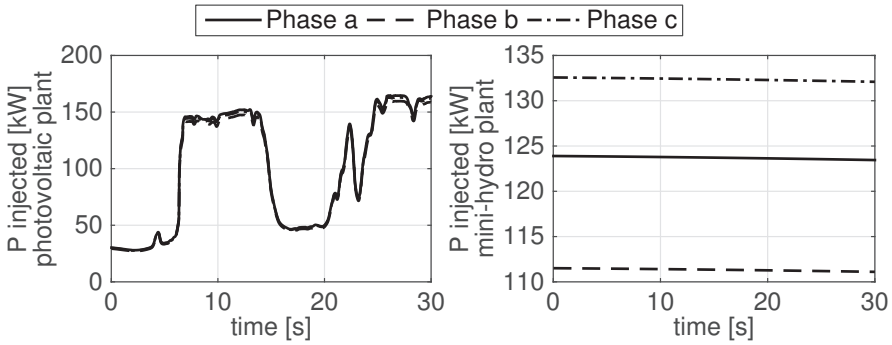

(b) Active power injected by the PV and mini-hydro plants.

Figure 2.11 – Time evolution of the absorbed/injected powers of loads/generators.

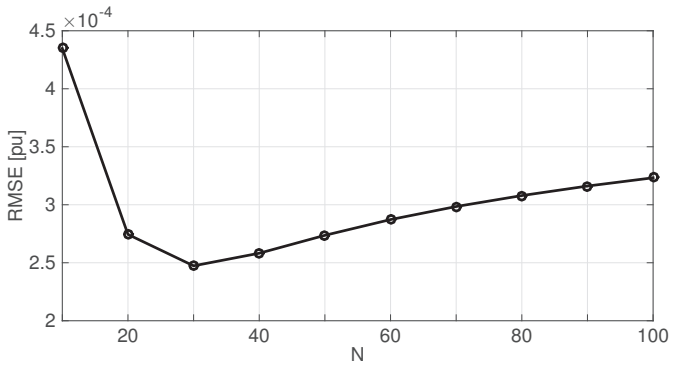

Figure 2.12 – RMSE of the DKF as a function of the parameter N.

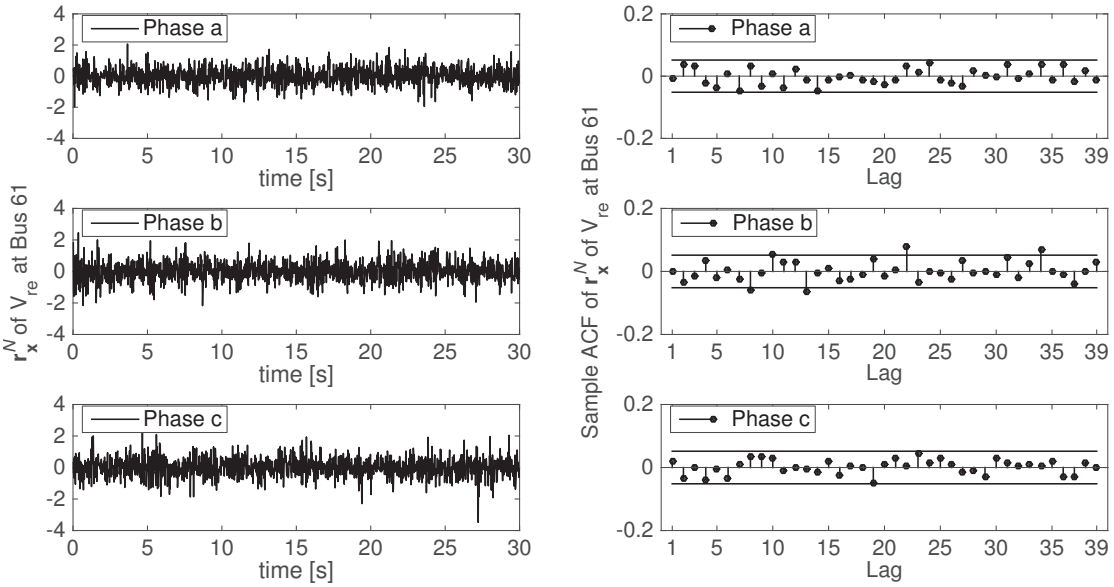

Figure 2.13 – Normalized residuals of the estimates of the real part of the voltage at bus #61. Left plot: time evolution of the residuals. Right plot: sample ACFs of the residuals.

Fig. 2.14 shows that, on average, the DKF errors are much smaller than those of the LWLS. In Fig. 2.15, it is interesting to observe that the DKF-RMSE time evolution exhibits some peaks corresponding to the quick changes of the PV power injection (see Fig. 2.11b), which result in fast changes of the system state as depicted in Fig. 2.16. However, the DKF is able to recover quite rapidly thanks to the inflation of $\mathbf{Q}$ operated by the heuristic method proposed in Section 2.4.1. Fig. 2.17 shows the time evolution of the element of $\mathbf{Q}$ corresponding to the real part of the voltage at bus #92 in phase *a*. Comparing Figs. 2.16 and 2.17, it is evident that this element of $\mathbf{Q}$ is inflated when fast changes of the corresponding state variable occur; then, during periods when the state variable varies smoothly, the corresponding element of $\mathbf{Q}$ decreases as expected.

As for the transmission network case, Fig. 2.18 shows that the $\text{DKF}_{\text{Q assessed}}$ is, on average, as accurate as a DKF that uses the best constant value of $\mathbf{Q}$ obtained from an extensive search. However, we recall that the advantage of assessing $\mathbf{Q}$ at each time-step is that the DKF can closely track the system state in different operating conditions, as shown in Figs. 2.16 and 2.17.

Finally, Fig. 2.19 verifies that (2.3) related to Theorem 1 in Section 2.3 numerically holds. For lack of space, only the first 40 buses are shown, but the results are similar for the remaining set of buses.

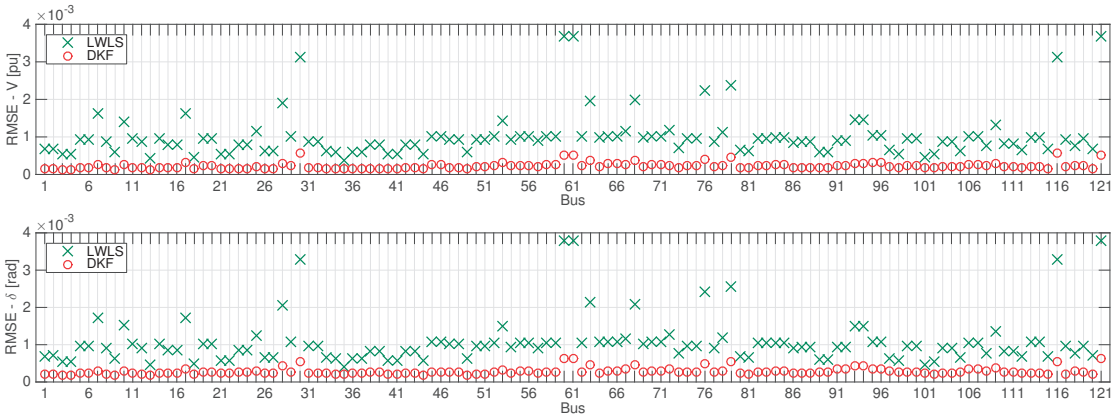

Figure 2.14 – RMSEs of the DKF and LWLS at each bus. The maximum RMSE among the three phases is shown.

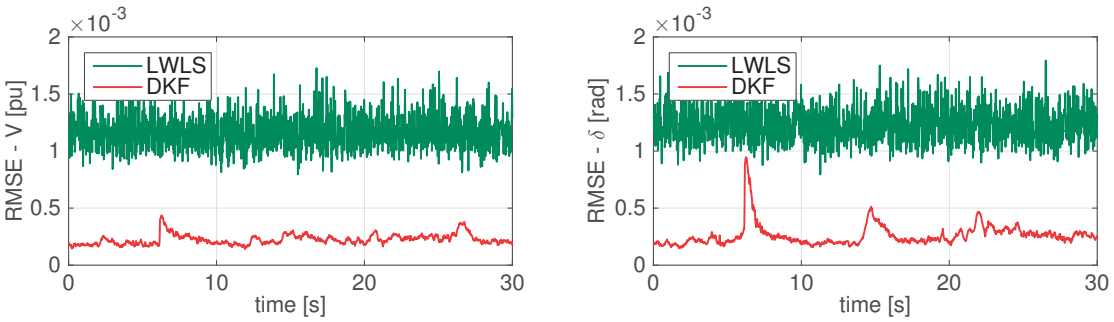

Figure 2.15 – Time evolution of the RMSEs of the DKF and LWLS.

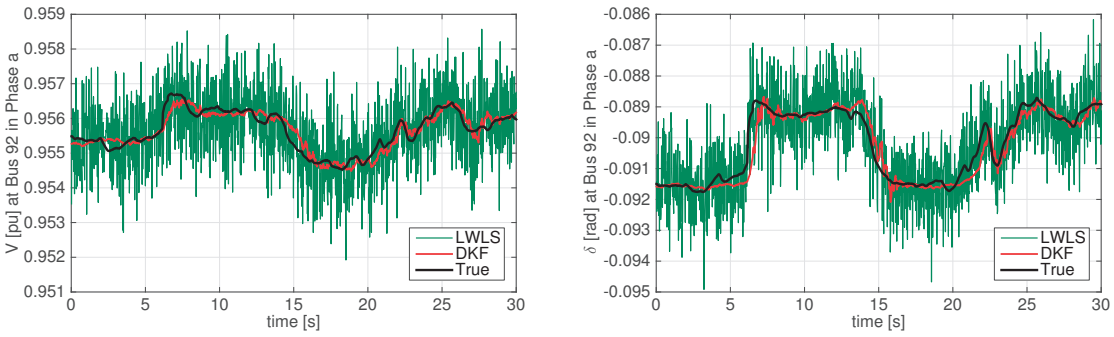

Figure 2.16 – Time evolution of the voltage magnitude V and phase-angle δ at bus #92 in phase *a*. The true value and the values estimated by DKF and LWLS are displayed.

Table 2.2 – Average computational time in milliseconds.

Network	n	m	LWLS	DKF
39-bus network	78	100	0.29 ms	0.39 ms
123-bus feeder	726	822	42 ms	73 ms

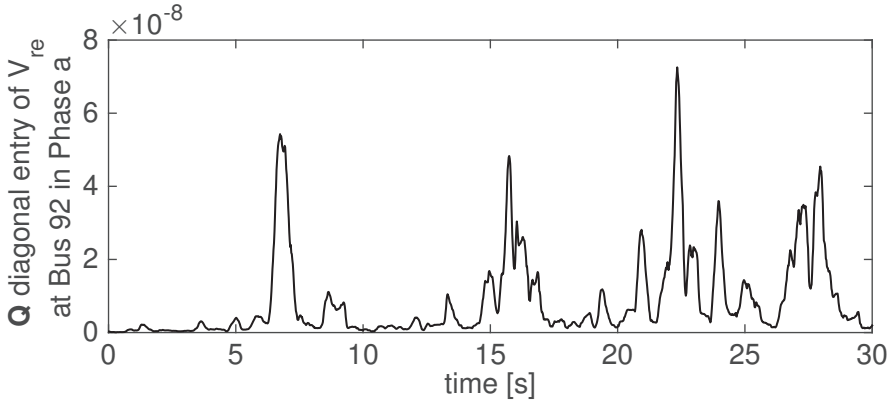

Figure 2.17 – Time evolution of the element of **Q** corresponding to the real part of the voltage at bus #92 in phase *a*.

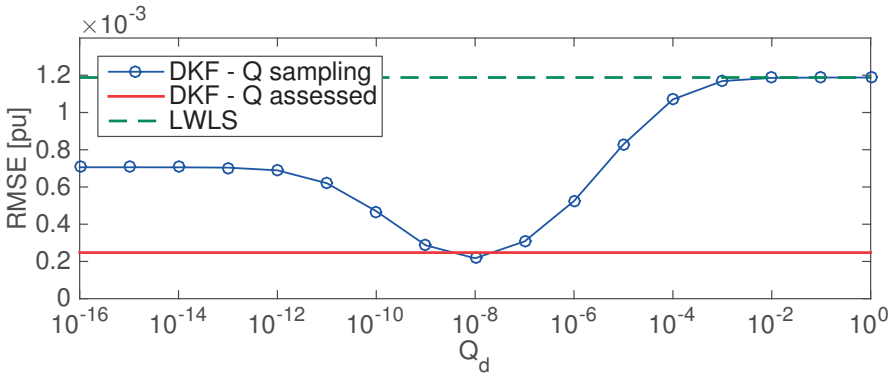

Figure 2.18 – RMSE of the $\text{DKF}_{\text{Q sampling}}$, $\text{DKF}_{\text{Q assessed}}$ and LWLS as a function of Q_d.

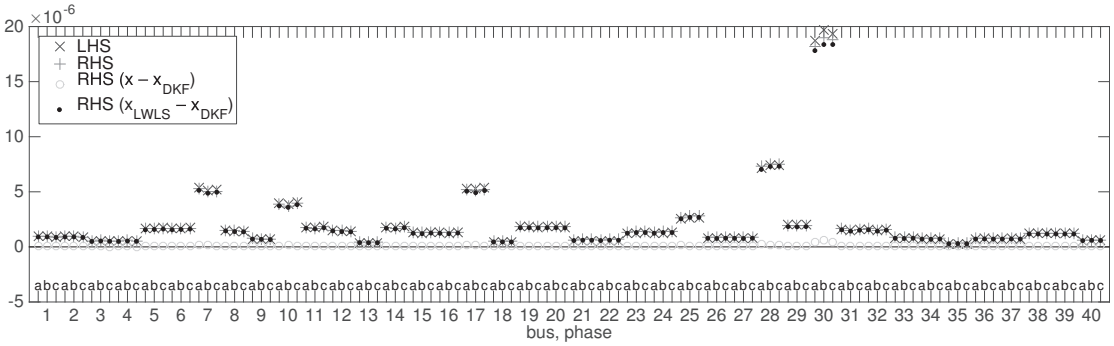

Figure 2.19 – Numerical validation of Theorem 1 for buses #1–40. We show the LHS vs. RHS of (2.3). The separate contribution of the two terms of the RHS is also shown.

Computational-time

The SE computational-times for the transmission network and the distribution feeder are inferred by using MATLAB 2014b that runs in an Apple MacBook Pro with a 2.5-GHz CPU and 16-GB RAM. In both case studies, we assumed $\mathbf{R}$ to be time-invariant so that the gain matrix $\mathbf{G}$ of the LWLS estimator is also time-invariant. Therefore, $\mathbf{G}$ could be inverted only once and, at every time-step, the computation of the LWLS solution reduces to a simple matrix multiplication. However, for the computational-time assessment we considered the general case in which $\mathbf{R}$ is time-variant and we solved the LWLS NE at every time-step.

Tab. 2.2 shows the computational times in milliseconds of the LWLS and DKF estimators for the New England 39-bus system and 123-bus test feeder. It can be seen that the LWLS is faster than the DKF, but both computational times are below 100 ms, which is compatible with real-time applications. In order to achieve a SE refresh-rate of 50 estimates-per-second, the state estimators can be pipelined. It is worth mentioning that if, as mentioned before, the LWLS gain matrix were computed only once, the LWLS computational time would be order of magnitudes lower. The time employed to estimate $\mathbf{Q}$ via the heuristic method is always much smaller than the computational time of the DKF equations; therefore, the computational burden added by the proposed $\mathbf{Q}$ assessment method is negligible.

2.5 New prediction-error covariance estimation method (PECE) for step-varying processes

The content of this section is based on [94].

The AKF presented in the previous Section 2.4 was able to provide satisfactory results when the system is in quasi-static conditions. Similarly, the methods presented in the literature review in Section 2.2 are conceived to estimate the stochastic parameters of time-invariant or slow-varying processes. However, these methods have some delay in tracking the state during step variations, which are common in power systems as they are associated, for instance, with the connection/disconnection of different components (mainly loads, generators and transmission lines). Still needed is a KF able to filter the measurement noise and to track sudden step-variations with minimum delay. In this section, we propose an AKF that addresses this problem by using a new method for inferring $\mathbf{P}_{k|k-1}$; this method is called *prediction-error covariance estimation* (PECE). Nevertheless, our proposed AKF is not specific for power-system SE only, actually it can be applied to every process where Assumptions #1–3 introduced in Section 2.5.1 hold.

The analytical formulation of the PECE method is given in Section 2.5.1. In Sections

2.5.2 and 2.5.3 we provide a performance assessment for the case of ideal processes and for power-system SE, respectively. The PECE method is compared with the method presented in [89], with our heuristic method presented in Section 2.4 and with the LWLS.

Let us consider a system described by the persistent process-model in (2.1). The process noise should be able to account for step variations. To this end, we enable the covariance matrix $\mathbf{Q}_k$ to be time-varying and unknown. In contrast, the measurement model is assumed to be linear, known and time-invariant. Hence, it can be defined as in (2.2) where $\mathbf{H}$ and $\mathbf{R}$ are time-invariant. We also assume that the system is fully observable, i.e., $\mathbf{H}$ has full rank. In the following we provide the DKF equations given in Section 1.4.3 where $\mathbf{H}$ and $\mathbf{R}$ lack of the subscript k as they are assumed to be time-invariant:

Prediction

$$\widehat{\mathbf{x}}_{k|k-1} = \widehat{\mathbf{x}}_{k-1|k-1} \tag{2.13}$$

$$\mathbf{P}_{k|k-1} = \mathbf{P}_{k-1|k-1} + \mathbf{Q}_k \tag{2.14}$$

Measurement update

$$\mathbf{L}_k = \mathbf{P}_{k|k-1}\mathbf{H}^T(\mathbf{H}\mathbf{P}_{k|k-1}\mathbf{H}^T + \mathbf{R})^{-1} \tag{2.15}$$

$$\widehat{\mathbf{x}}_{k|k} = \widehat{\mathbf{x}}_{k|k-1} + \mathbf{L}_k(\mathbf{z}_k - \mathbf{H}\widehat{\mathbf{x}}_{k|k-1}) \tag{2.16}$$

$$\mathbf{P}_{k|k} = (\mathbf{I} - \mathbf{L}_k\mathbf{H})\mathbf{P}_{k|k-1} \tag{2.17}$$

We also recall the innovation and its covariance matrix under the aforementioned assumptions:

$$\mathbf{y}_k = \mathbf{z}_k - \mathbf{H}\widehat{\mathbf{x}}_{k|k-1} \tag{2.18}$$

$$\mathbf{T}_k = \mathbf{H}\mathbf{P}_{k|k-1}\mathbf{H}^T + \mathbf{R}\,. \tag{2.19}$$

As it is known, the KF estimate is optimal if we use the optimal Kalman gain $\mathbf{L}$ that depends on matrices $\mathbf{P}_{k|k-1}$, $\mathbf{H}$ and $\mathbf{R}$. The matrix $\mathbf{P}_{k|k-1}$ contains the uncertainty of the process noise $\mathbf{Q}$. Assuming the knowledge of $\mathbf{H}$, the literature dealing with KF parameters estimation proposes several methods to infer the correct $\mathbf{R}$ and $\mathbf{Q}$ (see Section 2.2), but most of these methods are suitable for time-invariant or slow-varying systems. However, some systems are characterized by sudden and unpredictable state-steps. In these cases, given a certain process model, the Kalman gain has to be updated.

Our goal is to develop an AKF that filters effectively the measurement noise during quasi-static conditions and is also able to track step-variations of the system state. We consider a process that can be modeled as (2.1) with constant or slow-varying $\mathbf{Q}$ and

that exhibits state step-variations that violate the process model. Assuming $\mathbf{H}$ and $\mathbf{R}$ are known and time-invariant, the goal is to keep tracking the state in spite of these violations. We exploit the knowledge of the sample covariance matrix of the past and current innovations (1.31) in order to estimate the prediction-error covariance matrix $\mathbf{P}_{k|k-1}$, from which follows the name PECE method. Hence, we automatically update the Kalman gain before the measurement update. The PECE method consists in a constrained convex optimization problem based on maximum-likelihood estimation that ensures the positive semi-definiteness of $\mathbf{P}_{k|k-1}$.

2.5.1 Analytical formulation

The PECE method applies to cases where the following assumptions hold:

Assumption 1. The process model is the linear and time-variant persistent model described by (2.1). Specifically, we consider the general case in which the process-noise covariance matrix $\mathbf{Q}_k$ is unknown and changes as a function of time. Furthermore, we are interested in the case where the system state is characterized by step variations that violate the process model.

Assumption 2. The measurement model is linear, known and time-invariant. We assume to have the perfect knowledge of both the measurement matrix $\mathbf{H}$ and the measurement-noise covariance matrix $\mathbf{R}$.

Assumption 3. The system is assumed to be fully observable by using a number of measurements equal to or higher than the number of states: $m \geq n$ and matrix $\mathbf{H}$ has full rank.

If $\mathbf{Q}_k$ were known, the prediction-error covariance matrix $\mathbf{P}_{k|k-1}$ would be computed iteratively from (2.14) and all the other quantities of interest would derive from (2.15)–(2.17). However, this is not possible because of Assumption #1. The objective of PECE is to provide an estimate of $\mathbf{P}_{k|k-1}$ from the measurements, without direct estimation of $\mathbf{Q}_k$. The procedure is given in the following.

Given Assumption #1, the KF prediction equation is given by (2.13). In order to quickly react to step-variations of the system state, the PECE method takes advantage of the innovation $\mathbf{y}$ that contains the new information brought by the measurements at each time-step. In what follows, the PECE method's algorithm is presented in four steps.

- *Step* 1. At time-step k, after the computation of the predicted state $\widehat{\mathbf{x}}_{k|k-1}$ by means of (2.13) and when the new measurement set $\mathbf{z}_k$ is available, the innovation $\mathbf{y}_k$ is calculated by using (2.18).

- *Step* 2. In static conditions, the innovations represent a white Gaussian sequence

with covariance matrix $\mathbf{T}_\infty$, defined as

$$\mathbf{T}_\infty = \mathbf{H}\mathbf{P}_\infty\mathbf{H}^T + \mathbf{R}. \tag{2.20}$$

where $\mathbf{P}_\infty$ is the value of $\mathbf{P}_{k|k-1}$ as $k \to \infty$. An approximation of $\mathbf{T}_\infty$ is the sample innovation-covariance matrix $\widehat{\mathbf{C}}_k$, which is calculated at time-step k by considering a moving-window composed of N time-steps as

$$\widehat{\mathbf{C}}_k = \mathrm{cov}(\mathbf{y}_k, \mathbf{y}_{k-1}, ..., \mathbf{y}_{k-N+1}) \tag{2.21}$$

As it is known, for stationary processes the sample covariance tends to the true one as N increases. In non-stationary conditions, the true innovation-covariance matrix varies at each time-step and we denote it as $\mathbf{T}_k$. Thus, given the knowledge of the matrices $\mathbf{H}$ and $\mathbf{R}$ (Assumption #2), we can re-write (2.20) as (2.19), recalled here below:

$$\mathbf{T}_k = \mathbf{H}\mathbf{P}_{k|k-1}\mathbf{H}^T + \mathbf{R}. \tag{2.22}$$

Given the KF prediction equation (2.13), when the state has a sudden change, $\mathbf{T}_k$ changes as well. The sample matrix $\widehat{\mathbf{C}}_k$ follows the variations of the true matrix $\mathbf{T}_k$, because the innovations incorporate the information of the measurements. The PECE method exploits this feature in order to quickly react to the state changes, as explained in the following steps.

- *Step* 3. Estimate $\mathbf{P}_{k|k-1}$ from the innovation samples, using maximum likelihood estimation, as described in Theorem 3 below. This provides the estimate $\widehat{\mathbf{P}}_{k|k-1}$, which is symmetric and positive semi-definite; using (2.15), this estimate is used to calculate the Kalman gain $\mathbf{L}$ that is updated at every time-step. In quasi-static conditions, $\mathbf{L}$ remains fairly constant. When a state step-variation occurs, the KF prediction equation (2.13) is inaccurate, causing an increase of $\widehat{\mathbf{P}}_{k|k-1}$ and consequently of $\mathbf{L}$. Therefore, the KF trusts the measurements more than the predicted state, which is the right action to take in order to quickly react to the state variation.

Estimation of $\mathbf{P}_{k|k-1}$. A natural method for estimating $\mathbf{P}_{k|k-1}$ would consist in replacing in (2.22) the matrix $\mathbf{T}_k$ by the sample innovation-covariance $\widehat{\mathbf{C}}_k$ computed in Step 2 and solving for $\mathbf{P}_{k|k-1}$ (note that matrices $\mathbf{H}$ and $\mathbf{R}$ are known, by Assumption #2). However, this process, in general, will not produce a semi-definite matrix. A more adequate and more generally applied method is a ML estimation that can guarantee the positive semi-definiteness of $\mathbf{P}_{k|k-1}$.

The estimation procedure uses the following optimization problem:

$$\min_{\mathbf{\Sigma}} \quad \Big\{ -\log\Big[\det(\mathbf{\Sigma})\Big] + \mathrm{trace}(\mathbf{\Sigma}\mathbf{E}) \Big\} \tag{2.23}$$

$$\begin{aligned} \text{subject to:} \quad & \boldsymbol{\Sigma} \text{ real symmetric and } \boldsymbol{\Sigma} \succ \mathbf{0} \\ & \mathbf{I}_n - \boldsymbol{\Sigma} \succeq \mathbf{0}. \end{aligned}$$

In this optimization problem (i) the optimization variable is the $n \times n$, real matrix $\boldsymbol{\Sigma}$, assumed to be symmetric, (ii) $\mathbf{I}_n$ is the identity matrix of size n, (iii) $\mathbf{E}$ is a known and fixed matrix and (iv) the notation $\boldsymbol{\Sigma} \succ \mathbf{0}$ means that $\boldsymbol{\Sigma}$ is positive definite and the notation $\mathbf{I}_n - \boldsymbol{\Sigma} \succeq \mathbf{0}$ means that $\mathbf{I}_n - \boldsymbol{\Sigma}$ is positive semi-definite.

Theorem 2. *The optimization problem* (2.23) *is a convex problem; it has one unique optimal solution* $\widehat{\boldsymbol{\Sigma}}$.

The proof is given in Appendix A.2. Note that problem (2.23) is a MAXDET problem for which there exists efficient software. Problem (2.23) is modeled and solved with YALMIP employing the *sdpt3* solver [95, 96].

We can now describe the estimation procedure. First perform a QR-decomposition of the matrix $\mathbf{R}^{-\frac{1}{2}}\mathbf{H}$ and obtain

$$\mathbf{R}^{-\frac{1}{2}}\mathbf{H} = \mathbf{V} \begin{pmatrix} \mathbf{U} \\ \mathbf{0}_{m-n,n} \end{pmatrix} \tag{2.24}$$

where $\mathbf{U}$ is an upper triangular, real $n \times n$ matrix, $\mathbf{0}_{m-n,n}$ is the null rectangular matrix of dimensions $(m-n) \times n$ and $\mathbf{V}$ is an orthogonal matrix of dimensions $m \times m$. Note that $\mathbf{U}$ is invertible because $\mathbf{H}$ and $\mathbf{R}$ are full rank.

Second, let $\widehat{\mathbf{E}}_k$ be the square matrix of dimensions $n \times n$ made of the first n rows and columns of $\mathbf{V}^T\mathbf{R}^{-\frac{1}{2}}\widehat{\mathbf{C}}_k\mathbf{R}^{-\frac{1}{2}}\mathbf{V}$:

$$\widehat{\mathbf{E}}_k = \left(\mathbf{V}^T\mathbf{R}^{-\frac{1}{2}}\widehat{\mathbf{C}}_k\mathbf{R}^{-\frac{1}{2}}\mathbf{V}\right)(1\!:\!n, 1\!:\!n) \tag{2.25}$$

Theorem 3. *The maximum likelihood estimate of* $\boldsymbol{P}_{k|k-1}$ *based on the observation of the innovations is equal to*

$$\widehat{\mathbf{P}}_{k|k-1} = \mathbf{U}^{-1}\left(\widehat{\boldsymbol{\Sigma}}^{-1} - \mathbf{I}_n\right)\mathbf{U}^{-T} \tag{2.26}$$

where $\widehat{\boldsymbol{\Sigma}}$ *is the optimal solution of the problem* (2.23) *with* $\mathbf{E}$ *replaced by* $\widehat{\mathbf{E}}_k$. *The matrix* $\widehat{\mathbf{P}}_{k|k-1}$ *is symmetric and positive semi-definite.*

The proof is given in Appendix A.3.

2.5.2 Simulations and results for ideal processes

In this section, we evaluate the accuracy of the PECE method by considering ideal processes where the time evolution of the system state is controlled so that the true

value of every parameter of the process is known. The purpose is to verify whether the ability of the PECE method to track step-variations of the system state is not at the expense of its accuracy when there are no steps[3]. For this purpose, we first consider a process without step-variations in the system state and then study a process where we add a step to the state variables. For all the cases treated in this section, we assume $\mathbf{R}$ to be diagonal and constant:

$$\mathbf{R} = r\mathbf{I}_m \tag{2.27}$$

where r is a scalar and $\mathbf{I}_m \in \mathbb{R}^{m\times m}$ is the identity matrix.

The two case studies are described in detail here below:

- *Base case*: the process consists in a random walk as (2.1) with $\mathbf{Q}$ that is diagonal and constant:

  $$\mathbf{Q} = q\mathbf{I}_n \tag{2.28}$$

  where q is a scalar and $\mathbf{I}_n \in \mathbb{R}^{n\times n}$ is the identity matrix. We have tested the two possible conditions that can occur, i.e., $q/r < 1$ and $q/r > 1$.

- *Base case plus steps*: it consists in the same random walk processes of the *base case* plus state step-variations of intentionally large amplitudes that violate the process model.

It is worth observing that this section proves the effectiveness of the PECE method for generic physical processes, as it can be applied to every process, as long as Assumptions #1–3 of Section 2.5.1 hold.

The PECE method is compared with two other covariance-estimation methods:

- The method of Myers and Tapley [89], which will be called *Myers* henceforth in this chapter. In [89], the assessment of both $\mathbf{Q}$ and $\mathbf{R}$ is discussed. Whereas, we assume $\mathbf{R}$ is known, so that only $\mathbf{Q}$ has to be estimated. The formulation of the *Myers* method is recalled in Appendix A.4;
- Our heuristic method proposed in Section 2.4, which will be called *heuristic* henceforth in this chapter.

Three DKFs that use the three considered methods (PECE, *Myers* and *heuristic*) are run

[3] Indeed, a simple way to track state step-variations would be to always overestimate the value of $\mathbf{Q}$, as the heuristic method proposed in Section 2.4 does (see Fig. 2.20). Obviously, the filtering effectiveness is compromised when no steps are present. Another way would be to inflate $\mathbf{Q}$ only when the step occurs, as it is proposed in [37]. The problem is what value of $\mathbf{Q}$ should be set before and after the step.

in parallel. We assume that the DKFs have the knowledge of $\mathbf{R}$, but they do not know $\mathbf{Q}$.

The PECE, *Myers* and *heuristic* methods use a moving-window composed of N time-steps in order to assess the respective covariance matrices. It is important to recall that the PECE method uses N innovations to infer $\mathbf{P}_{k|k-1}$, whereas the *Myers* and *heuristic* methods use N state estimates to infer $\mathbf{Q}$. In Section 2.5.2, we assess the influence of N on the SE accuracy. The PECE method uses a moving-window composed of $N = 5\,000$ time-steps, as it has been found to be an effective trade-off between filtering performance and fast tracking of state step-variations. Also the moving-window length employed by *Myers* method is assumed to be $N = 5\,000$ time-steps. We choose $N = 30$ for *heuristic* method, because it does not need a large moving-window length to estimate $\mathbf{Q}$ (see Section 2.4.2).

Base case

Let us consider a multi-dimensional state $\mathbf{x} \in \mathbb{R}^n$, with $n = 6$. The process and measurement equations are

$$\begin{aligned}
\mathbf{x}_k &= \mathbf{x}_{k-1} + \mathbf{w}_{k-1} \\
\mathbf{z}_k &= \mathbf{x}_k + \mathbf{v}_k \\
\mathbf{w} &\sim \mathcal{N}(0, \mathbf{Q}) \\
\mathbf{v} &\sim \mathcal{N}(0, \mathbf{R})
\end{aligned}$$

in which $\mathbf{R}$ and $\mathbf{Q}$ are defined as in (2.27) and (2.28), respectively. First, we consider the case where $q/r < 1$, with $r = 10^{-7}$ and $q = 10^{-10}$. As a consequence, the true value of the KF prediction-error covariance matrix is $\mathbf{P}_\infty = 3.21 \cdot 10^{-9}\mathbf{I}_n$. Note that the important parameter is the ratio q/r. Indeed, different values of r and q resulting in the same ratio lead to similar results.

The estimated state $\widehat{\mathbf{x}}$ and the matrix $\mathbf{Q}$, which are used in the three DKFs, are initialized by using the initial conditions listed here below:

1. The state vector is initialized to $\mathbf{x}_0 = \mathbf{1}$ (where $\mathbf{1}$ is a vector of ones), which is different from the true state.
2. For the first $15\,000$ time-steps, we use $\mathbf{Q} = q_0\mathbf{I}_n$. To help the convergence of the initial state $\mathbf{x}_0$ towards the true one, we set a high value of $q_0 = 10^{-5}$.

Fig. 2.20 shows the time evolution of the third diagonal element of $\mathbf{P}_{k|k-1}$ estimated by the three methods and its true value (the other diagonal elements exhibit an analogous behavior). The time evolution of the RMSEs are shown in Fig. 2.21 for these three DKFs

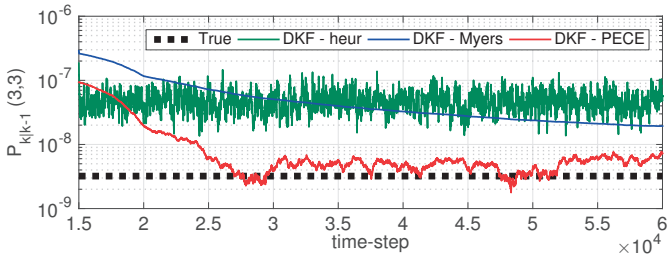

Figure 2.20 – *Base case*, $q = 10^{-10}$. Time evolution of the third diagonal element of $\mathbf{P}_{k|k-1}$ (the other diagonal elements exhibit an analogous behavior): true and estimated values.

plus a DKF that uses the exact value of $\mathbf{Q}$ denoted as $DKF_{Q\,exact}$. At time-step k, the estimation error vector $\mathbf{e}_k$ is defined as the difference between the estimated and the true state:

$$\mathbf{e}_k = \widehat{\mathbf{x}}_k^{est} - \mathbf{x}_k^{true}. \tag{2.29}$$

Note that the RMSE accounts for the errors of all the six state variables. Until the $15\,000^{th}$ time-step, the three DKFs use a large value of $\mathbf{Q}$ equal to $10^{-5}\mathbf{I}_n$, so that the estimation errors are the same for every DKF and remain large. Afterwards, the process covariances start to be assessed and the errors of the three DKFs decrease, thus reflecting the behavior of the $\mathbf{P}_{k|k-1}$ estimates. As visible in Fig. 2.20, the $\mathbf{P}_{k|k-1}$ inferred by the PECE method converges to the true value of $\mathbf{P}_{k|k-1}$ in about $10\,000$ time-steps, which corresponds to twice the moving-window length $N = 5\,000$. Afterwards, the $\mathbf{P}_{k|k-1}$ estimates oscillate around the true value of $\mathbf{P}_{k|k-1}$ (see the enlarged part of Fig. 2.21) and the estimation errors become similar to those of the DKF that uses the exact value of $\mathbf{Q}$. The convergence of the *Myers* method is much slower and the $\mathbf{P}_{k|k-1}$ estimates takes a longer time to converge to the true values, i.e., hundreds of thousands of time-steps. However, the estimates are characterized by smaller variations compared to the PECE method (see Fig. 2.20). The *heuristic* method's convergence phase lasts few time-steps, because it uses a small moving-window length $N = 30$. Then, it tends always to overestimate the value of $\mathbf{P}_{k|k-1}$. As a consequence, the measurement noise is not filtered effectively, which leads to significant estimation errors.

Let us now consider the case in which $q/r > 1$, with $r = 10^{-7}$ and $q = 10^{-6}$. The corresponding true value of $\mathbf{P}_\infty$ is $1.09 \cdot 10^{-6}\mathbf{I}_n$. Fig. 2.22 shows the time evolution of the third diagonal element of $\mathbf{P}_{k|k-1}$ for this case (the other diagonal elements exhibit an analogous behavior). The *Myers* and PECE methods estimate its precise true value, whereas the *heuristic* method provides again larger variances. It can be noted that the PECE method estimates immediately the correct value of $\mathbf{P}_{k|k-1}$, whereas the *Myers* method takes $5\,000$ time-steps to approach it. However, the estimation errors of these three DKFs are almost equal to those of the DKF that uses the exact value of $\mathbf{Q}$. We

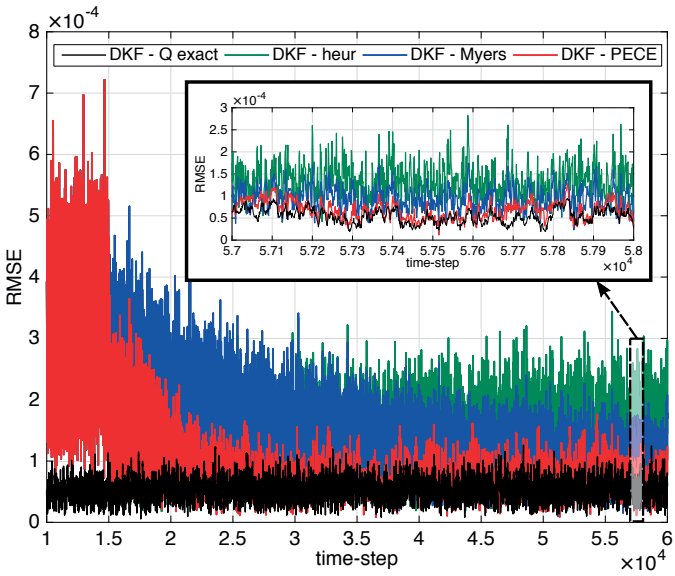

Figure 2.21 – *Base case*, $q = 10^{-10}$. Time evolution of the RMSEs.

do not show the RMSEs for this case, because they are indistinguishable and oscillate between $0.2 \cdot 10^{-3}$ and $1.6 \cdot 10^{-3}$. These results are caused by the predominance of the process noise, making simple its estimation from the samples. This case is not of high interest, because the process model has a limited influence on the KF solution. Indeed, the simple processing of the measurements leads to state estimates very close to the optimal ones.

Base case plus steps

Let us consider the same process of the *Base Case*, with $r = 10^{-7}$, $q = 10^{-10}$, and $\mathbf{x}_0 = \mathbf{1}$. For this case, we wait until the convergence phase is finished (time instant 0), and $1\,000$ time-steps later we simulate a state step-variation of amplitude 10^{-2}, which is significantly larger than the process-noise standard deviation. By the time the state change occurs, we expect $\mathbf{P}_{k|k-1}$ to increase, because the assumed persistent model in (2.1) is no longer accurate. Note that, as the step is applied to every state variable, they become correlated. In order to show the effect of the estimated off-diagonal elements of $\mathbf{P}_{k|k-1}$ on the state estimates, we add a further DKF, called PECE$_{diag}$. The latter uses the PECE method in which the variable $\boldsymbol{\Sigma}$ of the optimization problem (2.23) is diagonal.

Fig. 2.23 shows the time evolution of the third diagonal element of $\mathbf{P}_{k|k-1}$ estimated by the four DKFs when the step occurs, and Fig. 2.24 shows a further zoom of Fig. 2.23 (the other diagonal elements exhibit an analogous behavior). The trend of the off-diagonal elements of $\mathbf{P}_{k|k-1}$ is highly dependent on the specific simulation parameters. Their effect is evident by comparing the behavior of the DKF estimates given by the

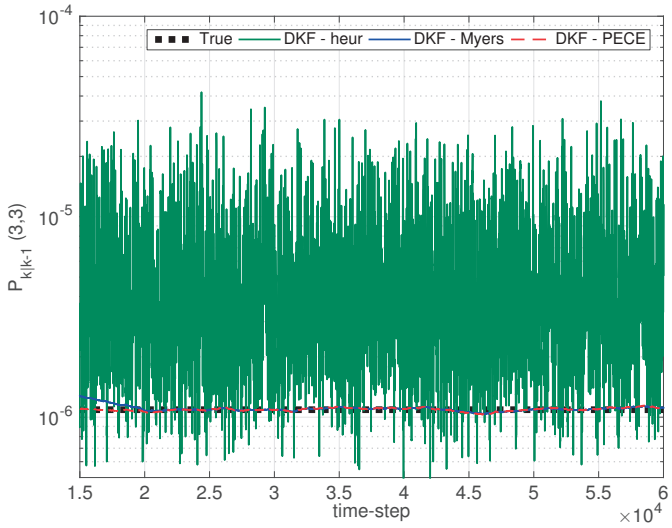

Figure 2.22 – *Base case*, $q = 10^{-6}$. Time evolution of the third diagonal element of $\mathbf{P}_{k|k-1}$ (the other diagonal elements exhibit an analogous behavior).

PECE and PECE$_{diag}$ methods. The DKF that uses the *Myers* method has a remarkable delay in inflating $\mathbf{P}_{k|k-1}$ and consequently in tracking the system state during and after the step, as is visible from the RMSEs in Fig. 2.25. This behavior is typical of the covariance-estimation methods that infer $\mathbf{Q}$ by exploiting only the knowledge of the past state estimates. It is known that $\mathbf{Q}$ influences the state estimates, and vice versa, as a closed-loop, therefore both take several time-steps to increase. At the time of the step, the *heuristic* method had smaller errors because it overestimates the value of $\mathbf{Q}$, as we have seen for the *base case*. Shortly after the step, the *heuristic* method inflates $\mathbf{Q}$ rapidly, so that the estimation errors decrease in only a few time-steps. Unlike the other two methods, the PECE method uses the past innovations and the innovation at the current time-step that already contains the information brought by the upcoming set of measurements. Then, it updates the value of $\mathbf{P}_{k|k-1}$ before the measurement update. Indeed, the PECE method is the only one able to increase $\mathbf{P}_{k|k-1}$ exactly by the time the step occurs (i.e, with no delay) as shown in Fig. 2.24. This characteristic enables the PECE method to immediately react to state step-variations. Fig. 2.25 shows that the estimation errors of the DKF that uses the PECE method are the smallest, both exactly when the step occurs and shortly afterwards. In Fig. 2.25, it is also evident that the DKF that uses the PECE method reacts faster than the DKF that uses the PECE$_{diag}$ method. Therefore, the estimated off-diagonal entries of $\widehat{\mathbf{P}}_{k|k-1}$ improve the state-tracking capability.

Finally, we consider a case in which $q/r > 1$ ($r = 10^{-7}$ and $q = 10^{-6}$) and a state step-variation is present. The step-variation is of amplitude 1 and occurs at the $1\,000^{th}$ time-step. Note that the step amplitude is larger than the case where $q/r < 1$, because a step amplitude of 10^{-2} would be comparable to the process noise. Fig. 2.26 shows

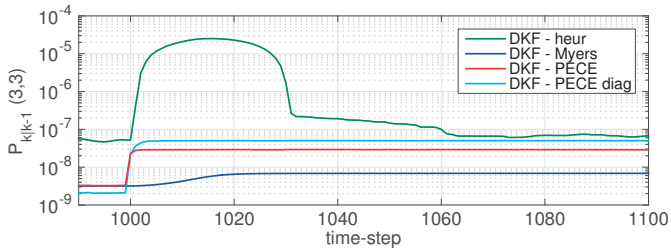

Figure 2.23 – *Base case plus steps*, $q = 10^{-10}$ (a step occurs at the $1\,000^{th}$ time-step). Time evolution of the third diagonal element of $\mathbf{P}_{k|k-1}$ (the other diagonal elements exhibit an analogous behavior).

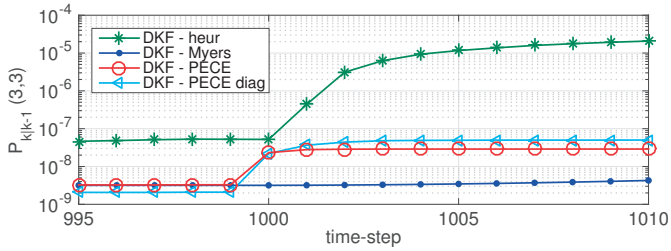

Figure 2.24 – *Base case plus steps*, $q = 10^{-10}$ (a step occurs at the $1\,000^{th}$ time-step). Further zoom of Fig. 2.23 close to the step-variation that occurs at the $1\,000^{th}$ time-step.

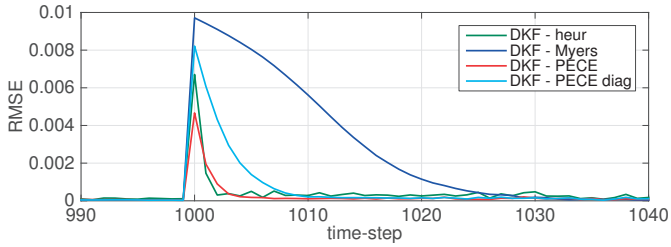

Figure 2.25 – *Base case plus steps*, $q = 10^{-10}$ (a step occurs at the $1\,000^{th}$ time-step). Time evolution of the RMSEs.

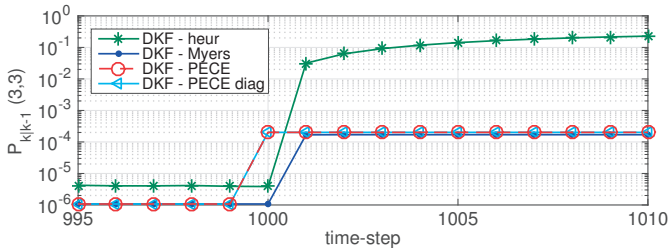

Figure 2.26 – *Base case plus steps*, $q = 10^{-6}$ (a step occurs at the $1\,000^{th}$ time-step). Time evolution of the third diagonal element of $\mathbf{P}_{k|k-1}$ (the other diagonal elements exhibit an analogous behavior).

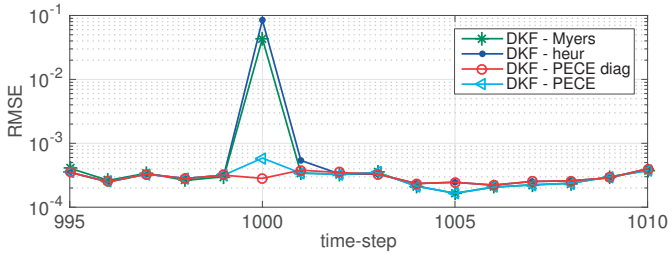

Figure 2.27 – *Base case plus steps*, $q = 10^{-6}$ (a step occurs at the $1\,000^{th}$ time-step). Time evolution of the RMSEs.

the time evolution of the third diagonal element of $\mathbf{P}_{k|k-1}$ estimated by the *heuristic*, *Myers*, PECE and PECE$_{diag}$ methods (the other diagonal elements exhibit an analogous behavior). As in the case where $q = 10^{-10}$, the PECE and PECE$_{diag}$ methods increase $\mathbf{P}_{k|k-1}$ as soon as the step occurs, whereas the *heuristic* and *Myers* methods react with a delay of one time-step. Indeed, only the PECE and PECE$_{diag}$ methods are characterized by limited errors during the step, as shown in Fig. 2.27. Note that, again, the accuracy of the PECE method is better than that of PECE$_{diag}$, due to the effect of the estimated off-diagonal elements of $\mathbf{P}_{k|k-1}$.

Influence of parameter N on the SE accuracy

The only parameter that has to be set in the PECE method is N, specifically the number of previous innovations used to calculate the sample innovation-covariance matrix in (2.21). In this section, we present the influence of N on the SE accuracy considering both the *base case* and the *base case plus steps* in which $q/r < 1$. As already explained for the *base case*, $q/r < 1$ is the case of interest where the noise filtering can be effective. The investigation involves the PECE and *Myers* methods. Unlike in the simulations related to the *base case* and *base case plus steps*, where the RMSEs was calculated at each time-step, here we show the RMSE that takes into account all the errors of the T considered time-steps. Besides, we show the median value of the RMSEs obtained in 10 different simulations. It is worth mentioning that we wait until the convergence

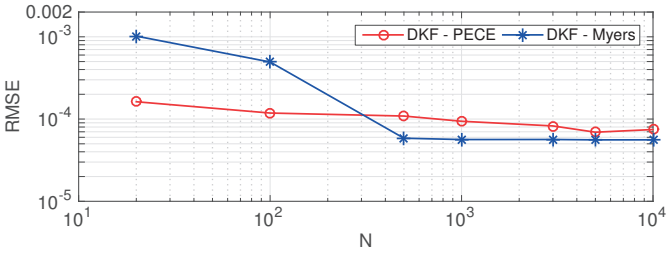

(a) *Base case* ($q = 10^{-10}$, $r = 10^{-7}$).

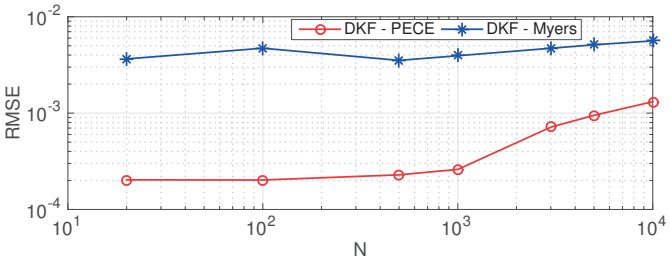

(b) *Base case plus steps* ($q = 10^{-10}$, $r = 10^{-7}$).

Figure 2.28 – RMSEs as a function of N for the PECE and *Myers* methods. In the *base case*, the RMSE is computed considering 2 000 time-steps. In the *base case plus steps*, the RMSE is computed considering the 30 time-steps after the state step-variation.

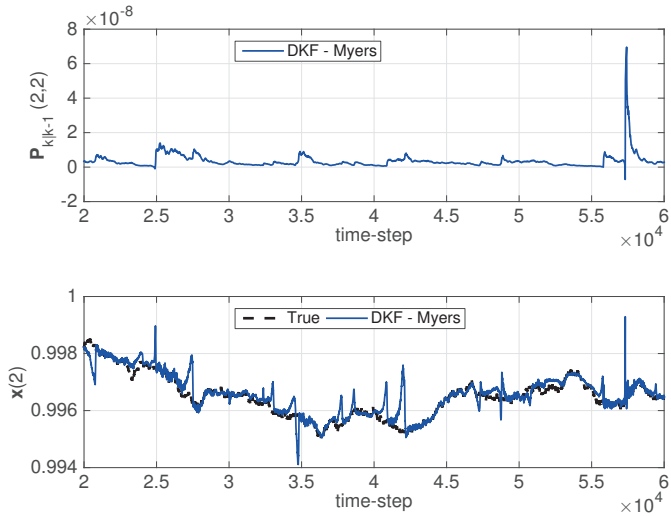

Figure 2.29 – *Base case*, $q = 10^{-10}$, $r = 10^{-7}$, $N = 100$. Time evolution of the 2^{nd} diagonal element of $\mathbf{P}_{k|k-1}$ and of the associated 2^{nd} element of the state vector: true state and state estimated by the DKF that uses the *Myers* method. This figure shows the numerical stability problems of the *Myers* method.

phase is finished before performing this assessment.

Fig. 2.28a shows the RMSEs as a function of N for the *base case*. The RMSE is computed by considering $T = 2\,000$ time-steps. The PECE method degrades the estimation accuracy as we consider a smaller number of innovations. The innovations are affected by the measurement noise that is not effectively filtered if a small number of innovations is used. The RMSEs of the *Myers* method remains quite stable and smaller than that of the PECE method for $N > 500$. Note that the use of a smaller value of N also leads to a faster convergence of the *Myers* method to the true value of $\mathbf{P}_{k|k-1}$ compared with Fig. 2.20. However, the accuracy of the *Myers* method drops for small values of N (i.e., $N = 20$ and $N = 100$) due to the fact that the positive semi-definiteness of $\mathbf{P}_{k|k-1}$ is not guaranteed by the *Myers* method. As a consequence, the KF numerical stability might be compromised and the KF solution sometimes diverges from the true state. This phenomenon is visible in Fig. 2.29 where $N = 100$: the state estimated by the DKF that uses the *Myers* method loses track of the true state in many occasions, e.g., when negative diagonal elements of $\mathbf{P}_{k|k-1}$ are estimated (i.e., at time-step $5.7 \cdot 10^4$). For the ideal case considered in this section, significant estimation errors related to this problem occur only for $N < 300$.

Fig. 2.28b shows the RMSEs as a function of N for the *base case plus steps*. The RMSE is computed by considering the $T = 30$ time-steps after the state step-variation. As expected, the PECE method outperforms the *Myers* method in the period following the step. In contrast with the *base case*, the smaller N is, the smaller the errors are, because the last innovations have a higher weight in the computation of the sample covariance (2.21).

2.5.3 Simulations and results for power-system state estimation

The effectiveness of the PECE method is here proven in the context of power-system SE via the procedure presented in Section 2.4.2. We use the New England 39-bus system and we consider the network operating conditions described in Section 2.4.2, except for the time evolution of the reactive power absorbed by the load at bus #4. Specifically, in order to show the behavior of the PECE method when a state step-variation occurs, we simulate a sudden drop of 90 MVAR of the reactive power at bus #4, which can be caused, for instance, by the disconnection of a shunt reactor. This event is shown in Fig. 2.30. In Fig. 2.31, we highlight the fact that the drop affects two time-steps as a result of the response to transients of the phasor-estimation algorithm of the PMU (see [97] for further details). The reactive-power drop produces step-wise perturbations in the state variables, which are similar to those of the *base case plus steps* in Section 2.5.2[4]. It

[4]We would like to clarify that the results do not change if we simulate a sudden variation of the active power only or of both active and reactive powers simultaneously, because the covariance assessment methods do not depend on what state variables experience the step-variation.

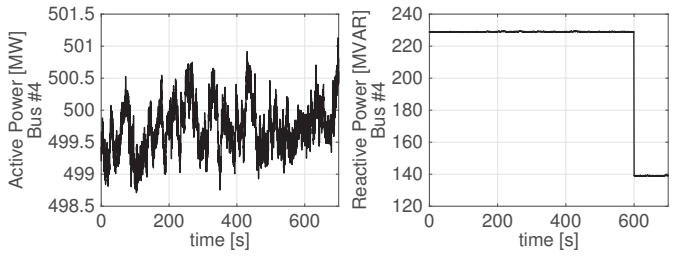

Figure 2.30 – Time profiles of the active and reactive power at bus #4. A drop of about 90 MVAR of reactive power occurs at 600 seconds.

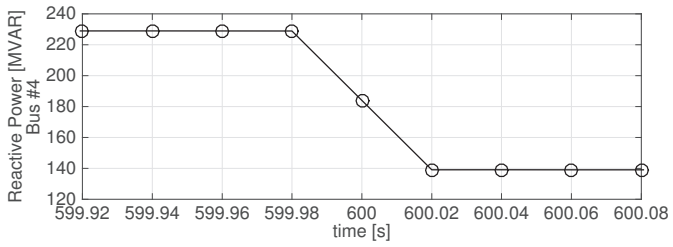

Figure 2.31 – Time profile of the reactive power at bus #4: zoom close to the 90 MVAR step-variation.

is well-known that in transmission networks the reactive power mainly influences the voltage magnitude; as we express the state in rectangular coordinates, both real and imaginary parts of the voltage are affected.

The network schematic and the measurement configuration are depicted in Fig. 2.1 in Section 2.4.2. We recall that the measurement configuration ensures the full-network observability, i.e., matrix $\mathbf{H}$ has full rank (Assumption #3 of Section 2.5.1 holds).

The measurement noise is assumed to be a Gaussian-white sequence where the covariance matrix $\mathbf{R}$ is known, time-invariant and diagonal. Further explanations can be found in Section 2.4.2. The standard deviations of both the real and imaginary parts of the measurements are assumed to be 0.33% of the full scales of the sensors.The voltage sensors' full scales are assumed to be equal to the rated voltage; the current sensors' full scales are assumed to be equal to twice the largest value of the current-injection magnitude at the respective bus in the considered simulation period. From the above-mentioned hypotheses, the linear measurement model is known and time-invariant (Assumption #2 of Section 2.5.1 holds).

Moreover, we use the process model given in (2.1) for the reasons already given in Section 1.4.3 (Assumption #1 of Section 2.5.1 holds).

Accuracy performance analysis

In the following we analyze the accuracy performance of five state estimators, i.e., four DKFs that use the *Myers*, *heuristic*, PECE and PECE$_{diag}$ methods, and the LWLS. As in Section 2.5.2, the *heuristic* method uses $N = 30$, whereas the PECE, *Myers* and PECE$_{diag}$ methods use $N = 5\,000$. The influence of parameter N on the SE accuracy for the specific application of power-system SE is presented later in this section.

The first part of the simulation consists in an initial phase of 300 seconds (corresponding to $15\,000$ time-steps as for the *base case* in Section 2.5.2) in which we keep a constant value of $\mathbf{Q}$ for the considered DKFs and their estimated states converge from a *flat-start initialization* towards the true state. For brevity, the initial phase is not shown in this section.

The time evolution of the RMSEs of the five considered state estimators is given in Fig. 2.32; it is composed of three sub-figures: Fig. 2.32a shows the entire simulation, Fig. 2.32b shows a portion of the simulation where the network is in quasi-static conditions, and Fig. 2.32c shows the portion of the simulation close to the state step-variation. The RMSEs of the *Myers* method exhibit high sporadic spikes that are clearly visible in Fig. 2.32a. This numerical stability issue of the *Myers* method has already been described at the end of Section 2.5.2 (in particular, see Fig. 2.29), and it is due to the fact that the *Myers* method does not ensure the positive semi-definiteness of $\mathbf{P}_{k|k-1}$. Note that the smaller N, the worse the numerical stability issue.

Fig. 2.32b shows the RMSEs when the network is in quasi-static conditions, i.e., the load powers are varying smoothly with no steps of significant amplitude. The errors of the four DKFs are comparable except for the occasional spikes of the *Myers* method, whereas the LWLS errors are about three times larger on average. We can observe that, unlike in the *base case* in Section 2.5.2, the accuracy of the *heuristic* method is just slightly worse than that of the other DKFs.

Fig. 2.32c shows the RMSEs during and after the step-variation. The LWLS keeps the same estimation accuracy, because at every time-step it relies only on the measurements taken at that time-step. The KF, instead, uses also the past information to compute the system state. As soon as the step occurs, $\mathbf{P}_{k|k-1}$ should be adapted in order to attribute a lower weight to the predicted state with respect to the measurements. In other words, the KF behavior should approach that of the LWLS. The *Myers* and *heuristic* methods detect the occurrence of the step with a time-step delay, because they use only the state estimates. Therefore, they are characterized by large estimation errors when the step occurs. After the step, the *heuristic* method recovers the correct state tracking faster than the *Myers* method. The PECE method is the only one that has a peak of the errors comparable to the one of LWLS. Indeed, it estimates the new $\mathbf{P}_{k|k-1}$ by using the innovations before the measurement update, so that the information

brought by the measurements at the time of the step is already taken into account in the Kalman gain. The accuracy of the PECE$_{diag}$ method is significantly worse than that of the PECE method, proving the importance of using a full matrix in the optimization problem (2.23). These results confirm those obtained for the *base case* in Section 2.5.2.

The reactive power step-variation affects mainly the real part of the voltage phasors at bus #4 and at the neighbor buses. Fig. 2.33 shows the time evolution of the real part of the voltage phasor (in pu of the rated voltage) at bus #4: the true value and the value estimated by the considered state estimators. It reflects the estimation errors shown in Fig. 2.32c. It is worth mentioning that some of the state variables estimated by the *Myers*, *heuristic* and PECE$_{diag}$ methods go even on the opposite direction of the true state variation. For instance, this undesired behavior occurs with the *Myers* and *heuristic* methods for the real part of the voltage phasor at bus #31, as shown in Fig. 2.34. This is due to the incorrect value of $\mathbf{P}_{k|k-1}$ estimated by these methods when the step occurs. These wrong estimates are other possible equilibrium points of the power system far from the true ones. Note that this behavior was observed also in [37].

Influence of parameter N on the SE accuracy

This section shows the influence of parameter N on the SE accuracy. This study is carried out separately for the network in quasi-static conditions and during the step-variation. In the first case, we consider the 100 seconds prior to the step. In the second case, we consider the 2 seconds following the step-variation. For both cases, we compute the RMSE for all the time-steps contained in the considered time-window and we show the median value of the RMSEs obtained in 10 different simulations. The RMSEs as a function of N are shown in Figs. 2.35a and 2.35b for the system in quasi-static conditions and during the step-variation, respectively. The accuracy of both the PECE and *Myers* methods are examined.

Concerning the system in quasi-static conditions, the estimation accuracy of both the PECE and *Myers* methods degrades as N diminishes. However, it can be seen that the accuracy of the PECE method is much better than that of the *Myers* method for all the considered values of N. This is mainly due to the numerical stability problem of the *Myers* method that we have previously discussed in the accuracy performance analysis.

As expected, also the study on the step-variation reveals that the PECE method outperforms the *Myers* method for all the considered values of N. The accuracies of both methods decrease as N decreases, which indicates an opposite trend with respect to the results of the ideal case in Section 2.5.2. Regarding the *Myers* method, the reason lies in more significant numerical stability problems. Instead, the worsening of the PECE method's accuracy as N decreases is due to the increasing effect of the measure-

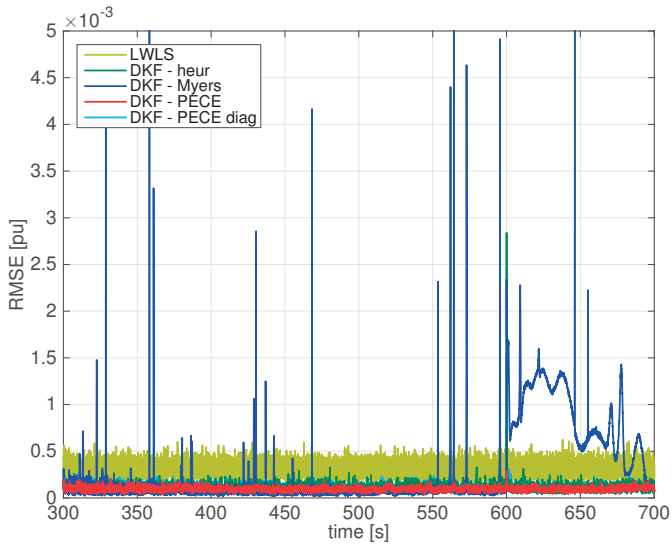

(a) Entire simulation.

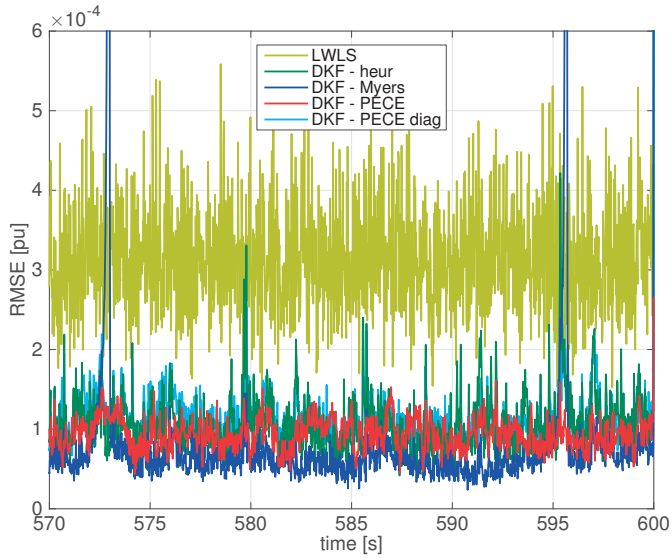

(b) Zoom of Fig. 2.32a during quasi-static conditions.

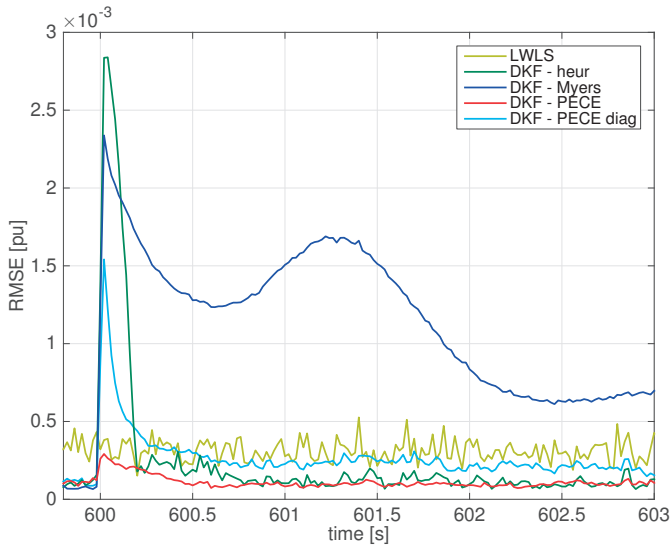

(c) Zoom of Fig. 2.32a on the state step-variation.

Figure 2.32 – Time evolution of the RMSEs.

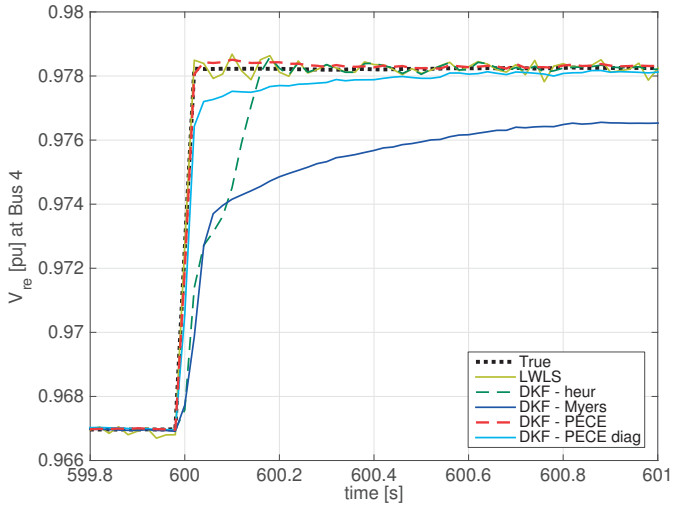

Figure 2.33 – Time evolution of the real part of the voltage at bus #4 that is the bus where the reactive power step-variation occurs.

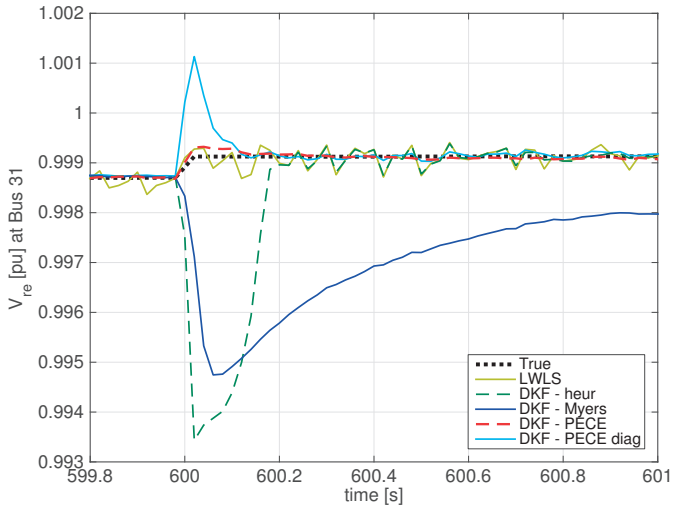

Figure 2.34 – Time evolution of the real part of the voltage at bus #31: true and estimated values.

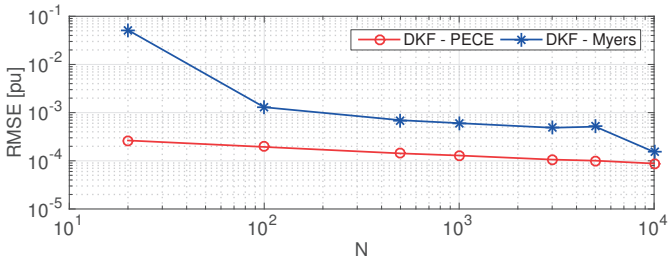

(a) Quasi-static conditions.

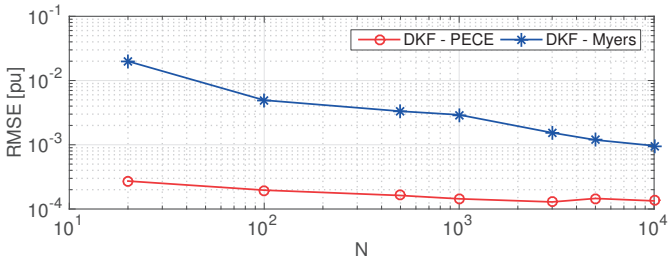

(b) State step-variation.

Figure 2.35 – RMSEs as a function of N for the PECE and *Myers* methods. For case (a) where the network is in quasi-static conditions, the RMSE is computed considering the 100 seconds prior to the step. For case (b) where the network state has a step-variation, the RMSE is computed considering the 2 seconds following the step.

ment noise on the sample covariance matrix (2.21). Indeed, we have observed that the small peak of the errors of the PECE method close to the step-variation has the same amplitude irrespectively of the value of N, whereas the errors after the step are highly affected by the measurement noise. The latter is not effectively filtered if a small value of N is set.

In conclusion, the PECE method guarantees a better accuracy than the *Myers* method for all the considered values of N in both quasi-static conditions and during the state step-variation.

Computational-time performance assessment

The remarkable estimation accuracy of the PECE method comes at the expense of the computational time. The latter is almost entirely devoted to solving the convex optimization problem of (2.23) that depends only on the state dimension n. We can instead neglect the time used to compute the sample covariance matrix (2.21), so that the computational time is not function of N. Fig. 2.36a shows the computational time of the PECE method as a function of n. Each value is an average over 100 simulations. These results are obtained by solving the optimization problem (2.23) with YALMIP employing the *sdpt3* solver implemented in MATLAB 2014b [95, 96]. The

laptop is an Apple MacBook Pro with a 2.5-GHz CPU, 16-GB RAM. The increase of the computational time shown in Fig. 2.36a is exponential as the y-axis is in logarithmic scale.

On the contrary, the computational time of the *Myers* and *heuristic* methods is significantly affected by the parameter N. Figs. 2.36b and 2.36c show the computational time of these methods, as a function of the state dimension n; the three curves refer to three values of N, i.e., 100, $1\,000$ and $10\,000$. Both methods are considerably faster than the PECE method. In particular, the *Myers* method is characterized by a computational time that increases exponentially as a function of n, and it remains below 100 milliseconds for the considered values of n. The *heuristic* method is the fastest one with a computation time always below 10 milliseconds.

2.6 Conclusions

In this chapter we compare the performance of the LWLS and DKF algorithms in terms of accuracy and computational time. This analysis is carried out by employing the following assumptions: (1) there are no systematic-errors, only random Gaussian-white noise is present; (2) the linear measurement-model is known; (3) we use only high time-resolution measurements from PMUs; (4) there are no bad-data and network model errors, thus, the SE accuracy is directly linked to the capability of reducing the measurement noise.

The first part of this chapter is dedicated to the definition and testing of a new heuristic method for the assessment of $\mathbf{Q}$ that is used in a DKF. The DKF employs the persistent process-model defined in (2.1). This method estimates $\mathbf{Q}$ based on the knowledge of the previous N state estimates. The method is straightforward to implement and the only parameter that needs to be set is N that requires a tuning stage. The case studies consist in the New England 39-bus system and the 123-bus test feeder that are assumed to be in quasi-static operating conditions. The theory predicts that DKF is more accurate than the LWLS as long as the process model is correct. We statistically validated the adequacy of the persistent process-model used in combination with the proposed heuristic method that infers $\mathbf{Q}$. Then, we showed that the DKF outperforms the LWLS in terms of accuracy, but the LWLS is faster in terms of computational time. However, both of them are able to estimate the system state in less than 100 ms for these case studies and are suitable for RTSE of networks of similar size. We observed that the proposed heuristic method is fast and able to adapt $\mathbf{Q}$ to the changing operating conditions of the network. We also noticed that the improvement of the DKF results with respect to the LWLS results is particularly pronounced when the redundancy level is low.

In the second part of this chapter, we proposed a new method, called prediction-error

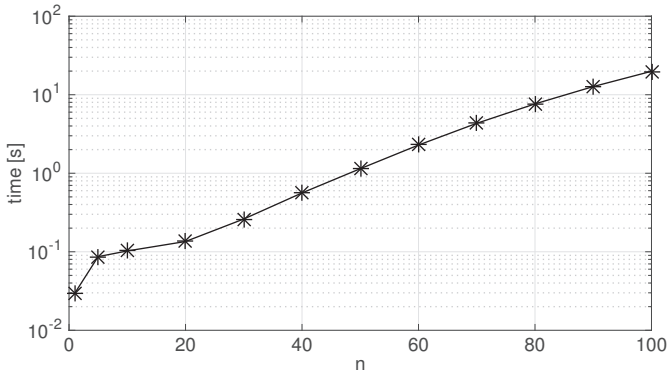

(a) *PECE method.*

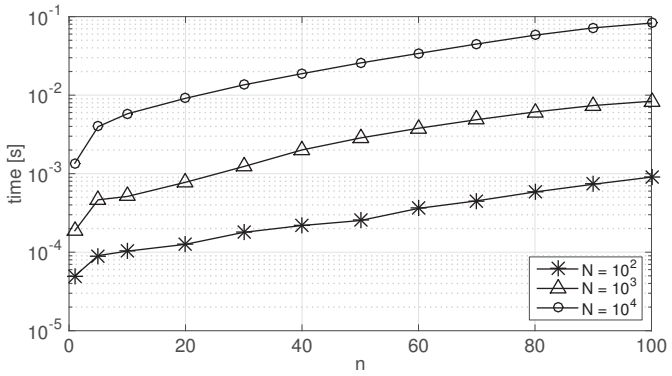

(b) *Myers method.*

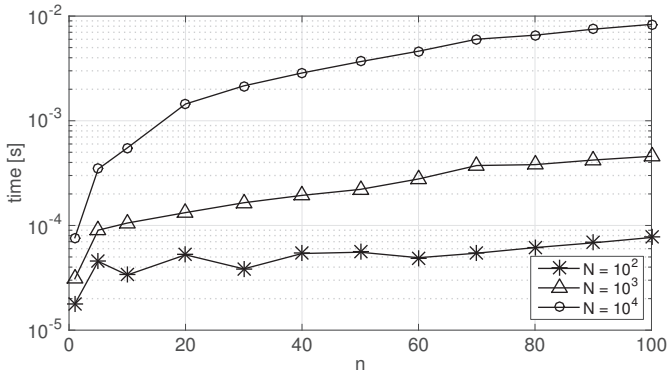

(c) *Heuristic method.*

Figure 2.36 – Computational time as a function of n. For the *Myers* and *heuristic* methods, multiple curves refer to different values of N.

covariance estimation (PECE), for the assessment of $\mathbf{P}_{k|k-1}$ that is suitable for SE of step-varying processes where the process-noise covariances are time-varying and unknown. It relies on the knowledge of a linear and time-invariant measurement model and was tested for a persistent process-model. The PECE method correctly estimates the value of $\mathbf{P}_{k|k-1}$ for a process characterized by constant noise-covariances, and tracks the system state even during large step-variations. To the best of our knowledge, no other method proposed in the literature relying on the same assumptions is able to achieve such accuracy performance. The PECE method makes use of a constrained convex optimization problem that computes $\mathbf{P}_{k|k-1}$ from the innovations and ensures the positive semi-definiteness of $\mathbf{P}_{k|k-1}$. Only parameter N has to be set, which is the number of previous innovations that are used to compute $\mathbf{P}_{k|k-1}$. We tested the PECE method for ideal cases and for DKF-SE of the New England 39-bus system where a large step-variation of the system state is simulated. We also give a comparison with the SE results of a LWLS, a DKF that use a value of $\mathbf{Q}$ assessed by the heuristic method presented in Section 2.4.1 and a DKF that use a value of $\mathbf{Q}$ assessed by the method presented in [89]. On one hand, the PECE method is faster than the other two methods in tracking state step-variations. On the other hand, it is computationally expensive for high-dimensional systems. It is also important to highlight that the PECE method estimates the full matrix $\mathbf{P}_{k|k-1}$, and we showed that the correct assessment of the off-diagonal entries of $\mathbf{P}_{k|k-1}$ plays an important role in the proper tracking of state step-variations. Future research will focus on a more general process model.

3 Linear state estimation with zero-injection equality constraints via LQ-decomposition

In this chapter, we discuss the problem of linear power-system state estimation with linear equality constraints associated with zero-injection buses. Specifically, we focus on the linear weighted-least-squares algorithm. We present various well-known approaches to handle zero-injections; then, we propose a method based on LQ-decomposition that strictly satisfies the equality constraints and reduces the dimension of the state vector. We demonstrate the performance improvement of the proposed method in terms of numerical stability and computational efficiency via numerical simulations conducted on the 39-bus New England test system.

3.1 Introduction

The content of this chapter is based on [98]. The presence of zero-injection buses is common in power systems. These buses are characterized by an injected power strictly equal to zero, which is the case of interconnection substations. Power-system SE can exploit zero-injections as an information that contains no error. Therefore, SE becomes a constrained optimization problem where zero-injections are the equality constraints.

Making reference to a WLS state estimator, a simple yet approximated way to include equality constraints is to convert the constraining equations in virtual measurements [39, 40]. The latter are defined in Section 1.1.1 as additional measurements with very small uncertainties. This method is approximated as it cannot strictly satisfy the zero-injection equalities. Besides, the main drawback of this approach is that the coefficient matrix[1] in the WLS NE may become poorly conditioned due to the disparity

[1]The *coefficient matrix* refers to the matrix that contains the coefficients of the variables in a set of linear equations.

of weights assigned to real-time measurements, virtual measurements (associated with zero-injections) and pseudo-measurements (associated with historical data or forecasts) [99, Chapter 22]. In Section 1.1.1 we clearly state the difference between virtual measurements and pseudo-measurements.

Alternatively, zero-injection equality constraints can be strictly satisfied by employing the method of Lagrange multipliers. However, in this case the state dimension increases and, in general, the modified coefficient matrix becomes not positive definite [100, 101]. The positive definiteness of the coefficient matrix is important to enhance the computational speed of the SE solution; with reference to the WLS, as $\mathbf{G}$ is positive definite, it can be decomposed in Cholesky factors so that the NE can be solved in an efficient way by forward/backward substitution.

Every approach that introduces the zero-injection information modifies the NE coefficient matrix and its condition. As the ill-conditioning of this matrix is a well-known and important problem, in the following we summarize the relevant techniques that have been proposed in the literature to alleviate this issue. In the context of non-linear WLS-SE, several approaches are described and compared in [102, 54] [6, Chapter 3]. The use of QR-decomposition (QRD) applied to the WLS NE considerably enhances the numerical stability at the expense of matrix sparsity and computation time [103, 104, 102, 105]. A comparative study focusing on numerical stability, computational efficiency, and implementation complexity is given in [102]. In [6, Chapter 3] various approaches are tested against different sources of ill-conditioning. The authors of [106] propose an iterative method to satisfy the zero-injection equality constraints.

Note that all the above-mentioned methodologies were conceived for non-linear iterative WLS-SE. When the measurements set contains only synchrophasor measurements provided by PMUs, the SE problem becomes linear. Power-system linear SE was firstly proposed in [29] and further investigated recently, e.g., [26, 72]. The measurement matrix linking measurements and state variables is exact (not a Jacobian), state-independent and constant in time. Consequently, the equality constraints associated with zero-injections are linear as well. As it is known, a constrained optimization problem that has only linear equality constraints can be solved for a set of variables reduced by the number of constraints. The problem becomes an unconstrained problem in a smaller number of variables.

In this chapter, we propose a method based on LQ-decomposition (LQD) to solve the problem of LWLS-SE with linear equality constraints, which has the following features:

1. the state dimension is reduced by the number of linear equality-constraints imposed by zero-injections;

2. the computation time is considerably decreased;

3. the numerical stability is improved;
4. the equality constraints are strictly satisfied;
5. the structure of the WLS NE is preserved;
6. the coefficient matrix remains positive-definite.

It is worth pointing out that the LQD of a generic matrix $\mathbf{W}$ corresponds to the QRD of $\mathbf{W}^T$. As the the NE structure is maintained, no extra modifications are required in the implementation of already-developed techniques, such as the widely used LNR method for bad-data processing [8]. The proposed method is compared with other well-known techniques that were initially introduced for handling zero-injections in non-linear WLS.

3.2 Linear State Estimation with Linear Equality Constraints

Let us consider a power-system with s buses and c zero-injection buses. We assume to have a measurement infrastructure composed exclusively of PMUs that provide real-time phasor measurements of nodal-voltages, nodal-current injections and current flows.

First, we recall the LWLS problem that uses real-time measurements from PMUs and pseudo-measurements, without considering zero-injections. We provide again the LWLS unconstrained optimization problem defined in Section 1.2 by making explicit the presence of $\mathbf{x}$:

$$\min_{\mathbf{x}} \quad J = \frac{1}{2}(\mathbf{z} - \mathbf{H}\mathbf{x})^T \mathbf{R}^{-1}(\mathbf{z} - \mathbf{H}\mathbf{x}) \tag{3.1}$$

resulting in the well-known NE:

$$\mathbf{G}\,\mathbf{x} = \mathbf{H}^T \mathbf{R}^{-1}\mathbf{z} \tag{3.2}$$

where these vectors and matrices are defined in Section 1.2. We recall that $\mathbf{x} \in \mathbb{R}^n$, $\mathbf{z} \in \mathbb{R}^m$ includes only real-time measurements and pseudo-measurements, $\mathbf{R}$ is diagonal and positive definite, and $\mathbf{G} = \mathbf{H}^T \mathbf{R}^{-1}\mathbf{H}$. Given that the network is observable, $\mathbf{H}$ is full rank and $\mathbf{G}$ is positive-definite. Therefore, $\mathbf{G}$ can be decomposed in Cholesky factors so that the NE can be solved in an efficient way by forward/backward substitution.

The presence of w zero-injection buses adds p equality constraints[2] to the problem in (3.1):

$$\begin{aligned} \min_{\mathbf{x}} \quad & J = \frac{1}{2}(\mathbf{z}-\mathbf{H}\mathbf{x})^T\mathbf{R}^{-1}(\mathbf{z}-\mathbf{H}\mathbf{x}) \\ \text{subject to:} \quad & \mathbf{C}\mathbf{x} = \mathbf{0} \end{aligned} \tag{3.3}$$

where $\mathbf{C}$ is the $p \times n$ measurement matrix related to the vector $\mathbf{i}_0$ of the current injections at the zero-injection buses, which is obviously a null vector $\mathbf{0}$.

Assumption 1. The network is fully observable with the combination of real-time measurements, pseudo-measurements and zero-injections.

This assumption implies that $m + p > n$, but not necessarily that $m > n$. Therefore, the network can also be unobservable by considering only real-time measurements and pseudo-measurements.

Note that $\mathbf{H}$ and $\mathbf{C}$ are exact matrices (i.e., not Jacobians). They are also constant in time as they do not depend on the network state, but only on the network model (i.e., network topology and electrical parameters). Therefore, $\mathbf{H}$ and $\mathbf{C}$ need to be recomputed only if a change in the network model occurs.

On the contrary, we let $\mathbf{R}$ to be time-variant. However, if $\mathbf{R}$ were assumed to be time-invariant, the formulations of the methods treated in this chapter would not change and the computational performances would be enhanced. The case of a time-invariant $\mathbf{R}$ is discussed in Section 3.3.2.

In what follows, we describe three methods that deal with zero-injection equality constraints in the context of LWLS-SE:

1. NE including virtual measurements, called *VM*;
2. NE with constraints, called *NE/C*;
3. NE derived from LQD, called *LQD*, which is the proposed method.

It is worth pointing out that the *VM* and *NE/C* methods have been widely discussed in the literature and we simply reformulate them for linear SE in Sections 3.2.1 and 3.2.2. Then, in Section 3.2.3 we present the proposed method based on LQD.

Finally, in Section 3.2.4 we recall the well-known QRD that improves the condition of the coefficient matrix in the NE.

[2] Specifically, $p = 2w$ in case of single-phase SE and $p = 6w$ in case of three-phase SE.

3.2.1 Normal equation with virtual measurements (VM)

One way to treat equality constraints in (3.3) is to represent them as virtual measurements. The augmented measurement vector including zero-injections is $\mathbf{z}_0 \in \mathbb{R}^{m+p}$ and the corresponding measurement-noise covariance matrix is $\mathbf{R}_0$. The measurement matrix is

$$\mathbf{H}_0 = \begin{bmatrix} \mathbf{H} \\ \mathbf{C} \end{bmatrix} \tag{3.4}$$

which has full rank thanks to Assumption 1 in Section 3.2. The NE becomes

$$\mathbf{H}_0^T \mathbf{R}_0^{-1} \mathbf{H}_0 \, \mathbf{x} = \mathbf{H}_0^T \mathbf{R}_0^{-1} \mathbf{z}_0 \, . \tag{3.5}$$

Compared to (3.2), the dimensions of the state and of the coefficient matrix do not change, whereas the measurement vector is larger. The coefficient matrix is expected to be more ill-conditioned as we added virtual measurements with small variances.

3.2.2 Normal equation with constraints (NE/C)

The optimization problem (3.3) can be solved by employing the Lagrange multipliers method, which leads to the following Lagrangian function to be minimized as

$$\min_{\mathbf{x},\boldsymbol{\lambda}} \quad \mathcal{L} = \frac{1}{2}(\mathbf{z} - \mathbf{H}\mathbf{x})\mathbf{R}^{-1}(\mathbf{z} - \mathbf{H}\mathbf{x}) + \boldsymbol{\lambda}\mathbf{C}^T\mathbf{x} \tag{3.6}$$

where $\boldsymbol{\lambda}$ is the vector of Lagrange multipliers. Deriving (3.6) with respect to $\mathbf{x}$ and $\boldsymbol{\lambda}$ yields

$$\begin{bmatrix} \alpha\mathbf{H}^T\mathbf{R}^{-1}\mathbf{H} & \mathbf{C}^T \\ \mathbf{C} & \mathbf{0} \end{bmatrix} \begin{bmatrix} \mathbf{x} \\ \boldsymbol{\lambda} \end{bmatrix} = \begin{bmatrix} \alpha\mathbf{H}^T\mathbf{R}^{-1}\mathbf{z} \\ \mathbf{0} \end{bmatrix} \tag{3.7}$$

where $\alpha = \min(R_{ii})$ is added as a scaling factor that improves the condition of the coefficient matrix [6, Chapter 3]. In general, the coefficient matrix in (3.7) is no longer positive definite.

3.2.3 Normal equation derived from LQ-decomposition (LQD)

The dimension of the optimization problem (3.3) can be reduced as it is linear with only linear equality constraints. To this end, we propose a method based on LQD that

is described in what follows. We apply the LQD only to $\mathbf{C}$:

$$\mathbf{C} = \mathbf{UV} = \begin{bmatrix}\mathbf{U}_1 \, \mathbf{0}\end{bmatrix} \begin{bmatrix}\mathbf{V}_1 \\ \mathbf{V}_2\end{bmatrix} = \mathbf{U}_1\mathbf{V}_1 \tag{3.8}$$

where $\mathbf{U}$ is a $p \times n$ lower triangular matrix and $\mathbf{V}$ is an $n \times n$ orthogonal matrix; then, $\mathbf{V}_1$ is of size $p \times n$, $\mathbf{V}_2$ is of size $(n-p) \times n$, and $\mathbf{U}_1$ is a $p \times p$ lower triangular matrix.

Proposition 1. The full state $\mathbf{x}$ can be written as:

$$\mathbf{x} = \mathbf{V}_2^T\mathbf{u} \tag{3.9}$$

where $\mathbf{u} \in \mathbb{R}^{n-p}$ is the new state vector that has a reduced number of variables.

Proof. First, the fact that $\mathbf{V}$ is orthogonal implies that

$$\mathbf{V}\mathbf{V}^T = \mathbf{I} \tag{3.10}$$

$$\mathbf{V}^T\mathbf{V} = \mathbf{I} \tag{3.11}$$

and from (3.10) we can also write

$$\mathbf{V}_1\mathbf{V}_1^T = \mathbf{I} \quad \mathbf{V}_2\mathbf{V}_2^T = \mathbf{I} \quad \mathbf{V}_1\mathbf{V}_2^T = \mathbf{0} \quad \mathbf{V}_2\mathbf{V}_1^T = \mathbf{0} \tag{3.12}$$

Second, using (3.8) and the fact that $\mathbf{Cx} = \mathbf{0}$, we can write

$$\mathbf{Cx} = \mathbf{U}_1\mathbf{V}_1\mathbf{x} = \mathbf{0}\,. \tag{3.13}$$

and thus

$$\mathbf{V}_1\mathbf{x} = \mathbf{0}\,. \tag{3.14}$$

Then, we use (3.11) and (3.14) to write

$$\mathbf{x} = \mathbf{V}^T\mathbf{V}\mathbf{x} = \mathbf{V}_1^T\mathbf{V}_1\mathbf{x} + \mathbf{V}_2^T\mathbf{V}_2\mathbf{x} = \mathbf{V}_2^T\mathbf{V}_2\mathbf{x} \tag{3.15}$$

Therefore, we can define a vector $\mathbf{u}$ such that

$$\mathbf{u} = \mathbf{V}_2\mathbf{x} \tag{3.16}$$

and equation (3.15) becomes

$$\mathbf{x} = \mathbf{V}_2^T\mathbf{V}_2\mathbf{x} = \mathbf{V}_2^T\mathbf{u}\,. \tag{3.17}$$

(QED)

Considering Proposition 1, the constrained optimization problem (3.3) can be written as an unconstrained optimization problem in a reduced number of variables as follows:

$$\min_{\mathbf{u}} \quad J = \frac{1}{2}(\mathbf{z} - \mathbf{H}\mathbf{V}_2^T\mathbf{u})^T\mathbf{R}^{-1}(\mathbf{z} - \mathbf{H}\mathbf{V}_2^T\mathbf{u}) \tag{3.18}$$

By defining a new $m \times (n-p)$ measurement matrix as

$$\widetilde{\mathbf{H}} = \mathbf{H}\mathbf{V}_2^T \tag{3.19}$$

the optimization problem (3.18) corresponds to the following NE:

$$\widetilde{\mathbf{H}}^T\mathbf{R}^{-1}\widetilde{\mathbf{H}}\,\mathbf{u} = \widetilde{\mathbf{H}}^T\mathbf{R}^{-1}\mathbf{z} \tag{3.20}$$

where $\widetilde{\mathbf{G}} = \widetilde{\mathbf{H}}^T\mathbf{R}^{-1}\widetilde{\mathbf{H}}$ is the coefficient matrix of size $(n-p) \times (n-p)$.

Note that the LQD of $\mathbf{C}$ and the computation of $\widetilde{\mathbf{H}}$ do not need to be performed at every time-step, because $\mathbf{C}$ is constant in time, except for seldom changes in the network model. Therefore, at every time-step we just need to solve the NE in (3.20).

Proposition 2. The coefficient matrix $\widetilde{\mathbf{G}}$ is positive definite.

Proof. $\widetilde{\mathbf{G}}$ is positive definite if both $\mathbf{R}$ and $\widetilde{\mathbf{H}}$ have full rank. $\mathbf{R}$ has full rank by construction, whereas we have to demonstrate it for $\widetilde{\mathbf{H}}$.

Since the number of rows of $\widetilde{\mathbf{H}}$ (m) is larger than the number of columns $(n-p)$ by Assumption 1, all we need to show is that the null space of $\widetilde{\mathbf{H}}$ is reduced to $\{\mathbf{0}\}$, i.e. we have to prove that

$$\widetilde{\mathbf{H}}\mathbf{u} = \mathbf{H}\mathbf{V}_2^T\mathbf{u} = \mathbf{0} \quad \Longrightarrow \quad \mathbf{u} = \mathbf{0}\,. \tag{3.21}$$

Using (3.4), we can write

$$\mathbf{H}_0\mathbf{V}_2^T\mathbf{u} = \begin{bmatrix} \mathbf{H}\mathbf{V}_2^T\mathbf{u} \\ \mathbf{C}\mathbf{V}_2^T\mathbf{u} \end{bmatrix} \tag{3.22}$$

where $\mathbf{H}\mathbf{V}_2^T\mathbf{u} = \mathbf{0}$ by assumption (3.21), whereas from (3.8) and using $\mathbf{V}_1\mathbf{V}_2^T = \mathbf{0}$ in (3.12) we derive $\mathbf{C}\mathbf{V}_2^T\mathbf{u} = \mathbf{U}_1\mathbf{V}_1\mathbf{V}_2^T\mathbf{u} = \mathbf{0}$.

Therefore, $\mathbf{H}_0\mathbf{V}_2^T\mathbf{u} = \mathbf{0}$, which implies that $\mathbf{V}_2^T\mathbf{u} = \mathbf{0}$, because $\mathbf{H}_0$ has full rank according to Assumption 1. Considering that $\mathbf{V}_2\mathbf{V}_2^T = \mathbf{I}$ in (3.12), it follows that $\mathbf{u} = \mathbf{0}$.

(QED)

The proposed method consists in the following steps:

Pre-computation of $\widetilde{\mathbf{H}}$:

1. Compute the LQD of $\mathbf{C}$ in order to find $\mathbf{V}_2$, as in (3.8);
2. Compute $\widetilde{\mathbf{H}}$ by using (3.19).

State estimation at every time-step:

1. In the NE (3.20), decompose $\widetilde{\mathbf{G}}$ in Cholesky factors and solve for $\mathbf{u}$;
2. Compute the full state $\mathbf{x}$ by using (3.9).

3.2.4 QR-decomposition (QRD)

As it is known, the numerical stability of the NE can be improved by using QRD [103, 104, 102]. This procedure can be applied to both equations (3.5) and (3.20) and the corresponding methods are called *VM+QRD* and *LQD+QRD*, respectively. On the contrary the QRD cannot be applied to the equation of the *NE/C* method, because of the different structure of the coefficient matrix in (3.7).

To describe the method, we make reference to the general NE (3.2). First, we apply the QRD to $\mathbf{R}^{-\frac{1}{2}}\mathbf{H}$ [103, 54]:

$$\mathbf{R}^{-\frac{1}{2}}\mathbf{H} = \mathbf{F}\mathbf{B} = [\mathbf{F}_1\ \mathbf{F}_2]\begin{bmatrix}\mathbf{B}_1\\ \mathbf{0}\end{bmatrix} \tag{3.23}$$

where $\mathbf{F}$ is an $m \times m$ orthogonal matrix, $\mathbf{B}$ is $m \times n$, and $\mathbf{B}_1$ is an $n \times n$ upper triangular matrix. The NE (3.2) can be re-written as follows:

$$\mathbf{H}^T\mathbf{R}^{-\frac{1}{2}}\mathbf{R}^{-\frac{1}{2}}\mathbf{H}\,\mathbf{x} = \mathbf{H}^T\mathbf{R}^{-\frac{1}{2}}\mathbf{R}^{-\frac{1}{2}}\mathbf{z} \tag{3.24}$$

and thus

$$\mathbf{B}^T\mathbf{F}^T\mathbf{F}\mathbf{B}\,\mathbf{x} = \mathbf{B}^T\mathbf{F}^T\mathbf{R}^{-\frac{1}{2}}\mathbf{z}\,. \tag{3.25}$$

The orthogonal matrix property $\mathbf{F}^T\mathbf{F} = \mathbf{I}$ yields

$$\mathbf{B}^T\mathbf{B}\,\mathbf{x} = \mathbf{B}^T\mathbf{F}^T\mathbf{R}^{-\frac{1}{2}}\mathbf{z}\,. \tag{3.26}$$

By using the matrix blocks in (3.23), we can further simplify (3.26) as follows:

$$\mathbf{B}_1\,\mathbf{x} = \mathbf{F}_1^T\mathbf{R}^{-\frac{1}{2}}\mathbf{z}\,. \tag{3.27}$$

This system of equations can be easily solved by backward substitution as $\mathbf{B}_1$ is upper triangular.

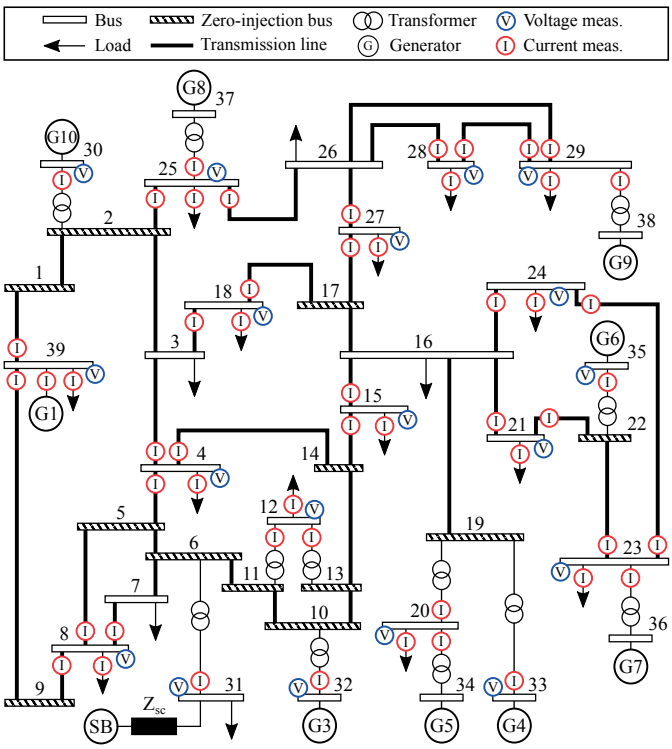

Figure 3.1 – Network topology of the New England 39-bus system together with the adopted measurement configuration.

3.3 Simulations and results

3.3.1 Test conditions

In this section, we compare the methods described in Section 3.2 in terms of numerical stability and computational efficiency. For sake of comparison, we also consider a LWLS, which we call *NZI*, that uses no zero-injection information, i.e., it corresponds to solve (3.2). We carry out single-phase SE for the 39-bus New England test system depicted in Fig. 3.1, where we reproduced the network operating conditions described in [91]. The network is assumed to be in static conditions.

The adopted measurement configuration is shown in Fig. 3.1. No pseudo-measurements are used. PMUs are installed in 19 buses; each PMU measures the nodal voltage, the nodal current-injection and all the current-flows in the lines departing from a bus. The set of real-time phasor measurements is composed of 19 voltages, 19 current-injections and 33 current flows ($m = 142$). This measurement placement aims at achieving the full-network observability even without accounting for the zero-injection information, so that we can also run the *NZI* estimator. Note that, in general, it is sufficient that Assumption 1 in Section 3.2 holds. Given that the number of state variables is $n = 78$, the redundancy level with only real-time measurements is $m/n = 1.8$. Considering

also the 12 zero-injection buses that add $p = 24$ equality constraints, the redundancy level is $(m + p)/n = 2.1$.

The true values of voltages and currents are obtained from a load-flow calculation. The phasor measurements are generated by adding Gaussian-white noise to the true values and are expressed in rectangular coordinates. The noise standard-deviations are expressed in polar coordinates: the magnitude standard-deviation is 0.17 % of the measured value and the phase-angle standard-deviation is 3 mrad. However, the diagonal entries of $\mathbf{R}$ need to be in rectangular coordinates; thus, these standard-deviations are projected from polar to rectangular coordinates by using the formulas described in [48, Chaper 6.4]. This procedure results in diagonal entries of $\mathbf{R}$ ranging from $1.6 \cdot 10^{-6}$ to $1.8 \cdot 10^{-3}$. With reference to the *VM* method, the augmented matrix $\mathbf{R}_0$ contains also the variances of the virtual measurements, which are computed as

$$\sigma^2_{VM} = \frac{\min(R_{ii})}{\gamma} = \frac{1.6 \cdot 10^{-6}}{\gamma} \tag{3.28}$$

where γ is a scalar that we use to modify the virtual-measurement variances.

3.3.2 Results

Tab. 3.1 summarizes the features of the considered methods and reports the results obtained for the adopted grid, which are discussed in what follows. We point out that the results of Tab. 3.1 are obtained by using $\gamma = 1$ for the virtual measurements.

We observe that the *LQD* method uses the least number of measurements (m) and estimates the least number of state variables $(n - p)$; therefore, we expect it to be the most computationally efficient, as proved later in this section. We recall that the reduction of the state dimension via LQD is not repeated at every time-step as it involves only matrix $\mathbf{C}$ that is constant in time.

As we consider $\mathbf{R}$ to be time-variant, each method has to solve a linear system of equation as $\mathbf{A}\mathbf{x} = \mathbf{b}$, where $\mathbf{A}$ is the coefficient matrix. Depending on the characteristics of $\mathbf{A}$, we solve the system with different methods. For instance, if $\mathbf{A}$ is full and positive definite, Cholesky factorization is the most efficient. We used the *backslash operator* "\" of MATLAB that automatically checks $\mathbf{A}$ and employs the fastest method, as reported in Tab. 3.1.

The condition number of the coefficient matrix quantifies the matrix ill-conditioning; thus, we use the condition number as numerical-stability indicator. The *VM* method has the highest condition number, although we set $\gamma = 1$, which means that we do not use lower variances for the virtual measurements. The QRD decreases significantly the condition number from 10^7 to 10^3. The *LQD* method also leads to a significant stability

Table 3.1 – Comparison of the considered methods.

Network	NZI	VM	NE/C	LQD	VM+QRD	LQD+QRD
$\mathbf{z}$ size	m	$m+p$	m	m	$m+p$	m
$\mathbf{x}$ size	n	n	$n+p$	$n-p$	n	$n-p$
Coeff. matrix: Type	Full	Full	Full	Full	Triangular	Triangular
Coeff. matrix: Positive def.?	YES	YES	NO	YES	YES	YES
Method used to solve Ax=b	Cholesky	Cholesky	LU fact.	Cholesky	Back. subst.	Back. subst.
Coeff. matrix: Cond. number	$2.5 \cdot 10^5$	$1.4 \cdot 10^7$	$1.8 \cdot 10^5$	$6.4 \cdot 10^4$	$3.7 \cdot 10^3$	$2.5 \cdot 10^2$
RMSE [pu]	$1.7 \cdot 10^{-3}$	$7.5 \cdot 10^{-4}$	$7.5 \cdot 10^{-4}$	$7.5 \cdot 10^{-4}$	$7.5 \cdot 10^{-4}$	$7.5 \cdot 10^{-4}$
MEP-ZIB [kW]	$36 \cdot 10^3$	70	10^{-2}	10^{-2}	70	10^{-2}
CPU time - mean value [μs]	380	420	480	260	510	380

improvement of three order of magnitudes, but we get the smallest condition number of 10^2 with the joint application of LQD and QRD.

The estimation accuracy is quantified by the RMSE of the state estimates in a simulation of $T = 1\,000$ time-steps; it is computed as

$$\text{RMSE} = \sqrt{\frac{1}{T+n}\sum_{k=1}^{T}\sum_{i=1}^{n}(x_{k,i}^{est} - x_{k,i}^{true})^2}\,. \tag{3.29}$$

In this specific case, every method provides the same RMSE, because the coefficient matrices are not highly ill-conditioned. Only the *NZI* method has a larger RMSE, because it does not exploit the zero-injection information.

We check whether the zero-injection equality constraints are satisfied by computing the maximum estimated power at the zero-injection buses (MEP-ZIB), which should be zero. The *VM* method does not strictly satisfy the constraints with $\gamma = 1$; the MEP-ZIB is 70 kW. Whereas, the *NE/C* and *LQD* methods are able to match the constraints; the MEP-ZIB is few tens of watts due to the numerical-accuracy limit. The CPU time averaged on $T = 1\,000$ time-steps indicates the computational efficiency. Simulations are carried out in MATLAB 2014b running on an Apple MacBook Pro with 2.5-GHz CPU and 16-GB RAM. It is also worth pointing out that the sparsity property of the matrices is not exploited by means of dedicated tools. First, let's examine the methods that do not employ the QRD. The *NE/C* method is the slowest. The *LQD* method improves the CPU time of 40% with respect to the *VM* method. Second, it can be seen that adding the QRD worsens the CPU time for this specific case. However, for smaller networks (approximately less than 20 buses), the QRD decreases the CPU time: applying the QRD and then solving by backward substitution is faster than solving directly the NE by Cholesky factorization. As we consider larger networks, the QRD becomes dominant in the computation time.

As a final observation, in LWLS-SE, if $\mathbf{H}$ and $\mathbf{R}$ are time-invariant, the coefficient matrix

Table 3.2 – Impact of the variance assigned to virtual measurements on numerical stability.

	VM $\gamma = 1$	VM $\gamma = 10^3$	VM $\gamma = 10^7$	VM+QRD $\gamma = 1$	VM+QRD $\gamma = 10^3$	VM+QRD $\gamma = 10^7$
Coeff. matrix: Condition number	$1.4 \cdot 10^7$	$1.4 \cdot 10^{10}$	$1.4 \cdot 10^{14}$	$3.7 \cdot 10^3$	$1.2 \cdot 10^5$	$1.2 \cdot 10^7$
RMSE [pu]	$7.5 \cdot 10^{-4}$	$7.5 \cdot 10^{-4}$	$8.4 \cdot 10^{-4}$	$7.5 \cdot 10^{-4}$	$7.5 \cdot 10^{-4}$	$7.5 \cdot 10^{-4}$
MEP-ZIB [kW]	70	10^{-2}	10^{-2}	70	10^{-2}	10^{-2}

of all the methods is constant in time and can be computed only once. At each time-step, the computation just consists in a matrix multiplication and the CPU time is dramatically decreased. Therefore, if $\mathbf{R}$ is assumed to be time-invariant, the CPU times of all the methods are in the order of few tens of μs for the considered example.

3.3.3 Impact of virtual-measurement variance on numerical stability

In Tab. 3.2, we illustrate the impact of virtual-measurement variance on numerical stability. We use the parameter γ to change the variance: larger γ corresponds to lower variance, as denoted by (3.28).

The case of $\gamma = 1$ is the same of Tab. 3.1. Setting $\gamma = 10^3$ we obtain a MEP-ZIB that is similar to the *NE/C* and *LQD* methods, but we worsen the condition number. When $\gamma = 10^7$, the ill-conditioning becomes severe and starts affecting the estimation accuracy. The QRD maintains the numerical stability even for high ill-conditioning levels.

3.4 Conclusions

In the context of linear SE with only linear equality constraints, the proposed method based on LQD strictly satisfies the equality constraints derived from zero-injections and reduces the number of state variables by the number of constraints. The structure of the NE remains the same, which enables the use of existing techniques linked to the WLS algorithm, such as the QR-decomposition and the LNR test. The positive semi-definiteness of the coefficient matrix is preserved so that the NE can be solved by employing efficient procedures. Tests were performed on the New England 39-bus system (that has 12 zero-injection buses) in order to assess the performance in terms of numerical stability and computational time with respect to other methods that handle equality constraints: the use of virtual measurements (VM) and the method of Lagrange multipliers (NE/C). The simulation results showed that the LQD method improves significantly both numerical stability and computational time compared to the other methods. Additionally, the combination of LQD and QRD further enhances

the numerical stability at the expense of the computational time.

4 Results of PMU-based state estimation of real networks

In this chapter, we present the results of real-time state estimation implemented in two real power systems: a distribution feeder and a sub-transmission network. State estimation is exclusively based on synchrophasor measurements provided by PMUs. We describe the network characteristics as well as the measurement infrastructure. Then, we provide a detailed analysis of the accuracy and computational performance of different state-estimation algorithms: linear weighted least squares (LWLS), least absolute value (LAV) and discrete Kalman filter (DKF).

4.1 Introduction

From the best of our knowledge, the implementation of PMU-based RTSE in a real power system is described only in one paper, i.e., [26], and further detailed in [27]. It consists in a three-phase LWLS installed in the 500-kV system of Virginia Electric and Power Company with the purpose of investigating phase-unbalance issues and of improving the tuning of protective relays. The state estimator provides 30 estimates-per-second by using voltage and current-flow synchrophasor measurements and has a redundancy level of 2.2. The implementation and testing are widely discussed, whereas the RTSE results are briefly presented.

In this chapter, we present the implementation and results of PMU-based RTSE for two real power-networks: a 20-kV feeder of the distribution network of the EPFL campus, and a portion of the 125-kV sub-transmission network of the city of Lausanne, which is operated by Service Industriels de Lausanne (SiL). The originality of this work lies in the use of synchrophasor measurements produced by PMUs installed in real networks. We compare the accuracy and computational performance of the LWLS, LAV and DKF estimators described in Chapters 1, 2 and 3.

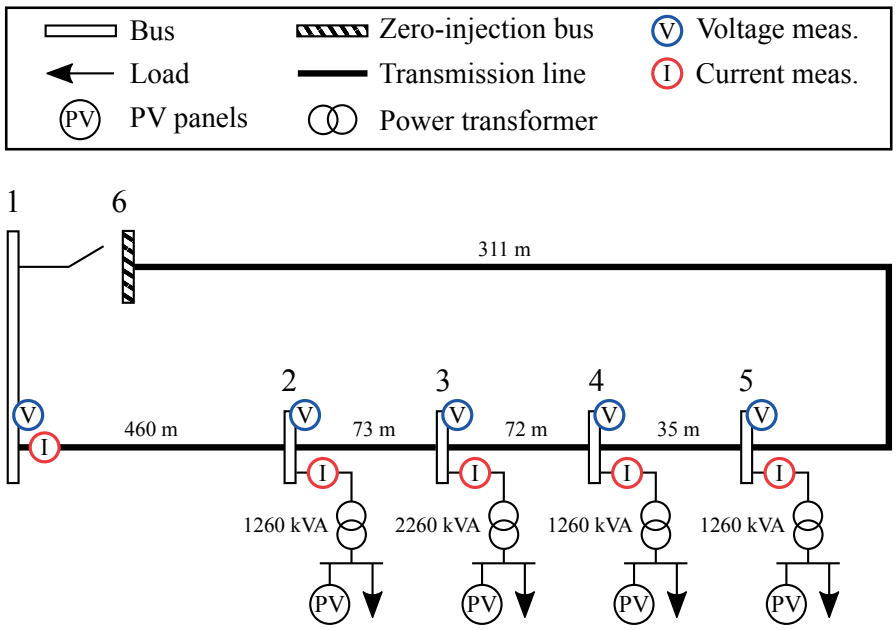

Figure 4.1 – Schematic of the monitored feeder of the EPFL-campus distribution network.

4.2 Distribution feeder of the EPFL-campus network

In the framework of the NanoTera S^3-Grids Swiss project [28, 107], we installed sensors and PMUs in a feeder of the EPFL-campus distribution network. The design and implementation of the measurement infrastructure comprising sensors, PMUs, telecommunication network and data processing are the result of a joint work of two EPFL laboratories: the distributed electric system laboratory (DESL) and the computer communications and applications laboratory 2 (LCA2). The purpose of the project is to evaluate the accuracy and computational performance of RTSE in a real active distribution network. We particularly focus on assessing the accuracy of the SE solution and we compare the results of various algorithms. In Section 4.2.1, we provide the characteristics of the monitored network as well as of the measurement infrastructure. Further device characteristics and implementation details can be found in [28]. The SE results are illustrated in Section 4.2.2.

4.2.1 Network characteristics and measurement infrastructure

The network schematic is depicted in Fig. 4.1. The feeder has a rated voltage equal to 20 kV line-to-line and is composed of 6 buses and 5 three-phase lines. Buses #2 to #5 represent secondary substations. Each substation supplies buildings where there are

offices, laboratories and a considerable amount of PV panels installed on the building roofs; thus, this is a typical example of active distribution network. Recently, a 750 kW - 560 kWh battery has been connected to bus #2 in the context of the SCCER-Furies Swiss project [108]. The transmission lines are underground cables with cross section equal to 150 mm^2. The line parameters are $R = 0.159$ ohm/km, $X = 0.113$ ohm/km, $B = 84.8\,\mu$S/km, and the line lengths are given in Fig. 4.1. We do not have any information about the mutual coupling between phases; therefore, we assume that the phases are totally independent. In this case, three-phase SE can be conducted separately for each phase. The feeder is operated in open-ring configuration where bus #6 is a zero-injection bus.

We installed combined voltage/current sensors at the root of the feeder (bus #1) and at the medium-voltage terminals of the transformers in every secondary substation (buses #2 to #5), as shown in Fig. 4.1. A sensor is installed in each of the three phases. The voltage sensors consist of 0.1-class capacity dividers and the current sensors consist of 0.5-class Rogowsky coils. The rated voltage of voltage sensors is the line-to-line rated voltage of the grid, i.e., 20 kV. The rated current of the sensors at bus #1 is 200 A and the one of the sensors at buses #2 to #5 is 40 A.

The signals that exit from the sensors at a given substation are provided to a PMU through shielded cables. The PMU synchrophasor-estimation algorithm is the enhanced interpolated discrete-Fourier-transform proposed in [97]. This algorithm adopts an acquisition time-window containing 3 periods of a signal at the nominal power-system frequency (e.g., 60 ms at 50 Hz) and is characterized by an average measurement reporting-latency of 44 ms. The PMU is characterized by a maximum TVE of 0.02 % (defined in [47]) that is maintained both in steady-state and in most dynamic conditions, irrespectively of the harmonic-distortion level. The synchrophasor-estimation algorithm is deployed on the field-programmable gate array (FPGA) of a National Instruments CompactRIO 9068. The CPU is used to perform other tasks, such as the streaming of the estimated quantities. The PMU synchronization is achieved by means of a GPS signal. The phasor estimates are generated every 20 ms and user-datagram-protocol (UDP) datagrams are encapsulated according to IEEE C37.118.2-2011 [109].

Single-pair high-speed digital subscriber line (SHDSL) modems transmit these datagrams to a server room over a secured and dedicated communication network composed of twisted pair cables (originally installed for telephony). Then, the datagrams are sent through optical fibers to a phasor data concentrator (PDC) located in another EPFL building.

The PDC and state estimator are hosted on a dedicated workstation and are coded in LabVIEW (the LWLS and DKF-heur algorithms are implemented in the real-time environment). This workstation is GPS-synchronized. The PDC is fully developed by

the DESL of EPFL and has two main functionalities: data aggregation that enables to gather data coming from multiple PMUs into phase-aligned datasets, and data pushing that enables to forward these datasets to further applications, such as SE. A thorough description of the architecture and performance of this PDC is given in [110]. We implement the so-called *absolute-time data-pushing logic*, i.e., the time-aligned datasets are reported at a constant reporting rate that is equal to the PMU reporting rate (50 times-per-second). By using such a logic, the latency variations introduced by the telecommunication media are completely nullified.

Once a complete set of measurements is available, it is pushed to the SE algorithm that runs at 50 estimates-per-second. The measurements and the SE solution are saved locally and then transferred on a database. We made the data publicly available on [107].

The full set of real-time measurements is composed of 5 three-phase voltage phasors and 5 three-phase current-injection phasors, i.e., 60 measurements. If the zero-injections at bus #6 are treated as virtual measurements, the state estimator has to process 66 measurements and provides 36 state variables, resulting in a redundancy level of 1.8. For the case of a LWLS that employs the method proposed in Chapter 3, there are 60 measurements and 30 state variables, resulting in a redundancy level of 2.

Derivation of the measurement-noise covariance matrix

The procedure to derive the diagonal elements of the measurement-noise covariance matrix $\mathbf{R}$ (used by LWLS and DKF) is based on the concepts introduced in Section 1.1.2 and is explained in the following. We disregard the contribution of random noise as we observed that the noises on the measured magnitudes and phase-angles are about a order of magnitude smaller than the sensor uncertainties. The latter are predominant also compared to the TVE value of PMUs; therefore, we neglect the PMU uncertainty in the computation of $\mathbf{R}$. However, when particularly fast and large voltage/current variations occur, such as during faults, the PMU error may be not negligible, as we will observe in Fig. 4.9. Under these assumptions, the measurement variances are evaluated from the limits of ratio error and phase displacement defined by the sensors' accuracy classes, which belong to type B standard uncertainties. We assume a normal distribution and we divide these limits by a coverage factor equal to 3 in order to obtain the standard deviations. The final step consists in the projection from polar to rectangular coordinates by using (1.7) and (1.8), because linear SE uses measurements in rectangular coordinates (see Section 1.1). More details are given here below.

The limits of ratio error and phase displacement for voltage and current sensors are plotted as a function of the measurand in Fig. 4.2. For the voltage sensors, the standard IEC-61869-3 [46] specifies the limits between $80\,\%$ to $120\,\%$ of rated voltage, as shown

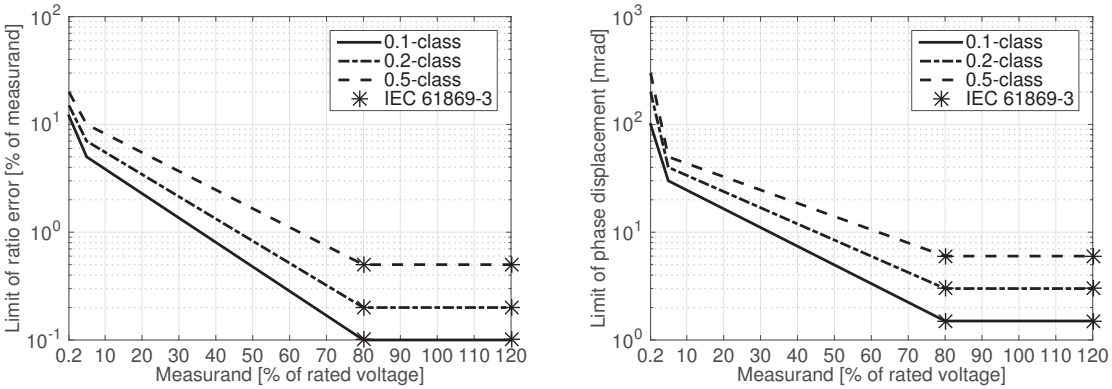

(a) Voltage sensors.

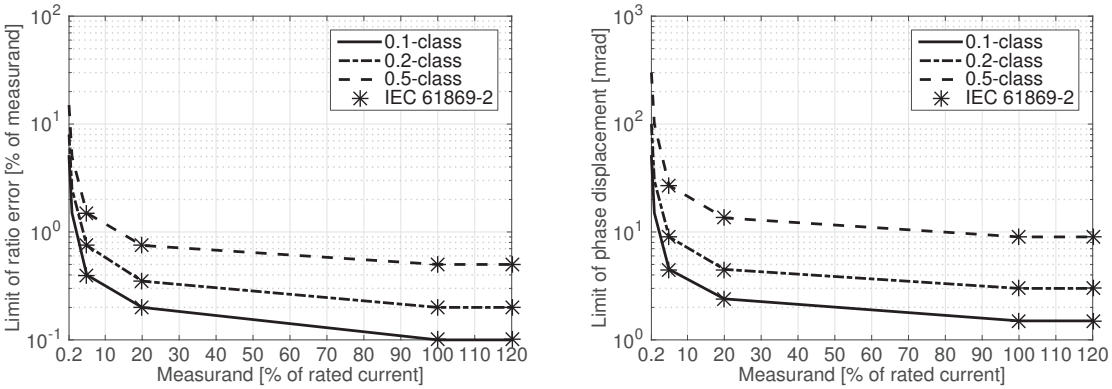

(b) Current sensors.

Figure 4.2 – Limits of ratio error and phase displacement of the sensors (classes 0.1, 0.2, 0.5).

in Fig. 4.2a. We define also the limits below $80\,\%$ of rated voltage in order to run SE even in abnormal conditions, such as in case of deep voltage sags; in particular, we define the limits at $0.2\,\%$ and $5\,\%$ of rated voltage and we linearly interpolate the values in between. If the voltage measurement is between 0 and $0.2\,\%$ of rated voltage, we assume the limit to remain equal, in absolute value, to the one at $0.2\,\%$ of rated voltage. For the current sensors, the standard IEC-61869-2 [45] specifies the limits at $5\,\%$, $20\,\%$, $100\,\%$ and $120\,\%$ of rated current and we added the limits at $0.2\,\%$ and $1\,\%$, as shown in Fig. 4.2b. Then, we linearly interpolate the values in between. If the current measurement is between 0 and $0.2\,\%$ of rated current, we assume the limit to remain equal, in absolute value, to the one at $0.2\,\%$ of rated current.

For example, let us consider a 0.1-class current sensor with rated current equal to $100\,\text{A}$ and a current-magnitude measurement equal to $20\,\text{A}$ (i.e., $20\,\%$ of the rated current). Considering Fig. 4.2b, the corresponding limits of ratio error and phase displacement are $0.2\,\%$ of $20\,\text{A}$ (i.e., $0.04\,\text{A}$) and $2.4\,\text{mrad}$, respectively. The standard-deviations are obtained by dividing these values by a coverage factor equal to 3. Then, we project the uncertainties from polar to rectangular coordinates by using (1.7) and (1.8). Finally, the measurement variances are the squared standard deviations.

The zero-injections at bus #6 are treated in different ways depending on the SE algorithm: (1) for the LWLS, we use the method proposed in Chapter 3; (2) for the DKF, zero-injections are virtual measurements (see Section 1.1.1) with variances equal to the smallest variance of the other real-time measurements; (3) for the LAV, zero-injections are additional constraints in the optimization problem.

4.2.2 State estimation results

In this section, we use the case study described in Section 4.2.1 in order to compare the results of the following state estimators:

- LWLS (see Section 1.2);
- LWLS that uses the LNR test to identify and remove bad data, called *LWLS - LNR* (see Section 1.2);
- LAV (see Section 1.3);
- DKF that uses the heuristic method proposed in Section 2.4 to estimate $\mathbf{Q}$, called *DKF - heur* (see Section 2.4);
- DKF that uses the PECE method proposed in Section 2.5 to estimate $\mathbf{P}_{k|k-1}$, called *DKF - PECE* (see Section 2.5).

We recall that we do not need a phase-angle reference for SE as PMUs directly measure the phase-angle [31]. However, in the figures where we plot the phase-angle as a function of time, we adopted a common phase-angle reference just for display purposes. Indeed, in real networks the power-system frequency is always different from the PMU reporting-rate (exactly 50 Hz); the changes of the phase-angle measurements are dominated by this frequency difference making not visible the changes due to network phenomena (note that for each mHz of difference, the phase-angle measurements rotate of 6.3 mrad per second). Therefore, we generate a phase-angle reference by rotating a phasor at each time-step k of a rotation angle θ_k computed as

$$\theta_k = 2\pi \frac{(f_k - f^s)}{f^s} \tag{4.1}$$

where f_k is the power-system frequency measured by the PMUs (we use the mean value of the frequencies measured by all the PMUs) and f^s is the PMU reporting-rate (50 Hz). Then, we subtract this phase-angle reference to every phase-angle that we plot as a function of time (e.g., right-graphs of Fig. 4.3a).

For the above-mentioned reasons, the DKF persistent process-model that we defined in Section 1.4.3 has to be adapted for the application in real networks. We need to add a state-transition matrix $\mathbf{A}_k$ that rotates the state of an angle θ_k at every time-step, which is defined as

$$\mathbf{A}_k = \begin{bmatrix} \cos(\theta_k) \cdot \mathbf{I}_{n/2} & -\sin(\theta_k) \cdot \mathbf{I}_{n/2} \\ \sin(\theta_k) \cdot \mathbf{I}_{n/2} & \cos(\theta_k) \cdot \mathbf{I}_{n/2} \end{bmatrix} \tag{4.2}$$

where $\mathbf{I}_{n/2}$ is the identity matrix of dimension $n/2$ and n is the state dimension. The DKF process-model becomes

$$\mathbf{x}_k = \mathbf{A}_k \mathbf{x}_{k-1} + \mathbf{w}_k \,. \tag{4.3}$$

The number of past state estimates used by the DKF-heur to infer $\mathbf{Q}$ is $N = 50$; this parameter was assessed by means of off-line simulations in a pre-tuning stage, as explained in Section 2.4.2. For DKF-PECE, the number of past innovations used to infer $\mathbf{P}_{k|k-1}$ is $N = 5\,000$ that is the same number employed in Section 2.5. The LWLS-LNR uses a threshold equal to 4 in the LNR test.

We consider a 100 s time window of measurements taken on November 17$^{\text{th}}$ 2014 at 11:12 a.m. (Swiss local time). In this time interval the network is in quasi-static conditions as there are no particular events taking place.

In Tab. 4.1, we report all the power-injection measurements at time-step 1 of the considered time window (power measurements are derived from voltage and current phasors). The convention for positive and negative signs of the power is reported in Fig.

Table 4.1 – Power-injection measurements at time-step 1.

Bus #	#1	#2	#3	#4	#5
$P_{inj,a}$ [kW]	94.1	-4.7	-20.3	-41.8	-27.1
$P_{inj,b}$ [kW]	104.2	-4.6	-19.3	-51.3	-28.0
$P_{inj,c}$ [kW]	93.4	-3.8	-20.0	-43.8	-25.3
$Q_{inj,a}$ [kVAR]	-12.1	2.0	-0.8	-1.0	-0.5
$Q_{inj,b}$ [kVAR]	-3.8	0.7	-0.2	-4.2	-3.5
$Q_{inj,c}$ [kVAR]	1.2	1.4	-0.5	-10.4	-3.4

1.1. All the loads absorb active power and the feeder imports about 100 kW per phase from the upstream grid. The reactive powers are considerably unbalanced among the three phases. In our case study, the reactive power generated by the cable capacitances is often equal or greater than the overall reactive power absorbed by the loads; this occurs in phases *a* and *b*, where the feeder behaves as a capacitor exporting reactive power to the upstream grid. On the contrary, in phase *c* there is an important reactive power absorption at bus #4 that forces the feeder to absorb reactive power.

Fig. 4.3 shows the time evolution of the voltage (magnitude and phase-angle) and powers (active and reactive) at bus #1 in the three phases *a, b, c*. In Fig. 4.4 we display a shorter time window (from 30 s to 40 s) in order to highlight fast changes that are not visible in Fig. 4.3. The high-resolution measurements of PMUs allow the tracking of very quick dynamics, such as the periodic steps in the active power starting at 36 s, which are similar to a square wave. It can be seen that the LWLS estimates follow closely the measured values. Small discrepancies are present due to the ratio error and phase displacement of the sensors as well as due to line-parameter errors. In Fig. 4.3a we can observe that the random noise on the measurements is quite small; the standard-deviation of this noise is below 10^{-4} pu and 0.1 mrad for the magnitude and phase-angle, respectively. This is the reason why we decided to neglect the random-noise contribution in the computation of the measurement-noise variances (see Section 4.2.1).

In Fig. 4.3 we also observe that there is no correlation between the time evolutions of voltages and power injections, because the power changes are too small to influence the voltage. This is due to stiffness of this grid that has short lines and high rated voltage. Essentially, the voltage fluctuations in Fig. 4.3a are caused by phenomena that are external to this feeder and the relative voltage drop between buses is extremely small. These observations are supported by Fig. 4.5 that compares the measured and estimated voltages at all the buses at time-step 1. The measurements are affected by the sensors' errors, whereas the voltage estimates look equal at all the buses. Indeed, the estimated voltage drop and phase-angle separation between buses are in the order

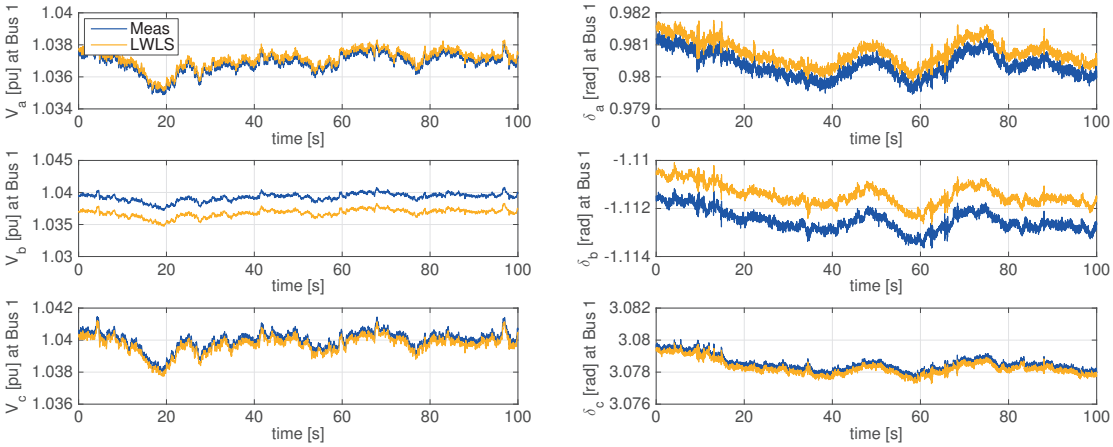

(a) Voltage magnitude and phase-angle.

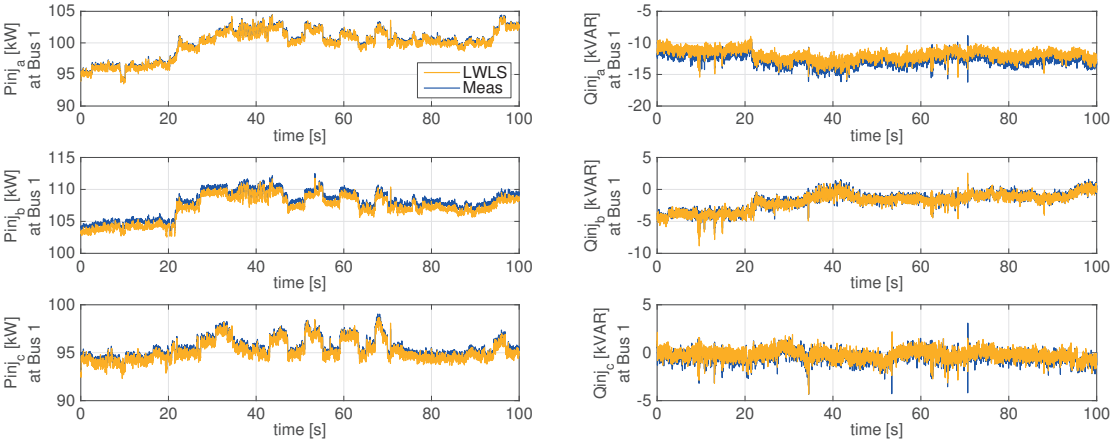

(b) Active- and reactive-power flows.

Figure 4.3 – Time evolution of voltages and powers at bus #1.

of 10^{-5} pu and 10^{-5} mrad, respectively, which are not visible. It is worth pointing out that the differences between measurements and estimates in Fig. 4.5 remain almost unchanged if we consider another time-step as they are mainly due to systematic errors of the sensors and marginally to random noise. For example, from Fig. 4.5 we observe that the difference between the measured and estimated value of $V_{1,b}$ is about 0.003 pu and this difference is kept constant in the entire time window shown in Fig. 4.3a.

As we measure the power injections at every bus, we can evaluate the correctness of the measurements by computing the sum of the active-power injections at all the buses, which represents the grid losses. In Fig. 4.6 we show the measured and estimated grid losses as well as the total reactive power produced by the cable lines. Measured and estimated values can be considered to be in agreement even if the difference in the grid losses appears to be significant. Indeed, the measured losses are computed as

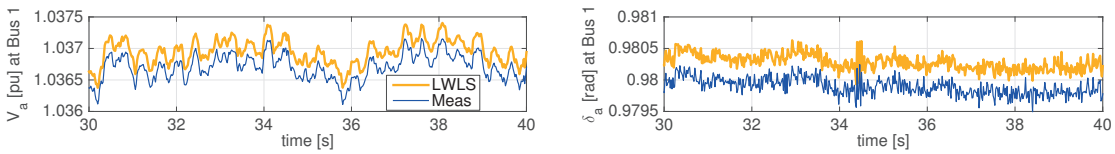

(a) Voltage magnitude and phase-angle.

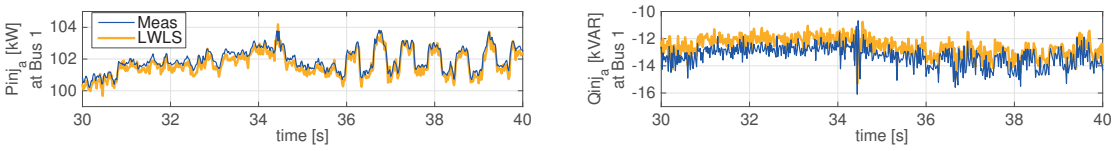

(b) Active- and reactive-power flows.

Figure 4.4 – Zoom of Fig. 4.3 from 30 s to 40 s in phase *a*.

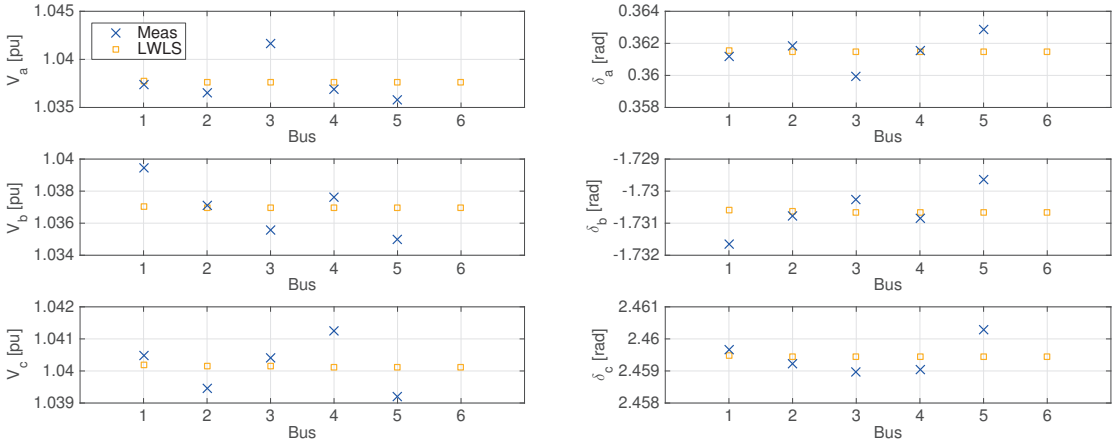

Figure 4.5 – Voltage magnitude and phase-angle at time-step 1.

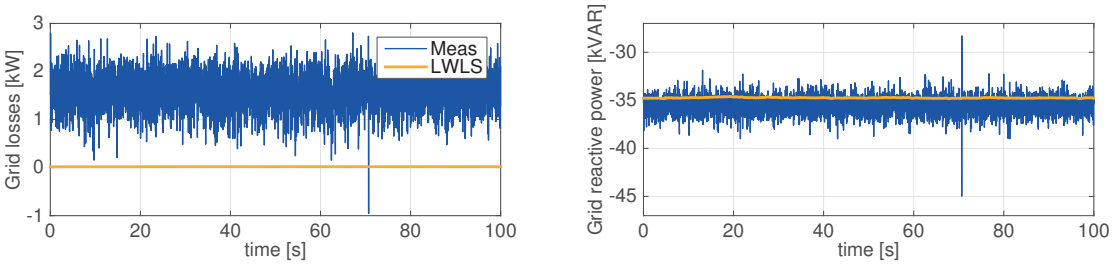

Figure 4.6 – Time evolution of the total grid losses and of the total reactive power produced by the cable lines.

the sum of all the measured power, thus, they contain the sum of the errors of all the measurements; whereas, the estimated losses are much more accurate, because SE exploits also the line parameters. Therefore, a difference of few kilowatts is expected. The estimated grid losses are in the order of a few tens of watts so that this network can be considered loss-free. On the contrary, it produces a considerable amount of reactive power (relative to the loads) that is often exported to the upstream grid, as can be seen also in Fig. 4.3b.

The SE accuracy is easy to be assessed in a simulation environment and it is derived from the difference between the true state (e.g., obtained from a load-flow computation) and the estimated one. Obviously, the true state of real networks is unknown and the measurement residuals are the accuracy indicators that quantify the matching between measurements and network model. In Section 1.2 we explained how the magnitudes of the LWLS normalized residuals are used to detect, identify and remove bad data in the measurement set. The normalized residuals should remain below a threshold (usually 3 or 4) when there are no bad data and network-model errors.

Fig. 4.7 displays the distributions of the LWLS normalized residuals for the $100\,\mathrm{s}$ time window of Fig. 4.3. The distribution statistics are visualized as box plots[1]. The mean value of the normalized residuals related to some voltage measurements are largely above 3. An on-site investigation allowed us to figure out that this result was caused by an improper installation of the sensors. The normalized residuals of the current measurements are below 3 except for an outlier in the real part of all the current measurements in phase *b*. This outlier corresponds to an event occurring at bus #3 at time-instant $70.66\,\mathrm{s}$ (see Figs. 4.3b and 4.6), which is probably due to the startup of a three-phase load. The power absorbed at bus #3 has a step change and the PMU synchrophasor-estimation algorithm is affected by error during step changes, as illustrated in [97]. The current residuals in phase *b* are the most affected by the

[1] Box plots provide a visualization of summary statistics for sample data and contain the following features. On each box, the central mark is the median, the edges of the box are the $25\,\%$ and $75\,\%$ percentiles, the two vertical lines extend to the most extreme data points not considered outliers (that corresponds to ± 2.7 standard deviations and $99.3\,\%$ coverage if the data are normally distributed), and outliers are plotted individually as circles.

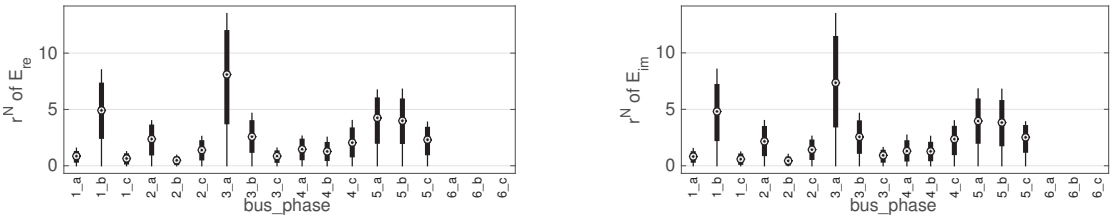

(a) Real and imaginary parts of the voltage measurements.

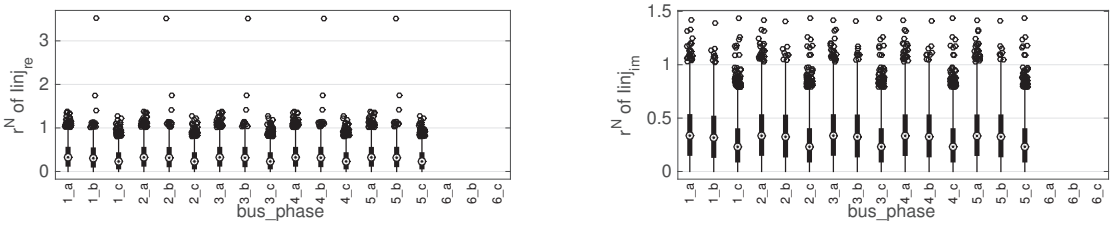

(b) Real and imaginary parts of the current-injection measurements.

Figure 4.7 – Statistics of the distributions of the normalized measurement-residuals of the LWLS.

measurement errors and we observe large current residuals at every bus although the step is present only at buses #1 and #3. This behavior is due to the fact that the current-injection measurements are highly interacting as can be seen by looking at the elements of the covariance matrix of the residuals, which is defined in (1.17). In the rows of current measurements, the off-diagonal entries related to the currents in the other buses are large compared to the diagonal entry. An error in one of the current measurements provokes large and almost equal residuals for all the current measurements in the same phase. Hence, bad data in the current-injection measurements can be detected but not identified in this case study.

In Fig. 4.8, we compare the absolute values of the residuals (not normalized) related to voltage and current-injection measurements obtained at time-step 1 with different state estimators (LWLS, LWLS-LNR, LAV and DKF-heur). Note that the LWLS-LNR The LWLS-LNR removes the measurements V_{3a}, V_{1b}, V_{5b}, because their normalized residuals exceed the selected threshold equal to 4. Note that, for sake of comparison with the other estimators, we display the LWLS-LNR residuals of V_{3a}, V_{1b}, V_{5b} even if these measurements are not used. The voltage residuals are similar for every SE algorithm and the maximum difference is in the order of 0.001 pu. Note that these residuals are in agreement with Fig. 4.7a (e.g., see $V_{3a,re}$). The current residuals of LWLS, LWLS-LNR and DKF-heur are almost identical, whereas the LAV gives different results at some buses, but the difference remains small as all the residuals are below 0.1 A.

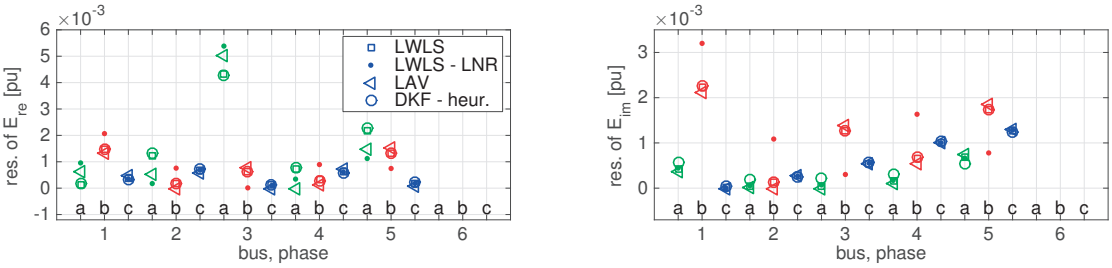

(a) Real and imaginary parts of the voltage measurements.

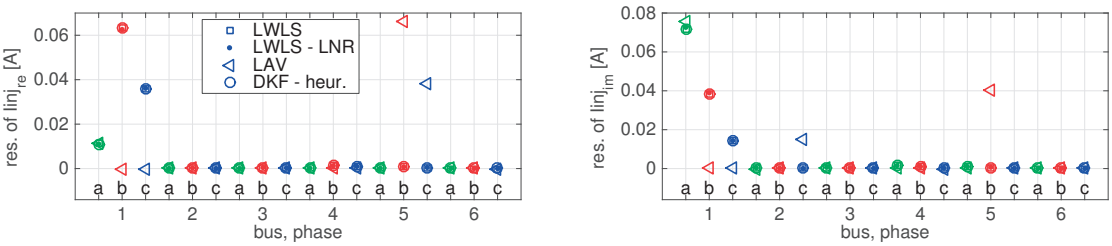

(b) Real and imaginary parts of the current-injection measurements.

Figure 4.8 – Absolute value of the measurement residuals (not normalized) at time-step 1.

LWLS vs. LAV

The accuracy and computational performance of LWLS and LAV estimators have already been compared in the literature for a coherent measurement set and in presence of bad data, e.g., in [34]. In this section, we perform this comparison by using real synchrophasor measurements.

Figs. 4.7a and 4.8a show that both approaches are able to identify the small anomalies that are present in the voltage measurements. Sometimes, current measurements are flagged as bad data during load inrushes that generate step changes in the waveforms acquired by PMUs. It is known that the PMU synchrophasor-estimation algorithm is affected by error during step changes (as illustrated in [97]), which can generate large current residuals. Such a case is depicted in Fig. 4.9 that shows the powers at bus #1 during a load inrush occurring at bus #3 in all the three phases. A particularly relevant mismatch between the measured and estimated values is visible at time 3.94 s. The normalized residual of all the currents raise up to 6; additionally, they are all very close due to the high interaction (already discussed in the description of Fig. 4.7b), which causes the LWLS-LNR to remove some correct measurements. At 3.94 s, the LWLS-LNR rejects in turn V_{3a}, I_{1b}, I_{5b}, I_{1a}, I_{1c}, V_{4b}. The removal of two constraints related to the current injections in phase b causes the estimates of these two currents to become extremely inaccurate (as demonstrated also in [111]). Indeed, the LWLS-LNR current estimates at buses #1 and #5 are in the order of 400 A, as shown in Fig. 4.10. This is due to the stiffness of this network that makes practically impossible to accurately

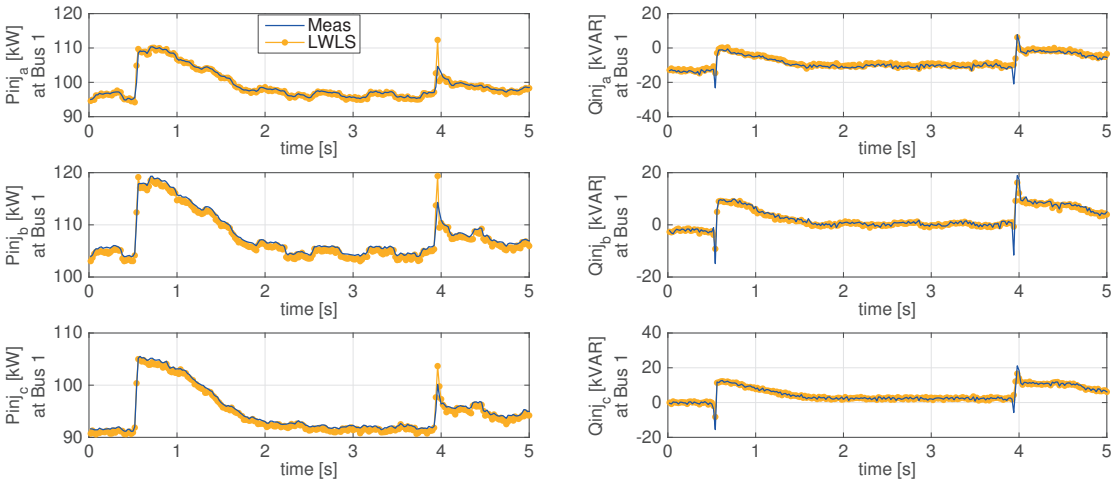

Figure 4.9 – *Load inrush at bus #3.* Time evolution of active- and reactive-power flows at bus #1.

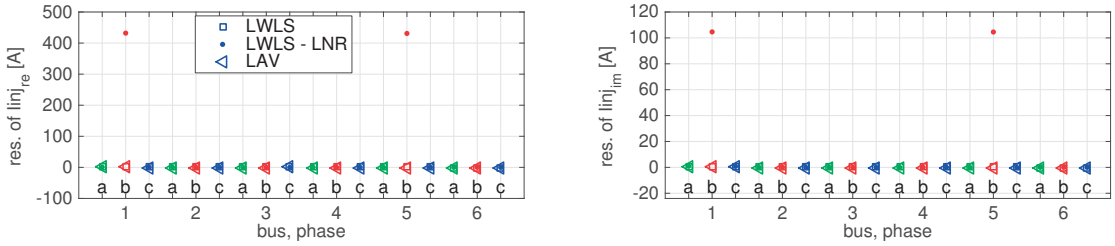

Figure 4.10 – Measurement residuals (not normalized) at time 3.94 seconds of the time-window displayed in Fig. 4.9. This is the instant when a perturbation in the power absorbed at bus #3 occurs.

estimate currents without using their measurements. On the contrary, the residuals of the LAV increase compared to normal conditions but remain below 1 A, because the LAV exploits all the available measurements.

The importance of correctly estimate the system state in such particular events is questionable; indeed, inrushes or similar events causing step perturbations cannot be tracked by using PMUs, because the PMU synchrophasor estimate is a kind of "average value" over the acquisition time-window. PMUs are able to accurately track only events characterized by time-constants that are larger than the acquisition time-window. However, the above-mentioned LWLS-LNR behavior is undesired and should be avoided; if small measurement errors can be neglected, a solution consists in augmenting the threshold of the LNR test.

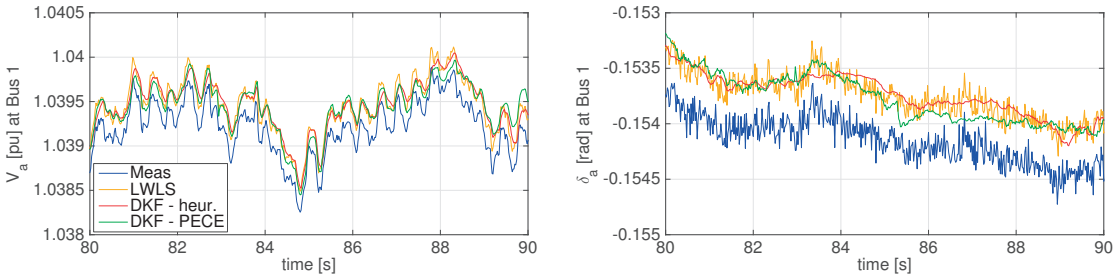

Figure 4.11 – *Quasi-static conditions.* Time evolution of the voltage magnitude and phase-angle at bus #1 in phase *a*.

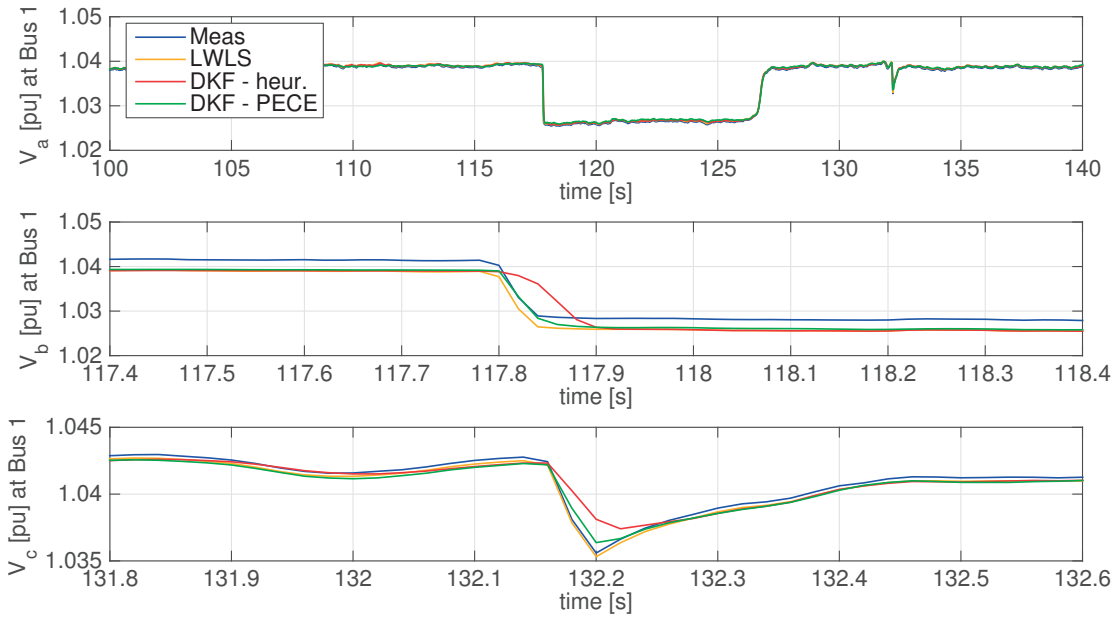

Figure 4.12 – *Step change.* Time evolution of the voltage magnitude at bus #1 in the three phases *a, b, c*. Note that we applied different time-scales in the x-axis of the three graphs.

Table 4.2 – Average computational time in milliseconds.

LWLS	LWLS-LNR	LAV	DKF-heur	DKF-PECE
0.16 ms	1.8 ms	3.5 ms	0.60 ms	690 ms

LWLS vs. DKF

Fig. 4.11 shows the time evolution of the voltage magnitude and phase-angle at bus #1 in phase *a* during a time window in which the network is in quasi-static conditions. The DKF-heur and the DKF-PECE provide similar estimates that follow the same path of the LWLS estimates, but a filtering effect is clearly visible.

We also consider the most challenging event for the DKF, which is a step change. In Fig. 4.12, a voltage dip causes multiple step changes in the voltage magnitude in the three phases. In the plot related to phase *a*, we show the entire voltage dip, in the plot related to phase *b* we show the step change occurring at 117.8 s and in the plot related to phase *c* we show a short voltage drop occurring at 132.2 s. It can be seen that the DKF-PECE is essentially as fast as the LWLS to follow the step change, whereas the DKF-heur has an evident delay.

These observations are in agreement with the results presented in Section 2.5.3.

Computational performance and latency

The computational times of the considered state estimators averaged over $5\,000$ time-steps are reported in Tab. 4.2. As expected, the LWLS is the fastest algorithm, followed by the DKF-heur. LWLS-LNR and LAV have comparable computational times in the order of few milliseconds, because the LWLS-LNR, at each time-step, has to compute the covariance matrix of the residuals and re-estimate the state as many times as the number of identified bad-data. For this case study, some voltage measurements are identified as bad data and removed at every time-step (see Fig. 4.7); on average, the LWLS-LNR rejects 2.8 measurements per time-step. Finally, DKF-PECE is much slower than the other algorithms; its accuracy in tracking step variations (see Fig. 4.12) is at the expense of the computational time, as already illustrated in Section 2.5.

The total time-latency of the process is the time interval between the central instant of the PMU acquisition time-window and the instant the state estimator provides the estimated state. Therefore, it comprises the contributions of PMU, telecommunication network, PDC and SE. As every PMU and the data-concentration workstation (where PDC and SE are implemented) are time-synchronized through the GPS, the latency of every element of the chain as well as the total latency can be assessed. Fig.

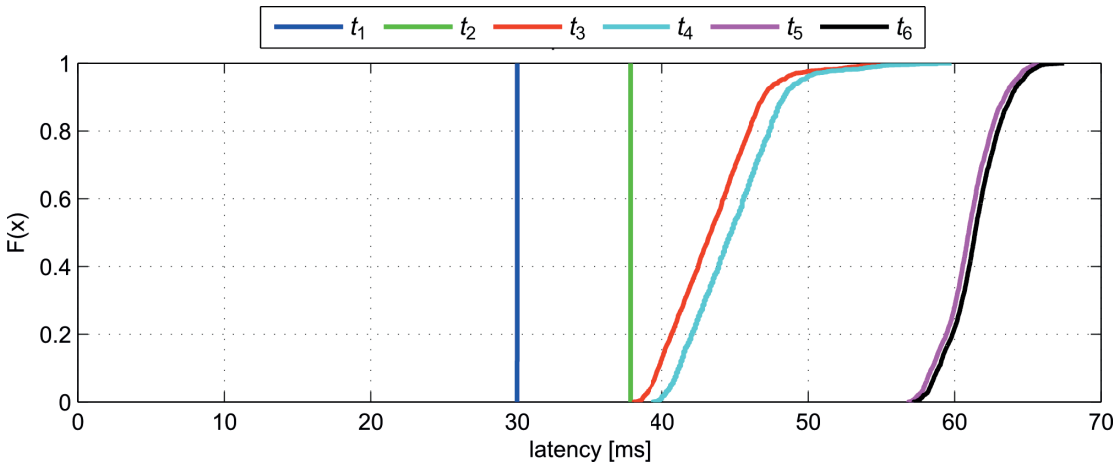

Figure 4.13 – Cumulative distribution functions of time latencies.

4.13 shows the total latency expressed as cumulative distribution functions of time differences between the various elements of the process. The PMU data sampling and synchrophasor estimation (t_1 and t_2) are deterministic as they are performed on an FPGA (note that t_1 is exactly half of the PMU acquisition time-window). The PMU data encapsulation (t_3) is performed on a CPU and is the most non-deterministic contribution to latency. The telecommunication network (t_4) adds a delay of approximately 1.5 ms. The pre-processing of the data performed by the PDC introduces an additional delay (t_5). Finally, the SE computational time is lower than 1 ms (we recall that LWLS and DKF-heur are implemented in real-time environment). The measured total-latency has a mean value of 61 ms and a standard deviation of 1.8 ms. Recently, the total latency was decreased to about 42 ms by improving t_3 and t_5.

4.3 Sub-transmission network of the city of Lausanne

In the context of a joint project between the network operator of Lausanne (Service Industriels de Lausanne – SiL) and the DESL of EPFL, a portion of the sub-transmission network of the city of Lausanne has been equipped with PMUs in order to enhance the real-time situation-awareness as well as to test new fault-location schemes. We provide the characteristics of the network and of the measurement infrastructure in Section 4.3.1; then, we present and discuss the results of different SE algorithms in Section 4.3.2.

4.3.1 Network characteristics and measurement infrastructure

A schematic of the monitored portion of the 125 kV sub-transmission network of the city of Lausanne is depicted in Fig. 4.14, which is composed of 7 buses and 10 three-

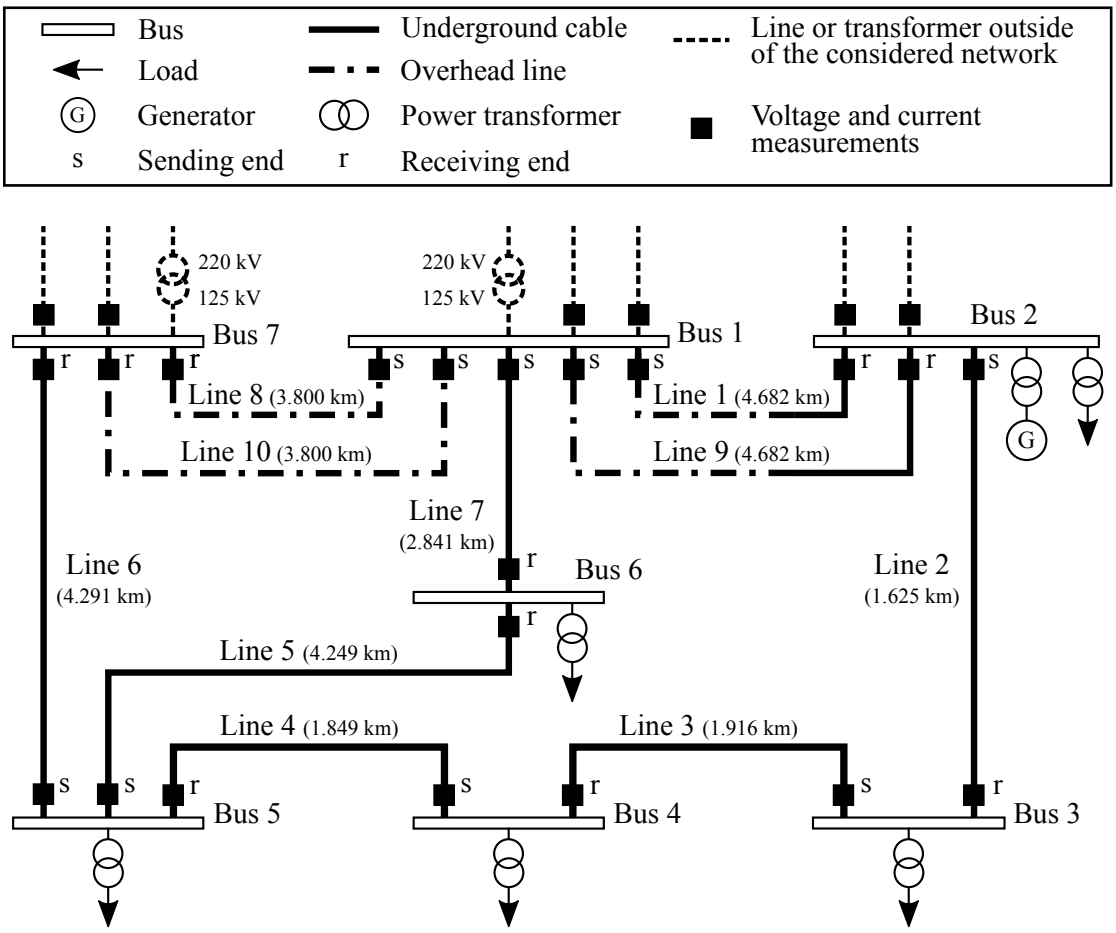

Figure 4.14 – Schematic of the monitored portion of the sub-transmission network of the city of Lausanne.

Table 4.3 – Line parameters: length L in km, resistance R in Ω/km, reactance X in Ω/km, and susceptance B in $\mu S/km$. The subscripts 0 and 1 stand for zero and positive sequence, respectively.

	L	R_0	X_0	B_0	R_1	X_1	B_1
Line #1	4.682	0.217	0.756	14.3	0.112	0.372	15.1
Line #2	1.625	0.168	0.093	63.2	0.051	0.205	63.2
Line #3	1.916	0.168	0.093	63.2	0.051	0.205	63.2
Line #4	1.849	0.185	0.102	60.4	0.051	0.210	60.4
Line #5	4.249	0.177	0.498	57.2	0.061	0.201	57.2
Line #6	4.291	0.168	0.093	63.2	0.051	0.205	63.2
Line #7	2.841	0.226	0.611	57.4	0.064	0.210	57.4
Line #8	3.800	0.420	1.272	1.8	0.159	0.410	2.8
Line #9	4.682	0.217	0.756	14.3	0.112	0.372	15.1
Line #10	3.800	0.420	1.272	1.8	0.159	0.410	2.8

phase lines. The sending- and receiving-ends of the lines (marked as “s” and “r”, respectively) are chosen based on the convention of Fig. 1.1. The lines mainly consist of underground cables with two exceptions: (1) lines #8 and #10 are two parallel overhead-lines, and (2) lines #1 and #9 are two parallel lines split in two sections, i.e., they depart from bus #1 as overhead lines and after 3.682 km they go underground until bus #2. The positive- and zero-sequence line parameters are reported in Tab. 4.3.

Buses #1 and #7 are connected to a higher voltage grid through step-up transformers. At buses #2 to #6 there are step-down transformers that supply distribution networks. Moreover, at buses #1, #2 and #7 there are departing lines that link this portion of the network to the remainder of the 125 kV network. The current-flows in these lines are measured by PMUs, but these lines are not considered in this chapter. We use the current-flow measurements in these lines only to derive the power-injection measurements at buses #1, #2 and #7 that are reported in Tab. 4.5. No zero-injection buses are present in this network.

The monitoring infrastructure is composed of 15 PMUs that receive voltage and current signals from existing PTs and CTs installed at both ends of each line. The accuracy classes are specified in Tab. 4.4; the rated voltage of PTs is 125 kV and the rated current of CTs is 600 A. The PMUs consist of National Instruments Grid and Automation Systems [112] that implements the synchrophasor-estimation algorithm presented in [97] and already illustrated in Section 4.2.1. A line breaker is present at both ends of each line and the breaker statuses are included in the PMU datagrams. Thus, we have the real-time knowledge of the network topology that is updated every 20 ms. The full set of measurements is composed of 20 three-phase voltage phasors and 20

Table 4.4 – Accuracy classes of PTs and CTs. The subscripts $send$ and rec refer to the sending- or receiving-end of the line, respectively.

	PT_{send}	CT_{send}	PT_{rec}	CT_{rec}
Line #1	0.2	0.2	0.2	0.2
Line #2	0.2	0.5	0.5	0.5
Line #3	0.5	0.5	0.2	0.5
Line #4	0.2	0.5	0.2	0.5
Line #5	0.2	0.2	0.5	0.5
Line #6	0.2	0.5	0.2	0.5
Line #7	0.2	0.2	0.5	0.5
Line #8	0.2	0.2	0.2	0.2
Line #9	0.2	0.2	0.2	0.2
Line #10	0.2	0.2	0.2	0.2

Table 4.5 – Power-injection measurements at time-step 1.

Bus #	#1	#2	#3	#4	#5	#6	#7
$P_{inj,a}$ [MW]	32.214	-18.307	-6.400	-9.108	-8.033	-5.576	15.262
$P_{inj,b}$ [MW]	32.276	-18.814	-6.221	-8.764	-7.703	-5.274	14.592
$P_{inj,c}$ [MW]	32.837	-19.287	-6.335	-8.895	-7.913	-5.359	15.047
$Q_{inj,a}$ [MVAR]	-3.337	0.343	-1.406	-2.376	0.005	-1.081	1.845
$Q_{inj,b}$ [MVAR]	-3.943	0.981	-1.510	-2.477	-0.029	-1.224	2.236
$Q_{inj,c}$ [MVAR]	-3.462	-0.079	-1.209	-2.104	0.328	-0.955	1.467

three-phase current-flow phasors, which leads to a redundancy level of 5.7. Such a high redundancy level was chosen in order to enable many different research studies and applications. Note that multiple voltage measurements are available at each bus. Overall, we estimate 42 state variables by using 240 measurements.

Each PMU is connected to a switch through an Ethernet cable and PMU data are streamed through optical-fiber to the PDC that is integrated in a workstation of the control center of Service industriels de Lausanne. We adopted the same PDC used to monitor the EPFL-network feeder, which is described in Section 4.2.1. The state estimator is implemented in the PDC workstation where a LWLS estimator runs in real-time. The same considerations on the derivation of the measurement-noise covariance matrix $\mathbf{R}$ for the distribution feeder (see Section 4.2.1) apply also to this case study.

Table 4.6 – Power-flow measurements at the sending-ends of the lines at time-step 1.

Line #	#1	#2	#3	#4	#5	#6	#7	#8	#9	#10
$P_{s,a}$ [MW]	10.739	3.008	-3.406	-12.526	-6.043	-14.513	-11.596	-0.358	10.611	-0.373
$P_{s,b}$ [MW]	10.532	2.131	-4.099	-12.862	-6.126	-14.437	-11.411	-0.064	10.450	-0.053
$P_{s,c}$ [MW]	10.670	2.281	-4.060	-12.977	-6.370	-14.518	-11.729	-0.250	10.937	-0.249
$Q_{s,a}$ [MVAR]	-0.105	0.456	-0.450	-2.184	-0.067	-1.569	-0.951	-0.881	-0.519	-0.880
$Q_{s,b}$ [MVAR]	-0.770	0.563	-0.421	-2.249	0.058	-1.815	-0.920	-0.944	-0.382	-0.927
$Q_{s,c}$ [MVAR]	-0.705	-0.490	-1.182	-2.653	-0.128	-1.669	-1.022	-0.637	-0.446	-0.652

Table 4.7 – Power-flow measurements at the receiving-ends of the lines at time-step 1.

Line #	#1	#2	#3	#4	#5	#6	#7	#8	#9	#10
$P_{r,a}$ [MW]	-10.717	-2.994	3.418	12.523	6.042	14.532	-11.618	0.358	-10.598	0.372
$P_{r,b}$ [MW]	-10.513	-2.122	4.097	12.860	6.141	14.464	-11.415	0.058	-10.432	0.069
$P_{r,c}$ [MW]	-10.652	-2.275	4.082	12.974	6.376	14.550	-11.736	0.249	-10.916	0.248
$Q_{r,a}$ [MVAR]	-0.266	-0.956	-0.192	1.642	-1.160	0.196	0.079	0.813	0.153	0.836
$Q_{r,b}$ [MVAR]	0.398	-1.088	-0.228	1.728	-1.276	0.456	0.052	0.884	0.020	0.896
$Q_{r,c}$ [MVAR]	0.334	-0.027	0.549	2.124	-1.107	0.299	0.152	0.575	0.076	0.593

4.3.2 State estimation results

In the following, the results of the state estimators listed in Section 4.2.2 are compared and discussed for the case study described in Section 4.3.1.

The DKF algorithm uses the process model defined in (4.3). The number of past state estimates used by the DKF-heur to infer $\mathbf{Q}$ is $N = 100$ and the number of past innovations used by the DKF-PECE to infer $\mathbf{P}_{k|k-1}$ is $N = 5\,000$. The LWLS-LNR uses a threshold equal to 4 in the LNR test.

We consider a 100 s time window of measurements taken on August 16$^{\text{th}}$ 2014 at 10 a.m. (Swiss local time) where the network is in quasi-static conditions as there are no particular events taking place.

A snapshot of the grid operating-conditions is presented in Tabs. 4.5, 4.6 and 4.7, which includes the measurements taken at time-step 1 of power-injections, sending-end power-flows and receiving-end power-flows, respectively (power measurements are derived from voltage and current phasors). The sending- and receiving-ends of the lines are specified in Fig. 4.14 and the conventions for positive and negative signs of power injections and flows are reported in Fig. 1.1. Note also that the power injections at buses #1, #2 and #7 are the aggregated powers of both the transformers and the departing lines that do not belong to the considered network (see Fig. 4.14). In Tab. 4.6, we can observe the presence of not negligible active-power flow unbalances among the phases (e.g., almost 1 MW difference between phases *a* and *b* of line #2) and between the two parallel lines #1 and #9 (about 300 kW in phase *c*). The same unbalances are

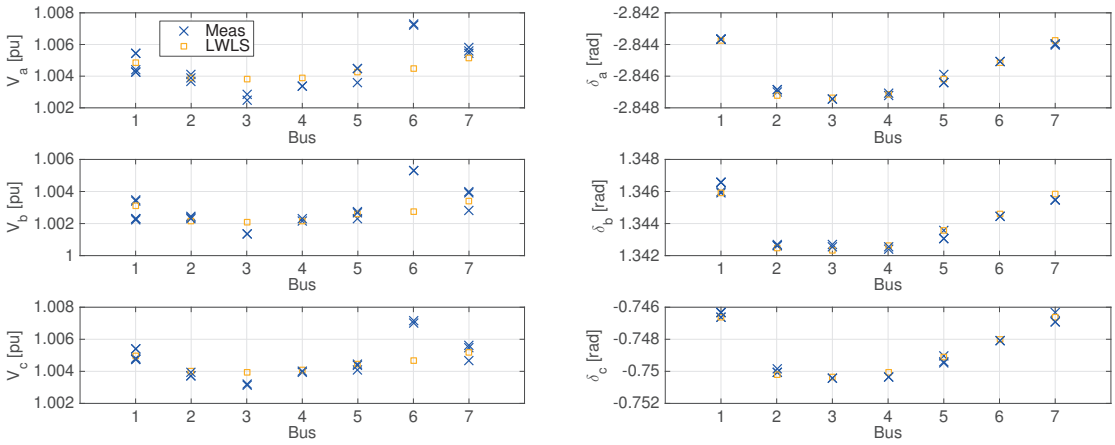

Figure 4.15 – Voltage magnitude and phase-angle at time-step 1.

present also at the receiving-ends, which proves that they are not due to measurement errors. This phenomenon is even more evident in the reactive-power flows (e.g., almost 1 MVAR difference between phases *a* and *c* of line #2). These considerations underline the importance of a three-phase state estimator. Comparing Tabs. 4.6 and 4.7, it can be seen that sending- and receiving-end active-power flows are consistent, which allows us to qualitatively presume that no gross measurement-errors are present.

Fig. 4.15 shows the voltage measurements and LWLS estimates at all the buses at time-step 1. The relative voltage drop between buses is quite small as all the voltages lie in a range of 0.001 pu; this is justified by the low reactive power flows (see Tabs. 4.6 and 4.7). On the contrary, higher active-power flows result in larger phase-angle separations in the order of a few milliradians. However, both voltage magnitude and phase-angle variations are small due to the stiffness of this grid. As for the distribution feeder case in Section 4.2, the mismatch between measured and estimated values is constant in time, because it is due to the systematic errors of the PTs. The random measurement-noise is again very small and can be disregarded.

From Fig. 4.14, we can notice that power-flow measurements are taken in all the lines departing from each bus (even in the interconnection lines departing from buses #1, #2, #7, which are external to the considered network). Therefore, we can compute the sum of all the active-power flows, which represents the grid losses. In Fig. 4.16 we show the measured and estimated grid losses as well as the total reactive power produced by the transmission lines. Considering that the measured values contains the sum of the errors of all the measurements, the estimated and measured values can be considered to be in good agreement. Therefore, this result quantifies the qualitative consideration regarding the absence of gross measurement-errors that we drew by comparing Tabs. 4.6 and 4.7. The total grid losses (about 100 kW) are very small compared to active-power flows, whereas the reactive power produced by the transmission lines is much larger than the reactive-power flows as they mainly consist of underground cables.

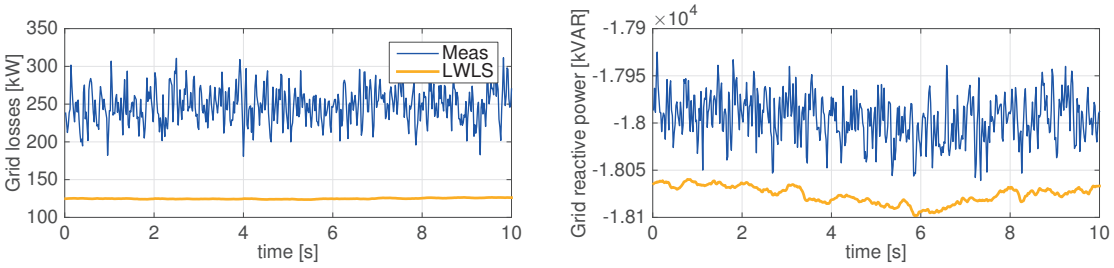

Figure 4.16 – Time evolution of the total grid losses and of the total reactive power produced by the transmission lines.

Fig. 4.17 displays the distributions of the LWLS normalized residuals for the considered 100 s time window. All the voltage measurements can be considered to be correct as their normalized residuals are below the selected threshold for bad-data identification, which is equal to 4. However, the majority of the normalized residuals related to current-flow measurements (both at the sending- and receiving-ends) are much larger than 4 and reach values up to 40. We can further comment that the high normalized residuals are not outliers that occurs once in a while, because they have median values up to 25. The classic cause of normalized residuals that are systematically large is network-model errors. As we are sure about the correctness of the topology, the main suspects are the line parameters. We exclude measurement errors as possible cause, because sending- and receiving-end current-flow measurements are coherent (see Tabs. 4.6 and 4.7) and the total power balance derived from the measurements is in agreement with the estimated one. Investigations on this theme are ongoing.

However, although these normalized residuals may appear quite high, we should remind that current-flow measurements are very sensitive to line-parameter errors. Indeed, if we carry out the same simulation by using only voltage and current-injection measurements (the current injections can be computed from the current-flows by means of the Kirchhoff's law, because we measure all the current-flows departing from each bus), all the normalized residuals fall below 2. In addition, the difference between measured and estimated currents expressed as a percentage of the current magnitudes is always below 6 %, which is acceptable.

In Fig. 4.18, we compare the distributions of the absolute values of the residuals related to the real part of the sending-end current-flow measurements (not normalized) obtained with different state estimators (LWLS, LWLS-LNR, LAV). We do not show the residuals related to the imaginary parts and to the receiving-end current-flows as they are almost identical. We do not show the DKF residuals neither as they are very similar to the LWLS ones. The LWLS-LNR always removes some current measurements so that the corresponding residuals should not exist, but, for sake of comparison with the other estimators, in Fig. 4.18 we show the difference between the estimated values and the measurements.

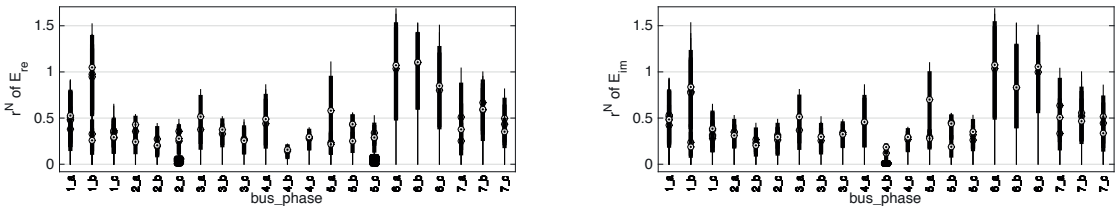

(a) Real and imaginary parts of the voltage measurements.

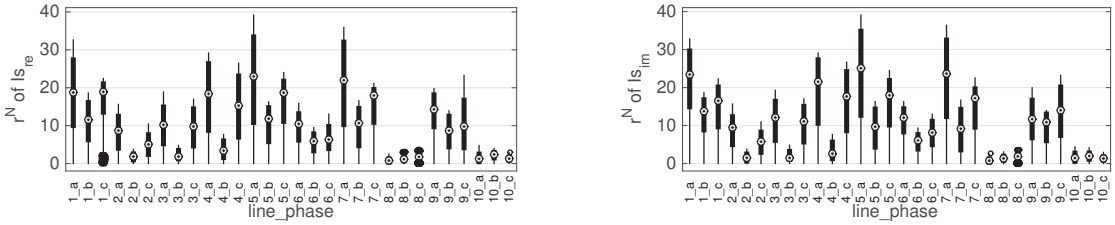

(b) Real and imaginary parts of the sending-end current-flow measurements.

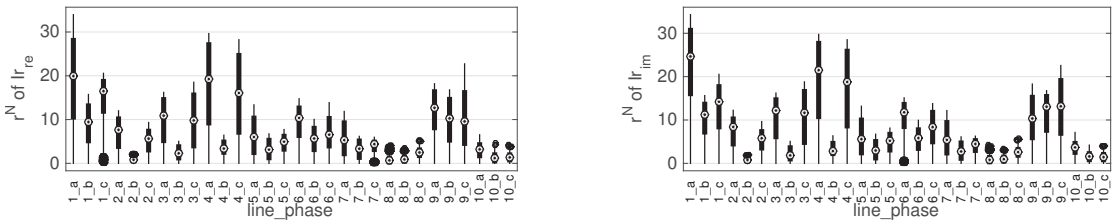

(c) Real and imaginary parts of the receiving-end current-flow measurements.

Figure 4.17 – Statistics of the distributions of the normalized measurement-residuals of the LWLS.

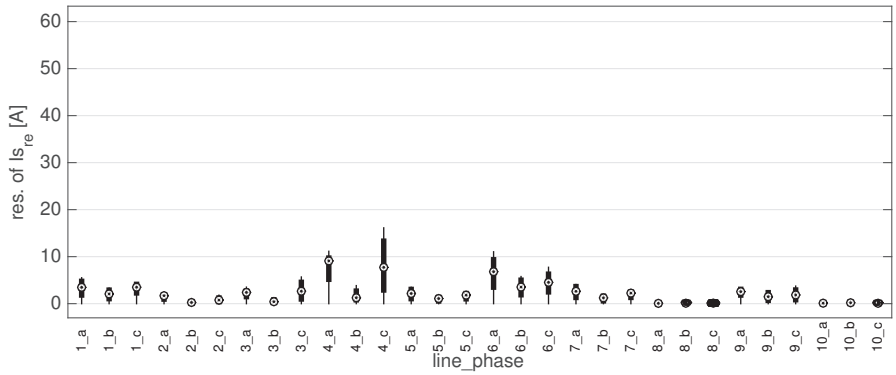

(a) LWLS.

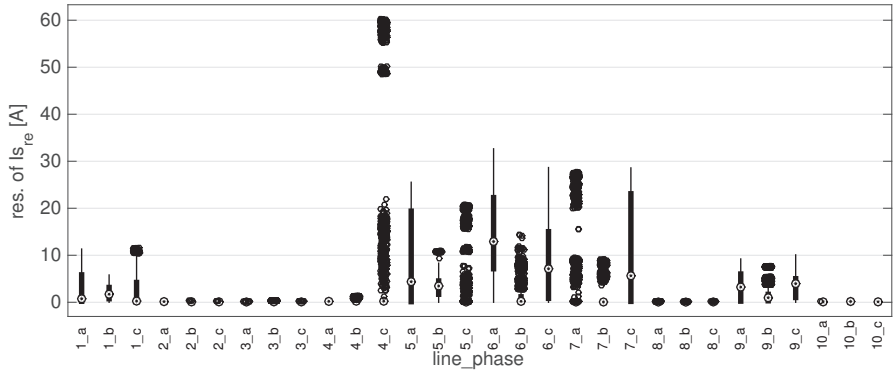

(b) LWLS-LNR.

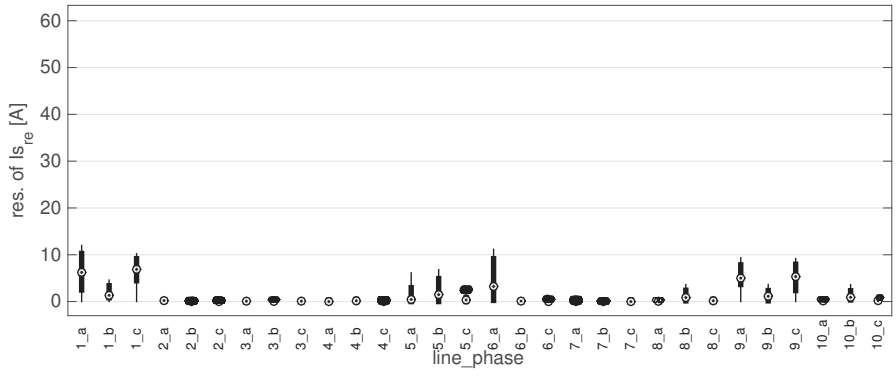

(c) LAV.

Figure 4.18 – Statistics of the distributions of the residuals of the sending-end current-flow measurements.

The residuals of the LWLS and LAV are always small: below 17 A and 11 A, respectively. Concerning the LWLS-LNR, the residuals with large mean value are related to the measurements that are most frequently rejected (e.g., Is_{6a}). The residuals of some measurements, e.g., Is_{4c}, have a small median value but many outliers that raise up to 60 A; it means that these measurements are rejected only in few time-steps, but when they are rejected the difference between measured and estimated value becomes large. On average, the LWLS-LNR rejects 17.2 current measurements per time-steps. However, these measurements should not be rejected, because, most likely, the reason of the high residuals is line-parameter errors. This situation leads the LAV and LWLS-LNR to provide significantly different results, as shown already in Fig. 4.10 for the distribution feeder case. As already mentioned, investigations on this subject are still ongoing.

LWLS vs. DKF

Here below we provide the comparison among LWLS, DKF-heur and DKF-PECE in quasi-static conditions and when a step change in the system state occurs.

Fig. 4.19 shows the time evolution of the voltage magnitude and phase-angle at bus #1 in phase *a* during a time window in which the network is in quasi-static conditions. We can notice the filtering capability of the two DKF algorithms with respect to the LWLS. The DKF-heur follow very closely the LWLS estimates, whereas the DKF-PECE moves away from the LWLS estimates for short time intervals.

In Fig. 4.20, a three-phase fault (due to a failure of a breaker placed externally to our network) causes a significant voltage dip of about 30 %. The left-graph shows the entire voltage dip and the right-graph shows only the initial voltage drop. Note that the voltage magnitude measurement provided by the PMU takes 5 time-steps to go from 1 pu to 0.8 pu, whereas it takes only 3 time-steps in Fig. 4.12. The reason is that in Fig. 4.12 the PMUs use the synchrophasor-estimation algorithm presented in [97] that has a 60 ms acquisition time-window, whereas the PMUs used another algorithm with an acquisition time-window of 100 ms when this three-phase fault occurred. Only recently the PMUs in the network of the city of Lausanne have been upgraded with the new algorithm that has a shorter acquisition time-window. As a consequence, the smoother PMU response to the step facilitates the DKF-heur that has enough time to increase $\mathbf{Q}$.

The estimates of the DKF-PECE and LWLS are overlapping, whereas the DKF-heur has a small delay, although its response can be considered quite fast as well. The DKF-heur is able to inflate the value of $\mathbf{Q}$ when this large step occurs, as shown in Fig. 4.21 for the diagonal element related to the real part of the voltage at bus #1 in phase *a*. After the step, the estimated $\mathbf{Q}$ comes back to its previous values.

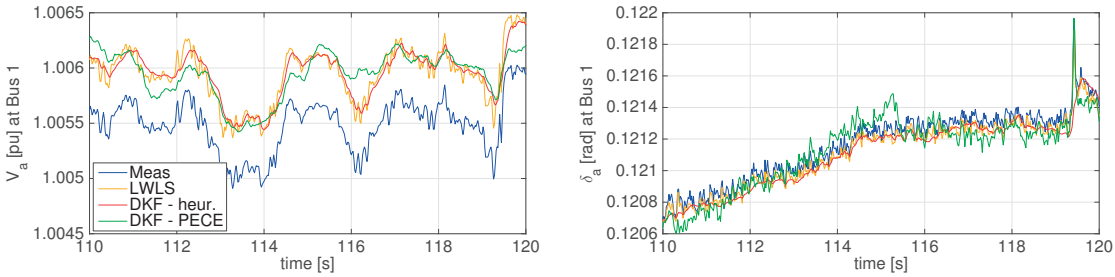

Figure 4.19 – *Quasi-static conditions.* Time evolution of the voltage magnitude and phase-angle at bus #1 in phase *a*.

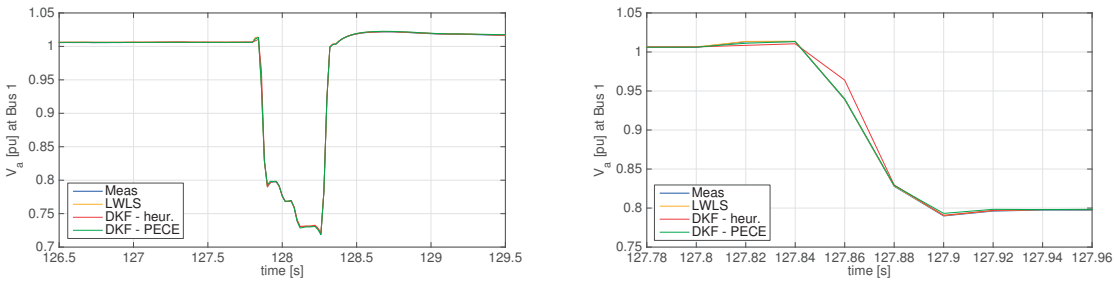

Figure 4.20 – *Step change.* Time evolution of the voltage magnitude at bus #1 in phase *a*. The left-graph shows the entire voltage dip; the right-graph shows only the initial voltage drop.

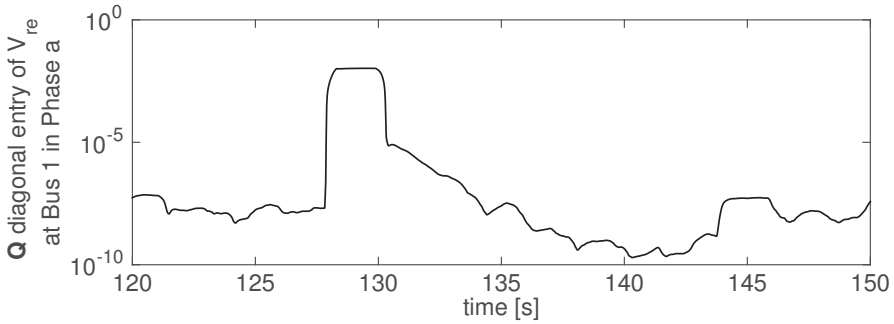

Figure 4.21 – *Step change.* Time evolution of the element of **Q** used by the DKF-heur corresponding to the real part of the voltage at bus #1 in phase *a*.

Table 4.8 – Average computational time in milliseconds.

LWLS	LWLS-LNR	LAV	DKF-heur	DKF-PECE
0.52 ms	46 ms	16 ms	2.0 ms	1330 ms

Computational performance and latency

The computational times of the considered state estimators averaged over $5\,000$ time-steps are reported in Tab. 4.8. LWLS and DKF-heur are the fastest algorithms, whereas DKF-PECE is largely the slowest. Unlike for the distribution feeder, the LWLS-LNR computational time becomes higher than the LAV one, because the former rejects a large number of current measurements per time-steps (17.2 on average), thus, it needs to re-estimate the state many times.

The time-latency of the process is almost the same of the distribution feeder presented in Section 4.2. Indeed, the elements of the SE process are the same except for the telecommunication network that in this case is totally composed of optic fiber. However, the latency of the telecommunication network is small (a few milliseconds) and does not influence significantly the total latency. The measured total latency has a mean value of about 41 ms and a standard deviation of 1 ms (we recall that the LWLS is implemented in real-time environment).

4.4 Conclusions

We presented the results of RTSE implemented in two real power systems consisting of a distribution feeder and a sub-transmission network. Network observability and a high redundancy level are achieved by using exclusively synchrophasor measurements.

First, we proved the feasibility of running RTSE at 50 estimates-per-second with a total time-latency below 70 ms. Note that this is valid for networks of similar size and for measurement infrastructures with the same latency performance. For instance, the latency can significantly change for networks of much larger size (as the SE computational-time increases) and if less deterministic telecommunication networks are employed (e.g., not dedicated wireless networks). In case of large-size networks, parallel state estimators could be computed for smaller sub-networks.

Second, we validated the theoretical findings of Chapters 1, 2, 3 via real-scale experiments. We compared the state estimates and the computational times of LWLS, LAV and DKF.

The filtering feature of the DKF that uses the $\mathbf{Q}$ assessment method proposed in Section

2.4.1 (called DKF-heur) is clearly visible by comparing its estimates with the LWLS ones. However, we noticed that the measurement noise contained in synchrophasor measurements is much lower than the systematic errors of the sensors. As the sensors' calibration sheets were not available, we could not compensate these systematic errors; consequently, the assumption made in Chapter 2 according to which systematic errors in the measurements are negligible is violated. Therefore, we cannot claim that the DKF-heur leads to an accuracy improvement in these case studies.

We also verified that the DKF based on the PECE method (called DKF-PECE) is able to immediately track the system state during steps, whereas the DKF-heur has a delay of a few time-steps. However, the DKF-PECE is computationally expensive, whereas DKF-heur is suitable for real-time implementation.

For the distribution-feeder case, SE enabled the identification of an incorrect installations of the sensors. For the sub-transmission network case, it was interesting to observe that many LWLS normalized residuals systematically exceed the selected threshold for bad-data identification when current-flow measurements are used, whereas they remain below the threshold when only current-injections are used. The residuals of current-flow measurements are sensitive to line-parameter errors that are the most probable cause of the high normalized residuals. However, investigations are still ongoing.

5 A new method based on real-time state estimation for fault location and protective relaying

In this chapter, we intend to prove that PMU-based RTSE exhibits unique accuracy, refresh rate and time determinism, which satisfy the requirements of fault location and, potentially, protective relaying. In this respect, we propose a new method based on LWLS-SE for fault detection and faulted-line identification. The proposed technique is validated by using a RTS where we model a distribution feeder and the PMU devices. Tests are conducted in order to validate the proposed method for many different scenarios: grounded and isolated neutral, different fault types (symmetric and asymmetric), low- and high-impedance faults occurring at different locations, passive and active networks. The accuracy and time-latency performances of the proposed method are evaluated.

5.1 Introduction

The content of this chapter is based on the reference [113] and is a shared contribution with the PhD dissertation of Marco Pignati that is the other co-main author of the work. In the introduction of this dissertation, we illustrated that the SE outcome is used by several control functions in existing EMSs. The high-refresh rate and low-latency of PMU-based RTSE can also enable the development of new protection and fault-location schemes exploiting the state estimates. In common practice, protective relaying and fault location are separated functions that have different time requirements: the former is a real-time process, whereas the latter is executed off-line after the fault clearing.

Nowadays, PMUs play an important role in several aspects of the operation of transmission networks [19]. Protection schemes have not undergone major changes for many years, but recent studies have shown that PMUs can be employed for protective

relaying [114, 115]. PMU data can also be used for adaptive setting of distance relays, as discussed in [116]. Fault-location methods are historically divided in two main categories: impedance-based techniques (e.g., [117]) and algorithms based on the traveling waves originated by the fault transient (e.g., [118]). These approaches can be further classified in one-terminal, two-terminals, multi-terminals and wide-area methods depending on the number of measurement points; additionally, synchronous or asynchronous measurements can be considered. In the last decade, an increasing number of PMU-based fault-location algorithms have been proposed (e.g., [119, 120]). In [121], the authors propose a wide-area fault locator using wavelet where bad-data in the measurement set are eliminated by means of LAV-SE. To the best of our knowledge, there are only two works that use PMU-based SE to directly infer the fault location, i.e., [122, 123]. In [122], phasor measurements provided by PMUs at the two terminals of the faulted line are used for SE. The state vector is augmented by the voltage at the faulted point and by the fault distance. The approach proposed in [123] is similar to that in [122], the difference lying in the fact that the state vector is composed only of the voltage at the faulted point and by the fault distance.

Distribution networks have usually a radial structure and are equipped with a limited number of breakers and measurement devices. For instance, a typical configuration of medium-voltage distribution networks consists in having a breaker at the root of each feeder, a PT in the primary substation and CTs on the secondary windings of the high-to-medium voltage transformers and, sometimes, also at the root of each feeder. Therefore, current practices related to protective relaying typically consist of basic schemes that change from country to country and are different depending upon the type of fault and network, as illustrated in [124]. Fault location usually consist in on-site investigation by repair crew. The increasing integration of distributed generation (DG) in distribution network is leading to substantial changes in the grid operation. In particular, fault management might experience major transformations as a gradual deployment of monitoring infrastructures is expected in the coming years [124]. Accurate fault location in distribution networks can expedite service restoration, thus reducing the duration of power outages. In the literature, a number of methods for fault location in distribution networks have been proposed, which are based on impedance measurements [125], traveling waves [126] or phasor measurements [127]. [124]

In this chapter, we present a new method for fault detection and faulted-line identification that exploits the results of LWLS-based RTSE using synchrophasor measurements. The formulation of the proposed method does not change regardless of the type of network (radial or meshed as well as with grounded, compensated or isolated neutral), the type of fault (symmetric or asymmetric), the fault impedance and the presence of DG. This method is able to locate the faulted component in real-time; therefore, it may theoretically combine the execution of protection and fault-location functions that are usually separated processes.

In the following sections, we describe the new above-mentioned methodology and we present a performance assessment in terms of fault-location accuracy and time-latency. We will show that this method is suitable for the time requirements of protective relaying.

5.2 The proposed method for fault detection and faulted-line identification

Hereafter in this chapter, the term *fault location* is used with the meaning of faulted-line identification. The proposed fault detection and location method relies on the following assumptions:

1. Exact knowledge of the network model (topology and line parameters), i.e., $\mathbf{H}$ is known with no errors;

2. A PMU is installed at every bus and measures voltage and current-injection synchrophasors;

3. The presence of bad data in the measurement set is not considered as the probability of having a fault and bad data simultaneously is assumed to be negligible.

Observations. Later in this section, we will see that Assumption 2 is crucial to ensure the network observability. Moreover, we assume to measure the current injections and not the current flows in order to limit the number of measurements that is already quite large for distribution networks.
We are aware of the fact that Assumption 1 is not perfectly valid in real systems and large network-model errors can degrade the fault location capabilities. However, it is reasonable to assume that the network topology and parameters are known with good accuracy. The topology can be constructed at the data concentration point by collecting the breaker/switch statuses that are streamed by PMUs as Boolean variables. The parameters of the network components usually have a standard configuration with known electrical parameters.
An extensive analysis with respect to network-model errors and a performance assessment including also current flows will be the subjects of future research.

The concept behind the proposed fault-location method is that a fault on a line modifies the network topology and can be modeled as an additional bus that absorbs the fault current. We use the LWLS for this application as low computational time is an important requirement; the DKF needs to employ the computational expensive PECE method presented in Section 2.5 in order to rapidly track step-varying events like faults. The method is explained in detail in the following.

Let us consider a power system with n buses and m lines. We can define m LWLS estimators that utilize the same measurement vector $\mathbf{z}$, but each one of them uses a different topology. The difference in the topology consists in the position of an additional bus that we call *virtual bus*: the state estimator #u ($u = 1, ..., m$) has the virtual bus in the middle of line #u. The state vector of each estimator, previously defined in (1.1), is augmented by the state variables related to the virtual bus as follows:

$$\mathbf{x}_{aug} = [V_{1_{re}}^{a,b,c}, ..., V_{n_{re}}^{a,b,c}, V_{n+1_{re}}^{a,b,c}, V_{1_{im}}^{a,b,c}, ..., V_{n_{im}}^{a,b,c}, V_{n+1_{im}}^{a,b,c}]^T \tag{5.1}$$

where $V_{n+1_{re}}^{a,b,c}$ and $V_{n+1_{im}}^{a,b,c}$ are respectively the real and imaginary parts of the voltage at the virtual bus that is placed in a different line for each state estimator. The measurement matrix $\mathbf{H}$ of each state estimator is modified accordingly.

Now it is clear why the network is observable for every state estimator only if we have a PMU at every bus (i.e., if Assumption 2 holds). Indeed, let us consider a generic line #u between buses #i and #h. If bus #i is not equipped with PMUs, the state estimator with the virtual bus on line #u has two consecutive buses (bus #i and the virtual bus) with no measurements; the observability criterion is not fulfilled for this state estimator.

During normal operating conditions, all the virtual buses absorb no current and the different topologies do not lead to significant differences in the outputs of the m state estimators: $\forall u,\ \mathbf{x}_{aug}^{u} \backsimeq \mathbf{x}_{true}$. Therefore, also the objective functions J of all the estimators are similar (the LWLS objective function is defined in (1.10)).

When a fault occurs in line #f between buses #i and #h, a fault current is drawn from an unknown position between these two buses. The topology of the state estimator #f is close to the real topology even if the fault is not located exactly in the middle of the line. Therefore, it should provide an estimated state close to the true one ($\mathbf{x}_{aug}^{f} \backsimeq \mathbf{x}_{true}$), whereas the estimated of the other estimators is more affected by the wrong topology ($\forall u \neq f,\ \mathbf{x}_{aug}^{u} \neq \mathbf{x}_{true}$). As a consequence, we assume that the faulted-line index corresponds to the index of the state estimator characterized by the lowest objective function. The phases of the virtual bus in which the estimated current differs from zero are the ones affected by the fault; hence, also the fault type is identified (i.e., 3-, 2- or 1-phase).

The detection of the fault is performed by comparing the mean of the objective functions of the m estimators, called J_{mean}, calculated at two consecutive time-steps k and $k-1$. When there is no fault, J_{mean} has a value that is quite stable in time. We observed that when a fault occurs, J_{mean} exhibits a sudden increase due to the increase of the objective functions. A fault is detected when the difference between the values of J_{mean} at two consecutive time-steps exceeds a certain threshold ε, i.e.,$J_{\text{mean},k} - J_{\text{mean},k-1} > \varepsilon$ (see Section 5.4.1). A tuning stage is required to estimate the value of this threshold.

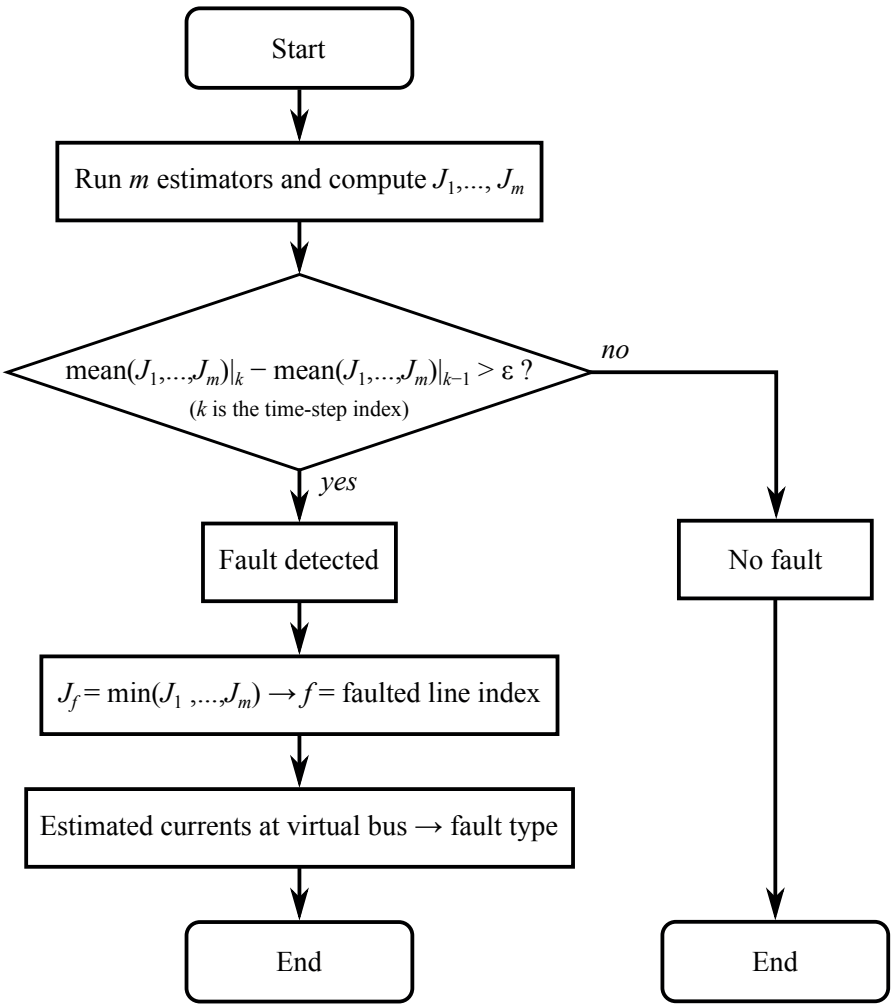

Figure 5.1 – Flowchart of the proposed fault detection and location method.

Further research is needed in order to design an algorithm for the estimation of this threshold.

A flowchart of the procedure described above is given in Fig. 5.1 and is explained in the following. For every new PMU-data set at a generic time-step k, we run m state estimators and we compute their objective functions $J_1, ..., J_m$. The mean value of these objective functions is $J_{\text{mean},k}$. Then, we calculate the difference between the values of J_{mean} at two consecutive time-steps k and $k-1$; if it exceeds a certain threshold ε, a fault is detected. If a fault is detected, the index of the state estimator with the minimum J corresponds to the faulted-line index. Let us suppose that line $\#f$ is identified as faulted, we infer the fault type from the magnitude of the current estimates in the virtual bus provided by the state estimator $\#f$.

In summary, the proposed method allows to:

- detect a fault;
- identify the faulted line;
- identify the fault type;

Observations. As long as a PMU is installed at every bus, the proposed method has no theoretical restrictions related to the type of network (meshed or radial with grounded, compensated or isolated neutral) and the type of fault (symmetric or asymmetric). Additionally, this method can be applied in the same way to any scenario, because it does not need any model of loads/generators and it has no prior knowledge of the fault type and of the neutral connection. The inputs consist only of the incoming set of measurements and the network model (topology and line parameters).
Once the faulted line is identified, classic one- or two-terminals fault-location methods can be employed in order to infer the fault location in the line. Indeed, the estimated values of current flows at the line terminals are made available by SE.

5.3 Simulation set-up

As stated in the introduction of this chapter, an interesting application of the proposed fault detection and location method is in distribution networks.Therefore, we evaluate its performance by building a real-time model of a distribution feeder as well as of the PMUs.

The considered network is a three-phase medium-voltage distribution feeder located in the Netherlands and operated by Alliander. It has a rated voltage equal to 10-kV and it is composed of 18 buses and 17 lines. The network schematic is depicted in Fig. 5.2. The lines are underground cables with cross sections between 95 and 240 mm^2. The lengths as well as the zero- and positive-sequence parameters of the cables are given in Tab. 5.1. The rated power of the medium-to-low voltage transformers at the secondary substations are given in Tab. 5.2.

A three-phase model of the network is built in SimPowerSystem^{TM} and the simulations are run by using an Opal-RT RTS. The lines are modeled as PI circuits. The equivalent circuit of the upstream grid is modeled with a fixed voltage source in series with a short-circuit impedance Z_{sc}. The value of Z_{sc} is computed by assuming a short-circuit power of 1 GVA and a resistance-to-reactance ratio $R_{sc}/X_{sc} = 1/10$. Loads are present at every bus except for bus #1 and are modeled as a star connection of impedances. In normal operating conditions, they absorb approximately 1/4 of the rated power of the secondary-substation transformers. In general, the power absorption is not balanced in the three phases. The real feeder is operated with isolated neutral, but we performed simulations with both grounded and isolated neutral.

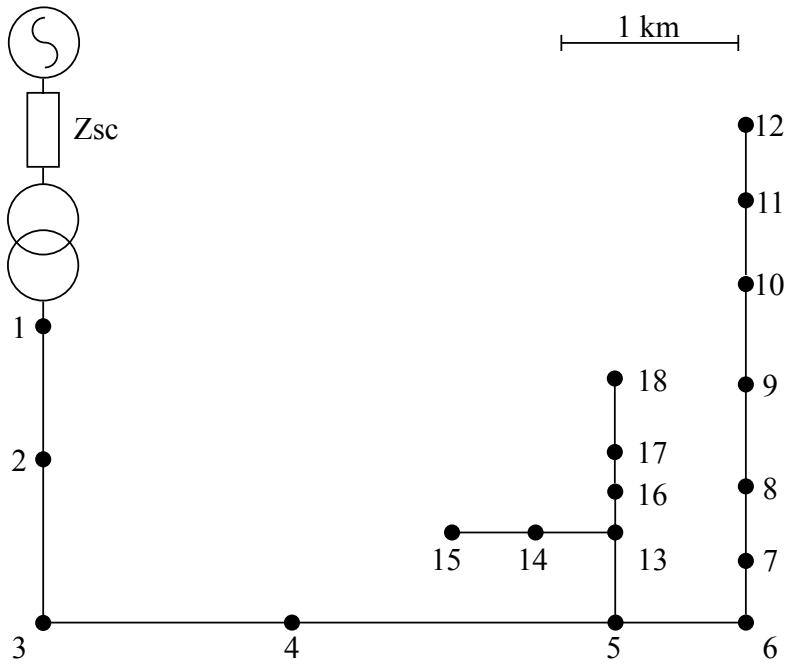

Figure 5.2 – Schematic of the 18-bus distribution feeder.

Table 5.1 – Line parameters: length L in km, resistance R in Ω/km, reactance X in Ω/km, and susceptance B in $\mu S/km$. The subscripts 0 and 1 stand for zero and positive sequence, respectively.

	L	R_0	X_0	B_0	R_1	X_1	B_1
$L_{1,2}$	0.745	1.057	0.910	73.4	0.139	0.075	147.9
$L_{2,3}$	0.929	1.057	0.910	76.0	0.139	0.075	147.2
$L_{3,4}$	1.438	0.844	0.197	12.0	0.159	0.087	145.0
$L_{4,5}$	1.813	1.041	0.855	71.2	0.141	0.076	149.4
$L_{5,6}$	0.706	0.815	0.100	14.1	0.162	0.089	141.4
$L_{6,7}$	0.320	0.815	0.100	14.1	0.162	0.089	141.4
$L_{7,8}$	0.431	0.815	0.100	14.1	0.162	0.089	141.4
$L_{8,9}$	0.592	0.815	0.100	14.1	0.162	0.089	141.4
$L_{9,10}$	0.564	0.815	0.100	14.1	0.162	0.089	141.4
$L_{10,11}$	0.454	0.815	0.100	14.1	0.162	0.089	141.4
$L_{11,12}$	0.422	1.237	1.354	56.0	0.357	0.082	106.2
$L_{5,13}$	0.511	1.060	0.920	73.8	0.139	0.075	147.7
$L_{13,14}$	0.457	1.060	0.920	73.8	0.139	0.075	147.7
$L_{14,15}$	0.472	1.060	0.920	73.8	0.139	0.075	147.7
$L_{13,16}$	0.227	1.240	1.380	53.4	0.356	0.082	106.8
$L_{16,17}$	0.218	1.240	1.380	53.4	0.356	0.082	106.8
$L_{17,18}$	0.417	1.192	0.975	87.4	0.373	0.088	100.0

Table 5.2 – Rated power of the transformers at the secondary substations.

	Rated Power [kVA]
Bus 2	160
Bus 3	250
Bus 4	400
Bus 5	200
Bus 6	250
Bus 7	1000
Bus 8	400
Bus 9	400
Bus 10	400
Bus 11	400
Bus 12	400
Bus 13	400
Bus 14	250
Bus 15	250
Bus 16	250
Bus 17	250
Bus 18	250

We place a PMU at every bus, which measure nodal voltage and current-injection phasors. The PMU is modeled in the SimPowerSystem^{TM} environment as illustrated in [128]. The PMU synchrophasor-estimation algorithm is an enhanced interpolated discrete-Fourier-transform that is described in [97]. The use of simulated PMUs makes the validation of the proposed method more realistic compared to the common practice of using the true phasors, especially concerning the time-latency assessment. Indeed, the PMU response-time during transients is included in the analysis, which is mainly affected by the acquisition-window length and by the position of the time-stamp within the window. A comparison of the time evolution of the fault-current magnitude estimated by the modeled PMU versus the idealized fault-current magnitude is given in Fig. 5.3. This PMU is characterized by an acquisition-window length of 3 periods and the time-stamp is centered in this window; consequently, the estimated magnitude takes 4 time-steps to reach the pre-fault accuracy level. This aspect is taken into account in the assessment of the total time-latency given in Section 5.4.5.

The simulated PMU introduces only the noise due to the synchrophasor-estimation algorithm. It is known that the robustness of fault detection and location algorithms against measurement uncertainties is a crucial aspect. Therefore, we added the errors of the sensors to the phasor magnitude and phase-angle estimated by the simulated PMU. We disregard the random noise, because we observed that the PMU measurements taken in the real network are characterized by magnitude and phase-angle

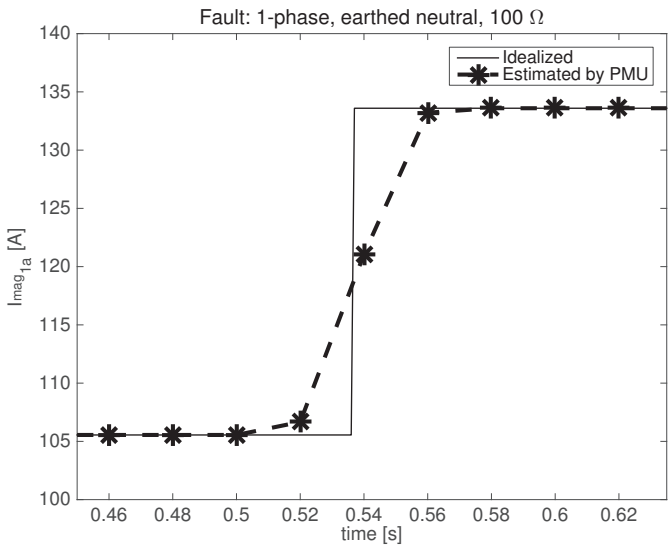

Figure 5.3 – Comparison between the fault-current magnitude estimated by the simulated PMU versus the idealized fault-current magnitude.

noises that are about a order of magnitude smaller than the systematic errors of voltage and current sensors.

We assume to use measurement PTs at every bus for the voltage measurements. Concerning the current measurements, we assume to use measurement CTs at the secondary substations (buses #2–#18) and 5P-class protective CTs at the primary substation (bus #1), because at bus #1 we need to measure the fault current. To assess the fault location performance for different error levels, we simulated the errors of 0.1-class and 0.5-class measurement transformers.

During a single-phase low impedance fault in the network with isolated neutral, we observed that the voltage in the faulted phase drops to 0.01 pu. In this specific case, we assume that the error limits of the PTs in the faulted phase are 10 times larger then those given above. For the 5P-class protective CTs, the standard [45] specifies a 5% limit for the composite error at the maximum current; we assume that this error corresponds to ± 3 % ratio error and ± 40 mrad phase-displacement.

The limits of ratio error and phase-displacement for PTs and CTs are given in the Standards IEC-61869-3 [46] and IEC-61869-2 [45], respectively; in Tab. 5.3, we report the limits used for the simulations in Section 5.4.

The procedure used to assess the accuracy of the proposed fault-location method is described in the following:

1. A model corresponding to a certain fault scenario is implemented and run in SimPowerSystem^{TM} by using an Opal-RT RTS. During a fault, the simulated PMUs

Table 5.3 – Limits of ratio error and phase displacement for PTs and CTs.

Sensor	class	ratio error	phase-displacement
protective CT	5P	$\pm 3\%$	± 40 mrad
measurement PT	0.1	$\pm 0.1\%$	± 1.5 mrad
measurement CT	0.1	$\pm 0.1\%$	± 1.5 mrad
measurement PT	0.5	$\pm 0.5\%$	± 6 mrad
measurement CT	0.5	$\pm 0.5\%$	± 9 mrad

estimate the synchrophasors at 50 measurements-per-second;

2. a set of measurements is obtained by adding the errors of the sensors to the phasor magnitude and phase-angle inferred in step 1. These errors are randomly generated between the limits specified in Tab. 5.3.

3. The set of measurements computed in step 2 is given to the m state estimators described in Section 5.2, which return m estimated states. Then, m values of J are computed and the index of the estimator exhibiting the lowest J coincides with the index of the inferred faulted-line. The fault-location method is successful if the inferred faulted line coincides with the real faulted line;

4. Steps 2 and 3 are repeated $M = 1000$ times in order to simulate many different combinations of sensor errors. The number of times the fault-location method is successful is equal to M_s;

5. The accuracy of the fault location method is represented by the percentage of successes, which is computed as

$$Accuracy = \frac{M_s}{M} \cdot 100\,. \tag{5.2}$$

5.4 Results

The accuracy of the proposed fault location method has been extensively tested and in this section we present the simulation results. The test scenarios refer to different combinations of the following factors:

- Network with grounded or isolated neutral;
- Low- or high-impedance faults (1 Ω or 100 Ω);
- Symmetric faults (3-phase) or asymmetric faults (2-phase and 1-phase);

- Fault location: the fault is simulated in three lines ($L_{4,5}$, $L_{9,10}$, $L_{13,16}$) at 1/4 or 1/2 of the line length;

- Different class of the measurement transformers (0.1 or 0.5);

- Other factors: different operating conditions including the presence of DG and fault in a bus.

5.4.1 Fault detection

The fault-detection principle explained in Section 5.2 is proven here below. Fig. 5.4 shows the time evolution of the objective functions of the $m = 17$ state estimators for the specific case of a 3-phase 100Ω fault at 1/4 of line $L_{13,16}$. The fault occurs between 0.5 and 0.52 seconds. Before the fault, the values of all the objective-functions are always close to each other; in the time-steps after the fault, a quick separation of the objective functions provokes a sudden change of the mean of the m objective-functions computed at two consecutive time-steps. Thus, the difference between the values of J_{mean} at two consecutive time-steps exceeds a pre-set threshold and a fault is detected (see Fig. 5.1). A complete separation of the objective functions occurs three time-steps after the fault, according to the PMU response-time (see Fig. 5.3).

During the post-fault condition, it is evident that the LWLS with the virtual bus in line $L_{13,16}$ maintains the lowest value of J; therefore, the fault location algorithm correctly identifies the fault in line $L_{13,16}$. Note that J of the LWLS with the virtual bus in line $L_{13,16}$ has a small increase after the fault as well, because the position of the virtual bus (1/2 of the line) does not coincide with the fault point (1/4 of the line).

It is worth observing that the identification of a fault in line $L_{13,16}$ is challenging, because line $L_{13,16}$ and its neighbor lines ($L_{5,13}$, $L_{13,14}$ and $L_{16,17}$) are short (218 to 510 meters), and the virtual buses in these lines are all quite close to the fault. Indeed, in Fig. 5.4 we can see that the objective functions of the respective state estimators are lower than the others. As a consequence, when large measurement errors are present, a mis-estimation of the faulted line is more likely to occur. However, this consideration implies that when the algorithm fails to identify the faulted line, it locates the fault in one of the adjacent lines, not at the opposite side of the network.

Fig. 5.5 is equivalent to Fig. 5.4, but for a fault at 1/2 of line $L_{13,16}$. We observe that J of the LWLS with the virtual bus in line $L_{13,16}$ maintains a similar value even after the fault, because the position of the virtual bus and the fault point coincide; thus, this state estimator is using the correct topology even during the post-fault condition.

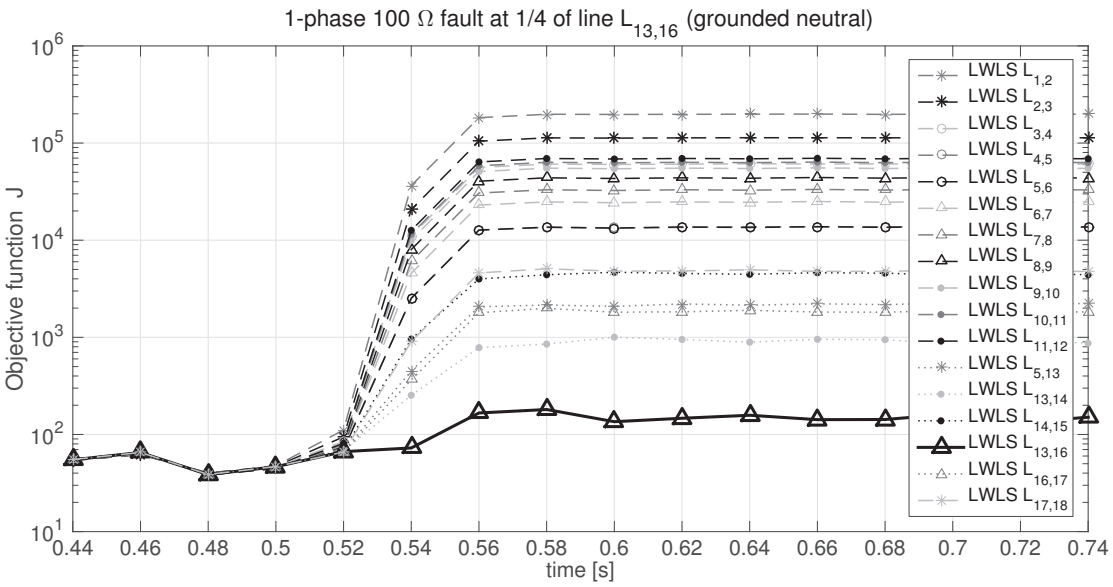

Figure 5.4 – Time evolution of the objective functions of the $m = 17$ state estimators when a 3-phase 100Ω fault occurs at 1/4 of line $L_{13,16}$. The fault inception is between 0.5 and 0.52 seconds.

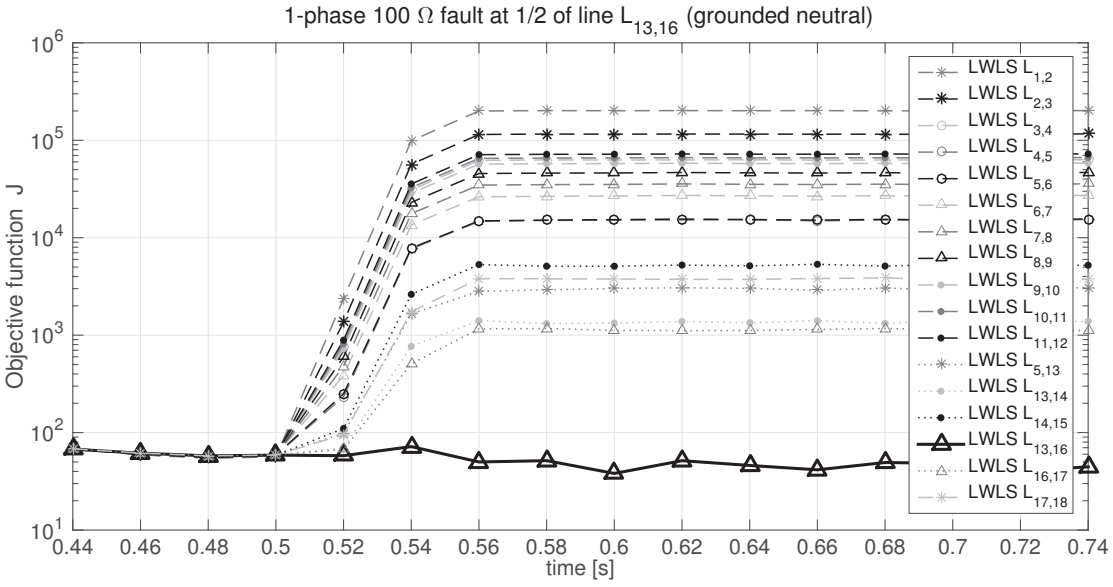

Figure 5.5 – Time evolution of the objective functions of the $m = 17$ state estimators when a 3-phase 100Ω fault occurs at 1/2 of line $L_{13,16}$. The fault inception is between 0.5 and 0.52 seconds.

Table 5.4 – Accuracy for 3-phase 1 Ω fault (neutral grounded)

Fault position		Sensor's class	
		0.1	0.5
$L_{4,5}$	1/4	100%	100%
	1/2	100%	100%
$L_{9,10}$	1/4	100%	100%
	1/2	100%	100%
$L_{13,16}$	1/4	100%	100%
	1/2	100%	100%

Table 5.5 – Accuracy for 3-phase 100 Ω fault (neutral grounded)

Fault position		Sensor's class	
		0.1	0.5
$L_{4,5}$	1/4	100%	82%
	1/2	100%	88%
$L_{9,10}$	1/4	98%	51%
	1/2	99%	52%
$L_{13,16}$	1/4	71%	24%
	1/2	97%	27%

Table 5.6 – Accuracy for 2-phase 1 Ω fault (neutral grounded)

Fault position		Sensor's class	
		0.1	0.5
$L_{4,5}$	1/4	100%	100%
	1/2	100%	100%
$L_{9,10}$	1/4	100%	100%
	1/2	100%	100%
$L_{13,16}$	1/4	100%	100%
	1/2	100%	100%

Table 5.7 – Accuracy for 2-phase 100 Ω fault (neutral grounded)

Fault position		Sensor's class	
		0.1	0.5
$L_{4,5}$	1/4	100%	69%
	1/2	100%	74%
$L_{9,10}$	1/4	90%	36%
	1/2	95%	40%
$L_{13,16}$	1/4	63%	13%
	1/2	84%	15%

Table 5.8 – Accuracy for 2-phase 1 Ω fault (neutral isolated)

Fault position		Sensor's class	
		0.1	0.5
$L_{4,5}$	1/4	100%	100%
	1/2	100%	100%
$L_{9,10}$	1/4	100%	100%
	1/2	100%	100%
$L_{13,16}$	1/4	100%	100%
	1/2	100%	100%

Table 5.9 – Accuracy for 2-phase 100 Ω fault (neutral isolated)

Fault position		Sensor's class	
		0.1	0.5
$L_{4,5}$	1/4	99%	69%
	1/2	100%	69%
$L_{9,10}$	1/4	91%	34%
	1/2	96%	35%
$L_{13,16}$	1/4	64%	12%
	1/2	85%	13%

Table 5.10 – Accuracy for 1-phase 1 Ω fault (neutral grounded)

Fault position		Sensor's class	
		0.1	0.5
$L_{4,5}$	1/4	100%	100%
	1/2	100%	100%
$L_{9,10}$	1/4	100%	100%
	1/2	100%	100%
$L_{13,16}$	1/4	100%	100%
	1/2	100%	100%

Table 5.11 – Accuracy for 1-phase 100 Ω fault (neutral grounded)

Fault position		Sensor's class	
		0.1	0.5
$L_{4,5}$	1/4	100%	78%
	1/2	100%	96%
$L_{9,10}$	1/4	94%	41%
	1/2	98%	42%
$L_{13,16}$	1/4	89%	23%
	1/2	96%	26%

Table 5.12 – Accuracy for 1-phase 1 Ω fault (neutral isolated)

Fault position		Sensor's class	
		0.1	0.5
$L_{4,5}$	1/4	100%	99%
	1/2	100%	100%
$L_{9,10}$	1/4	100%	97%
	1/2	100%	99%
$L_{13,16}$	1/4	100%	97%
	1/2	100%	99%

Table 5.13 – Accuracy for 1-phase 100 Ω fault (neutral isolated)

Fault position		Sensor's class	
		0.1	0.5
$L_{4,5}$	1/4	99%	72%
	1/2	100%	84%
$L_{9,10}$	1/4	91%	34%
	1/2	96%	34%
$L_{13,16}$	1/4	79%	14%
	1/2	91%	18%

5.4.2 Faulted line identification

The accuracies of the proposed fault-location method for every test scenario are given in Tabs. 5.4–5.13. The accuracy values were approximated to the lowest integer. The tables include the results for 0.1-class and 0.5-class measurement transformers (see Tab. 5.3).

Using 0.1-class sensors, the proposed method guarantees an excellent accuracy for low-impedance faults and a satisfactory accuracy for most of the high-impedance faults. Note that high-impedance faults are typically very difficult to locate and require dedicated techniques. If we increase the errors of the sensors by using 0.5-class sensors, the accuracy remains almost unchanged for low-impedance faults, whereas it is considerably degraded for high-impedance faults.

The above-mentioned results apply to faults at 1/4 and 1/2 of the line, proving the fact that the method is still effective even if the virtual bus does not exactly coincides with the fault position. A fault in proximity of a bus is a critical case, because little measurement errors can cause the fault locator to fail in identifying the faulted line; however, we recall that even when the fault locator fails, the fault is very likely to be identified in one of the lines adjacent to the faulted line. Therefore, we are still able to limit the estimated fault location to an area that is close to the fault point.

As a conclusion, we can state that the proposed algorithm is able to locate the faulted line irrespectively of the neutral connection, fault type, fault impedance and fault position. Moreover, the use of precise sensors enhances considerably the fault location accuracy.

5.4.3 Faulted bus identification

A fault in a bus can be easily detected and identified by directly using the measurements of the PMU installed at the faulted substation. For example, let us consider a network with isolated neutral and let us assume that a 1-phase fault occurs in a bus. The faulted bus is identified by means of an algorithm that analyze the voltage and current measurements of the PMU at the faulted bus: the voltage zero-sequence component becomes suddenly different from zero and the current magnitude in the faulted phase has a sudden jump of tens of Amperes.

5.4.4 Influence of operating conditions and distributed generation

The SE results, and consequently the proposed fault locator, should be marginally affected by the network operating conditions. Therefore, we performed numerical simulations with different operating conditions that include the presence of DG. We

created two scenarios, which are listed here below:

1. The powers absorbed by the loads are tripled;
2. The powers absorbed by the loads are reduced to one tenth and three generators are placed at buses #4, #10, #17 so that the feeder becomes active. The generators consist in variable-pitch wind turbines driving 160 kW squirrel-cage asynchronous generators running at nominal speed. The generator production is abundantly larger than the load demand and the feeder exports power towards the upstream grid.

The fault-location accuracies found for these scenarios are very similar to the values in Tabs. 5.4–5.13.

5.4.5 Computational time and latency

The assessment of the speed of the algorithm in identifying the faulted line is a metric of interest when comparing fault-location algorithms. In this section, we focus on two time latencies:

1. the computational time of the proposed method, i.e., the time needed to perform the procedure depicted in the flowchart of Fig. 5.1;
2. the total time-latency of a real system implementing the proposed method.

First, we just consider the computational time of the procedure described in Section 5.2, which is implemented in MATLAB® 2014b running on an Apple MacBook Pro with a 2.5 GHz CPU, 16 GB RAM. The average computational time for the specific case of Section 5.3 is 11.0 ms. It is worth mentioning that the 17 state estimators are computed in series. Note also that if we consider other case studies, this time is affected by the network size and the number of measurements.

Second, the total time-latency of a real fault-location system represents the time between the occurrence of a fault and the identification of its location. In order to obtain reliable and correct estimates of the post-fault synchrophasors, the PMUs have to process a dataset of waveforms that does not contain the step that occurs at the fault inception. To clarify this aspect, Fig. 5.6 shows that when a fault occurs (e.g., in the gray area), three acquisition windows (W_1, W_2, W_3) contain a step in the waveform; therefore, the phasor estimation resulting from these windows is corrupted and not reliable. We remind that the adopted synchrophasor-estimation algorithm [97] uses a window containing three periods of the fundamental frequency. W_4 is the first post-fault acquisition window, which contains a step-free waveform so that the respective

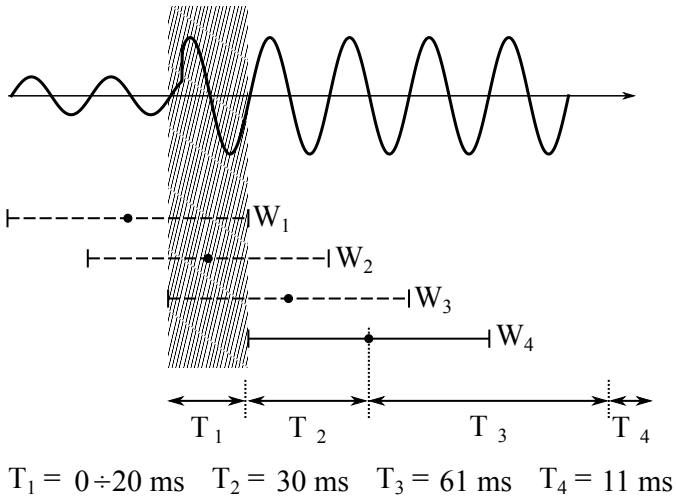

Figure 5.6 – Overall time-latency of the proposed method in identifying faults.

synchrophasor estimate is correct. After these considerations, we list the four main contributions to the total latency in the following:

1. T_1: the time between the fault event and the first sample of window W_4. Depending on when the fault occurs in the gray area of Fig. 5.6, T_1 can vary between 0 and 20 ms;
2. T_2: the time corresponding to half of the acquisition window length used by the synchrophasor-estimation algorithm. With reference to the synchrophasor-estimation algorithm described in [97], T_2 is equal to 30 ms at 50 Hz;
3. T_3: the time between the center of the acquisition window and the moment the set of measurements is made available to the state estimators. This time includes many stages, such as the encapsulation of the synchrophasor packets done in the PMUs, the latency of the telecommunication network, the decapsulation of the packets at the data collection point, and the time-alignment of the synchrophasors. The latency of the telecommunication network is the key aspect of T_3, which can be considerably different if we use a wired or a wireless network and if the network is fully dedicated to the PMU data streaming or it is shared with other functions. In [28], a detailed analysis on a real feeder equipped with PMUs shows that T_3 is equal to 61 ms for that specific set-up. The communication layer is a dedicated network consisting of a mix of telephone cables and fiber;
4. T_4: the time needed to execute the procedure depicted in Fig. 5.1. As mentioned above, the mean value of T_4 for the specific case of Section 5.3 is 11 ms.

Therefore, the total latency can vary between 102 and 122 ms, depending on the instant of the fault inception. This latency is compatible with the requirements of

protective relaying so that we can place the proposed methodology also in the context of protections. In order to maintain the same time performance also for networks of much larger size, the network should be split into smaller sub-networks and the proposed method can be applied separately to each sub-network.

5.5 Conclusions

The new fault detection and faulted-line identification method proposed in this chapter exploits the knowledge of the network state made available by low latency and high refresh-rate RTSE based on PMUs. This method does not need any model of loads/generators and it has no prior knowledge of the fault type and of the neutral connection. We assumed to have a PMU at every bus and we compared the objective functions of multiple LWLS estimators. The performance evaluation was carried out for a real distribution feeder modeled in a RTS. The simulated scenarios included feeders with grounded and isolated neutral, symmetric and asymmetric faults with low- and high-impedance at different locations. We showed that the proposed method is able to locate the faulted line with very good accuracy for low- and high-impedance faults when 0.1-class sensors are used. Whereas, if 0.5-class sensors are employed, the accuracy is significantly decreased for high-impedance faults. Additionally, this method is also resilient to the presence of high amount of DG.

Finally, we showed that the total latency of a real system implementing the proposed method ranges from 102 to 122 ms for the considered network. It is well known that protections are a crucial power-system component and much more detailed tests have to be performed in order to claim that this method can be used for protective relaying. However, we can state that both accuracy and latency performance do match the requirements of protection schemes and are likely to be further improved in the coming years thanks to the advancement of PMU and telecommunication technologies.

Conclusions

An increasing number of PMUs are being installed in power systems in order to enhance the situational awareness and to develop new categories of applications based on synchrophasor measurements. In the near future, we expect to have more networks becoming observable just with synchrophasor measurements. PMUs are commonly associated with transmission systems, but are gaining consideration also in the context of distribution networks that need fast control schemes due to the presence of highly volatile DG or for fault location purposes.

In this dissertation, we present and analyze the advantages of using a measurement infrastructure exclusively composed of PMUs for power-system SE. The latter becomes a linear and not iterative process that uses a set of phase-aligned synchrophasor measurements and is characterized by high refresh-rate (tens of estimates-per-second) and sub-second time-latency. We studied and compared different linear SE algorithms (LWLS, LAV and DKF) with particular focus on the DKF. Indeed, the literature lacks of a thorough study on the DKF in this specific context. It is important to point out that we did not only performed tests in a simulation environment, but we also implemented RTSE in real networks that are pervasively equipped with PMUs. Therefore, we discussed the results of the above-mentioned linear state estimators using real synchrophasor measurements.

In Chapter 2, we extensively studied the DKF algorithm with the goal of improving the estimation accuracy by filtering the measurement noise. We assumed that the measurement model is known and the measurements are affected only by random noise while no systematic errors are present. We adopted a persistent process-model that is characterized by unknown and time-varying uncertainties, because the power-system operating conditions are continuously varying. The power-system state is usually characterized by smooth variations (quasi-static conditions), but exhibits also step changes associated, for instance, with the connection/disconnection of loads, generators and transmission lines. We designed a heuristic method that continuously updates the process-noise variances used by the DKF; it is effective in quasi-static conditions and is prone to real-time implementation. Then, we proposed a method, called prediction-error covariance estimation (PECE), that, in addition to effectively

filter the measurement noise in quasi-static conditions, is able to follow the state during step changes. The PECE method estimates the prediction-error covariances by means of a constrained convex optimization-problem that has a unique solution. It ensures the positive semi-definiteness of the estimated prediction-error covariance matrix, which is a necessary requirement for the DKF numerical stability. Both the heuristic and PECE methods use a set of previous state estimates and innovations, respectively, contained in a moving time-window of N time-steps. It is worth noting that N is the only parameter to be set and can be inferred from off-line simulations. With respect to the heuristic method, the PECE method is based on a rigorous theory and is able to cope with step-varying processes, but it has a significantly higher computational burden. Moreover, we provided a theorem that theoretically proves the better accuracy of the DKF with respect to the LWLS as long as the process model is correct.

The accuracy and computational performances of the two above-presented methods were extensively tested via numerical simulations. We considered the New England 39-bus system and the 123-bus test feeder and we reproduced quasi-static conditions as well as step changes in the system state. First, we make reference to networks in quasi-static conditions and to the DKF employing the heuristic method: (1) we statistically validated the adequacy of the persistent process-model; (2) we numerically validated the theoretical finding about the better accuracy of the DKF with respect to the LWLS. Second, we simulated a step change in the state variables and we showed that the DKF employing the PECE method accurately tracks the state, whereas the DKF employing the heuristic method exhibits a significant delay. The computational time of the DKF employing the heuristic method is comparable with the LWLS one for the adopted case studies, whereas the PECE method is computationally more expensive.

The information associated with zero-injection buses (that are very common in power systems) can be treated in different ways for SE. In the WLS algorithm, zero injections are usually represented as virtual measurements (i.e., measurements with zero value and low variance) or are embedded as equality constraints by means of the method of Lagrange multipliers. However, both methods can be improved for the case of LWLS with only linear equality constraints. In Chapter 3, we proposed a method based on LQD that strictly satisfies the equality constraints and reduces the dimension of the state vector by the number of constraints. The structure of the NE is preserved and the coefficient matrix is positive definite. Therefore, the problem becomes more computationally efficient as there are less state variables. Standard techniques exploiting the characteristics of the NE, such as QRD or the LNR test, can be applied in the same way. Additionally, we demonstrated that the problem becomes less ill-conditioned. Tests were conducted on the New England 39-bus system that has 12 zero-injection buses. The LQD-based method outperforms other commonly-employed methods (a LWLS including virtual measurements and a LWLS using the method of Lagrange multipliers) in terms of numerical stability and computational time.

In Chapter 4, we illustrated the field implementation of RTSE in two real power-systems: the EPFL-campus distribution network and the sub-transmission network of the city of Lausanne. We deployed PMUs at every bus in order to achieve the network observability and a high redundancy level by using exclusively synchrophasor measurements. We described the components of the measurement infrastructure comprising sensors, PMUs, telecommunication network and PDC. We showed that RTSE can run at 50 estimates-per-second with a total time-latency below 70 ms. Note that this is valid for networks of similar size and for measurement infrastructures with the same latency performance.

Then, we presented and extensively discussed the results of different linear SE algorithms (LWLS, LAV and DKF) for the two case studies. Therefore, we had the possibility to verify the theoretical findings of Chapters 1, 2, 3 with real-scale experiments. We noticed that the measurement noise contained in synchrophasor measurements is much lower than the systematic errors of the sensors. As the calibration sheets of the sensors were not available, we could not compensate these systematic errors; consequently, we are violating the assumption made in Chapter 2 according to which systematic errors in the measurements are negligible. Indeed, we observed that the DKF and LWLS estimates are similar. Although the DKF filtering action is visible, the accuracy improvement is marginal. The numerical results of Chapter 2 are confirmed for the case of step changes in the state variables: the DKF employing the PECE method reacts immediately, whereas the DKF employing the proposed heuristic method has a delay of a few time-steps. For the distribution-feeder case, SE enabled the identification of an incorrect installations of the sensors. For the sub-transmission network case, many LWLS normalized residuals systematically exceed the selected threshold for bad-data identification. Most probably, this is due to line-parameter errors that highly affect the residuals related to current-flow measurements.

The accuracy level, refresh rate and time-determinism of the estimated state provided by PMU-based RTSE enable to improve or even completely rethink existing power-system applications. Fault management may belong to the latter category, as we demonstrated in Chapter 5. We proposed a fault detection and faulted-line identification method based on LWLS-RTSE. It does not need any model of loads/generators and has no prior knowledge of the fault type and of the neutral connection, even though it requires that a PMU is installed at every bus. We assume that every PMU measure the voltage and current-injection phasors at the respective bus. The performance evaluation was carried out for a real distribution feeder modeled in a RTS. The simulated scenarios included feeders with grounded and isolated neutral, symmetric and asymmetric faults with low- and high-impedance at different locations. We showed that the proposed method is able to locate the faulted line with very good accuracy for low- and high-impedance faults when 0.1-class sensors are used. Whereas, if 0.5-class sensors are employed, the accuracy is significantly decreased for high-impedance faults. Additionally, the proposed method maintain the same accuracy irrespectively

from the network operating conditions, even in presence of large amount of DG. Finally, we showed that the total latency of a real system implementing the proposed method ranges from 102 to 122 ms for this case study. It is well known that protections are a crucial power-system component and much more detailed tests have to be performed in order to claim that this method can be used for protective relaying. However, we can state that both accuracy and latency performance do match the requirements of protection schemes and are likely to be further improved in the coming years thanks to the advancement of PMU and telecommunication technologies.

Possible directions for future research:

- A missing point of the study on the DKF is the treatment of bad data, which is also marginally addressed in the literature. Future research may focus on the development of bad-data detection and identification algorithms specifically designed for DKF applied to power-system SE, which can exploit both residuals and innovations.
- Concerning the analysis of the SE results for the two real networks, we are currently investigating the problem linked to the high normalized residuals related to current-flow measurements in the sub-transmission network. Moreover the availability of such PMU-based measurement infrastructures enable many different practical and theoretical future studies, such as optimization of the latency of each component, PMU-data conditioning, line-parameter estimation, analysis of other recorded events, etc.
- Regarding fault location using PMU-based RTSE, future work may focus on the validation of the proposed method for meshed networks, the inclusion of current-flow measurements and the evaluation of the impact of line-parameter errors on the fault-location accuracy. Another important aspect may be the development of a method that relaxes the assumption of having a PMU at every bus; then, it automatically follows the study on the optimal placement of PMUs.

A Appendix

A.1 Derivation of the measurement matrix H

In this appendix we derive the elements of the measurement matrix $\mathbf{H}$ defined in (1.5) for three types of measurements: voltage phasors, current-injection phasors and current-flow phasors. The three blocks of $\mathbf{H}$ related to these measurements are called $\mathbf{H}_V$, $\mathbf{H}_{I_{\text{inj}}}$ and $\mathbf{H}_{I_{\text{flow}}}$, respectively.

The matrix block related to the voltage-phasor measurements $\mathbf{H}_V$ is simply composed of zeros and ones. The elements of $\mathbf{H}_V$ are defined in what follows:

$$\mathbf{H}_V = \begin{bmatrix} \mathbf{H}_V^1 & \mathbf{H}_V^2 \\ \mathbf{H}_V^3 & \mathbf{H}_V^4 \end{bmatrix} \tag{A.1}$$

where

$$H_{V\,hl,re}^{1\,ip,re} = \begin{cases} 1, \text{ if } i = h \text{ and } p = l \\ 0, \text{ if } i \neq h \text{ or } p \neq l \end{cases} \tag{A.2}$$

$$H_{V\,hl,im}^{2\,ip,re} = 0 \tag{A.3}$$

$$H_{V\,hl,re}^{3\,ip,im} = 0 \tag{A.4}$$

$$H_{V\,hl,im}^{4\,ip,im} = \begin{cases} 1, \text{ if } i = h \text{ and } p = l \\ 0, \text{ if } i \neq h \text{ or } p \neq l \end{cases} \tag{A.5}$$

In (A.2)–(A.5), the superscripts refer to the bus i, the phase p and the real re or imaginary im part of the measurements; whereas, the subscripts refer to the bus h, the phase l and the real re or imaginary im part of the state variables. For instance, $H_{V\,hl,im}^{2\,ip,re}$ is the scalar that links the measurement $V_{i,re}^{p}$ with the state variable $V_{h,im}^{l}$.

The current-injections are related to the voltages through the so-called *network admittance matrix* denoted by $\mathbf{Y}$. Therefore, we need to briefly recall the admittance matrix structure (a detailed description is given in [1, Chapter 8] and [6, Chapter 2.2]). For a three-phase network of s buses, $\mathbf{Y}$ is a $3s \times 3s$ complex matrix:

$$\mathbf{Y} = \begin{bmatrix} \mathbf{Y}_{11} & \mathbf{Y}_{12} & \cdots & \mathbf{Y}_{1s} \\ \mathbf{Y}_{21} & \mathbf{Y}_{22} & \cdots & \mathbf{Y}_{2s} \\ \vdots & \vdots & \ddots & \vdots \\ \mathbf{Y}_{s1} & \mathbf{Y}_{s2} & \cdots & \mathbf{Y}_{ss} \end{bmatrix} \tag{A.6}$$

By considering the three phases (a, b, c), the generic element $\mathbf{Y}_{ih}$ can be written as the following 3×3 complex matrix:

$$\mathbf{Y}_{ih} = \begin{bmatrix} Y_{ih}^{aa} & Y_{ih}^{ab} & Y_{ih}^{ac} \\ Y_{ih}^{ba} & Y_{ih}^{bb} & Y_{ih}^{bc} \\ Y_{ih}^{ca} & Y_{ih}^{cb} & Y_{ih}^{cc} \end{bmatrix} \tag{A.7}$$

The admittance matrix can be also written in terms of the real and imaginary parts:

$$\mathbf{Y} = \mathbf{G} + j\mathbf{B} \tag{A.8}$$

where j denotes the imaginary unit of complex numbers.

The current-injection phasor I_i^p at bus $i \in \mathcal{S}$ in phase $p \in \mathcal{P}$ can be expressed in terms of the state variables (i.e., the voltage phasors) as

$$I_i^p = \sum_{h=1}^{s} \sum_{l \in \mathcal{P}} Y_{ih}^{pl} V_h^l \,. \tag{A.9}$$

The real and imaginary parts of I_i^p are

$$I_{i,re}^p = \sum_{h=1}^{s} \sum_{l \in \mathcal{P}} \left[G_{ih}^{pl} V_{h,re}^l - B_{ih}^{pl} V_{h,im}^l \right] , \tag{A.10}$$

$$I_{i,im}^p = \sum_{h=1}^{s} \sum_{l \in \mathcal{P}} \left[G_{ih}^{pl} V_{h,im}^l + B_{ih}^{pl} V_{h,re}^l \right] . \tag{A.11}$$

The block of $\mathbf{H}$ related to the current-injection phasor measurements can be derived

in a straightforward way from (A.10) and (A.11):

$$\mathbf{H}_{I_{\text{inj}}} = \begin{bmatrix} \mathbf{H}^1_{I_{\text{inj}}} & \mathbf{H}^2_{I_{\text{inj}}} \\ \mathbf{H}^3_{I_{\text{inj}}} & \mathbf{H}^4_{I_{\text{inj}}} \end{bmatrix} \tag{A.12}$$

where

$$H^{1\ ip,re}_{I_{\text{inj}}\,hl,re} = G^{pl}_{ih} \tag{A.13}$$

$$H^{2\ ip,re}_{I_{\text{inj}}\,hl,im} = -B^{pl}_{ih} \tag{A.14}$$

$$H^{3\ ip,im}_{I_{\text{inj}}\,hl,re} = B^{pl}_{ih} \tag{A.15}$$

$$H^{4\ ip,im}_{I_{\text{inj}}\,hl,im} = G^{pl}_{ih} \tag{A.16}$$

In (A.13)–(A.16), the superscripts and subscripts have the same meaning as in (A.2)–(A.5).

The expression of the current-flow phasor measurements as a function of the state variables can be derived by considering the two-port π-model of a generic three-phase network branch $u \in \mathcal{D}$ between buses i and h, as shown in Fig. A.1. The model parameters are 3×3 complex matrices; therefore, the π-longitudinal impedance $\mathbf{z}_{ih,L}$ and the two π-transverse admittances $\mathbf{y}_{ih,T}$ and $\mathbf{y}_{hi,T}$ can be expressed in rectangular coordinates as

$$\mathbf{z}_{ih,L} = \mathbf{r}_{ih,L} + j\mathbf{x}_{ih,L} \tag{A.17}$$

$$\mathbf{y}_{ih,T} = \mathbf{g}_{ih,T} + j\mathbf{b}_{ih,T} \tag{A.18}$$

$$\mathbf{y}_{hi,T} = \mathbf{g}_{hi,T} + j\mathbf{b}_{hi,T} \tag{A.19}$$

where

- $\mathbf{r}_{ih,L}$ and $\mathbf{x}_{ih,L}$ are, respectively, the π-longitudinal resistance and reactance;
- $\mathbf{g}_{ih,T}$ and $\mathbf{b}_{ih,T}$ are, respectively, the π-transverse conductance and susceptance from the side of bus i.
- $\mathbf{g}_{hi,T}$ and $\mathbf{b}_{hi,T}$ are, respectively, the π-transverse conductance and susceptance from the side of bus h;

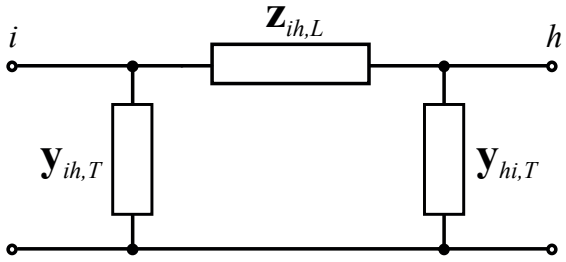

Figure A.1 – Two-port π-model of a generic three-phase network branch. Note that the model parameters are 3×3 complex matrices.

The matrix of the π-longitudinal impedance $\mathbf{z}_{ih,L}$ has the following structure:

$$\mathbf{z}_{ih,L} = \begin{bmatrix} r^{aa}_{ih,L} + jx^{aa}_{ih,L} & r^{ab}_{ih,L} + jx^{ab}_{ih,L} & r^{ac}_{ih,L} + jx^{ac}_{ih,L} \\ r^{ba}_{ih,L} + jx^{ba}_{ih,L} & r^{bb}_{ih,L} + jx^{bb}_{ih,L} & r^{bc}_{ih,L} + jx^{bc}_{ih,L} \\ r^{ca}_{ih,L} + jx^{ca}_{ih,L} & r^{cb}_{ih,L} + jx^{cb}_{ih,L} & r^{cc}_{ih,L} + jx^{cc}_{ih,L} \end{bmatrix} \tag{A.20}$$

where a, b and c are the three phases. The diagonal entries are the self-impedances of each phase and the off-diagonal entries are the mutual impedances between the phases. The matrix of the π-transverse admittance $\mathbf{y}_{ih,T}$ is written as follows (note that $\mathbf{y}_{hi,T}$ has the same structure):

$$\mathbf{y}_{ih,T} = \begin{bmatrix} g^{aa}_{ih,T} + jb^{aa}_{ih,T} & g^{ab}_{ih,T} + jb^{ab}_{ih,T} & g^{ac}_{ih,T} + jb^{ac}_{ih,T} \\ g^{ba}_{ih,T} + jb^{ba}_{ih,T} & g^{bb}_{ih,T} + jb^{bb}_{ih,T} & g^{bc}_{ih,T} + jb^{bc}_{ih,T} \\ g^{ca}_{ih,T} + jb^{ca}_{ih,T} & g^{cb}_{ih,T} + jb^{cb}_{ih,T} & g^{cc}_{ih,T} + jb^{cc}_{ih,T} \end{bmatrix} \tag{A.21}$$

We can also define the π-longitudinal admittance $\mathbf{y}_{ih,L}$ as the inverse of $\mathbf{z}_{ih,L}$:

$$\mathbf{y}_{ih,L} = \mathbf{z}^{-1}_{ih,L} \, . \tag{A.22}$$

In general, the current-flow is different at the two ends of the branch. Therefore, we indicate as I^p_{ih} the current-flow phasor at branch u in phase $p \in \mathcal{P}$ from the side of bus i, and as I^p_{hi} the current-flow phasor from the side of bus h. The expression of I^p_{ih} as a function of the state variables (i.e., the voltage phasors) is

$$I^p_{ih} = \sum_{l \in \mathcal{P}} \left[y^l_{ih,L}(V^l_i - V^l_h) + y^l_{ih,T} V^l_i \right] \, . \tag{A.23}$$

The real and imaginary parts of I^p_{ih} are:

$$I^p_{ih,re} = \sum_{l \in \mathcal{P}} [g^{pl}_{ih,L}(V^l_{i,re} - V^l_{h,re}) - b^{pl}_{ih,L}(V^l_{i,im} - V^l_{h,im}) + g^{pl}_{ih,T} V^l_{i,re} - b^{pl}_{ih,T} V^l_{i,im}] \tag{A.24}$$

$$I^p_{ih,im} = \sum_{l\in\mathcal{P}}[g^{pl}_{ih,L}(V^l_{i,im} - V^l_{h,im}) + b^{pl}_{ih,L}(V^l_{i,re} - V^l_{h,re}) + g^{pl}_{ih,T}V^l_{i,im} + b^{pl}_{ih,T}V^l_{i,re}] \quad \text{(A.25)}$$

The block of $\mathbf{H}$ related to the current-flow phasor measurements can be derived in a straightforward way from (A.24) and (A.25):

$$\mathbf{H}_{I_{\text{flow}}} = \begin{bmatrix} \mathbf{H}^1_{I_{\text{flow}}} & \mathbf{H}^2_{I_{\text{flow}}} \\ \mathbf{H}^3_{I_{\text{flow}}} & \mathbf{H}^4_{I_{\text{flow}}} \end{bmatrix} \quad \text{(A.26)}$$

where

$$H^{1\ ihp,re}_{I_{\text{flow}}il,re} = g^{pl}_{ih,L} + g^{pl}_{ih,T} \quad \text{(A.27)}$$

$$H^{1\ ihp,re}_{I_{\text{flow}}hl,re} = -g^{pl}_{ih,L} \quad \text{(A.28)}$$

$$H^{2\ ihp,re}_{I_{\text{flow}}il,im} = -(b^{pl}_{ih,L} + b^{pl}_{ih,T}) \quad \text{(A.29)}$$

$$H^{2\ ihp,re}_{I_{\text{flow}}hl,im} = b^{pl}_{ih,L} \quad \text{(A.30)}$$

$$H^{3\ ihp,im}_{I_{\text{flow}}il,re} = b^{pl}_{ih,L} + b^{pl}_{ih,T} \quad \text{(A.31)}$$

$$H^{3\ ihp,im}_{I_{\text{flow}}hl,re} = -b^{pl}_{ih,L} \quad \text{(A.32)}$$

$$H^{4\ ihp,im}_{I_{\text{flow}}il,im} = g^{pl}_{ih,L} + g^{pl}_{ih,T} \quad \text{(A.33)}$$

$$H^{4\ ihp,im}_{I_{\text{flow}}hl,im} = -g^{pl}_{ih,L} \quad \text{(A.34)}$$

In (A.27)–(A.34), the superscripts refer to the two terminal buses i and h of the branch, the phase p and the real re or imaginary im part of the measurements; whereas, the subscripts refer to the bus i or h, the phase l and the real re or imaginary im part of the state variables. For instance, $H^{2\ ihp,re}_{I_{\text{flow}}il,im}$ is the scalar that links the measurement $I^p_{ih,re}$ with the state variable $V^l_{i,im}$.

A.2 Proof of Theorem 2

In this Appendix, we give the proofs of Theorem 2 in Section 2.5.1.

The objective function is convex and the set of feasible $\mathbf{\Sigma}$ is convex [129, Chapter 7.1.1, p. 355–357]. Furthermore, the infimum of the objective function cannot occur when $\lambda_{\min}(\mathbf{\Sigma}) \to 0$ (where $\lambda_{\min}$ denotes the smallest eigenvalue) because the objective function becomes infinite when $\lambda_{\min}(\mathbf{\Sigma}) \to 0$. As the feasible set is bounded (because

of the condition $\mathbf{I}_n - \mathbf{\Sigma} \succeq \mathbf{0}$), it follows that the optimization problem has a finite minimum, which is attained for one or several values of $\mathbf{\Sigma}$. Furthermore, $\log[\det(\mathbf{\Sigma})]$ is strictly concave [130, Lemma 6.2.2 p.101] and $\mathrm{trace}(\mathbf{\Sigma E})$ is linear in $\mathbf{\Sigma}$, therefore the objective function is strictly convex. It follows that the minimum is reached at one unique value of $\mathbf{\Sigma}$.

(QED)

A.3 Proof of Theorem 3

In this Appendix, we give the proofs of Theorem 3 in Section 2.5.1.

First, note that the innovations form a Gaussian random vector with zero mean and covariance matrix given by (2.22). By [129, Chapter 7.1.1, p. 355–357], it follows that the ML estimation of the covariance matrix of the innovation is obtained as the optimal value of $\mathbf{T}$ in the following optimization problem (recall that $\mathbf{H}$ and $\mathbf{R}$ are fixed and known):

$$\begin{aligned} \min_{\mathbf{T},\mathbf{P}} \quad & \Big\{\log[\det(\mathbf{T})] + \mathrm{trace}(\mathbf{T}^{-1}\mathbf{C}_k)\Big\} \\ \text{subject to:} \quad & \mathbf{T} = \mathbf{HPH}^T + \mathbf{R} \\ & \mathbf{P} \text{ real symmetric and } \mathbf{P} \succeq \mathbf{0}. \end{aligned} \tag{A.35}$$

Second, we show that the feasible sets of the optimization problems (2.23) and (A.35) are equivalent. More precisely, there is a one-to-one mapping between any feasible $\mathbf{\Sigma}$ of Problem (2.23) and a feasible $(\mathbf{T}, \mathbf{P})$ pair of Problem (A.35). In one direction, given $\mathbf{\Sigma}$, $\mathbf{T}$ and $\mathbf{P}$ are obtained by

$$\mathbf{P} = \mathbf{U}^{-1}\left(\mathbf{\Sigma}^{-1} - \mathbf{I}_n\right)\mathbf{U}^{-T} \tag{A.36}$$

$$\mathbf{T} = \mathbf{HPH}^T + \mathbf{R} \tag{A.37}$$

We need to prove that if $\mathbf{\Sigma}$ satisfies the conditions of Problem (2.23), then $\mathbf{P} \succeq \mathbf{0}$. To show this, observe that $\mathbf{\Sigma} \succ \mathbf{0}$ and $\mathbf{I}_n - \mathbf{\Sigma} \succeq \mathbf{0}$ therefore $\mathbf{\Sigma}^{-1} - \mathbf{I}_n \succeq \mathbf{0}$ [131, Appendix C]. This in turn implies that $\mathbf{P} = \mathbf{U}^{-1}\left(\mathbf{\Sigma}^{-1} - \mathbf{I}_n\right)\mathbf{U}^{-T} \succeq \mathbf{0}$.

In the reverse direction, given $\mathbf{T}$ and $\mathbf{P}$, $\mathbf{\Sigma}$ is obtained by

$$\mathbf{\Sigma} = \left(\mathbf{UPU}^T + \mathbf{I}_n\right)^{-1} \tag{A.38}$$

Similarly, we need to show that if $\mathbf{P}$ satisfies the condition of Problem (A.35) then $\mathbf{\Sigma}$ is well defined, $\mathbf{\Sigma} \succ \mathbf{0}$ and $\mathbf{I}_n - \mathbf{\Sigma} \succeq \mathbf{0}$. First observe that $\mathbf{P} \succeq \mathbf{0}$ therefore $\mathbf{UPU}^T \succeq \mathbf{0}$

and $\mathbf{U}\mathbf{P}\mathbf{U}^T + \mathbf{I}_n \succeq \mathbf{I}_n$. Thus $\mathbf{U}\mathbf{P}\mathbf{U}^T + \mathbf{I}_n \succ \mathbf{0}$ and is invertible. It follows that $\mathbf{\Sigma}$ is well defined and $\mathbf{\Sigma} \succ \mathbf{0}$. Furthermore, $\mathbf{\Sigma}^{-1} = \mathbf{U}\mathbf{P}\mathbf{U}^T + \mathbf{I}_n \succeq \mathbf{I}_n$ and thus $\mathbf{\Sigma}^{-1} \preceq \mathbf{I}_n$ [131, Appendix C].

Third, we show that the values of the objective functions differ by a constant when $\mathbf{\Sigma}$ and $(\mathbf{T}, \mathbf{P})$ are mapped by the above correspondence. Indeed, by (A.37)

$$\begin{aligned}
\mathbf{R}^{-\frac{1}{2}}\mathbf{T}\mathbf{R}^{-\frac{1}{2}} &= \mathbf{R}^{-\frac{1}{2}}\mathbf{H}\mathbf{P}\mathbf{H}^T\mathbf{R}^{-\frac{1}{2}} + \mathbf{I}_m \\
&= \mathbf{V}\begin{pmatrix} \mathbf{U} \\ \mathbf{0}_{m-n,n} \end{pmatrix}\mathbf{P}\begin{pmatrix} \mathbf{U}^T & \mathbf{0}_{m-n,n} \end{pmatrix}\mathbf{V}^T + \mathbf{I}_m \\
&= \mathbf{V}\begin{pmatrix} \mathbf{U}\mathbf{P}\mathbf{U}^T & \mathbf{0}_{n,m-n} \\ \mathbf{0}_{m-n,n} & \mathbf{0}_{m-n,m-n} \end{pmatrix}\mathbf{V}^T + \mathbf{I}_m \\
&= \mathbf{V}\begin{pmatrix} \mathbf{U}\mathbf{P}\mathbf{U}^T + \mathbf{I}_n & \mathbf{0}_{n,m-n} \\ \mathbf{0}_{m-n,n} & \mathbf{I}_{m-n} \end{pmatrix}\mathbf{V}^T
\end{aligned} \tag{A.39}$$

Therefore, noticing that $\det(\mathbf{V})\det(\mathbf{V}^T) = 1$ and using rules for block-diagonal matrices:

$$\det(\mathbf{R})^{-1}\det(\mathbf{T}) = \det\left(\mathbf{U}\mathbf{P}\mathbf{U}^T + \mathbf{I}_n\right) = \det(\mathbf{\Sigma})^{-1} \tag{A.40}$$

Taking the inverse of (A.39) gives

$$\begin{aligned}
\mathbf{R}^{\frac{1}{2}}\mathbf{T}^{-1}\mathbf{R}^{\frac{1}{2}} &= \\
&= \mathbf{V}\begin{pmatrix} \mathbf{U}\mathbf{P}\mathbf{U}^T + \mathbf{I}_n & \mathbf{0}_{n,m-n} \\ \mathbf{0}_{m-n,n} & \mathbf{I}_{m-n} \end{pmatrix}^{-1}\mathbf{V}^T \\
&= \mathbf{V}\begin{pmatrix} \mathbf{\Sigma} & \mathbf{0}_{n,m-n} \\ \mathbf{0}_{m-n,n} & \mathbf{I}_{m-n} \end{pmatrix}\mathbf{V}^T
\end{aligned} \tag{A.41}$$

and thus

$$\mathbf{T}^{-1}\mathbf{C}_k = \mathbf{R}^{-\frac{1}{2}}\mathbf{V}\begin{pmatrix} \mathbf{\Sigma} & \mathbf{0}_{n,m-n} \\ \mathbf{0}_{m-n,n} & \mathbf{I}_{m-n} \end{pmatrix}\mathbf{V}^T\mathbf{R}^{-\frac{1}{2}}\mathbf{C}_k \tag{A.42}$$

Using the property that $\mathrm{trace}(\mathbf{A}\mathbf{B}) = \mathrm{trace}(\mathbf{B}\mathbf{A})$ it comes

$$\begin{aligned}
&\mathrm{trace}(\mathbf{T}^{-1}\mathbf{C}_k) = \\
&= \mathrm{trace}\left(\begin{pmatrix} \mathbf{\Sigma} & \mathbf{0}_{n,m-n} \\ \mathbf{0}_{m-n,n} & \mathbf{I}_{m-n} \end{pmatrix}\mathbf{V}^T\mathbf{R}^{-\frac{1}{2}}\mathbf{C}_k\mathbf{R}^{-\frac{1}{2}}\mathbf{V}\right) \\
&= \mathrm{trace}\left(\begin{pmatrix} \mathbf{\Sigma} & \mathbf{0}_{n,m-n} \\ \mathbf{0}_{m-n,n} & \mathbf{I}_{m-n} \end{pmatrix}\begin{pmatrix} \mathbf{E}_k & \mathbf{E''}_k \\ \mathbf{E'}_k & \mathbf{E'''}_k \end{pmatrix}\right) \\
&= \mathrm{trace}(\mathbf{\Sigma}\mathbf{E}_k) + \mathrm{trace}(\mathbf{E'''}_k)
\end{aligned} \tag{A.43}$$

where $\mathbf{E'}_k, \mathbf{E''}_k, \mathbf{E'''}_k$ are sub-blocks of appropriate sizes and $\mathbf{E}_k$ is defined in (2.25).

Putting together (A.40) and (A.43) gives the following relation between the objective functions:

$$\log\det(\mathbf{T}) + \mathrm{trace}(\mathbf{T}^{-1}\mathbf{C}_k) = -\log\det(\mathbf{\Sigma}) + \mathrm{trace}(\mathbf{\Sigma}\mathbf{E}_k) + \alpha \tag{A.44}$$

where $\alpha = \log\det(\mathbf{R}) + \mathrm{trace}(\mathbf{E'''}_k)$ is a constant.

It follows from all the above that $\mathbf{\Sigma}$ is optimal for Problem (2.23) if and only if $(\mathbf{T}, \mathbf{P})$ is optimal for Problem (A.35), when $\mathbf{\Sigma}$ and $(\mathbf{T}, \mathbf{P})$ are mapped by (A.36) to (A.38). (QED)

A.4 Covariance estimation method of Myers and Tapley

In [89], Myers and Tapley propose a simple covariance-matching method to assess both $\mathbf{Q}$ and $\mathbf{R}$. We assume that $\mathbf{R}$ is known, so that only $\mathbf{Q}$ has to be estimated. At time-step k, the value of $\mathbf{Q}_k$ is inferred by using the following procedure:

- Compute N vectors ($i = 1, ..., N$):

$$\mathbf{g}_i = \widehat{\mathbf{x}}_{k-i|k-i} - \mathbf{A}_{k-i-1}\widehat{\mathbf{x}}_{k-i-1|k-i-1}\ ; \tag{A.45}$$

- Then, compute the sample covariance matrix:

$$\widehat{\mathbf{M}}_k = cov(\mathbf{g}_1, ..., \mathbf{g}_i, ..., \mathbf{g}_N)\ ; \tag{A.46}$$

- Compute the estimated process-noise covariance matrix:

$$\widehat{\mathbf{Q}}_k = \widehat{\mathbf{M}}_k - \frac{1}{N}\sum_{i=2}^{N+1}\left(\mathbf{A}_{k-i}\mathbf{P}_{k-i|k-i}\mathbf{A}_{k-i}^T - \mathbf{P}_{k-i+1|k-i+1}\right). \tag{A.47}$$

In stationary conditions, $\widehat{\mathbf{Q}}$ approaches the true value as the parameter N increases. In case of variations of the process stochastic parameters, the smaller N, the faster the KF reaction.

Bibliography

[1] J. Grainger and W. Stevenson, *Power system analysis*. McGraw-Hill, 1994.

[2] F. Schweppe and J. Wildes, "Power system static-state estimation, part I: Exact model," *Power Apparatus and Systems, IEEE Transactions on*, vol. PAS-89, pp. 120–125, Jan 1970.

[3] F. Schweppe and D. Rom, "Power system static-state estimation, part II: Approximate model," *Power Apparatus and Systems, IEEE Transactions on*, vol. PAS-89, pp. 125–130, Jan 1970.

[4] F. Schweppe, "Power system static-state estimation, part III: Implementation," *Power Apparatus and Systems, IEEE Transactions on*, vol. PAS-89, pp. 130–135, Jan 1970.

[5] A. Monticelli, *State estimation in electric power systems: a generalized approach*, vol. 507. Springer Science & Business Media, 1999.

[6] A. Abur and A. Exposito, *Power system state estimation: theory and implementation*, vol. 24. CRC, 2004.

[7] A. Monticelli and F. F. Wu, "Network observability: Identification of observable islands and measurement placement," *IEEE Transactions on Power Apparatus and Systems*, vol. PAS-104, pp. 1035–1041, May 1985.

[8] A. Monticelli and A. Garcia, "Reliable bad data processing for real-time state estimation," *Power Apparatus and Systems, IEEE Transactions on*, vol. PAS-102, pp. 1126–1139, May 1983.

[9] T. Van Cutsem, M. Ribbens-Pavella, and L. Mili, "Hypothesis testing identification: A new method for bad data analysis in power system state estimation," *Power Apparatus and Systems, IEEE Transactions on*, vol. PAS-103, pp. 3239–3252, Nov 1984.

[10] K. A. Clements and P. W. Davis, "Multiple bad data detectability and identifiability: A geometric approach," *IEEE Transactions on Power Delivery*, vol. 1, pp. 355–360, July 1986.

[11] F. Wu and W.-H. Liu, "Detection of topology errors by state estimation (power systems)," *Power Systems, IEEE Transactions on*, vol. 4, pp. 176–183, Feb 1989.

[12] W. H. E. Liu, F. F. Wu, and S. M. Lun, "Estimation of parameter errors from measurement residuals in state estimation (power systems)," *IEEE Transactions on Power Systems*, vol. 7, pp. 81–89, Feb 1992.

[13] J. Zhu and A. Abur, "Identification of network parameter errors," *IEEE Transactions on Power Systems*, vol. 21, pp. 586–592, May 2006.

[14] L. L. Grigsby *et al.*, *The electric power engineering handbook*. CRC, 2012.

[15] F. F. Wu, "Power system state estimation: a survey," *International Journal of Electrical Power & Energy Systems*, vol. 12, no. 2, pp. 80–87, 1990.

[16] F. F. Wu, K. Moslehi, and A. Bose, "Power system control centers: Past, present, and future," *Proceedings of the IEEE*, vol. 93, no. 11, pp. 1890–1908, 2005.

[17] A. Garcia, A. Monticelli, and P. Abreu, "Fast decoupled state estimation and bad data processing," *IEEE Transactions on Power Apparatus and Systems*, vol. PAS-98, pp. 1645–1652, Sept 1979.

[18] A. Phadke and J. Thorp, *Synchronized Phasor Measurements and Their Applications*. Power Electronics and Power Systems, Springer US, 2008.

[19] N. Data and N. S. G. Network Management Task Team, "Naspi 2014 survey of synchrophasor system networks - results and findings," Tech. Rep. TR 95-041, NASPI Technical Report, July 2015.

[20] M. Zhou, V. A. Centeno, J. S. Thorp, and A. G. Phadke, "An alternative for including phasor measurements in state estimators," *IEEE Trans. Power Syst.*, vol. 21, pp. 1930–1937, November 2006.

[21] T. Yang, H. Sun, and A. Bose, "Transition to a two-level linear state estimator—part I: Architecture," *IEEE Transactions on Power Systems*, vol. 26, no. 1, pp. 46–53, 2011.

[22] T. Yang, H. Sun, and A. Bose, "Transition to a two-level linear state estimator—part II: Algorithm," *IEEE Transactions on Power Systems*, vol. 26, no. 1, pp. 54–62, 2011.

[23] N. M. Manousakis, G. N. Korres, J. N. Aliprantis, G. P. Vavourakis, and G.-C. J. Makrinas, "A two-stage state estimator for power systems with PMU and SCADA measurements," in *PowerTech, 2013 IEEE Grenoble*, pp. 1–6, IEEE, 2013.

[24] M. Glavic and T. Van Cutsem, "Tracking network state from combined SCADA and synchronized phasor measurements," in *Bulk Power System Dynamics and Control-IX Optimization, Security and Control of the Emerging Power Grid (IREP), 2013 IREP Symposium*, pp. 1–10, IEEE, 2013.

[25] M. Göl and A. Abur, "A hybrid state estimator for systems with limited number of PMUs," *IEEE Transactions on Power Systems*, vol. 30, no. 3, pp. 1511–1517, 2015.

[26] K. D. Jones, J. S. Thorp, and R. M. Gardner, "Three-phase linear state estimation using phasor measurements," in *IEEE PES Gen. Meet.*, Vancouver Canada, July 21-25 2013.

[27] L. Zhang, A. Bose, A. Jampala, V. Madani, and J. Giri, "Design, testing, and implementation of a linear state estimator in a real power system," *IEEE Transactions on Smart Grid*, vol. PP, no. 99, pp. 1–8, 2016.

[28] M. Pignati, M. Popovic, S. Barreto, R. Cherkaoui, G. Dario Flores, J.-Y. Le Boudec, M. Mohiuddin, M. Paolone, P. Romano, S. Sarri, T. Tesfay, D.-C. Tomozei, and L. Zanni, "Real-time state estimation of the EPFL-campus medium-voltage grid by using PMUs," in *Sixth Conf. on Innov. Smart Grid Techn. (ISGT 2015)*, pp. 1–5, Washington, DC, USA, Feb 17-20 2015.

[29] A. Phadke, J. Thorp, and K. Karimi, "State estimlatjon with phasor measurements," *IEEE Transactions on Power Systems*, vol. 1, no. 1, pp. 233–238, 1986.

[30] A. Abur, "Impact of phasor measurements on state estimation," in *Electrical and Electronics Engineering, 2009. ELECO 2009. International Conference on*, pp. I–3–I–7, Nov 2009.

[31] J. Zhu and A. Abur, "Effect of phasor measurements on the choice of reference bus for state estimation," in *IEEE PES Gen. Meet.*, Tampa, Florida, June 24-28 2007.

[32] T. E. Dielman, "Least absolute value regression: recent contributions," *Journal of Statistical Computation and Simulation*, vol. 75, no. 4, pp. 263–286, 2005.

[33] R. E. Kalman, "A new approach to linear filtering and prediction problems," *Trans. of the ASME-Journal of Basic Eng.*, pp. 33–45, 1960.

[34] M. Göl and A. Abur, "LAV based robust state estimation for systems measured by PMUs," *IEEE Transactions on Smart Grid*, vol. 5, pp. 1808–1814, July 2014.

[35] M. Göl and A. Abur, "A robust PMU based three-phase state estimator using modal decoupling," *IEEE Transactions on Power Systems*, vol. 29, pp. 2292–2299, Sept 2014.

[36] M. Gol, *Incorporation of PMUs in power system state estimation*. PhD thesis, Northeastern University, 2014.

[37] J. Zhang, G. Welch, G. Bishop, and Z. Huang, "A two-stage Kalman filter approach for robust and real-time power system state estimation," *IEEE Transactions on Sustainable Energy*, vol. 5, pp. 629–636, April 2014.

[38] M. E. Baran and A. W. Kelley, "A branch-current-based state estimation method for distribution systems," *IEEE Trans. Power Syst.*, vol. 10, pp. 483–491, February 1995.

[39] C. A. Fantin, M. R. C. Castillo, B. E. B. de Carvalho, and J. B. A. London, "Using pseudo and virtual measurements in distribution system state estimation," in *Transmission Distribution Conference and Exposition - Latin America (PES T D-LA), 2014 IEEE PES*, pp. 1–6, Sept 2014.

[40] J. Liu, J. Tang, F. Ponci, A. Monti, C. Muscas, and P. Pegoraro, "Trade-offs in PMU deployment for state estimation in active distribution grids," *Smart Grid, IEEE Transactions on*, vol. 3, no. 2, pp. 915–924, 2012.

[41] E. Caro, A. J. Conejo, and R. Mínguez, "Power system state estimation considering measurement dependencies," *IEEE Trans. Power Syst.*, vol. 24, no. 4, pp. 1875–1885, 2009.

[42] C. Muscas, M. Pau, P. A. Pegoraro, and S. Sulis, "Effects of measurements and pseudomeasurements correlation in distribution system state estimation," *IEEE Trans. on Instr. and Meas.*, vol. 63, no. 12, pp. 2813–2823, 2014.

[43] B. I. des Poids et Mesures, C. électrotechnique internationale, and O. internationale de normalisation, *Guide to the Expression of Uncertainty in Measurement*. International Organization for Standardization, 1995.

[44] M. Paolone, A. Borghetti, and C. A. Nucci, "A synchrophasor estimation algorithm for the monitoring of active distribution networks in steady state and transient conditions," in *Power Syst. Comp. Conf. (PSCC)*, Wroclaw, Poland, August 18-22 2014.

[45] *Instrument transformers Part 2: Additional Requirements for current transformers*. IEC Std 61869-2, 2012.

[46] *Instrument transformers Part 3: Additional Requirements for inductive voltage transformers*. IEC Std 61869-3, 2011.

[47] "IEEE Standard for Synchrophasor Measurements for Power Systems," *IEEE Std C37.118.1-2011 (Revision of IEEE Std C37.118-2005)*, pp. 1–61, 2011.

[48] F. Milano, *Advanced Techniques for Power System Modelling, Control and Stability Analysis*. London, U.K.: The Institution of Engineering and Technology - IET, 2015.

[49] K. Nishiya, J. Hasegawa, and T. Koike, "Dynamic state estimation including anomaly detection and identification for power systems," in *IEE Proceedings C-Generation, Transmission and Distribution*, vol. 129, pp. 192–198, IET, 1982.

[50] G. Valverde and V. Terzija, "Unscented Kalman filter for power system dynamic state estimation," *IET Gener., Transm. and Distr.*, vol. 5, pp. 29–37, January 2011.

[51] A. Leite da Silva, M. C. Filho, and J. Cantera, "An efficient dynamic state estimation algorithm including bad data processing," *Power Engineering Review, IEEE*, vol. PER-7, pp. 49–49, Nov 1987.

[52] K. A. Clements, G. R. Krumpholz, and P. W. Davis, "Power system state estimation residual analysis: An algorithm using network topology," *IEEE Transactions on Power Apparatus and Systems*, vol. PAS-100, pp. 1779–1787, April 1981.

[53] M. Göl and A. Abur, "Observability and criticality analyses for power systems measured by phasor measurements," *IEEE Transactions on Power Systems*, vol. 28, pp. 3319–3326, Aug 2013.

[54] A. Monticelli, "Electric power system state estimation," *Proceedings of the IEEE*, vol. 88, no. 2, pp. 262–282, 2000.

[55] L. Mili, M. G. Cheniae, N. S. Vichare, and P. J. Rousseeuw, "Robust state estimation based on projection statistics (of power systems)," *IEEE Transactions on Power Systems*, vol. 11, pp. 1118–1127, May 1996.

[56] G. Welch and G. Bishop, "An introduction to the Kalman filter," Tech. Rep. TR 95-041, Dep. of Computer Science, University of North Carolina, July 2006.

[57] A. S. Debs and R. E. Larson, "A dynamic estimator for tracking the state of a power system," *IEEE Trans. Power Appar. and Syst.*, vol. PAS-89, pp. 1670–1678, September 1970.

[58] A. L. Da Silva, M. Do Coutto Filho, and J. De Queiroz, "State forecasting in electric power systems," in *IEE Proceedings C-Generation, Transmission and Distribution*, vol. 130, pp. 237–244, IET, 1983.

[59] A. K. Sinha and J. K. Mandal, "Dynamic state estimator using ANN based bus load prediction," *IEEE Transactions on Power Systems*, vol. 14, pp. 1219–1225, Nov 1999.

[60] K.-R. Shih and S.-J. Huang, "Application of a robust algorithm for dynamic state estimation of a power system," *IEEE Transactions on Power Systems*, vol. 17, pp. 141–147, Feb 2002.

[61] E. A. Blood, M. D. Ilic, J. Ilic, and B. H. Krogh, "A Kalman filter approach to quasi-static state estimation in electric power systems," in *2006 38th North American Power Symposium*, pp. 417–422, Sept 2006.

[62] E. Blood, B. Krogh, and M. Ilic, "Electric power system static state estimation through Kalman filtering and load forecasting," in *Power and Energy Society*

General Meeting-Conversion and Delivery of Electrical Energy in the 21st Century, 2008 IEEE, pp. 1–6, IEEE, 2008.

[63] A. Jain and N. R. Shivakumar, "Impact of PMU in dynamic state estimation of power systems," in *2008 40th North American Power Symposium*, pp. 1–8, Sept 2008.

[64] A. Jain and N. R. Shivakumar, "Phasor measurements in dynamic state estimation of power systems," in *TENCON 2008 - 2008 IEEE Region 10 Conference*, pp. 1–6, Nov 2008.

[65] A. Jain and N. R. Shivakumar, "Power system tracking and dynamic state estimation," in *Power Syst. Conf. and Expos. (PSCE), 2009*, Seattke, WA, IEEE, March 15-18 2009.

[66] F. C. Schweppe and R. D. Masiello, "A tracking static state estimator," *IEEE Transactions on Power Apparatus and Systems*, vol. PAS-90, pp. 1025–1033, May 1971.

[67] S. J. Julier and J. K. Uhlmann, "New extension of the Kalman filter to nonlinear systems," in *AeroSense'97*, pp. 182–193, International Society for Optics and Photonics, 1997.

[68] F. Aminifar, M. Shahidehpour, M. Fotuhi-Firuzabad, and S. Kamalinia, "Power system dynamic state estimation with synchronized phasor measurements," *IEEE Transactions on Instrumentation and Measurement*, vol. 63, pp. 352–363, Feb 2014.

[69] A. Sharma, S. C. Srivastava, and S. Chakrabarti, "Testing and validation of power system dynamic state estimators using real time digital simulator (RTDS)," *IEEE Transactions on Power Systems*, vol. 31, pp. 2338–2347, May 2016.

[70] I. Arasaratnam and S. Haykin, "Cubature Kalman filters," *IEEE Transactions on Automatic Control*, vol. 54, pp. 1254–1269, June 2009.

[71] L. Zanni, S. Sarri, M. Pignati, R. Cherkaoui, and M. Paolone, "Probabilistic assessment of the process-noise covariance matrix of discrete Kalman filter state estimation of active distribution networks," in *Intern. Conf. Probab. Meth. Appl. to Power Syst. (PMAPS)*, Durham, UK, July 7-10 2014.

[72] S. Sarri, L. Zanni, M. Popovic, J.-Y. Le Boudec, and M. Paolone, "Performance assessment of linear state estimators using synchrophasor measurements," *IEEE Transactions on Instrumentation and Measurement*, vol. 65, pp. 535–548, March 2016.

[73] R. K. Mehra, "Approaches to adaptive filtering," *IEEE Transactions on Automatic Control*, vol. 17, pp. 693–698, Oct. 1972.

[74] D. Alspach, "A parallel filtering algorithm for linear systems with unknown time varying noise statistics," *IEEE Transactions on Automatic Control*, vol. 19, pp. 552–556, Oct. 1974.

[75] C. Hilborn Jr and D. G. Lainiotis, "Optimal estimation in the presence of unknown parameters," *IEEE Transactions on Systems Science and Cybernetics*, vol. 5, pp. 38–43, Jan. 1969.

[76] R. L. Kashyap, "Maximum likelihood identification of stochastic linear systems," *IEEE Transactions on Automatic Control*, vol. 15, pp. 25–34, Feb. 1970.

[77] T. Bohlin, "Four cases of identification of changing systems," *in: R. K. Mehra and D. G. Lainiotis, eds., System identification advances and case studies*, vol. 126, Academic Press, New York, 1976.

[78] V. A. Bavdekar, A. P. Deshpande, and S. C. Patwardhan, "Identification of process and measurement noise covariance for state and parameter estimation using extended Kalman filter," *Journal of Process control*, vol. 21, pp. 585–601, Apr. 2011.

[79] R. K. Mehra, "On the identification of variances and adaptive Kalman filtering," *IEEE Transactions on Automatic Control*, vol. 15, pp. 175–184, Apr. 1970.

[80] B. Carew and P. R. Belanger, "Identification of optimum filter steady-state gain for systems with unknown noise covariances," *IEEE Transactions on Automatic Control*, vol. 18, pp. 582–587, Dec. 1973.

[81] P. R. Bélanger, "Estimation of noise covariance matrices for a linear time-varying stochastic process," *Automatica*, vol. 10, pp. 267–275, May 1974.

[82] R. G. Reynolds, "Robust estimation of covariance matrices," *IEEE Transactions on Automatic Control*, vol. 35, pp. 1047–1051, Sep. 1990.

[83] B. J. Odelson, M. R. Rajamani, and J. B. Rawlings, "A new autocovariance least-squares method for estimating noise covariances," *Automatica*, vol. 42, pp. 303–308, Feb. 2006.

[84] B. J. Odelson, A. Lutz, and J. B. Rawlings, "The autocovariance least-squares method for estimating covariances: application to model-based control of chemical reactors," *IEEE Transactions on Control Systems Technology*, vol. 14, pp. 532–540, May 2006.

[85] B. M. Åkesson, J. B. Jørgensen, N. K. Poulsen, and S. B. Jørgensen, "A generalized autocovariance least-squares method for Kalman filter tuning," *Journal of Process control*, vol. 18, pp. 769–779, Aug. 2008.

[86] M. R. Rajamani and J. B. Rawlings, "Estimation of the disturbance structure from data using semidefinite programming and optimal weighting," *Automatica*, vol. 45, pp. 142–148, Jan. 2009.

[87] Y. Zhen and J. Harlim, "Adaptive error covariances estimation methods for ensemble Kalman filters," *Journal of Computational Physics*, vol. 294, pp. 619–638, Aug. 2015.

[88] G. Noriega and S. Pasupathy, "Adaptive estimation of noise covariance matrices in real-time preprocessing of geophysical data," *IEEE Transactions on Geoscience and Remote Sensing*, vol. 35, pp. 1146–1159, Sep. 1997.

[89] K. Myers and B. D. Tapley, "Adaptive sequential estimation with unknown noise statistics," *IEEE Transactions on Automatic Control*, vol. 21, pp. 520–523, Aug. 1976.

[90] V. Krishnan, *Nonlinear filtering and smoothing: an introduction to martingales, stochastic integrals, and estimation*. Courier Dover Publications, 2005.

[91] A. Pai, *Energy function analysis for power system stability*. Norwell, MA: Kluwer, 1989.

[92] J.-Y. L. Boudec, *Performance Evaluation of Computer and Communication Systems*. EPFL Press, 2010.

[93] W. Kersting, "Radial distribution test feeders," in *Power Engineering Society Winter Meeting, 2001. IEEE*, vol. 2, pp. 908–912 vol.2, 2001.

[94] L. Zanni, J. Y. L. Boudec, R. Cherkaoui, and M. Paolone, "A prediction-error covariance estimator for adaptive Kalman filtering in step-varying processes: Application to power-system state estimation," *IEEE Transactions on Control Systems Technology*, vol. PP, no. 99, pp. 1–15, 2016.

[95] J. Lofberg, "YALMIP: A toolbox for modeling and optimization in MATLAB," in *Computer Aided Control Systems Design, 2004 IEEE International Symposium on*, pp. 284–289, IEEE, 2004.

[96] K.-C. Toh, M. J. Todd, and R. H. Tütüncü, "SDPT3—a MATLAB software package for semidefinite programming, version 1.3," *Optimization methods and software*, vol. 11, no. 1-4, pp. 545–581, 1999.

[97] P. Romano and M. Paolone, "Enhanced interpolated-DFT for synchrophasor estimation in FPGAs: Theory, implementation, and validation of a PMU prototype," *Instrumentation and Measurement, IEEE Transactions on*, vol. 63, pp. 2824–2836, Dec 2014.

[98] L. Zanni, J. Y. L. Boudec, R. Cherkaoui, and M. Paolone, "Linear power-system state estimation with zero-injection equality constraints via LQ-decomposition," *Submitted to IEEE Transactions on Power Systems*.

[99] C. L. Lawson and R. J. Hanson, *Solving least squares problems*, vol. 15. SIAM, 1995.

[100] F. Aschmoneit, N. Peterson, and E. Adrian, "State estimation with equality constraints," in *Proc. 10th PICA Conf*, pp. 427–430, sn, 1977.

[101] F. F. Wu, W. H. E. Liu, and S. M. Lun, "Observability analysis and bad data processing for state estimation with equality constraints," *IEEE Transactions on Power Systems*, vol. 3, pp. 541–548, May 1988.

[102] L. Holten, A. Gjelsvik, S. Aam, F. F. Wu, and W. H. E. Liu, "Comparison of different methods for state estimation," *IEEE Transactions on Power Systems*, vol. 3, pp. 1798–1806, Nov 1988.

[103] A. Simoes-Costa and V. H. Quintana, "A robust numerical technique for power system state estimation," *IEEE Transactions on Power Apparatus and Systems*, vol. PAS-100, pp. 691–698, Feb 1981.

[104] J. W. Gu, K. A. Clements, G. R. Krumpholz, and P. W. Davis, "The solution of ill-conditioned power system state estimation problems via the method of Peters and Wilkinson," *IEEE Transactions on Power Apparatus and Systems*, vol. PAS-102, pp. 3473–3480, Oct 1983.

[105] G. N. Korres, "A robust method for equality constrained state estimation," *IEEE Transactions on Power Systems*, vol. 17, pp. 305–314, May 2002.

[106] Y. Guo, W. Wu, B. Zhang, and H. Sun, "An efficient state estimation algorithm considering zero injection constraints," *IEEE Transactions on Power Systems*, vol. 28, pp. 2651–2659, Aug 2013.

[107] "EPFL Smart Grid." http://smartgrid.epfl.ch. Accessed: 2017-02-13.

[108] "SCCER - FURIES, Shaping the future swiss electrical infrastructure." http://sccer-furies.epfl.ch. Accessed: 2017-02-13.

[109] "IEEE Standard for Synchrophasor Data Transfer for Power Systems," *IEEE Std C37.118.2-2011 (Revision of IEEE Std C37.118-2005)*, pp. 1–53, 2011.

[110] A. Derviskadic, P. Romano, M. Pignati, and M. Paolone, "Architecture and experimental validation of a low-latency phasor data concentrator," *IEEE Transactions on Smart Grid*, vol. PP, no. 99, pp. 1–1, 2016.

[111] L. Zanni, D. Colangelo, R. Cherkaoui, and M. Paolone, "Impact of synchrophasor measurement types and uncertainties on the accuracy of distribution system linear state estimators," in *PowerTech, 2015 IEEE Eindhoven*, pp. 1–6, IEEE, 2015.

[112] "National Instrument Grid Automation System." http://www.ni.com/white-paper/52556/en/. Accessed: 2016-09-08.

[113] M. Pignati, L. Zanni, P. Romano, R. Cherkaoui, and M. Paolone, "Fault detection and faulted line identification in active distribution networks using synchrophasors-based real-time state estimation," *IEEE Transactions on Power Delivery*, vol. 32, pp. 381–392, Feb 2017.

[114] P. Navalkar and S. Soman, "Secure remote backup protection of transmission lines using synchrophasors," *Power Delivery, IEEE Transactions on*, vol. 26, pp. 87–96, Jan 2011.

[115] J. O'Brien, A. Deronja, A. Apostolov, A. Arana, M. Begovic, S. Brahma, G. Brunello, F. Calero, H. Faulk, Y. Hu, G. Kobet, H. Kirkham, Y. Liao, C. W. Liu, Y. Lu, D. Lukach, K. Martin, J. Mooney, J. Murphy, K. Narendra, D. Novosel, M. Patel, E. Price, S. Saygin, V. Skendzic, R. Taylor, D. Tziouvaras, and S. Ward, "Use of synchrophasor measurements in protective relaying applications," in *2014 67th Annual Conference for Protective Relay Engineers*, pp. 23–29, March 2014.

[116] F. Chunju, L. Shengfang, Y. Weiyong, and K. K. Li, "Study on adaptive relay protection scheme based on phase measurement unit (PMU)," in *2004 Eighth IEE International Conference on Developments in Power System Protection*, vol. 1, pp. 36–39 Vol.1, April 2004.

[117] S. Das, S. Santoso, A. Gaikwad, and M. Patel, "Impedance-based fault location in transmission networks: theory and application," *IEEE Access*, vol. 2, pp. 537–557, 2014.

[118] F. H. Magnago and A. Abur, "Fault location using wavelets," *IEEE Transactions on Power Delivery*, vol. 13, pp. 1475–1480, Oct 1998.

[119] K.-P. Lien, C.-W. Liu, C.-S. Yu, and J. A. Jiang, "Transmission network fault location observability with minimal PMU placement," *IEEE Transactions on Power Delivery*, vol. 21, pp. 1128–1136, July 2006.

[120] Q. Jiang, X. Li, B. Wang, and H. Wang, "PMU-based fault location using voltage measurements in large transmission networks," *IEEE Transactions on Power Delivery*, vol. 27, pp. 1644–1652, July 2012.

[121] M. Korkalı and A. Abur, "Robust fault location using least-absolute-value estimator," *IEEE Transactions on Power Systems*, vol. 28, pp. 4384–4392, Nov 2013.

[122] M. Shiroei, S. Daniar, and M. Akhbari, "A new algorithm for fault location on transmission lines," in *Power Energy Society General Meeting, 2009. PES '09. IEEE*, pp. 1–5, July 2009.

[123] A. Öner and M. Göl, "Fault location based on state estimation in PMU observable systems," in *2016 IEEE Power Energy Society Innovative Smart Grid Technologies Conference (ISGT)*, pp. 1–5, Sept 2016.

[124] "Protection of distribution systems with distributed energy resources," tech. rep., Joint Working Group B5/C6.26/CIRED, March 2015.

[125] J. Mora-Flòrez, J. Melèndez, and G. Carrillo-Caicedo, "Comparison of impedance based fault location methods for power distribution systems," *Electric Power Systems Research*, vol. 78, no. 4, pp. 657 – 666, 2008.

[126] A. Borghetti, M. Bosetti, C. Nucci, M. Paolone, and A. Abur, "Integrated use of time-frequency wavelet decompositions for fault location in distribution networks: Theory and experimental validation," *Power Delivery, IEEE Trans. on*, vol. 25, pp. 3139–3146, Oct 2010.

[127] J. Ren, S. Venkata, and E. Sortomme, "An accurate synchrophasor based fault location method for emerging distribution systems," *Power Delivery, IEEE Transactions on*, vol. 29, pp. 297–298, Feb 2014.

[128] P. Romano, M. Pignati, and M. Paolone, "Integration of an IEEE std. c37.118 compliant PMU into a real-time simulator," in *the 2015 IEEE PowerTech Conference*, 2015.

[129] S. Boyd and L. Vandenberghe, *Convex Optimization*. Cambridge University Press, 2004.

[130] B. Gärtner and J. Matousek, *Approximation algorithms and semidefinite programming*. Springer Science & Business Media, 2012.

[131] A. Van den Bos, *Parameter estimation for scientists and engineers*. New York City, NY: John Wiley & Sons, 2007.

LORENZO ZANNI

Chemin du Bochet 33 ⋄ 1025 Saint Sulpice, Switzerland
+41 078 679 67 18 ⋄ lorenzo.zanni@epfl.ch

RESEARCH INTERESTS

- Smart grids
- Real-time monitoring of power systems via phasor measurement units (PMUs)
- Power-system state estimation
- Fault location and protective relaying

EDUCATION

École Polytechnique Fédérale de Lausanne (EPFL) April 2013 - Present
PhD in Energy, SCI-STI-RC Group and DESL *Lausanne, Switzerland*

- Thesis title: "Power-System State Estimation based on PMUs: Static and Dynamic Approaches – from Theory to Real Implementation" (supervisor: Dr. Rachid Cherkaoui, co-supervisor: Prof. Mario Paolone).

Northeastern University (NEU) Oct. 2015 - Dec. 2015
Visiting researcher, Prof. Ali Abur's Power Systems Group *Boston, USA*

- Research related to the PhD thesis.

University of Bologna Sep. 2010 - Dec. 2012
M.Sc. in Electrical Engineering *Bologna, Italy*

- Thesis title: "Advanced state estimation for unbalanced distribution networks" (supervisor: Prof. Carlo Alberto Nucci).
- Final mark: 110/110 with honors.

University of Bologna Sep. 2007 - Dec. 2010
B.Sc. in Electrical Engineering *Bologna, Italy*

- Thesis title: "Calculation of induced over-voltages in overhead lines due to indirect lightnings via the finite-element method" (supervisor: Prof. Mario Paolone).
- Final mark: 110/110 with honors.

PROFESSIONAL EXPERIENCE

ALSTOM TIS (Transport Information Solution) Jun. 2010 - Jul. 2010
Internship *Bologna, Italy*

- Design of the electrical substations for the supply of high-speed trains.

SCIENTIFIC PUBLICATIONS

Book Chapters

1. M. Paolone, J.-Y. Le Boudec, S. Sarri and L. Zanni, "Static and recursive PMU-based state estimation processes for transmission and distribution grids", Chapter 6 of the book: F. Milano, "Advances in Power System Modelling, Control and Stability Analysis", Institute of Engineering and Technology (IET), 2016.

Journal papers

2. S. Sarri, L. Zanni, M. Popovic, J.-Y. Le Boudec, and M. Paolone, "Performance assessment of linear state estimators using synchrophasor measurements," *IEEE Trans. on Instrumentation and Measurement*, vol. 65, no. 3, pp. 535–548, Mar. 2016.

3. M. Pignati, L. Zanni, P. Romano, R. Cherkaoui and M. Paolone, "Fault Detection and Faulted-Line Identification in Active Distribution Networks using Synchrophasors-based Real-Time State Estimation," in *IEEE Trans. on Power Delivery*, vol. 32, no. 1, pp. 381–392, 2017.

4. L. Zanni, J.-Y. Le Boudec, R. Cherkaoui and M. Paolone, "A Prediction-Error Covariance Estimator for Adaptive Kalman Filtering in Step-Varying Processes: Application to Power-System State Estimation," in *IEEE Trans. on Control Systems Technology*, vol.-, no.-, pp.-, 2016.

5. L. Zanni, J.-Y. Le Boudec, R. Cherkaoui and M. Paolone, "Linear Power-System State Estimation with Zero-Injection Equality Constraints via LQ-Decomposition," Submitted to *IEEE Trans. on Power Systems*.

Conference papers

6. M. Paolone, M. Pignati, P. Romano, S. Sarri, L. Zanni, and R. Cherkaoui, "A Hardware-in-the-Loop Test Platform for the Real-Time State Estimation of Active Distribution Networks using Phasor Measurement Units," in *Proc. Cigr SC6 Colloquium*, Yokohama, Japan, 6–9 Oct. 2013.

7. L. Zanni, S. Sarri, M. Pignati, R. Cherkaoui, and M. Paolone, "Probabilistic assessment of the process-noise covariance matrix of discrete Kalman filter state estimation of active distribution networks," in *Proc. 13th International Conference on Probabilistic Methods Applied to Power Systems (PMAPS)*, Durham, U.K., 7–10 Jul. 2014, pp. 1–6.

8. M. Pignati, L. Zanni, S. Sarri, R. Cherkaoui, J.-Y. Le Boudec and M. Paolone, "A pre-estimation filtering process of bad data for linear power systems state estimators using PMUs," in *Proc. 18th Power Systems Computation Conference (PSCC)*, Wroclaw, Poland, 18–22 Aug. 2014, pp. 1–8.

9. M. Pignati, M. Popovic, S. Barreto, R. Cherkaoui, G. D. Flores, J.-Y. Le Boudec, M. Mohiuddin, M. Paolone, P. Romano, S. Sarri, T. Tesfay, D.-C. Tomozei and L. Zanni, "Real-time state estimation of the EPFL-campus medium-voltage grid by using PMUs," in *Proc. 6th IEEE PES ISGT USA, Washington*, DC, USA, 18–20 Feb. 2015, pp. 1–5.

10. L. Zanni, D. Colangelo, R. Cherkaoui, and M. Paolone, "Impact of Synchrophasor Measurement Types and Uncertainties on the Accuracy of Distribution System Linear State Estimators," in *Proc. IEEE PowerTech, Eindhoven*, Netherlands, 29 Jun.–02 Jul. 2015, pp. 1–6.

11. D. Colangelo, L. Zanni, M. Pignati, P. Romano, M. Paolone, J.-P. Braun, and L.-G. Bernier, "Architecture and Characterization of a Calibrator for PMUs Operating in Power Distribution Systems," in *Proc. IEEE PowerTech, Eindhoven*, Netherlands, 29 Jun.–02 Jul. 2015, pp. 1–6.

12. S. Sarri, M. Pignati, P. Romano, L. Zanni and M. Paolone, "A hardware-in-the-loop test platform for the performance assessment of a PMU-based real-time state estimator," in *Proc. IEEE PowerTech, Eindhoven*, Netherlands, 29 Jun.–02 Jul. 2015, pp. 1–6.

13. M. Hoefling, F. Heimgaertner, M. Menth, K. V. Katsaros, P. Romano, L. Zanni, and G. Kamel, "Enabling resilient smart grid communication over the information-centric C-DAX middleware," in *Proc. International Conference and Workshops on Networked Systems*, Cottbus, Germany, 9–12 Mar. 2015, pp. 1–8.

AWARDS

- Best Paper Award at the 13$^{\text{th}}$ International Conference on Probabilistic Methods Applied to Power Systems (PMAPS), 2014.
  L. Zanni, S. Sarri, M. Pignati, R. Cherkaoui, and M. Paolone, "Probabilistic assessment of the process-noise covariance matrix of discrete Kalman filter state estimation of active distribution networks," in *Proc. 13th International Conference on Probabilistic Methods Applied to Power Systems (PMAPS)*, Durham, U.K., 7–10 Jul. 2014, pp. 1–6.
- Best Poster Award at the 2$^{\text{nd}}$ Annual Conference SCCER-FURIES, 25 Nov. 2015.
  P. Romano, A. Derviskadic, L. Zanni, M. Pignati, J.-Y. Le Boudec, and M. Paolone, "Real-time state estimation of the EPFL-campus medium voltage grid by using PMUs".

RESEARCH PROJECTS

NanoTera S^{3}Grid – SmartGrids April 2013 - April 2017

· Development of new technologies dedicated to the real-time monitoring and management of smart grids with validation in the EPFL-campus distribution network (`smartgrid.epfl.ch`).

RT-PMU January 2014 - January 2017

· Real-time monitoring of the sub-transmission network of the city of Lausanne (operated by Services industriels de Lausanne – SiL) via state estimation based on phasor measurement units.

SUPERVISED STUDENTS

- Derviskadic, A., "Development of a PMU-based RTSE of sub-transmission networks: theory and experimental validation based on the Lausanne 125 kV grid", M.Sc. Thesis project, Spring Semester 2014-2015.

TEACHING EXPERIENCE

- *Analyse and Numérique*, Undergraduate class, EPFL, 2015.
- *Smart-grid Technologies*, Graduate class, EPFL, 2015-present.
- *Distribution de l'énergie électrique*, Undergraduate class, EPFL, 2016-present.
- *Conversion d'énergie*, Undergraduate class, EPFL, 2016-present.

PEER REVIEWS

- IEEE Trans. on Industrial Informatics, since 2015
- IEEE Trans. on Control Systems Technology, since 2016
- Elsevier Electric Power Systems Research Journal (EPSR), since 2015
- Elsevier Sustainable Energy, Grids and Networks Journal (SEGAN), since 2015
- 19$^{\text{th}}$ Power Systems Computation Conference (PSCC), 2016
- IEEE PES General Meeting, 2016
- Innovative Smart Grid Technologies Conference (ISGT), 2016

LANGUAGE SKILLS

Italian	Native
English	Fluent
French	Fluent